UNIVERSITY OF OKLAHOMA

GRADUATE COLLEGE

# ESTABLISHING THREE-DIMENSIONAL SUPER-RESOLUTION MICROSCOPY METHODS FOR QUANTIFYING INTRACELLULAR NANOPARTICLE DISTRIBUTION

A DISSERTATION

SUBMITTED TO THE GRADUATE FACULTY

in partial fulfillment of the requirements for the

Degree of

DOCTOR OF PHILOSOPHY

By

VINIT SHETH

Norman, Oklahoma

2023

ESTABLISHING THREE-DIMENSIONAL SUPER-RESOLUTION MICROSCOPY METHODS FOR QUANTIFYING INTRACELLULAR NANOPARTICLE DISTRIBUTION

A DISSERTATION APPROVED FOR THE
STEPHENSON SCHOOL OF BIOMEDICAL ENGINEERING

BY THE COMMITTEE CONSISTING OF

Dr. Stefan Wilhelm, Chair

Dr. Wei R. Chen

Dr. Qinggong Tang

Dr. John P. Masly

**Acknowledgments**

First, I would like to thank my PhD advisor, Dr. Stefan Wilhelm, to whom I owe a tremendous debt of gratitude for your never-ending mentorship and support. Thank you for giving me the opportunity to join your lab and for helping me grow into the researcher I am today. I greatly appreciate the independence you allowed me to have while always being open to discussing the scientific directions we are taking.

Next, I would like to thank my PhD committee members, Dr. Wei R. Chen, Dr. Qinggong Tang, and Dr. John P. Masly for your continuous support and advice throughout my PhD journey.

Thanks to Dr. Nathan Donahue, Dr. Wen Yang, Dr. Lin Wang, Dr. Alex Frickenstein, Dr. Seren Hamsici, Dr. Gokhan Gunay and Dr. Emi Kiyotake for all of your help and friendship over the years, I have learned so much from all of you. I would further like to thank Dr. Tingting Gu and the staff of the Samuel Roberts Noble Microscopy Laboratory, as well as Ben Fowler and the staff of the Oklahoma Medical Research Foundation Imaging Core Facility, the training and mentorship you have given me in the use of light microscopes has been essential to the research described in this dissertation. Thanks to Dr. Paul DeAngelis, Dixy Green, Dr. Joerg Bewersdorf, Dr. Ons M'Saad, Dr. Xuxin Chen, and Meredith Jones for your assistance in getting our collaborated manuscript to the height of being published in ACS Nano.

I would also like to thank Hamilton Young, Amberlynn Demko, James Lowe, Yuxin He, Majood Haddad, Alyssa Holden, Sarah Butterfield, and Emmy Francek for your help with experiments over the years. I also thank Mohammad Jamei and Jeesoo Park, who

will be continuing on my work on applying super-resolution microscopy to study nanoparticle intracellular distribution.

I would like to give a special thanks to my undergraduate mentees, Abbie Thomas and Rylee Newport. Thank you for your never-ending help and support throughout all the highs and lows of our research. I have learned as much from the both of you as I hope you have learned from me. You are amazing scientists, and I wish you all the best in your own graduate studies. The future is bright, and I look forward to seeing all the great results you will produce!

Finally, I would like to thank my family and friends, whose support and encouragement have greatly helped me get through this long journey. No matter how far apart we may be physically, we have always been and always will be together.

## Table of Contents

## List of Figures

### Chapter 1:



### Chapter 2:

## List of Tables

### Chapter 1:



### Chapters 2 and 3:



### Chapter 4:

**Abstract**

The systemic administration of nanomedicine formulations has been described as a promising treatment option for solid tumors at both preclinical and clinical stages. However, these treatments are currently limited to improved safety over the administration of free drugs, while improvements to efficacy have been limited by a noted low accumulation of nanoparticles in cancer cells. The mechanisms for nanoparticle delivery across tumor blood vessels into the tumor microenvironment are not fully understood as a result of the physical limitations of the current standard methods of visualizing nanoparticle accumulation and intracellular transport in cancer cells. Most intracellular vesicles typically involved with the transport of nanoparticles across tumor blood vessels are sized smaller than the spatial resolution limit of light microscopy (~200 nm laterally), whereas electron microscopes, which provide sufficient lateral resolutions for visualizing these vesicles, are typically limited to thin biological samples, making it difficult to acquire three-dimensional (3D) visualizations of cells. To address these challenges, in this dissertation, quantitative 3D super-resolution light microscopy methods were applied to study the intracellular distribution of metallic and organic nanoparticle formulations in cultured cancer cells. We employed a method known as expansion microscopy, which involves embedding cell samples within swellable hydrogels to physically enlarge the sample >10X their original size for super-resolution imaging. Intracellular label-free metallic nanoparticles were visualized with light scattering imaging, while organic nanoparticles were visualized with internalized fluorescent tags. Since expansion microscopy is compatible with the labeling of intracellular features, this method enables the determination of the precise location of nanoparticles within cells, which can

be used for studying intracellular nanoparticle trafficking with high spatial resolution in 3D. The successful application of this method will empower new research in nanomedicine for the development of safer and more effective treatments.

## Objectives and Aims

This dissertation presents methods of visualizing and quantifying inorganic and organic nanoparticle distribution in cultured cancer cells with three-dimensional super-resolution microscopy towards the goal of studying nanoparticle transport mechanisms across tumor blood vessels to improve the delivery of nanomedicines to solid tumors.

In Chapter 1, we review nanoparticle transport pathways and mechanisms across tumor blood vessels. Nanoparticle transport across tumor blood vessels is a key step in nanoparticle delivery to solid tumors. However, the specific pathways and mechanisms of this nanoparticle delivery process are not fully understood. Here, we explore the biological and physical characteristics of the tumor vasculature and the tumor microenvironment and discuss how these features affect nanoparticle transport across tumor blood vessels. We discuss biological and physical methods to deliver nanoparticles into tumors and explore paracellular and transcellular nanoparticle transport pathways.

In Chapter 2, our aim was to establish a method for visualizing label-free metallic nanoparticle distribution in cultured cells with three-dimensional super-resolution microscopy. Super-resolution microscopy can transform our understanding of nanoparticle-cell interactions. Here, we established a super-resolution imaging technology to visualize nanoparticle distributions inside mammalian cells through the use of protein-retention expansion microscopy (proExM). The cells were exposed to metallic nanoparticles and then embedded within different swellable hydrogels to enable quantitative three-dimensional (3D) imaging approaching electron microscopy-like resolution using a standard light microscope. By exploiting the nanoparticles' light

scattering properties, we demonstrated label-free imaging of intracellular nanoparticles with ultrastructural context.

In Chapter 3, our aim was to improve the maximum spatial resolution that we had achieved in Chapter 2 for the quantitative analysis of metallic nanoparticle intracellular distribution. We adopted an alternative expansion microscopy protocol, pan-ExM, which provides significantly higher resolution than proExM, and allows for the quantitative analysis of label-free nanoparticle distribution within individual intracellular vesicles in 3D. We validated relative differences between nanoparticle cellular accumulation for various surface modifications using mass spectrometry and determined the intracellular nanoparticle spatial distribution in 3D for entire single cells.

In Chapter 4, our aim was to establish a method for visualizing organic nanoparticle distribution in cultured cells with three-dimensional super-resolution microscopy. Organic nanoparticles, particularly liposomes, are more clinically relevant for the treatment of cancers than metallic nanoparticles because of their improved biocompatibility and versatile cargo carrying capabilities. We adopted a new expansion microscopy protocol known as Magnify, which better retains lipids, the primary component of liposomes, in expanded cells than pan-ExM. Here, we demonstrated that Magnify allows for the 3D-super-resolution visualization of fluorescent large-molecule cargo encapsulated in liposomes within intracellular vesicles of cell.

Finally, in Chapter 5, we conclude with a summary of our main findings and discussions of how our methods can be applied for studies towards improving the efficacy of nanomedicine for treating solid tumors, limitations, and future directions.

This super-resolution imaging platform technology may be broadly used to understand the nanoparticle intracellular fate in fundamental and applied studies to potentially inform the engineering of a new generation of safer and more effective nanomedicines.

# Chapter 1: Strategies for Delivering Nanoparticles across Tumor Blood Vessels

## 1.1. Introduction

There are over 10 million cancer related deaths worldwide each year with a projected increase in annual new cases.[1] As a result, there is a need for safe and effective treatments. The four cancer treatment strategies that are commonly used in the clinic are: (i) cytoreductive surgery; (ii) radiation therapy; (iii) chemotherapy; and (iv) immunotherapy.[2] Nanomedicine can be applied to each of these four treatment regimens at the preclinical and clinical stages. For example, nanoparticles have been applied in imaging guided surgery;[3,4] as agents for localizing heat or radiation to tumors and overcoming radiation resistance; [5–7] as clinically approved chemotherapeutic drugs, such as Doxil® and Abraxane®;[8] and in the development of safer and more effective immunotherapeutics.[9] To elicit clinical benefits, all of these strategies have a common need for efficient nanoparticle tumor delivery.

The most direct way to deliver nanoparticles into a solid tumor is by intratumoral injection.[10] While this approach may result in a large number of nanoparticles localized within the tumor, its usefulness and practicality are limited. For example, nanoparticles tend to distribute inhomogeneously throughout the tumor microenvironment upon local administration due to the relatively dense extracellular matrix that limits nanoparticle diffusion.[11] In addition, it may not be feasible to treat metastatic tumors with many neoplastic lesions throughout the body via local injections, meaning that systemic administration is needed.[12]

Systemically administered nanoparticles have shown promise at both preclinical and clinical stages for diagnosis and treatment of cancer, however, there are several delivery barriers that nanoparticles need to overcome *en route* to solid tumors. Each barrier is tied to the distinct phase of the nanoparticle's journey to reach its destination, outlined in the so-called CAPIR cascade. This 5-step cascade describes nanoparticles during: (i) **c**irculation throughout the blood stream; (ii) **a**ccumulation in the tumor microenvironment; (iii) **p**enetration deeper through tumor tissues; (iv) **i**nternalization into tumor cells; and (v) and **r**elease of their therapeutic payloads.[13]

The typical nanoparticle tumor delivery efficiency has been quantified to be ~0.7% (median) of the injected nanoparticle dose.[14] As outlined in Figure 1.1, there are several reasons for this low nanoparticle delivery efficiency. Upon injection into the blood stream, nanoparticles are subject to proteins adsorbing onto their surfaces, forming what is known as a protein corona. The protein corona changes the nanoparticle physiochemical properties from a synthetic identity to a biological identity and may affect pharmacokinetics, biodistribution, and toxicity.[15–18] Among these adsorbed proteins are opsonins, which may trigger phagocytosis in macrophages and other cells to swiftly remove circulating nanoparticles from the bloodstream.[19,20] Nanoparticle accumulation in off-target organs greatly reduces the amount of nanoparticles that are in circulation.[21] As a result, there has been much research focused on increasing the nanoparticle blood circulation time by reducing nanoparticle interactions with serum proteins and immune cells. The most common method to achieve this goal is coating nanoparticle surfaces with anti-fouling polymers, such as poly(ethylene glycol), PEG.[22] Recently, nanoparticle surface modification with cellular membranes, such as membranes from red blood cells,

has emerged as an alternative method to camouflage nanoparticles and to increase blood circulation times.[23] In addition, Chan et al. have shown that there is a nanoparticle dose threshold for clearance from circulation. By administering doses of nanoparticles above the threshold (> 1 trillion nanoparticles in mice), the nanoparticle uptake rates of liver phagocytes, such as Kupffer cells, can be overwhelmed to reduce liver clearance. This strategy has been reported to result in nanoparticle tumor delivery efficiencies of up to 12% of the injected dose, with nanoparticles being found within 93% of tumor cells.[24]

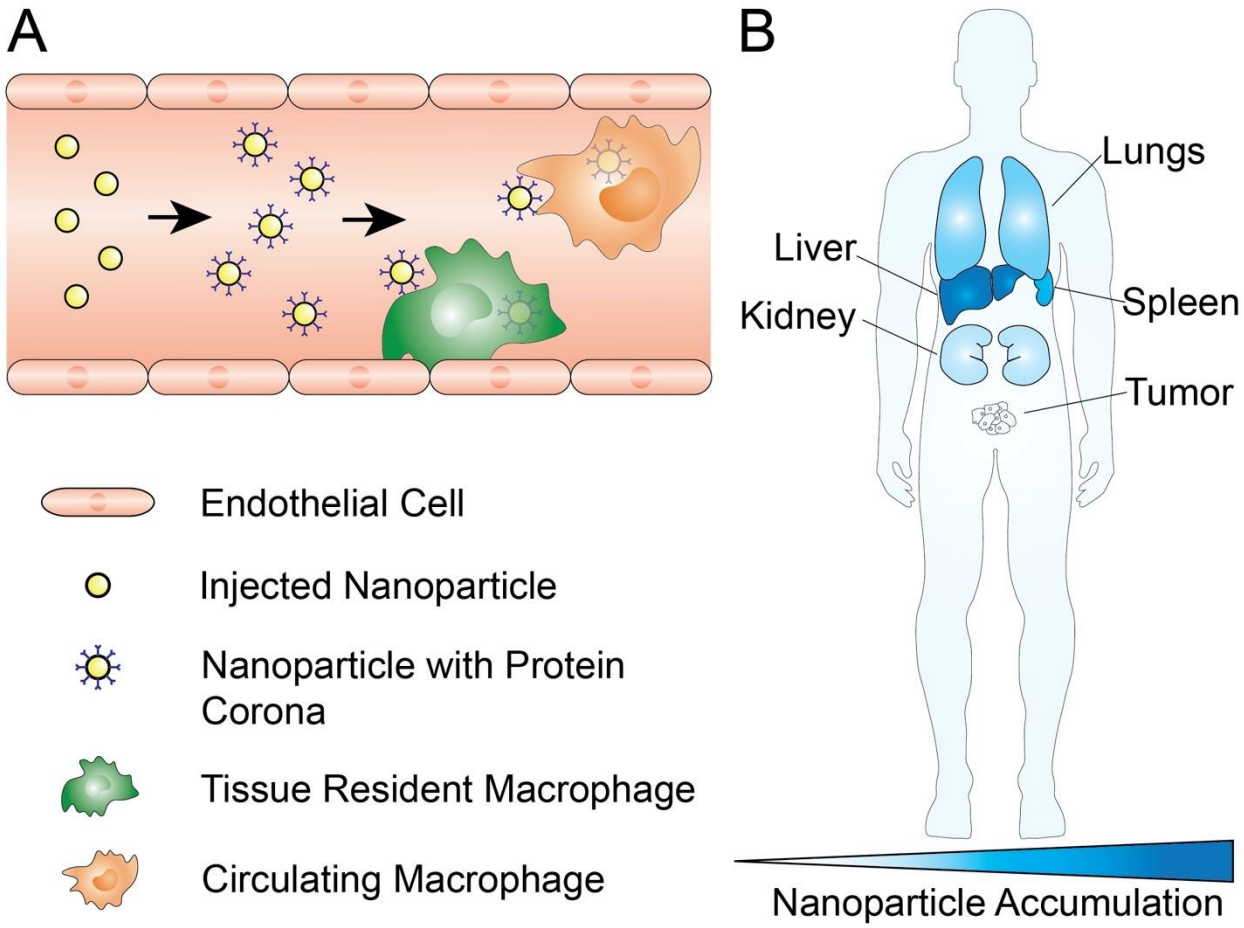


**Figure 1.1 Barriers to nanoparticle uptake into the tumor microenvironment.** A) After nanoparticles are introduced to the bloodstream, various proteins adhere to their surfaces, forming what is known as the protein corona; among them are opsonins, which trigger the phagocytosis of the nanoparticles by immune cells such as free or fixed macrophages. B) Off target accumulation of nanoparticles in organs results in fewer nanoparticles reaching the tumor microenvironment. The liver and spleen are typically responsible for a majority of the nanoparticle accumulation, followed by the lungs. This accumulation is largely dependent on the size of the nanoparticle. Due to the filtration limit of kidneys being roughly 6 nm, larger nanoparticles do not greatly accumulate in kidneys, however, the kidneys have a much larger role in the accumulation of smaller nanoparticles.

The next barrier for nanoparticles is the extravasation from the tumor blood vessels into the tumor microenvironment.[11,25] The longstanding paradigm of the enhanced permeability and retention (EPR) effect suggests that nanoparticles passively leak out from tumor vasculature between gaps in endothelial cells, coupled with poor lymphatic drainage of the tumor tissue.[26] Nanoparticle extravasation through leaky vasculature may occur through convection and diffusion, and may be limited by the increased interstitial fluid pressure observed in solid tumors.[27,28] In contrast to passive nanoparticle transport across tumor blood vessels as suggested by the EPR effect, transcytosis has been proposed as an active nanoparticle transport pathway since as early as the 1990s.[29] Chan et al. reported that only 3%-25% of gold nanoparticles reach solid tumors by passive transport, depending on nanoparticle size, indicating that up to 75%-97% of nanoparticles undergo active transcytosis transport. Interestingly, these studies were done with gold nanoparticle doses higher than the dose threshold for improved tumor delivery of ~1 trillion nanoparticles in mice as reported by Chan et al. in a later study, with nanoparticle doses ranging from $2x10^{12}$ - $1x10^{14}$ nanoparticles, depending on size.[24,30] There may be a possibility that the nanoparticle extravasation mechanisms are affected by changes in nanoparticle dose. More research is needed to determine how nanoparticle dose may alter and affect extravasation mechanisms, pathways, and tumor delivery efficiency.

In this chapter, we discuss the specific properties of the tumor microenvironment and vasculature that need be considered for effective nanoparticle transport and tumor delivery. We review the common endocytic pathways that nanoparticles may undergo for transcellular transport across tumor endothelial cells, and how these endocytic pathways

may be exploited by specific nanoparticle designs for delivering nanomedicines to solid tumors.

## 1.2. The tumor microenvironment and vasculature

### 1.2.1 The tumor microenvironment

Solid tumors are generally composed of malignant parenchyma, and the surrounding benign tumor stroma.[14] Although the isolated stroma cannot form tumors when planted into host animals, it is essential in supporting tumor growth and architecture of the tumor microenvironment.[31] The tumor stroma is composed of diverse cell types, including cancer-associated fibroblasts and immune cells. Cancer-associated fibroblasts produce and remodel the extracellular matrix (ECM), and at the same time secret growth factors that induce angiogenesis or suppress immune cells with the goal to support tumor growth.

Many types of immune cells are found in solid tumors and execute various functions. Briefly, CD8+ cytotoxic T Cells, CD4+ Th1 helper T cells, NK cells, M1 macrophages and dendritic cells are generally considered as tumor inhibiting, while regulatory T cells (Treg), CD4+ Th2 helper T cells and M2 macrophages are immune suppressing, thus promoting angiogenesis, tumor growth, and metastasis.[32,33] Tumor and stromal cells are embedded in the ECM composed of collagen, fibronectin, fibrin, hyaluronan, and proteoglycans, which provide the mechanical support of the tumor microenvironment. At the same time, plenty of functional cytokines and growth factors, such as vascular endothelial growth factor (VEGF), disperse throughout the entire tumor

forming the non-cellular stroma together with the ECM. In addition, solid tumors are characterized by abnormal vasculature, low pH, hypoxia, high interstitial pressure, and crosstalk between individual tumor cell types.[11,34] All these complex components interplay in forming the tumor microenvironment and affect tumor development as well treatment responses (Figure 1.2).

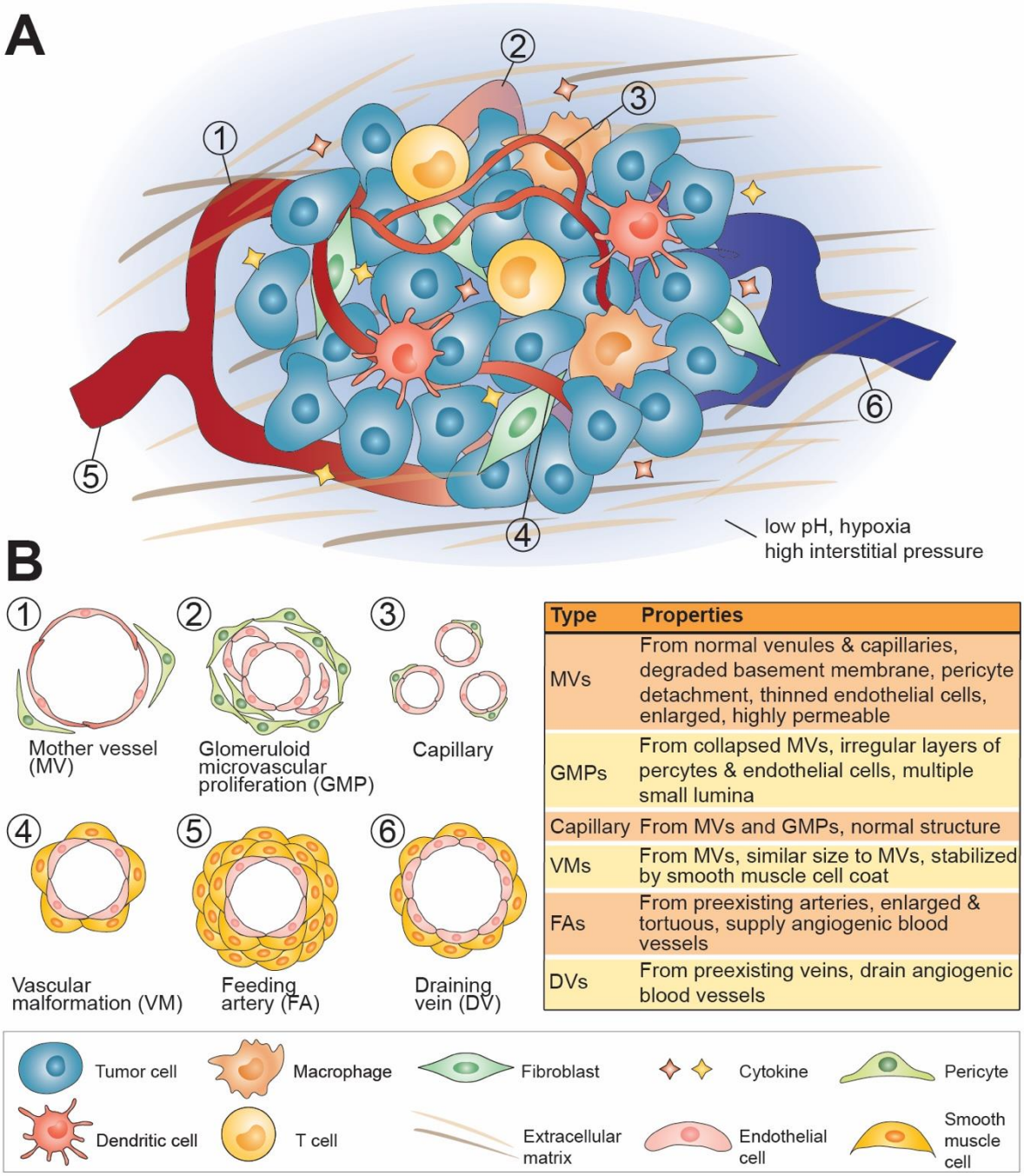


**Figure 1.2: Tumor architecture.** A solid tumor is composed of malignant parenchyma and benign tumor stroma that supports tumor growth and structure. There are diverse types of stromal cells including cancer-associated fibroblasts, immune cells, and other cells forming the cellular part of tumor stroma. The noncellular parts of the tumor stroma including extracellular matrix and cytokines surround and interact with the embedded cells. An abnormal vascular network is always observed in a solid tumor, which is essential for tumor supply. In addition, low pH, hypoxia, and high interstitial pressure are

characteristics of solid tumors. All these tumor components interplay to form a complex microenvironment and drive the tumor development. B) The tumor vasculature is highly abnormal and at least six types of blood vessels with different characteristics have been distinguished.

Besides the complex composition of solid tumors, the phenotype and ratio of both tumor and stroma cells are highly heterogeneous between different patients, different loci within the same patient, and even different sites within the same tumor.[35,36] The tumor development is dynamic and at different development stages, the microenvironment shows variable characteristics.[37] For example, cell plasticity, i.e., the ability of tumor cells to transform and switch their phenotype, is a considerable challenge in the development of cell targeted therapies.[38,39] Characteristics of the tumor microenvironment, as well as its interactions with nanoparticles, have been reviewed in greater detail by Mukherjee et al.[11]

### 1.2.2 Angiogenesis and tumor vasculature

Angiogenesis and neoangiogenesis are VEGF-dependent processes of forming new blood vessels from preexisting vessels to supply nutrients and oxygen to tumors for development and growth.[40] In some tumors, tissue growth is so fast that tumor cells are located relatively far away from blood vessels, which induces hypoxia, i.e., oxygen deprivation. Hypoxic cells then overexpress VEGF leading to neoangiogenesis by recruitment of bone marrow derived endothelial progenitor cells to the tumor vascular bed, where these cells mature and release other pro-angiogenic growth factors.[11,41] The newly formed tumor blood vessels are known to lack some of the structural integrity that is seen in healthy blood vessels. For example, tumor blood vessels may exhibit gaps between endothelial cells, and smooth muscle cells, pericytes, and basement membrane may be missing or exhibit discontinuity as a result of an abnormal expression of certain growth factors, such as angiopoietin-1.[42]

Dvorak et al. described six distinct types of tumor blood vessels: (i) mother vessels (MVs); (ii) glomeruloid microvascular proliferations (GMPs); (iii) capillaries; (iv) vascular malformations (VMs); (v) feeding arteries (FAs); and (vi) draining veins (DVs) (Figure 1.2).[43] Mother vessels are the first angiogenic blood vessels to form from existing venules and capillaries after the degradation of basement membrane, which provides structural support, and the detachment of pericytes, which help control blood flow.[44] This process allows for blood vessel expansion through the intravascular hydrostatic pressure, given that the two aforementioned vessel features that prevent vessel growth are removed, resulting in a thinned and highly permeable endothelium. When MVs collapse, GMPs are formed that accumulate pericytes and macrophages, while also making new basement membrane. Alternatively, MVs can accumulate smooth muscle cells and perivascular collagen to become VMs, which effectively reduces their permeability. Through arteriovenogenesis, FAs and DVs are formed from existing healthy veins and arteries, to supply and drain blood to and from the other types of tumor blood vessels.[31]

These differences in blood vessel structure are important to note for nanomedicine delivery purposes, as nanoparticles may likely interact with each type of blood vessel differently, which could result in varying nanoparticle delivery efficiencies throughout a single solid tumor. The differences could be potentially exploited, however, by designing nanoparticles that specifically target features that are present in some types of tumor vessels but not others, such as pericytes,[45] for better tumor accumulation and localization.

The intercellular gaps between endothelial cells in tumor blood vessels form the basis for nanoparticle extravasation according to the EPR effect. The EPR effect suggests that nanoparticles extravasate passively from tumor blood vessels to the tumor

microenvironment by convection and diffusion through the leaky vasculature. In addition, it is suggested that the impaired lymphatic system within solid tumors reduces nanoparticle clearance.[26] However, it has recently been suggested that the peritumoral lymphatic system drains nanoparticles from tumors and returns them to blood circulation in a size dependent manner.[46] The EPR effect has been a longstanding paradigm in cancer nanomedicine, and has been exploited as the main delivery mechanism for different types of nanoparticles to tumors, including inorganic (such as noble metal, oxide, upconversion and carbon-based nanoparticles) and organic nanoparticles (such as liposomes or lipid-based nanoparticles, polymeric nanoparticles and dendrimers).[25,47–54] However, it is not the only pathway for nanoparticles to cross tumor blood vessels, as depicted in Figure 1.3. In general, we can differentiate two nanoparticle transport pathways: (i) paracellular transport by diffusion through intercellular gaps; and (ii) transcellular nanoparticle transport by going through tumor endothelial cells.

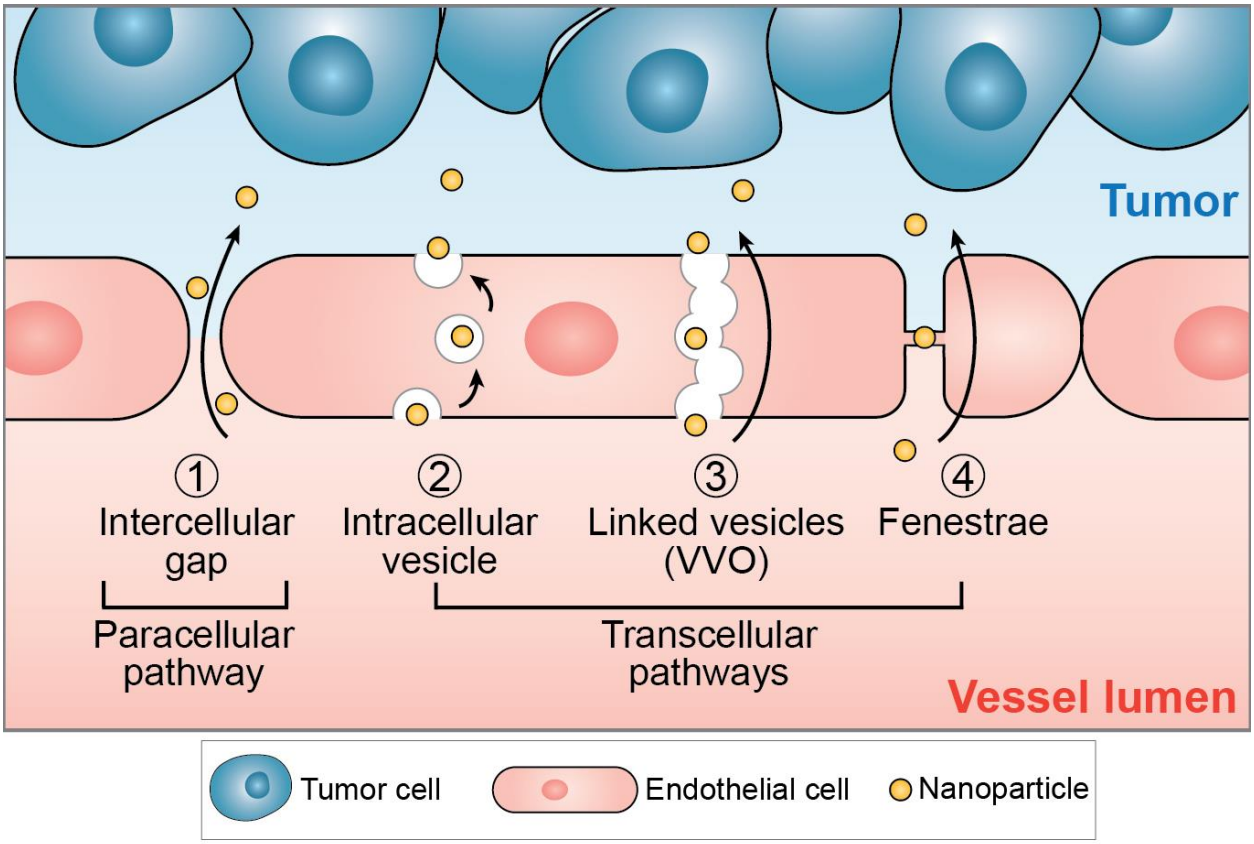


**Figure 1.3: Nanoparticles can extravasate from tumor vascular lumen into the tumor microenvironment by both paracellular 1) and 2–4) transcellular pathways.** For the paracellular pathway, nanoparticles transport passively through gaps in the endothelium, i.e., between adjacent endothelial cells. These intercellular gaps (up to 2 µm in size) result from the abnormal vessel structures caused by rapid tumor angiogenesis and are fundamental for the enhanced permeability and retention (EPR) effect. For transcellular pathways, nanoparticles get transported actively into the tumor microenvironment via intracellular vesicles or through transcellular pores. 2) When transported by intracellular vesicles, nanoparticles first enter the cell and locate in vesicles through endocytosis, then get transported across the cytoplasm, and finally exit the cell through exocytosis. 3) VVO and 4) fenestrae are both trans-endothelial pathways for nanoparticle transport. While VVOs are intracellular organelles composed of linked vesicles, fenestrae represent transcellular pores spanned by a fenestral diaphragm.

Transcellular nanoparticle transport is enabled by endocytic vesicles in tumor endothelial cells that deliver nanoparticles from the apical side of the cell to the basal side.[55] Particularly, it has recently been found that specific subsets of tumor endothelial cells govern nanoparticle transport into solid tumors, which comprise about 21% of the tumor endothelium.[56] While endocytosis is the primary mechanism and pathway for transcellular transport, there are a few alternatives. One of these alternative transcellular pathways may be mediated by vesiculo-vacuolar organelles (VVOs) inside tumor endothelial cells. Little is known about this VVO-mediated transport pathway. However, VVOs have been characterized by Dvorak et al. as membrane-bound, linked vesicles and vacuoles that create a channel for macromolecules to cross the endothelium.[57] VVOs are rarely observed in cultured endothelial cells under standard culture methods and may occur at greater frequency *in vivo.*[58] Further work is needed to determine if the VVO-mediated pathway is a viable transport route for nanoparticles and nanomedicines. Another potential nanoparticle transport pathway is through fenestrae, i.e., transcellular pores that are typically found in liver sinusoidal and glomerular endothelial cells,[59,60] which have also been observed and documented in tumor vessels, for example in mother vessels (MVs) and capillaries (Figure 1.3).[61] To understand and probe the nanoparticle transport mechanisms across tumor vasculature, the use of 3D microfluidic models that more truthfully recapitulate the tumor microenvironment *in vitro* may be of value.[62,63]

## 1.3. The entry of nanoparticles into the tumor microenvironment

### 1.3.1 Overview of existing paradigms

The field of cancer nanomedicine has gone through many advancements over the past few decades since the first electron micrograph of tumor cells in 1947, as summarized chronologically in Figure 1.4.[64] The introduction of liposomes and their later conjugation with antibodies for specific, active targeting, known as immunoliposomes, further serve as major milestones in the origin of the field.[65–67] In the 1970s and 1980s, methods of improving nanoparticle tumor delivery were already underway, as noted by the discovery that locally heating a tumor can cause an increase in nanoparticle extravasation until blood vessel destruction occurs.[68,69] Reports of receptor mediated endocytic nanoparticle uptake into tumor cells opened the door to the possibility of controlling cell specific nanoparticle delivery.[70]

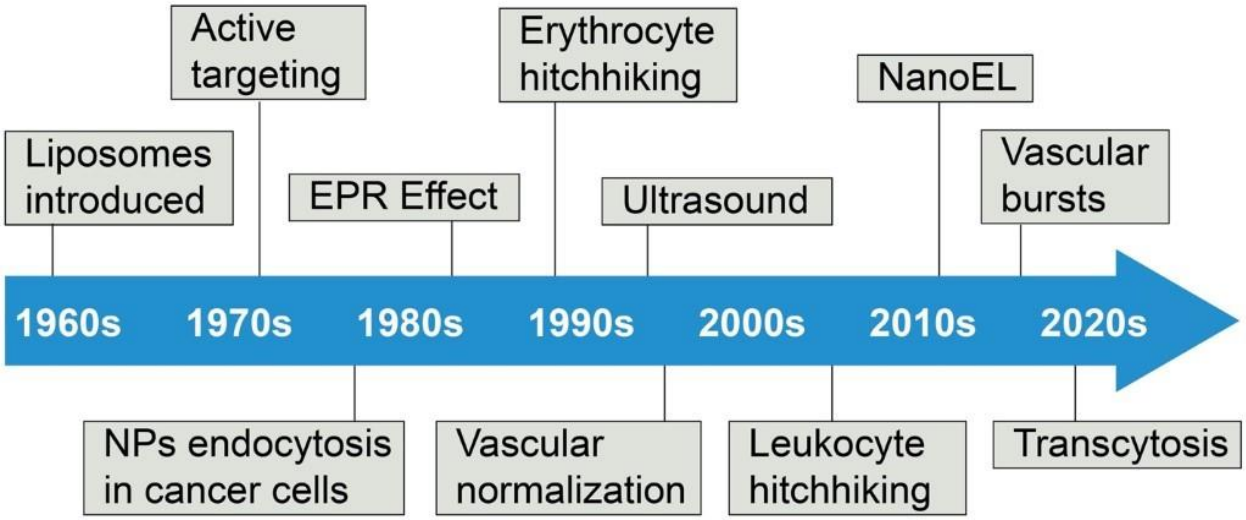


**Figure 1.4: Timeline of different suggested nanoparticle-tumor accumulation pathways and methods.** Since the first suggestion of nanotechnology, there have been many different pathways and methods suggested to explain and improve the extravasation of nanoparticles in to the TME.

The longstanding delivery paradigm in cancer nanomedicine, the EPR effect, was introduced in 1986 to explain that nanoparticles accumulate in tumors as a result of vascular leakiness and poor lymphatic drainage.[71] However, the well noted low nanoparticle tumor accumulation has brought the impact of the EPR effect into question.[14] Consequently, a variety of work has been done to find ways that improve nanoparticle tumor delivery and to understand the mechanisms behind it.

One of the earlier methods was erythrocyte hitchhiking, which involved removing erythrocytes from a patient, loading them with drugs, and re-administering them back into the patient.[72] This process has since evolved to have the removed erythrocytes conjugated to drug carrying nanoparticles, so that they would accumulate in the nearest downstream organ from the injection site.[73]

The concept of vascular normalization was then proposed as an extension of typical anti-angiogenic treatments. These combined treatments aim to make the tumor vasculature more functionally similar to normal vasculature by removing excessive endothelial cells that make up immature blood vessels, resulting in a less constricted delivery of therapeutics to tumors. Anti-angiogenic treatments are then applied to constrict the tumor vasculature to starve the tumor of nutrients needed for its survival.[74,75] It was recently shown that gold nanoparticles can accomplish this, along with inhibiting angiogenesis, by disrupting the signaling between tumor cells and endothelial cells.[76,77]

The use of ultrasound has been explored, as the tensile pressure of ultrasonic waves on tumors can cause blood vessel perforation and micro-convection in the tumor interstitium, leading to higher nanoparticle extravasation.[78] Later studies have shown that

ultrasound waves can be used to release drugs from liposomes[79] and microbubbles, with the ability to convert the latter into nanobubbles.[80]

Several years later, leukocyte hitchhiking was discussed, functioning similarly to erythrocyte hitchhiking, as it was shown that antigen-specific T cells can be removed and loaded with viral vectors, which will target tumors and transfer the viral vectors once re-administered.[81] It was shown that intravenously administered nanoparticles can be phagocytosed by monocytes, allowing for photothermal therapy to be applied. These cells will then travel to the tumor microenvironment and differentiate into tumor-associated macrophages (TAMs) to migrate into the hypoxic tumor core, where near-IR irradiation can destroy the TAMs and heat up the nanoparticles to destroy the surrounding tissue.[7] Recently, it was shown that photothermal therapy can be combined with vascular disruption agents that cause gold nanoparticles to aggregate at targeted locations, for an improved photothermal ablation of tumor cells.[82]

The physical methods described here are summarized in Table 1.1**,** along with current advances in their applications. Others methods, such as electroporation and the use of magnetic fields, are summarized in greater detail in a recently published review article by Mitragotri et al.[83]

**Table 1.1.** Examples of nanoparticle delivery mechanisms across tumor vasculature

| Method | Year First Described | Process | Description | Ref. |
|---|---|---|---|---|
| Active targeting liposomes | 1979 | Biological | Involves the attachment of specific antibodies or other molecules to the nanoparticle surface for targeting of complementary receptors on cancer cells. The tumor penetrating peptide, iRGD, and its derivatives, are widely used examples. | 66,67,84,85 |
| Heat Treatment | 1979 | Physical | Local heating of tumors several degrees above the average temperature has been shown to significantly increase the extravasation of nanoparticles until vessel destruction occurs. Photosensitive and paramagnetic nanoparticles are being studied to improve these effects. | 68,69,86 |
| Erythrocyte Hitchhiking | 1987 | Biological/Cell Mediated | This process has evolved from erythrocytes being removed from the patient and loaded with drugs and readministered to removed erythrocytes being conjugated with drug carrying nanoparticles and readministered to localize at the nearest downstream organ from the injection site.<br><br>Work has also been done on coating nanoparticles with intact membranes from erythrocytes containing the typically expressed surface proteins for improved circulation. | 23,72,73 |
| Vascular Normalization | 1996 | Biological | This is an extension of typical anti-angiogenic treatments which aim to make tumor vasculature more functionally similar to normal vasculature by removing excessive endothelial cells that make up immature blood vessels, for a less constricted delivery of therapeutics to tumors before cutting off the blood supply to the tumor.<br><br>Anti-angiogenic nanoparticles loaded with anti-cancer drugs are being explored as a method of simultaneously normalizing tumor vasculature and deliver cytotoxic drugs. | 74,75,87 |
| Ultrasound | 1999 | Physical | The tensile pressure from ultrasonic waves directed at tumors have been shown to cause blood vessel perforation via cavitation, as well as microconvection that results in higher extravasation. | 78,79 |

| | | | | |
|---|---|---|---|---|
| | | | Ultrasound has also been used to cause the release of drugs such as doxorubicin from liposomes upon insonation, possibly through the formation of transient pores or other membrane defects | |
| Leukocyte Hitchhiking | 2005 | Biological/Cell Mediated | Antigen-specific T cells can be removed and loaded with viral vectors, that once readministered, will target tumors and transfer the viral vectors.<br><br>Intravenously administered nanoparticles can be phagocytosed by monocytes, which travel to the tumor microenvironment and differentiate in to tumor-associated macrophages (TAMs) to migrate in to the hypoxic tumor core. Near-IR irradiation can be directed towards the tumor, which destroys the TAMs and heats up the nanoparticles to destroy surrounding tissues.<br><br>The membranes of leukocytes can be coated on to nanoparticles in a similar manner as discussed above with erythrocytes, which could be applied to tumor targeting. | 7,81,88 |

Significant work has also been done to describe the extravasation of nanoparticles from tumor vasculature based on the biological properties of endothelial cells. Leong et al. suggested that certain nanoparticles, such as titanium and gold nanoparticles, can induce the widening of gaps between endothelial cells by disrupting interactions between pairs of vascular endothelial cadherin, in a size and surface roughness dependent manner, allowing for nanoparticles to leak out of the vasculature, in a process they named NanoEL.[89–91] A different paracellular pathway mechanism called vascular bursts was proposed by Kataoka et al., who suggested that dynamic vents open and close at endothelial cell junctions, causing fluid to flow outwards into the tumor interstitium and carrying nanoparticles with it.[92] It has also been suggested that these types of vents can be induced by picosecond pulsed laser irradiation for improved nanoparticle transport across endothelial barriers.[93]

In a recent paper by Chan et al., the contribution of paracellular nanoparticle transport across tumor blood vessels was quantified using a so-called Zombie model, a fixed tumor-bearing mouse model with blood artificially circulating with a peristaltic pump. Given that fixed cells cannot perform active transport, the only nanoparticles that could accumulate in a solid tumor were those that passively leaked from intercellular gaps. The passive paracellular transport pathway was found to only contribute to 3%-25% of the total nanoparticle tumor accumulation seen in living control tumor-bearing mice.[30] Combined with transmission electron micrographs of nanoparticles inside intracellular vesicles within tumor endothelial cells, this study suggests that nanoparticles primarily take active transcellular routes to transport from tumor blood vessels into the tumor microenvironment.

### 1.3.2 Endocytosis mechanisms of tumor endothelial cells

For nanoparticles to transcytose across the tumor endothelium, they first need to endocytose into tumor endothelial cells. There are many different pathways that have been defined for endocytosis, but not all of them may be useful for transcytosis. The most common of these pathways are clathrin-mediated endocytosis, caveolae-mediated endocytosis, and macropinocytosis (Figure 1.5). While caveolae-mediated endocytosis is the pathway that is most associated with transcytosis across endothelial barriers, clathrin-mediated endocytosis is well-noted as a transcytotic mechanism for crossing the blood-brain barrier. It has also been suggested that both clathrin-mediated and macropinocytosis contribute to blood vessel permeability as well.[94–96] Several groups have reported the endocytic cell uptake of various nanoparticles, with suggestions that nanoparticles take multiple different uptake routes.[97,98] Understanding the mechanisms behind these endocytosis pathways will allow for targeting of specific transport routes to deliver nanomedicines more efficiently into tumors.

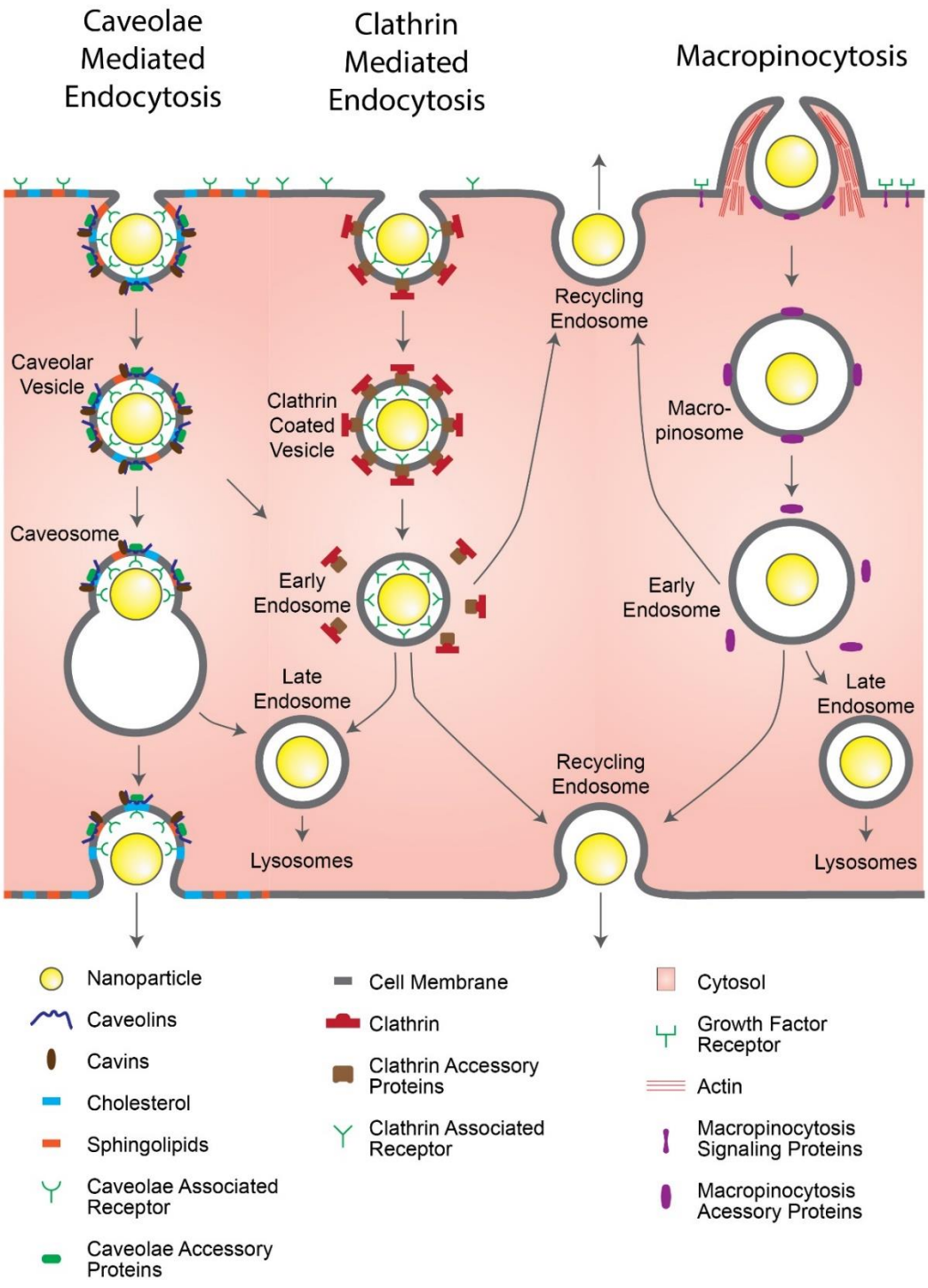


**Figure 1.5. Common endocytic pathway mechanisms in endothelial cells.** The specific pathways that nanoparticles take to enter endothelial cells vary, with the receptors that trigger the pathways as well as the nanoparticles' destination varying with the pathways themselves. Cell membrane invaginations are a typical occurrence for the receptor-mediated endocytic pathways of caveolae-mediated endocytosis and clathrin-

mediated endocytosis, however, caveolar vesicles are typically trafficked to the endoplasmic reticulum before being exocytosed, while clathrin coated vesicles are typically trafficked to lysosomes for degradation. The growth factor triggered macropinocytosis involves a heavy actin remodeling to nonspecifically engulf fluid in the area, packaging any contents in to a macropinosomes, which are also typically trafficked to lysosomes for degradation.

#### 1.3.2.1 Clathrin-mediated endocytosis

Clathrin-mediated endocytosis is a receptor specific form of endocytosis that uses vesicles coated with the triskelion protein, clathrin, to internalize materials that bind to its surface receptors.[99] Clathrin does not directly bind to the cell membrane or its specific receptors, and as such, requires several other proteins for binding and vesicle formation.[100] Specific proteins of note are the AP-2 complex, which serves as an intermediate between the cell membrane and clathrin,[101] the clathrin assembly lymphoid myeloid leukemia protein (CALM), which helps control vesicle size,[102] and dynamin, which regulates the maturation of clathrin coated pits and also catalyzes the snipping of the vesicle from the membrane.[103] The vesicles formed in this process are typically sized at around 80 – 100 nm. However, it has been shown that nanoparticles (522 nm in size) conjugated with transferrin, a clathrin-mediated endocytosis tracer, have been uptaken by clathrin coated vesicles in HeLa cells, indicating that there is a potential variability in the vesicle size.[102,104]

Following the snipping of the vesicles, the clathrin coat is disassembled, allowing the removed proteins to be reused for other clathrin-mediated endocytosis events.[105] At this stage, the vesicles are sorted based on their ligand and receptor contents to early endosomes for trafficking to either late endosomes and are transported to lysosomes for degradation (seen with the epidermal growth factor), or are recycled back to the membrane with the contents exocytosed (seen with the transferrin).[106–108] The recycling endosome has been shown to traffic to either the apical surface or the basal/basolateral surfaces in other cell types such as blood-brain barrier endothelial cells and epithelial cells, which could be useful as a transcytotic pathway for nanoparticle tumor

delivery.[109,110] Clathrin-mediated endocytosis has been of particular interest for blood-brain barrier permeability,[111,112] though it may still be relevant for nanoparticle extravasation in tumor vasculature. This concept is evidenced by Bendas et al., who used liposomes conjugated with antibodies against vascular cell adhesion molecule 1 (VCAM-1), which is expressed on activated tumor endothelial cells, to access a clathrin-mediated uptake pathway in a mouse xenograft tumor model (Colo677 - human lung cancer).[113] Further research is needed to determine if a basal recycling endosome pathway can be exploited for the transcytotic delivery of nanomedicine across tumor blood vessels.

#### 1.3.2.2 Caveolae-mediated endocytosis

Caveolae-mediated endocytosis is another form of receptor specific endocytosis that is based on caveolae, membrane invaginations that are furnished with cholesterol and sphingolipids.[114] Caveolae are not ubiquitous; most cell types contain caveolae; however, they are more prevalent in endothelial cells, epithelial cells, smooth and striated muscle cells, adipocytes, and fibroblasts.[115] Alongside their endocytic capabilities, they have several other functions, including reducing the tension a cell experiences under mechanical stress [116], regulating intracellular signal transduction,[117] and mediating neurovascular coupling.[118]

The caveolin family of proteins serve major roles in the functions of caveolae. Caveolin-1 is a cholesterol-binding structural protein that surrounds the invaginations and is necessary for the formation of caveolae.[119] Caveolin-2 has a role in signal regulation and is dependent upon caveolin-1.[120] Caveolin-3 is similar to caveolin-1, however, it is

mostly found in muscle cells.[121] The more recently discovered cavin family of proteins also serve essential structural roles for the formation of caveolae.[122] Dynamin has also been shown to be involved in the scission of the endocytic vesicle of caveolae from the plasma membrane, as it does in clathrin-mediated endocytosis, forming vesicles that are typically 50-100 nm wide.[55,123] While caveolin coats do not disassemble before fusing with endosomes unlike clathrin, their vesicles share a similarity in having multiple destinations based on their cargo.[108,124] These endosomes can be trafficked to lysosomes for degradation or trafficked to the Golgi bodies and endoplasmic reticulum for transcytotic purposes.[125,126] This characteristic makes caveolar endocytosis particularly attractive for the delivery of nanoparticles across tumor vasculature.

Malik et al. have demonstrated the targeting of caveolae-mediated endocytosis in bovine lung microvessel endothelial cells using polymer nanoparticles coated with fluorescently tagged albumin, a caveolae-mediated endocytosis tracer.[127] Similarly, Astilean et al. have shown the specific targeting of caveolae-mediated endocytosis in NIH:OVCAR-3 cells (human ovarian cancer) using nanoparticles made of albumin, conjugated with folic acid for folate receptor alpha targeting, as this marker is overexpressed on these cells.[128,129] *In vivo* targeting of caveolae has been demonstrated by Schnitzer et al., who used gold nanoparticles conjugated with aminopeptidase P antibodies to target caveolae in the lung endothelium of rats,[130] or gold nanoparticles conjugated with annexin A1 antibodies to target caveolae in the tumorous lung endothelium of rats.[131] These experiments have shown that nanoparticles can be modified in specific ways to target and to exploit transcytosis in tumor endothelial cells using different transport mechanisms, including caveolae mediated transport.

#### 1.3.2.3 Macropinocytosis

Macropinocytosis is a nonspecific form of fluid phase endocytosis that involves membrane extensions for relatively large-volume engulfment.[132] This process is triggered and controlled by growth factor signaling, which causes the remodeling of actin in the cytoskeleton to create membrane ruffles that then close back in towards the rest of the membrane.[133,134] The resulting vesicles, known as macropinosomes, vary greatly in size, typically ranging from 500 nm to 2,500 nm, though sizes as low as 200 nm and as high as 5,000 nm are also possible.[135,136]

Similarly to clathrin coated vesicles, macropinosomes can either mature from early endosomes to late endosomes before trafficking to lysosomes for degradation or can recycle their contents back to the apical or basal/basolateral membrane.[109,137] The visualization of macropinosomes is somewhat less direct than the previously discussed vesicles; while clathrin-coated vesicles and caveolae can be visualized optically with fluorescently tagged antibodies against clathrin heavy/light chain and caveolin-1, macropinosomes have no such marker.[132] Consequently, alternative methods had to be employed, with the most commonly used of them being visualizing the uptake of fluorescently tagged dextran,[138] an established macropinocytosis tracer, or by visualizing the rearrangement of fluorescently tagged f-actin.[139] Receptor tyrosine kinase activation and the oncogene RAS have been established as macropinocytosis triggers, with the process usually being positively regulated by environmental factors, such as nutrient availability through the amino acid activated mammalian target of rapamycin complex 1 (mTORC1).[140,141] Macropinocytosis has been suggested to be highly upregulated in cancers occurring from RAS mutations and serves the cancer cells' primary method for

their increased nutrient collection needs.[142] The increased level of uptaken proteins results in a higher availability of amino acids following lysosomal degradation, leading to higher mTORC1 activity.[143]

#### 1.3.2.4 Other endocytic or transcellular pathways

The described endocytic pathways are major cell uptake routes, but they are not the only endocytic or transcytotic pathways that occur in endothelial cells. One of these endocytic pathways is phagocytosis, which is typically associated with immune cells, such as macrophages, neutrophils, and dendritic cells, with an endosome formation and intracellular fate that is relatively similar to that of macropinocytosis.[144] While phagocytosis is not a niche for endothelial cells, they are still capable of performing it.[145,146]

Certain clathrin and caveolae independent pathways that are also independent of dynamin and lack a defined protein coat for encapsulating endocytic cargo.[147] One of these pathways is termed the clathrin independent carriers and GPI enriched endocytic compartments (CLIC/GEEC) pathway, which is used for the endocytosis of many glycosylphosphatidylinositol anchored proteins, and certain toxins and viruses. CLIC/GEEC endosomes are formed through the activation of the ADP-ribosylation factor 1 (ARF1), where CLICs are formed at the front of migratory cells, and the GEECs that are formed from this fuse with early endosomes.[148,149] A similar pathway is dependent on the ADP-ribosylation factor 6 (ARF6), known as the ARF6-associated pathway. Here, ARF6 is activated and inactivated to control membrane trafficking and recycling. It is currently

unknown whether the ARF6-associated pathway and the CLIC/GEEC pathway are truly distinct pathways.[147]

Another endocytic pathway that is potentially prevalent in endothelial cells is lipid raft mediated endocytosis. This pathway is based on cholesterol and sphingolipid rich microdomains on the cell membrane. However, the existence of lipids rafts is a matter of debate in the literature given that they have not been visualized yet *in vivo.*[150,151]

One pathway that is particularly important for cancer nanomedicine delivery is known as the C-end Rule (CendR) pathway, a neuropilin-1 mediated uptake that is similar to macropinocytosis, and is specific to peptides with a C-terminal arginine or lysine, and is the method that the tumor penetrating peptide, iRGD, takes after it is cleaved by αV integrins on the surface of tumor cells.[152,153] The previously mentioned VVOs and fenestrae are also possible routes, though more work will be needed to determine their feasibilities for nanomedicine delivery purposes.

## 1.4. Tools and techniques to investigate nanoparticle transport pathways across tumor endothelial cells

The specific targeting of endocytic pathways would be the first step in designing nanoparticles that transcytose through tumor blood vessel endothelial cells. A common method of accomplishing this is through the modification of the nanoparticle surfaces with protein or peptide ligands that are specific to endocytic receptors, along with necessary intermediates, as previously mentioned with the transferrin, albumin, and folic acid conjugations.[104,127,128,154–156] Table 1.2 lists several common nanoparticle surface ligands,

the receptors that these ligands target, and the pathways these ligands are internalized by cells.

**Table 1.2.** Surface receptors for targeting specific endocytic pathways *in vitro* and *in vivo.*

| **Surface Receptor Target** | **Targeting Molecule** | **Pathway** | **Specificity** | **Nanoparticle Examples** | **Ref.** |
|---|---|---|---|---|---|
| Annexin A1 | mAnnA1 | Caveolae | mAnnA1 is specific to Annexin A1 on caveolae of tumor endothelium in humans, rats, and mice, Annexin A1 is not prevalent in caveolae from healthy tissues | -Conjugated to AuNPs for targeting tumor endothelium in rats injected with 13762 mammary adenocarcinoma cells | 131 |
| GP60 | Albumin | Caveolae | GP60 is specific for albumin across the continuous endothelium | -Conjugated to polymer NPs for targeting BLMVECs<br>-Conjugated to iron oxide NPs for targeting U87MG tumors in mice | 127,157–159 |
| Folate receptor alpha (FRα) | Folic acid | Caveolae | FRα is overexpressed in epithelial malignancies, has limited expression in healthy cells | -Conjugated to albumin NPs for targeting NIH:OVCAR3 cells | 128 |
| Aminopeptidase P (APP) | mAPP | Caveolae | APP is expressed in the endothelium of lungs, kidneys, and livers | -Conjugated to AuNPs for targeting the lung endothelium of athymic, nude mice | 130 |

| | | | | | |
|---|---|---|---|---|---|
| CD36 – Scavenger Receptor Class B (SR-B) | A variety of ligands including LDLs and thrombospondin | Caveolae | CD36 is located on many types of cells past endothelial cells, such as macrophages and platelets, and binds to many different ligands | -Phosphatidylcholine conjugated to lipid NPs for targeting macrophages in C57BL/6 mice | 119,160 |
| CD204 - Scavenger Receptor Class A (SR-A) | A variety of ligands including acetylated LDLs and lipopolysaccharide | Caveolae and Clathrin | CD204 is located on many types of cells past endothelial cells such as macrophages and epithelial cells, and binds to many different ligands. | -anti-CD204 conjugated to micelles for targeting macrophages in mice | 161–163 |
| LDL Receptor Family | A variety of ligands including LDLs and lactoferrin | Caveolae and Clathrin | LDL receptors are located on many types of cells past endothelial cells such as macrophages and epithelial cells, overexpressed in liver tumors, and binds to many different ligands. | -Apolipoprotein-B lipid NPs for targeting HepG2 tumors in mice | 164–166 |
| Neonatal FC Receptor | IgG FC,<br>Albumin | Clathrin | Neonatal FC receptor is specific to epithelial and endothelial cells in humans and mice | -Conjugated to PLA-PEG-MAL NPs for crossing the intestinal epithelium after oral administration in mice | 167–169 |

| | | | | | |
|---|---|---|---|---|---|
| Transferrin Receptor | Transferrin | Clathrin | Highly expressed in solid tumor cells, as well as in blood brain barrier endothelial cells | -Conjugated to PLGA NPs for targeting brain capillary endothelial cells and astrocytes<br>-Conjugated to AuNPs for targeting S.C. Neuro2A tumors in mice | 170–173 |
| Vascular cell adhesion molecule (VCAM-1) | Anti-VCAM-1 | Clathrin | VCAM-1 is expressed on activated endothelial cells in tumors and during inflammation | -Conjugated to PEG-liposomes for targeting bEnd.3 cells and tumor vasculature in a CD1 nude, human Colo 677 xenograft mouse model | 113 |
| Epidermal Growth Factor Receptor (EGFR) | Epidermal Growth Factor | Macropinocytosis | Present across many different cell types in the body but is overexpressed in many tumor cell lines. EGFR also binds to many other types of growth factors | -Conjugated to AuNPs for targeting EMT-6 mammary carcinomas in mice | 174,175 |
| αV Integrins | iRGD | C-end Rule (CendR) | Specific to αV integrins on tumor endothelium as well as angiogenic endothelium<br>After binding to αV integrins, iRGD is cleaved in to CRDGK/R and then | -Conjugated to micelles for targeting 22Rv1, PC-3, PPC1, MIA PaCa-2, and BT474 tumors in mice | 152,153,176 |

| | | | | | |
|---|---|---|---|---|---|
| | | | binds to neuropilin-1 | | |

**Abbreviations:** AuNP – gold nanoparticle; LDL – low-density lipoprotein; MAL-maleimide; NP – nanoparticle; PEG; poly(ethylene glycol); PLA – polylactic acid; PLGA - poly(lactic-co-glycolic acid)

A solid understanding of how the different pathways function and contribute to nanoparticle cellular uptake is necessary for exploiting them for efficient nanomedicine delivery. Methods for isolating a pathway's contribution to the total uptake via pathway inhibition, pathway visualization methods, and models for more accurate uptake studies are discussed in this section.

### 1.4.1 Inhibiting endocytic pathways

Many methods have been employed for studying the pathways that nanoparticles take, both with and without active targeting. The use of small molecule inhibitors has been a popular method for blocking an endocytic pathway and observing changes in cellular uptake, through methods such as fluorescent microscopy analysis,[177] flow cytometry,[178] inductively coupled plasma mass spectrometry,[179–181] and radioactive decay measurements.[182] A common control for these studies is cooling the cells being studied to 4°C, as this nonspecifically inhibits all endocytosis.[183] Table 1.3 lists several endocytosis inhibitors that have been studied, the pathways they inhibit, their mechanism of action, and their reported efficiency. However, direct comparisons of the inhibitors listed here are difficult because of the differences in cell types, nanoparticles, and inhibitor concentrations used, leading to the need for further studies that directly test the efficiencies of many different inhibitors on the uptake of multiple tracers for each pathway.

**Table 1.3.** Small molecule endocytosis inhibitors and their effectiveness**.**

| **Inhibitory Agent** | **Pathway Inhibited** | **Inhibition Mechanism** | **Uptake Inhibition Effectiveness** | **Considerations** | **Ref.** |
|---|---|---|---|---|---|
| Methyl-β-cyclodextrin (MβCD) | Caveolae Mediated Endocytosis and Clathrin Mediated Endocytosis | Removes cholesterol from the plasma membrane | -53% inhibition of lactosylceramide in HUVECs<br>-56% inhibition of transferrin in HUVECs<br>-80 % inhibition of 20 nm & 40 nm polystyrene NPs in HUVECs<br>-36 % inhibition of 100 nm & 200 nm polystyrene NPs in HUVECs | This has been shown to affect multiple pathways | 184–186 |
| N-ethylmaleimide (NEM) | Caveolae Mediated Endocytosis | Inactivating the ATPase NEM-sensitive factor | -75% inhibition of albumin gold complex in BLMVECs and BAECs<br>-<80% inhibition of cationic liposomes in Cos-7 cells | Has been shown to stimulate macropinocytosis in various epithelial cell lines | 187–191 |
| Filipin | Caveolae Mediated Endocytosis | Removes cholesterol from the plasma membrane | -70% inhibition of albumin-gold complexes in BLMVECs, BAECs, and RFCs<br>-40% inhibition in WGA-PEG-PLA NPs encapsulating CdSe/ZnS quantum dots in CaCo-2 cells | Sterols and sphingolipids likely play a role in clathrin mediated endocytosis | 98,182,192,193 |
| Nystatin | Caveolae Mediated Endocytosis | Removes cholesterol from the plasma membrane | -80% inhibition of BODIPY-LacCer in rat fibroblasts<br>-No significant inhibition of PEG-PHDCA NPs in rat brain endothelial cells | Sterols and sphingolipids likely play a role in clathrin mediated endocytosis | 177,192–196 |

| | | | | | |
|---|---|---|---|---|---|
| Genistein | Caveolae Mediated Endocytosis | Tyrosine kinase inhibitor, and also inhibits the recruitment of dynamin II. | -80% inhibition of BODIPY-LacCer in rat fibroblasts<br>-15% inhibition of heparosan based micelles in B16 cells<br>-No significant inhibition of heparosan based micelles in A549 or MGC80-3 cells | This can also inhibit clathrin mediated endocytosis and clathrin and caveolae independent endocytosis pathways that are dependent on tyrosine kinase phosphorylation or dynamin II | 97,177,195,197–199 |
| Fumonisin B1 (FB1) | Caveolae Mediated Endocytosis | Blocks glycosphingolipid formation by inhibiting the acetylation of sphingosine and dihydrosphingosine,. | -60-80% inhibition of BODIPY-LacCer in CHO-K1 cells | Sterols and sphingolipids likely play a role in clathrin mediated endocytosis | 193,199–201 |
| Indomethacin | Caveolae Mediated Endocytosis | Increases the amount of arachidonate in the cell, preventing plasmalemmal vesicles from being formed, while also causing existing vesicles to resurface. | -50% inhibition of [$^3$H] folic acid in monkey kidney epithelial cells<br>-No significant inhibition of heparosan based micelles in A549, MGC80-3, or B16 cells | This may stimulate the caveolae independent endocytosis in certain cell types | 97,202–205 |
| Chlorpromazine | Clathrin Mediated Endocytosis | Translocates clathrin and AP-2 in to intracellular vesicles from the plasma membrane. | -80% inhibition of transferrin in rat fibroblasts<br>-20% inhibition of heparosan based micelles in A549 cells<br>-25% inhibition of heparosan based micelles in MGC80-3 cells<br>-20% inhibition of heparosan based | Cells can possibly quickly adapt to chlorpromazine in the presence of transferrin to use alternative uptake pathways, limiting the inhibitory effect | 97,177,194,206 |

| | | | | | |
|---|---|---|---|---|---|
| | | | micelles in B16 cells | | |
| Potassium Depletion | Clathrin Mediated Endocytosis | Dissociates clathrin lattices on the plasma membrane. | -80% inhibition of transferrin in rat fibroblasts<br>-50% inhibition of chitosan nanoparticles in A549 cells | This has been suggested to slightly inhibit clathrin independent pathways, though the mechanism by which it might is unknown | 177,197,207 |
| Dynasore | Clathrin Mediated Endocytosis and Caveolae Mediated Endocytosis | Inhibits the GTPase activity of dynamin | -<75% inhibition of transferrin in HeLa cells<br>-<60% inhibition of carboxylate-modified polystyrene beads in HeLa cells | This has been shown to affect multiple pathways<br><br>This has been shown to enhance TGFβ signaling, which could have off-target effects in certain studies | 123,208–210 |
| Chloroquine | Clathrin Mediated Endocytosis | Prevents the transition of type 2 clathrin coated pits to type 3 clathrin coated pits, preventing the formation of clathrin coated vesicles. | -85% inhibition of TGFβ1 in Mv1Lu cells<br>-<80% inhibition of cationic liposomes in Cos-7 cells | This has been shown to enhance TGFβ signaling, which could have off-target effects in certain studies | 189,210 |
| Cytochalasin D | Macropinocytosis | Binds to actin filaments, preventing the association and disassociation of subunits at the binding sites. | -<60 inhibition of FITC-dextran in monocyte derived dendritic cells<br>-50% inhibition of 50-50 PLGA NPs in rabbit conjunctival epithelial cells | This also inhibits phagocytosis and other actin polymerization dependent processes | 178,211–213 |

| | | | | | |
|---|---|---|---|---|---|
| 5-(N-Ethyl-N-Isopropyl) Amiloride (EIPA) | Macropinocytosis | Inhibits $Na^+/H^+$ exchange to disrupt actin polymerization | -90% inhibition of TMR-dextran in T24 cells<br>-60% inhibition of positively charged polystyrene NPs in HeLa cells | This also inhibits phagocytosis and other actin polymerization dependent processes | 142,178,214,215 |
| Wortmannin | Macropinocytosis | Blocks the activity of the phosphoinositide 3-kinase (PI3), which prevents membrane ruffling | -<90% inhibition of fluorescein dextran in murine bone marrow-derived macrophages<br>-60% inhibition of PFBT NPs in J774A.1 cells | This also inhibits phagocytosis, and possibly also clathrin mediatae d endocytosis | 134,178,216,217 |
| Imipramine | Macropinocytosis | Inhibits the ruffling of plasma membranes, and potentially inhibits redox signaling. | -95% inhibition of FITC-dextran in RAW 264.7 macrophages<br>-50% inhibition of AuNPs in Madin Darby canine kidney cells | The mechanism of inhibition for this inhibitor is not yet fully understood | 178,218 |
| Colchicine | Macropinocytosis and Macrophage Endocytosis | Decreases cell motility by preventing tubulin polymerization to block microtubule formation. | -37% inhibition of intratracheally delivered gold colloids in macrophages of Syrian golden hamsters<br>-15% inhibition of heparosan based micelles in A549 cells<br>-15% inhibition of heparosan based micelles in MGC80-3 cells<br>-11% inhibition of heparosan based micelles in B16 cells | This has been shown to affect multiple pathways | 97,219,220 |
| Rottlerin | Macropinocytosis and Fluid Phase Endocytosis | Inhibits protein kinase C | -<90 inhibition of lucifer yellow in monocyte derived dendritic cells | This has been shown to affect multiple pathways | 211,221 |

| | | | | | |
|---|---|---|---|---|---|
| | | delta (PKCδ) activity | | | |
| Brefeldin A | Vesicle Trafficking | Inhibits the formation of COP1 coats on vesicles to pr event ER-Golgi trafficking | -99.6% inhibition of lunasin in THP-1 macrophages<br>-40% inhibition in WGA-PEG-PLA NPs encapsulating CdS e/ZnS quantum dots in CaCo-2 cells | This has been shown to inhibit transcytosis and has been suggested to also inhibit endocytosis | 98,222–224 |
| Dextran Sulfate | Scavenger Receptor Mediated Endocytosis | Competitively binds to scavenger receptors on endothelial cells, such a stabilin-1 and stabilin-2. | -42% inhibition of succinylated bovi ne serum albumin in BMECs<br>-66% inhibition of DOPG liposomes and a 75% inhibition of DOPC liposomes in venular endothelial cells of zebrafish embryo compared to arterial endothelial cells | This is not a specific binding, as dextran sulfate will also bind to the mannose receptor | 225–228 |

**Abbreviations:** CHO – Chinese hamster ovary cells; NP – nanoparticle; AuNP – gold nanoparticle; HUVECs – human umbilical vein endothelial cells; BLMVECs – bovine lung microvessel endothelial cells; BAEC – bovine aortic endothelial cells; RFCs - rat epididymal fat pad; LacCer - Lactosylceramides; WGA – wheat germ agglutinin;

It is worth noting that there are certain considerations that must be taken into account for the use of these small molecule inhibitors. First, these cell treatments are not typically 100% specific or efficient in blocking a particular cell uptake pathway, meaning that it must be determined if the remaining uptake can be attributed to either remnants of the pathway being blocked, or to regular uptake from other pathways. Second, close attention must be paid to the mechanism of action of the inhibitors in question, as it is possible that they can affect the uptake of pathways other than the one that is intended; for example, Fumonisin B1 inhibits caveolae-mediated endocytosis by blocking sphingolipid formation through the inhibition of the acylation of sphingosine and dihydrosphingosine.[199] However, it has also been suggested that sphingolipid synthesis could be necessary for clathrin-mediated endocytosis as well.[229] Similarly, a widely used stimulant for macropinocytosis, phorbol-12-myristate-13-acetate (PMA), has been shown to inhibit caveolae mediated endocytosis.[178,203] There also exists a possibility that the blocking of one pathway increases the uptake in other pathways from what typically occurs, producing results that do not accurately reflect normal physiologic conditions. Third, the specificity of the tracer must be considered, given that there is the possibility for certain tracers to take other pathways as well; for example, albumin, a known tracer for caveolae-mediated endocytosis, has been shown to be uptaken through clathrin-mediated endocytosis when attached to the FC neonatal receptor[167] rather than the typical gp60.[157]

Finally, the size of the nanoparticles being used must be considered, given that there are finite sizes of the endocytic vesicles being studied. Figure 1.6 demonstrates the typical size ranges of these vesicles, as well as those of their most common tracers and

commonly used nanoparticle sizes. While it has been shown that these vesicles can be dynamic and holding larger nanoparticles than what their typical sizes suggest,[104] it is likely that this will need to be determined on a case-by-case basis, taking in to account factors such as nanoparticle material, surface charge, shape, and which specific ligands and receptor combos are being used. All of these different considerations imply that further experiments and analysis past just changing uptake with the inhibitor treatment would be required to determine a single pathway's contribution to the uptake of the tracer or nanoparticle being studied.

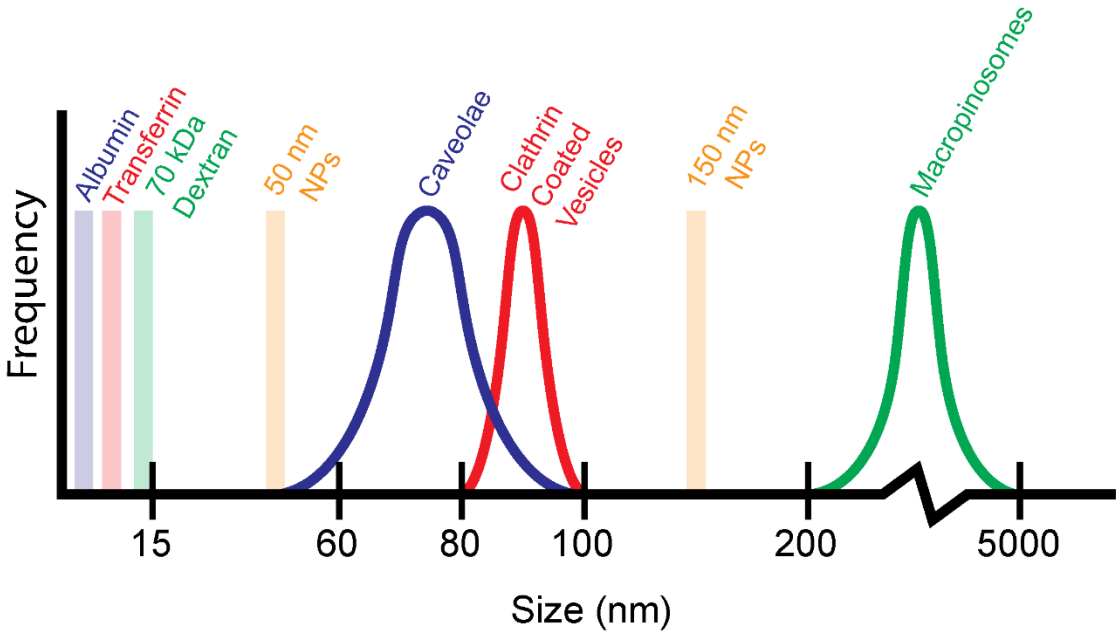


Size of Vesicles

| Vesicle | Vesicle Size (nm) | Max Nanoparticle Size (nm) | Ref. |
|---|---|---|---|
| Caveolae | 50 -100 | 250 nm folate coated polycaprolactane NPs in ARPE-19 cells | [55], [129] |
| Clathrin Coated Vesicles | 80 -100 | 522 nm transferrin coated polystyrene NPs in HeLa cells | [102], [104] |
| Macropinosomes | 2000 - 5000 | N/A | [135] |

**Figure 1.6. Typical sizes of vesicles formed during endocytosis.** The reported size ranges of vesicles formed by the three most common endocytosis pathways are shown, along with typical tracers used in endocytosis studies, albumin for caveolae-mediated pathway, transferrin for clathrin-mediated pathway, and 70 kDa dextran for macropinocytosis. Further studies are needed to compare the sizes of each of these vesicles directly for the same cell type and with the same tracers. While intracellular vesicles exhibit reported size limitations, there are reported cases of caveolae expanding to carry 100 nm nanoparticles. Since all of the tracers are well below the typical sizes of endocytosis vesicles, meaning that each vesicle type can physically accommodate each tracer type, there is a factor of specificity for endocytosis uptake of nanoparticles (and tracers) that is beyond physical size.

An alternative method of studying uptake pathways that has been explored is the genetic alteration of cells to knock down or knock out the expression of relevant proteins. This can be accomplished through the use of small interfering RNA (siRNA) duplexes that cleave its complementary mRNA that codes for target proteins, resulting in the degradation of that mRNA, transiently silencing the expression of the protein in question.[230,231] The inhibition of endocytic pathways has been demonstrated both *in vitro* and *in vivo* for various cell types, by targeting proteins such as caveolin-1, clathrin heavy chain, and PAK-1 (a macropinocytosis signaling protein).[194,232–235] For *in vivo* systems, the knockdown can be either localized or global.[236,237] While this method is more specific, siRNA is known to be unstable in blood, immunogenic, and cannot easily cross cell membranes.[238] Therefore, for siRNA treatments to be efficient, they need a carrier, with a liposome formulation known as Lipofectamine being a common choice.[239] Alternatively, a permanent, heritable method of gene knockout is achieved through the use of the CRISPR-Cas system.[240]

### 1.4.2 Methods for visualizing and studying endocytic pathways

Optical microscopy, such as confocal laser scanning microscopy, has been applied for visualizing these uptake pathways, either by fluorescently tagging associated proteins, tracers, or the nanoparticles themselves. This method is somewhat effective, though there is a considerable limitation in its effectiveness, stemming from the physical limitations of optical microscopy - the diffraction limit of light is roughly 200 nm.[241] While this is sufficient for visualizing whole cells, it is difficult to accurately see certain subcellular processes. Electron microscopy methods have been employed for imaging at sub-

nanometer resolution.[242] However, transmission electron microscopy comes at the cost of requiring thin tissue slices for imaging, typically 50-100 nm thick, resulting in a loss of 3D information,[243] which can make differentiating between different types of vesicles and channels difficult or requiring laborious imaging and image processing of multiple sections.

Efforts have been made to surpass the optical diffraction limit without the limitations presented by electron microscopy, and several super resolution microscopy methods have resulted. One such method is near field scanning optical microscopy (NSOM), which surpasses the optical diffraction limit by using a probe that is positioned close to the sample at a distance that is shorter than the excitation wavelength being imaged. However, this method also requires expensive and specialized equipment.[244] Other methods, such as stochastic optical reconstruction microscopy (STORM) and stimulated emission depletion (STED) achieve super resolution by assigning fluorescent and non-fluorescent states to fluorophores, either randomly to create a reconstructed data map, or in a targeted manner that does not require post processing, at the cost of elevated photobleaching concerns.[245] An alternative method called expansion microscopy has been developed that involves anchoring the proteins found in a cell or tissue sample to a superabsorbent hydrogel and allowing it to expand in water, mechanically stretching the sample so that objects smaller than the diffraction limit would be made larger, and therefore, resolvable.[246,247]

Given that blood vessels in living organisms are not static, physical stresses on endothelial cells and nanoparticles must also be taken into account for more informative *in vitro* studies. One of these stresses that has been studied is shear stress, which is

caused by the movement of a fluid across constraining walls (blood through blood vessels, in this case) – it has been found that this can cause cytoskeletal rearrangement in endothelial cells.[248,249] Microfluidic models have been employed to simulate the physiological shear conditions in blood vessels. This was demonstrated in a 2D flow model by Volkov et al., who showed that shear stress is critical for the uptake of cadmium telluride quantum dots and silicon dioxide nanoparticles in human umbilical vein endothelial cells.[250] Lipke et al. developed 3D microfluidic chips that model tumor microvascular networks, which are now commercially available prefabricated through the company SynVivo, to test the efficacy of anti-cancer drugs in metastatic and nonmetastatic breast cancer cells.[62] Chan et al. have demonstrated a 3D microfluidic model of entire blood vessel networks that can be coated with endothelial cells for a much closer representation of *in vivo* conditions in an *in vitro* system, designed by casting dissolvable 3D printed models of vessel network derived from 3D fluorescent imaging in polydimethylsiloxane.[63] Laser ablation has also been explored as a method for generating highly accurate and precise vascular networks within hydrogels through the degradation of the hydrogel with a pulsed laser on an image-guided control system, so that cells can then be seeded in the newly formed channels.[251,252] These strategies for engineering vasculature for *in vitro* studies and implantations, along with several others, are discussed in detail in recently published reviews by Vunjak-Novakoiv et al.[253] and Slater et al.[254]

The uptake of nanoparticles *in vivo* is, by nature, more difficult to visualize and study. It is possible that transcytosis rates in tumor blood vessels decrease with age, and that vessels without pericytes have lower transcytosis rates than those with pericytes, given that it has recently been shown that transcytosis through the blood brain barrier is

impaired with age, coupled with a loss of pericytes,[255] so this might be considered for *in vivo* nanoparticle uptake studies. *Ex vivo* imaging and other quantification methods have been particularly useful for the analysis of nanoparticle accumulation in tumors and organs, i.e. resecting the mass of interest and then imaging and/or quantifying nanoparticle uptake with standard *in vitro* techniques.[256–258] True *in vivo* imaging to visualize nanoparticle transport is possible through a variety of methods. Intravital microscopy (IVM) is a common method of accomplishing this goal using principles of confocal laser scanning and multiphoton microscopy,[259] as demonstrated by Lo et al., who used IVM to visualize the uptake of mesoporous silica nanoparticles into hepatocytes.[260] This can be further improved with tissue clearing methods such as the hydrogel based CLARITY and the chemical based CUBIC that minimize the effects of light scattering from tissue samples,[261] shown by Chan et al. to be effective with gold nanoparticles and liposomes.[262–265] Another tissue clearing method, vDISCO, works on whole intact mice.[266] Light sheet fluorescent microscopy can then be used for fast, high resolution, optically sectioned images.[267] These concepts are covered in great detail in a review by Weissleder et al.[268] Tissue clearing and light sheet microscopy have been combined with machine learning algorithms to create a framework for quantifying and analyzing brain vasculature, called the Vessel Segmentation and Analysis Pipeline (VesSAP), for automatic, unbiased, and scalable vasculature analysis.[269] The use optical and electron microscopy methods could provide answers to the questions that surround the complex mechanisms behind nanoparticle accumulation in solid tumors.

## 1.5. Conclusions

Efficient nanoparticle delivery to tumors requires fundamental understanding of the active and passive transport pathways and mechanisms that nanoparticles use to cross the tumor endothelium.[36] Further knowledge of the different types of tumor blood vessels and how these different vessel types affect nanoparticle transport will be instrumental. The design of tumor targeted nanoparticles that can undergo selective transcellular transport across tumor endothelial cells represents a new frontier in cancer nanomedicine research. Future studies will focus on spatiotemporal characterization of nanoparticle interactions with different tumor blood vessel types and the relationships between nanoparticle physicochemical properties and specific endocytosis and transcytosis pathways in tumor endothelial cells. It has been shown that engineered T cells carrying multilamellar lipid nanoparticles on their surface retain much more of their cargo after crossing endothelial barriers compared to T cells carrying lipid coated PLGA nanoparticles.[270] For this reason, in addition to ultrastructural imaging approaches, there is a need to characterize nanoparticle physiochemical properties, including changes in the nanoparticle protein corona composition, before and after transport across tumor blood vessels. Such research may identify pathways, mechanisms, and specific biomolecules involved in trans-endothelial transport and nanoparticle tumor delivery. The successful design of nanoparticles that selectively transport therapeutic and imaging payloads across tumor blood vessels will enable a new generation of safer and more effective cancer nanomedicines for clinical translation.

## Chapter 2: Three-Dimensional Super-Resolution Microscopy for Visualizing Metallic Nanoparticle Localization Within Cells

### 2.1 Introduction

Developing safer and more effective nanomedicines requires new imaging tools and methods to quantify nanoparticle spatiotemporal distributions at cellular, sub-cellular, and ultrastructural levels.[271] These quantitative data have the potential to guide nanoparticle engineering with the goal of controlling nanoparticle interactions with cells.[272,273]

Conventional biological transmission electron microscopy (TEM) can achieve a spatial resolution of ~2 nm to provide ultrastructural information of cell and tissue sections.[274] However, the imaging depth in TEM is typically limited to very thin biological samples. With section thicknesses of ~100 nm or less, it is difficult to achieve 3D imaging of entire cells or tissues with TEM, as the exact stacking of images from different sections is challenging.[275,276] On the other hand, capturing the full 3D volume of biological samples using standard optical microscopes is relatively straightforward.[262–265,277,278] Unfortunately, the spatial resolution in standard optical imaging is diffraction-limited to ~200-250 nm.[241] This resolution limitation presents a major challenge to the imaging of nanoparticles in their ultrastructural context within cells and tissues. Optical imaging methods capable of overcoming the aforementioned diffraction limit are termed super-resolution imaging methods.[279] One such method is expansion microscopy, a hydrogel-based 3D super-resolution imaging technique in which samples are physically expanded 4 to 20-fold. This expansion process leads to reported spatial resolutions of nearly 10 nm, which provides valuable ultrastructural information.[246,280]

An additional challenge in optical microscopy of nanoparticles is the need for detection agents, often attached as fluorescent labels to the nanoparticle surface.[281] These modifications may alter the nanoparticle surface chemistry and physiochemical properties, affecting how the nanoparticles interact with cells.[107,282–284] Therefore, a label-free nanoparticle imaging method is desirable that provides information about the 3D intracellular nanoparticle distribution with ultrastructural resolution.[285]

In this study, we explored and established the combination of expansion microscopy protocols with scattered light imaging of label-free metallic nanoparticles to quantify intracellular nanoparticle distributions. Scattered light imaging involves the illumination of metallic nanoparticles and subsequent light detection at the same wavelength as the illumination light.[286] Expansion microscopy relies on anchoring proteins in biological samples to a swellable poly(acrylamide-co-sodium acrylate) based hydrogel.[246,287] The subsequent water absorption expands the protein-hydrogel hybrid samples by a linear factor of approximately 4X isotropically, resulting in an equivalent substantial increase in the achievable spatial resolution of standard light microscopes. Recent expansion microscopy protocols enable expansion factors up to 10X for single expansions and up to 20X for iterative expansions.[280,288–290] Expansion microscopy protocols have demonstrated utility for various applications, including the computational diagnosis in early breast lesions,[247] studying cell-material interfaces,[291] and visualizing the anatomical structures of whole zebrafish larvae.[292] We combined different expansion microscopy protocols with label-free scattered light imaging of intracellular metallic nanoparticles, as shown in Figure 2.1.

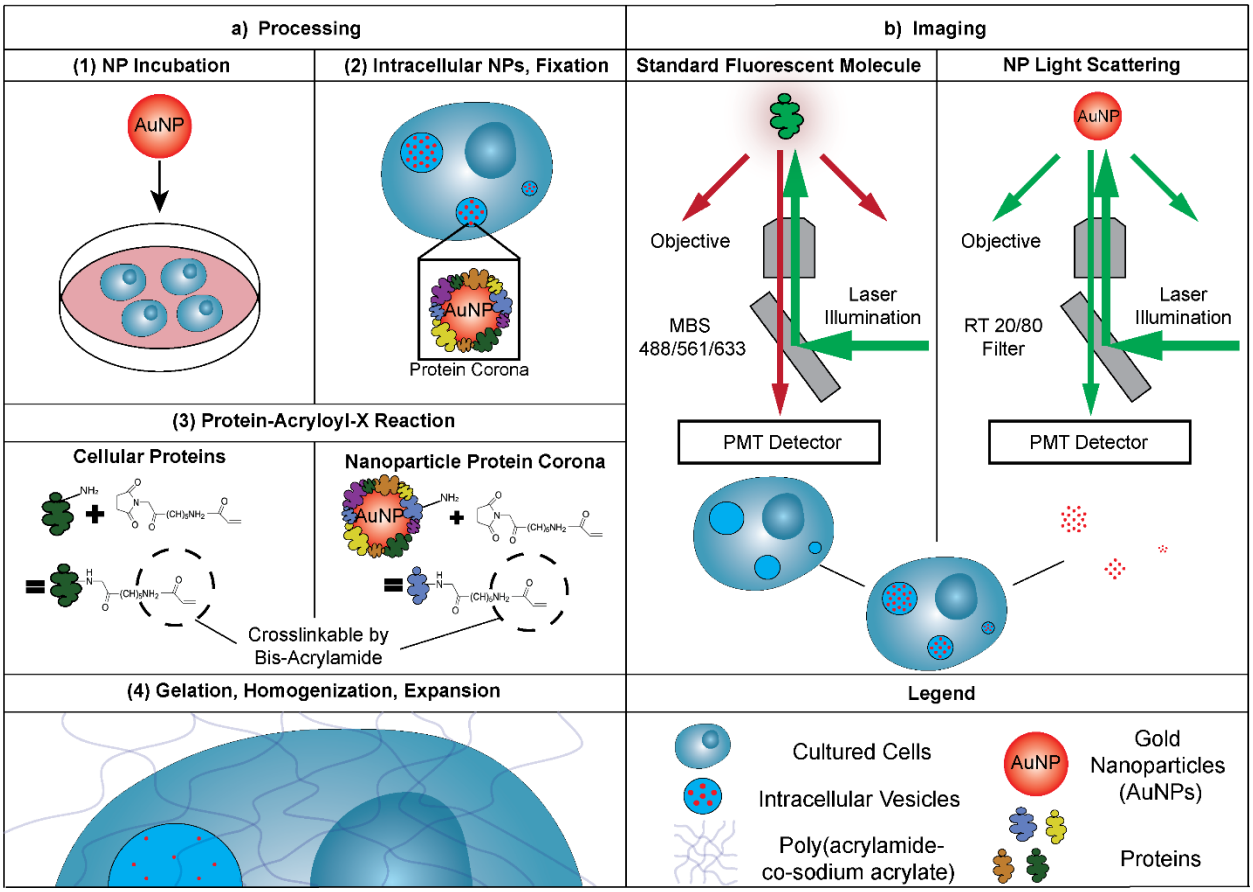


**Figure 2.1. Overview of the combination of expansion microscopy and scattered light imaging of label-free nanoparticles. (a)** We first treated cultured cells with gold nanoparticles (AuNPs). Following fixation with paraformaldehyde, we processed the cells through protein retention expansion microscopy (proExM). In proExM, the proteome of the cells is treated with Acryloyl-X, SE, a molecule that binds to primary amines in proteins, which then gets incorporated into a swellable gel matrix. The protein corona adsorbed onto the surface of intracellular AuNPs, is also incorporated into the gel matrix by the Acryloyl-X, SE treatment. We then homogenized the samples with Proteinase K before swelling them in ultrapure $H_2O$. While the AuNPs do not physically expand along with the anchored intracellular protein, they remain in their initial relative positions within the cells. **(b)** We accomplished label-free nanoparticle imaging by exploiting the efficient light scattering properties of inorganic nanoparticles. We used a narrow light detection window around the illumination laser wavelength (+/- 5 nm) to collect the scattered light, while effectively rejecting the emission light from standard fluorophores. This imaging method allows the nanoparticle light scattering signal to be overlayed with the fluorescence signal from stained expanded cells to allow for the localization of nanoparticles within individual vesicles.

## 2.2 Results and Discussion

### 2.2.1 Achieving super-resolution imaging with expansion microscopy

The diffraction limit of visible light microscopy presents a barrier to the ultrastructural imaging and analysis of intracellular nanoparticles. This challenge is illustrated in Figure 2.2a, showing a diffraction-limited confocal laser scanning microscopy (CLSM) image of cultured murine triple-negative breast cancer epithelial (4T1) cells. Since most intracellular features are smaller in size than the optical diffraction limit,[293] super-resolution microscopy is needed to resolve nanoparticle distributions with ultrastructural context and accuracy.

To address this need, we adopted the protein retention expansion microscopy (proExM) protocol, a protease-based variant of the original expansion microscopy protocol where cellular proteins are anchored directly to a swellable gel matrix.[287,294] Using this protocol, we achieved a ~4X linear expansion of cultured cells resulting in super-resolved images. Figures 2.2b, S2.1 show 4T1 cells processed with the proExM protocol. In Figure 2.2c, we determined a linear expansion factor of 4.1X. We then further quantified the increase in image resolution in Figure S2.2a. We found that line profiles across non-expanded nuclei had 1.3 +/- 0.1 pixel intensity peaks/μm, whereas expanded nuclei had 5.4 +/- 0.1 pixel intensity peaks/μm (following correction for expansion factors, see Methods section) ($n$=3).

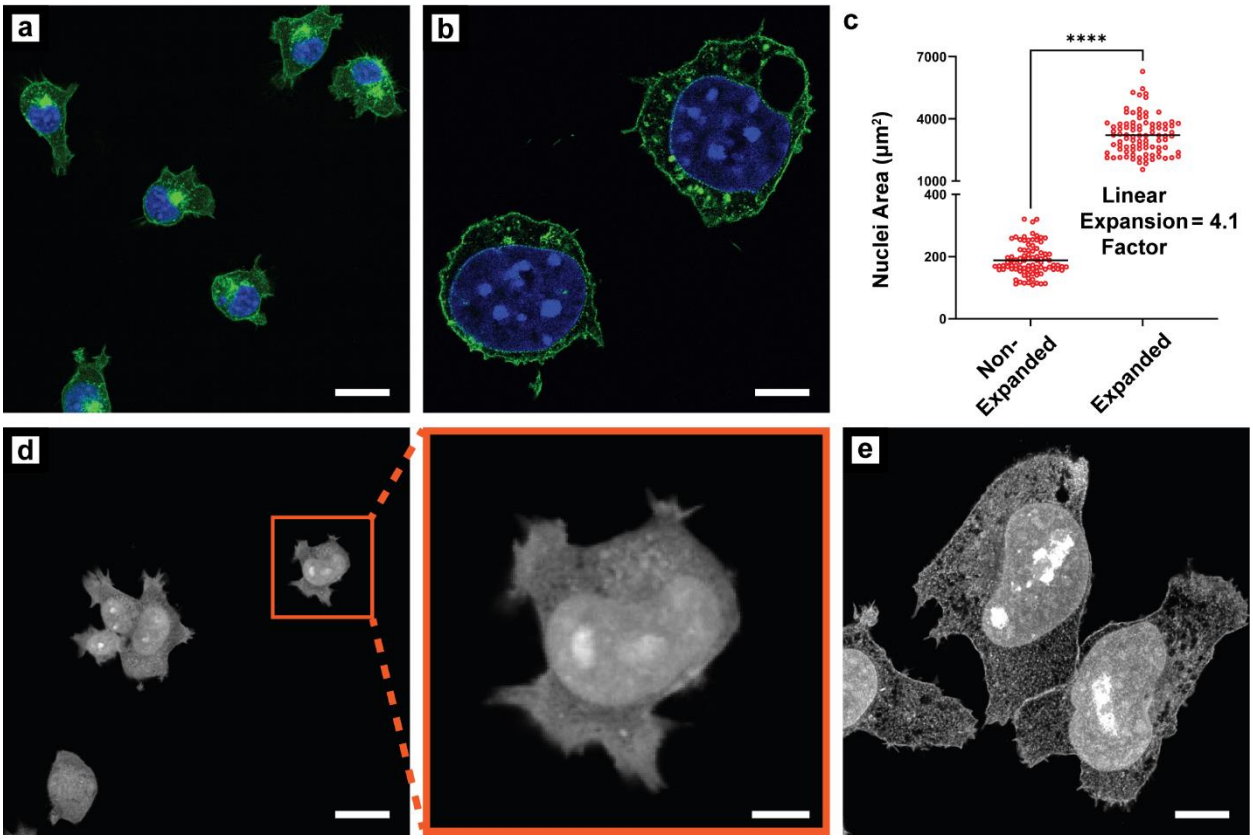


**Figure 2.2: Expansion microscopy of 4T1 mammary tumor mouse cells. (a)** Non-expanded 4T1 cells labeled with the DNA stain, 4′,6-diamidino-2-phenylindole (DAPI) (blue) for nuclei visualization and the glycoprotein stain, wheat germ agglutinin WGA-CF488A (green) for cell membrane visualization. **(b)** Expanded 4T1 cells stained with DAPI and WGA-CF488A. **(c)** Quantitative analysis of the nuclei area in $\mu m^2$ of non-expanded and expanded cells, measured on ImageJ. The mean values (solid black line) were used to calculate the linear expansion factor of 4.1X (n=90) using Equation 1. An unpaired one-tailed t-test resulted in a statistically significant difference in the means of the nuclei areas between the two groups (****$p<0.0001$). **(d)** Non-expanded cells bulk (pan) stained with NHS-AF555 to visualize the entire proteome of the cell (left) and a digital magnification of the cell in the red box by a factor of 4.1X (right). **(e)** Expanded cells pan-stained with NHS-AF555, demonstrating a clear increase in image resolution and contrast compared to the digital magnification image. The scale bars indicate 20 µm for the unmagnified images and 5 µm for the magnified image. Scale bars for images of expanded cells are the original length as obtained by the microscope (i.e. not corrected for expansion factors).

### 2.2.2 Imaging intracellular features through bulk staining

Next, we adopted a bulk (pan) staining protocol to fluorescently label most of the cell's proteome.[280] This staining increased the overall imaging contrast and is based on an N-Hydroxysuccinimide (NHS) ester-activated fluorescent dye (NHS-AF555) that binds covalently to available primary amine groups. Figure 2.2d demonstrates non-expanded 4T1 cells stained with NHS-AF555 and a 4.1X digital magnification to compare against expanded cells stained with NHS-AF555 in Figure 2.2e. These images illustrate that the expanded cells were visually less blurry than the digitally magnified cell image, which supports that the proteome's bulk (pan) staining helps resolve the local protein densities to reveal the cellular nanoarchitecture by standard light microscopy.[280] We quantified this observation with line profiles in the same manner as mentioned above and found that the non-expanded NHS-AF555 stained cells had 0.9 +/- 0.1 pixel intensity peaks/µm, whereas expanded NHS-AF555 cells had 4.6 +/- 0.1 pixel intensity peaks/µm (Figure S2.2b) ($n$=3).

The pan-staining approach further enables the imaging of intracellular compartments and vesicles of various sizes. Since intracellular vesicles are primarily fluid-filled compartments, they provide contrast against the other protein-rich and fluorescently stained areas throughout the cytoplasm.[295] In Figure 2.2e, intracellular vesicles are seen as dark areas within the cytoplasm. A decrease in pixel intensity of nearly 99% from the highest value occurs based on the line profile analysis. Using a combination of pan-staining and proExM, we spatially resolved more individual intracellular vesicles than with pan-staining alone (Figures 2.2d and 2.2e).

### 2.2.3 Label-free nanoparticle imaging in cells through light scattering

We then confirmed the feasibility of label-free nanoparticle imaging within cells using 55-nm gold nanoparticles (AuNPs) as a model nanoparticle system. Label-free imaging enables studying interactions between nanoparticles and cells of interest without adding fluorophores to the nanoparticles. This label-free approach is desirable because fluorophore labeling can change the nanoparticle surface chemistry and physicochemical properties resulting in differing cellular interactions.[107,282–284] We selected quasi-spherical 55-nm AuNPs because the size-dependent uptake of AuNPs into mammalian epithelial cells peaks at around 50 nm in diameter.[296,297] Furthermore, this nanoparticle size limits the potential for size restrictions on uptake since most intracellular vesicles of interest for nanoparticle uptake are larger than 60 nm.[293]

We accomplished label-free nanoparticle imaging by exploiting the efficient light scattering properties of inorganic nanoparticles.[286] We used a narrow light detection window around the illumination laser wavelength (typically +/- 5-10 nm) to collect the scattered light. (Figure 2.1b) This approach further helps to efficiently reject any potential stray emission light from fluorophores, which is an elegant way of adding another imaging channel to the CLSM system to exclusively image the nanoparticles.[265]

Next, we synthesized citrate-coated 55-nm AuNPs based on previously reported methods.[154,298,299] We characterized the AuNPs with dynamic light scattering (DLS) (Table S1) to quantify nanoparticle size and polydispersity, determined the zeta potential (Table S2), and used UV-Vis spectrophotometry (Figure S2.3a) to estimate the nanoparticle molar concentrations. Furthermore, we also characterized the AuNPs with transmission electron microscopy (TEM) (Figure S2.4a-b). We then coated the AuNPs

with 10-kDa methoxy-terminated poly(ethylene glycol)-orthopyridyl disulfide (mPEG-OPSS) polymers for increased colloidal stability. The successful conjugation of PEG polymers to the AuNPs surface was confirmed by DLS measurements that showed an increase in the hydrodynamic diameter by ~35.9 +/- 0.7 nm for PEG-AuNPs compared to citrate-coated AuNPs, with the expected zeta potential being near neutral[300] (Table S1, S2) (*n*=3). The observed hydrodynamic diameter size increase aligns with our previous work involving similar successful conjugations.[300,301] We further confirmed the surface conjugation of mPEG-OPSS to the AuNPs qualitatively with TEM through negative staining with uranyl acetate, resulting in a visible halo around the AuNPs (Figure S2.4c).

Next, we incubated 4T1 cells with 200-pM PEG-AuNPs for 24 hours. We then washed, fixed, and stained the cells with either DAPI and a glycoprotein stain, wheat germ agglutinin (WGA-CF488A), or NHS-AF555 alone. While cell membranes and other biological features can also scatter light, the light scattering efficiencies of these biological materials are orders of magnitude lower than that of metallic nanoparticles.[265] We used cells without nanoparticle treatment as a threshold baseline to remove the light scattering background signal. Figure 2.3a shows the light scattering signal obtained from intracellular AuNPs using CLSM following the thresholding method. We then demonstrated that the nanoparticle light scattering imaging did not interfere with the emission of fluorophores that were excited using the same laser wavelength. Using the NHS-AF555 dye and a laser illumination wavelength of 561 nm, we show in Figure 2.3b that nanoparticle light scattering imaging is compatible with the NHS-AF555 pan staining. No visible signal from the NHS-AF555 dye is detected in the nanoparticle light scattering imaging channel following thresholding to remove the background light. Our approach

allows the label-free detection of intracellular nanoparticles and is fully compatible with conventional fluorescence staining and imaging.

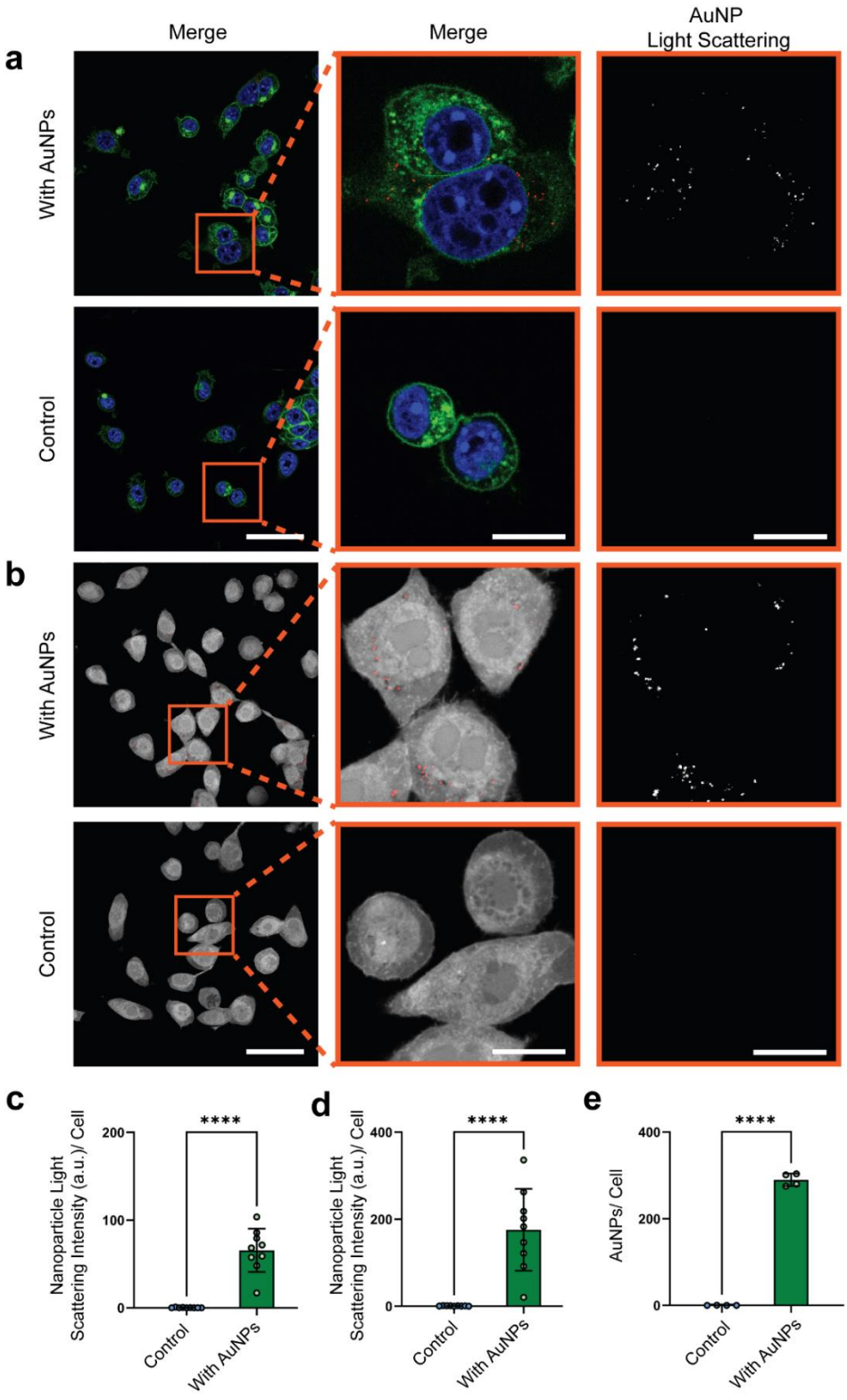


**Figure 2.3: Label-free imaging of nanoparticles in non-expanded 4T1 cells via light scattering imaging.** 4T1 cells were incubated with 55-nm PEG-AuNPs for 24 h before

being washed, fixed, and stained. The overlay of the stained cells and light scattering (red) are shown first, followed by a magnification of all the channels, and then only the light scattering channel for cells with or without PEG-AuNPs shown in grayscale. Images were thresholded against parallel controls not incubated with AuNPs to remove the light scattering background signal. **(a)** Cells stained with DAPI (blue) and WGA-CF488A (green). **(b)** Cells stained with NHS-AF555 (gray). The scale bars indicate 50 μm for the unmagnified images and 15 μm for the magnified images. The nanoparticle light scattering signal intensity from the PEG-AuNPs was measured on ImageJ by the integrated density of the light scattering signal in regions of interest drawn around the membrane of the cells stained with (**c**) DAPI and WGA-CF488A or (**d)** NHS-AF555. An unpaired one-tailed t-test resulted in a significant statistical difference in the means of the two groups (****$p<0.0001$) ($n=9$). **(e)** Inductively coupled plasma mass spectrometry (ICP-MS) measurements of 4T1 cells with or without PEG-AuNP incubation to quantify gold nanoparticle cell uptake. Unpaired one-tailed t-test (****$p<0.0001$) ($n=4$). Bars indicate mean +/- standard deviation (SD).

We then quantified the signal intensity of the nanoparticle light scattering channel as a measurement of relative intracellular AuNP content. Figures 2.3c and 2.3d demonstrate the ImageJ software-based quantification of the nanoparticle light scattering intensity of individual cells stained with DAPI and WGA-CF488A or NHS-AF555, respectively. In both cases, there was a statistically significant difference (****$p<0.0001$) in the light scattering intensity measured from the cells treated with PEG-AuNPs compared to those not treated. Furthermore, the measured signal intensity of the cells not treated with PEG-AuNPs was close to the expected background signal.

We then validated that the nanoparticle light scattering signal can be acquired at various wavelengths using multiple laser types. Figure S2.5 shows RAW 264.7 macrophages that were incubated with 55-nm AuNPs coated with 5-kDa methoxy-terminated poly(ethylene glycol)-thiol (mPEG-SH) (Table S1). The AuNPs within the same group of cells were visualized using four different laser lines: a 488-nm argon laser, a 561-nm diode-pumped solid-state laser, a 594-nm helium-neon laser, and a 633-nm helium-neon laser. Our results confirm that nanoparticle light scattering imaging is broadly attainable and independent of a specific laser wavelength. We observed in Figure S2.5 that the 561-nm laser provided the strongest nanoparticle light scattering signal, which was expected given that the 561-nm laser has the closest wavelength to the peak extinction wavelength of 55-nm AuNPs (Figure S2.3). Therefore, we continued to use this laser wavelength for all subsequent nanoparticle light scattering imaging.

Next, we validated that the detected imaging signal in the nanoparticle light scattering channel was indeed due to the presence of gold within the cells. We used inductively

coupled plasma mass spectrometry (ICP-MS) as a quantitative elemental analysis method to determine the gold content of cells with and without PEG-AuNPs incubation.[300,301] The ICP-MS results revealed a cellular gold content equivalent to ~290 +/- 13 PEG-AuNPs/cell for 4T1 cell samples incubated with PEG-AuNPs, while the non-treated control cells exhibited a gold content that was close to the background (Figure 2.3e) (*n*=4).

To further validate that the nanoparticle light scattering signal was due to intracellular AuNPs, we treated 4T1 cells that were incubated with PEG-AuNPs with a gold etching solution consisting of KI and $I_2$.[302] Given that the cells were permeabilized with 0.1% (V/V) Triton X-100 following fixation, the KI/$I_2$ etchant dissolved both intracellular and extracellular AuNPs. We imaged the same group of cells before and after the gold etchant treatment (Figure S2.6a-b). Qualitatively, the images confirm that the nanoparticle light scattering signal visibly disappears after the etching. We then quantified the corresponding decrease in nanoparticle light scattering signal intensities in these cells. Figure S6c demonstrates that the nanoparticle light scattering signal was reduced to near background levels following etching. This result further confirms that intact AuNPs are needed to produce an efficient nanoparticle light scattering signal.

### 2.2.4 Nanoparticle light scattering signal is not affected by photobleaching

We then confirmed one of the major advantages of the nanoparticle light scattering imaging method, which is the signal's imperviousness to photobleaching. Photobleaching is a common challenge in fluorescence imaging that involves the irreversible degradation

of organic fluorophores due to repetitive excitation and emission cycles, i.e. repeated or continuous laser exposure.[303] In contrast, nanoparticle light scattering imaging takes advantage of the inherent scattering properties of metallic nanoparticles. This property is not altered by laser exposure. Therefore, the nanoparticle light scattering signal does not photobleach.

To demonstrate this advantage, we first synthesized fluorescently tagged 55-nm AuNPs. We selected the organic fluorophore cyanine 5 (Cy5) for its commonly reported use in nanoparticle labeling.[262,304–306] Using DLS, we measured an increase in the average hydrodynamic diameter of these nanoparticles compared to citrate-coated AuNPs by 44.3 +/- 3.0 nm, confirming the successful preparation of Cy5-PEG-AuNPs (Table S1) (*n*=3). To verify the functionality of the Cy5 fluorophore on the nanoparticle surface, we ran an agarose gel electrophoresis experiment to visualize the variations in migration distances compared to different groups as well as their corresponding fluorescence emissions through a 0.5% agarose gel (Figure S2.7a). We then further validated the functionality of the Cy5 fluorophore on the nanoparticle surface by measuring the fluorescence emission spectra of Cy5-AuNPs, PEG-AuNPs, and Cy5-PEG using a spectrofluorometer. The results demonstrated highly similar fluorescence emission spectra from the Cy5-AuNPs and the Cy5-PEG with minimal detected emission from the PEG-AuNPs (Figure S2.7b).

We then incubated 4T1 cells with Cy5-PEG AuNPs for 24 hours. Figure S2.8a shows the same group of cells imaged over a 30-minute timelapse at an imaging rate of 1 image/minute. Here, the Cy5 fluorescence signal noticeably decreased in intensity throughout the timelapse, while the nanoparticle light scattering signal did not. We

quantified these results by measuring the signal intensities of both channels in individual cells across the timelapse with ImageJ. Figure S2.8b demonstrates a clear imperviousness of light scattering signals to photobleaching, while the Cy5 fluorescence intensity dropped by over 50% throughout the timelapse.

The imperviousness of nanoparticle light scattering imaging to photobleaching is particularly advantageous for expansion microscopy, given that large Z-stacks with many sections are required for the 3D imaging of expanded cells. Depending on the cell thickness and step size determined by the optical section thickness,[277,307] an average non-expanded eukaryotic cell may take around 10-20 Z-steps to image at a high objective. Following an isotropic 4X expansion, 40-80 Z-steps would be needed to image an expanded cell at the same step size. The repeated exposure to the laser excitation light can cause the emission of typical fluorophores bound to the surface of nanoparticles to photobleach throughout the Z-stack acquisition. This sequential data acquisition process inherently results in signal intensities toward the top of the cell being significantly weaker than the ones detected near the bottom of the cell. Such differences in signal intensities from nanoparticles throughout a single image stack would make quantitative signal intensity analysis unreliable, demonstrating an additional advantage of nanoparticle light scattering imaging for expansion microscopy.

### 2.2.5 Combining expansion microscopy with nanoparticle light scattering imaging

Next, we asked whether we could combine fluorescent labeling of cells with label-free scattered light imaging of nanoparticles to determine cell uptake and intracellular

nanoparticle distributions. We observed that the nanoparticles could be visualized in their original relative positions within cells after the hydrogel expansion. This observation is likely due to the nanoparticle protein corona being crosslinked into the polyacrylamide-based gel matrix introduced during the proExM procedure. During this process, the cellular proteome is covalently attached to the gel matrix via Acryloyl-X, SE, a small molecule that binds to primary amines in proteins. The labeled proteins are crosslinked similarly into the gel matrix as the acrylamide monomers.[294]

We can use this behavior to crosslink proteins on the nanoparticle surface within the polyacrylamide-based gel. Nanoparticles form a protein corona upon encountering biological fluids. This corona represents a protein shell that spontaneously forms around the nanoparticle surface.[19,156] The corona proteins will crosslink into the polyacrylamide gel matrix during the Acryloyl-X, SE treatment, allowing the nanoparticles to become crosslinked and retained within these hydrogels. We confirmed the presence of surface proteins isolated from nanoparticle surfaces upon fetal bovine serum (FBS) incubation qualitatively with sodium dodecyl sulfate-polyacrylamide gel electrophoresis (SDS-PAGE). We used FBS as a model protein source since we performed the cell culture and nanoparticle incubation experiments using FBS. Figure S2.9 demonstrates the visible protein bands on the lanes of citrate-coated AuNP and PEG-AuNP upon FBS incubation. In contrast, no visible protein bands appeared on the lanes of either AuNP type without FBS incubation.

We then investigated whether the combination of expansion microscopy and nanoparticle light scattering imaging would allow for the in-depth analysis of nanoparticle accumulation within individual intracellular vesicles. Figure 2.4a shows expanded 4T1

cells incubated with PEG-AuNPs, stained with NHS-AF55. The intracellular vesicles are visible in expanded cells stained with NHS-AF555 as dark areas, with nanoparticles now visible within these intracellular compartments.

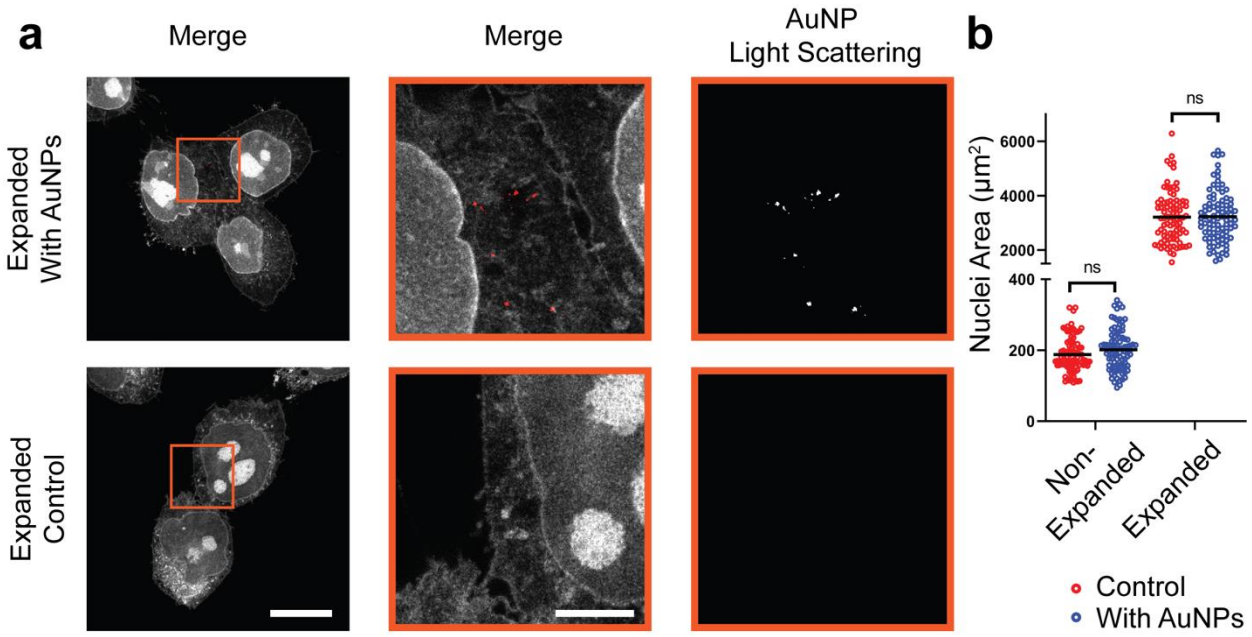


**Figure 2.4: Expansion microscopy is compatible with nanoparticle light scattering imaging. (a)** Expanded 4T1 cells with or without PEG-AuNPs stained with NHS-AF555 (gray). The overlay of the stained cells and light scattering (red) are shown first, followed by a magnification of both channels, and then only the light scattering channel for cells with or without AuNPs shown in grayscale. **(b)** ImageJ-based quantitative analysis of the nuclei area in $\mu m^2$ of non-expanded- and expanded cells both with and without AuNPs (n=90). Black lines represent means. A two-way ANOVA with Šidák's multiple comparison test did not show statistical significance (p=0.99 for both groups). The scale bars indicate 50 μm in the unmagnified images and 15 μm in the magnified images, not corrected for expansion factors.

We then asked whether the presence of AuNPs in a cell sample would affect the proExM expansion factor. Figure 4b shows no statistically significant difference (p=0.84) in the mean nuclei cross-sectional area of 4T1 cells containing AuNPs compared to controls for both non-expanded and expanded cells. A linear expansion factor of ~4.0X for cells containing AuNPs was determined, compared to a linear expansion factor of ~4.1X in controls. These results demonstrate the quantification of nanoparticle light scattering signals within individual vesicles in 3D.

We then explored the use of fluorescent endocytosis tracers with proExM and nanoparticle light scattering imaging. To identify the vesicle types that the AuNPs accumulated in, we attempted a super-resolution colocalization analysis of the nanoparticle light scattering signal of AuNPs co-incubated with specific fluorescent endocytosis tracers. Here, we selected tetramethylrhodamine-conjugated transferrin (TRITC-transferrin), a marker for clathrin-mediated endocytosis, as transferrin can be retained within cells following protein fixation.[106,308] In Figure S2.10, we show 4T1 cells co-incubated with PEG-AuNPs and 25 µg/mL TRITC-transferrin. Since we demonstrated that fluorescence staining and nanoparticle light scattering imaging are compatible with expansion microscopy, the super-resolution colocalization analysis for the TRITC and nanoparticle signals would be possible. However, we observed a significant decrease in the fluorescent signal from the TRITC-transferrin following proExM. This decrease is likely due to the volumetric expansion resulting in the separation or loss of fluorophores, limiting our capabilities to do accurate colocalization analysis. To potentially address this issue in future work, perhaps a fluorescent secondary antibody targeting against transferrin could be employed to improve the signal intensity.[309]

We next explored the different cell lines, nanomaterials, and surface conjugations to demonstrate the generalizability of our method. Previous work determined that coating the surface of 55-nm AuNPs with the polysaccharide heparosan (HEP-AuNPs) (Table S1, S2, Figure S2.3a, S2.4d) results in high nanoparticle uptake within DC 2.4 dendritic cells.[301] We used these dendritic cells and incubated the cells with HEP-AuNPs to demonstrate our method's generalizability across a different cell type and nanoparticle surface modification (Figure S2.11). We further demonstrated in Figure S2.12 the generalizability using a different nanomaterial, i.e. 60-nm streptavidin-coated silver nanoparticles (60-nm Strep-AgNPs) (Table S1, S2, Figure S3b, S4e) in RAW 264.7 macrophages. For consistency with other experiments, the 561-nm laser was used for the AgNPs light scattering imaging.

We then explored the ability to visualize smaller nanoparticle sizes. It has been shown that the nanoparticle light scattering imaging method is feasible for nanoparticle diameters down to ~20 nm in diameter.[286] Figure S2.13a shows RAW 264.7 macrophages after incubation with 40-nm streptavidin-coated AgNPs (Table S1, S2, Figure S2.3b, S2.4f), demonstrating the expected nanoparticle light scattering signal. However, as shown in Figure S2.13b, the nanoparticle light scattering signal is no longer visible in these cells following the proExM expansion process. We hypothesized that the surface-adsorbed proteins on the 40-nm Strep-AgNPs were not sufficiently crosslinking into the polyacrylamide-based gel matrix to hold the nanoparticles in place, resulting in a loss of nanoparticles during sample expansion. We found that this limitation can be overcome by increasing the crosslinker density of the gel matrix. By doubling the N,N′-methylenebisacrylamide crosslinker concentration in the gelation solution, we could

better retain and visualize 40-nm Strep-AgNPs within expanded cells (Figure S2.13c). However, this workaround came at the cost of a decrease in expansion factor by >25% (i.e. ‘tighter’ gel structures do not expand as much).[310]

We further assessed if a percentage of intracellular 55-nm AuNPs was lost during the proExM process. We approached this question qualitatively by imaging the same group of cells before and after the proExM process, as shown in Figure S2.14a. Here, we observed a similar amount of nanoparticle light scattering signal in the cells before and after expansion. However, we could not quantitatively compare the nanoparticle light scattering signal between the two groups since a higher laser power was required to visualize intracellular AuNPs within expanded cells than non-expanded cells.

To address this challenge, we quantified the gold content of each residual solution from the proExM process through ICP-MS to determine intracellular gold content loss. Figure S2.14b shows that there was no significant difference ($p>0.99$) in the detected gold content of residual solutions from samples that were treated with AuNPs compared to untreated controls (see Methods section). These data suggest that the standard proExM process does not result in an appreciable loss of intracellular 55-nm AuNPs.

We then wondered whether the AuNP retention in cells throughout the proExM process resulted from intracellular AuNP aggregation, given that we have already established a size correlation to AuNP leakage in Figures S2.12 and S2.13. To address this question, we incubated HEP- and PEG-AuNPs in culture media (DMEM), complete culture media (DMEM +10% FBS + 1% penicillin-streptomycin (P/S)), or an artificial lysosomal fluid[311] for 3 hours before comparing their colloidal stability to AuNPs incubated in ultrapure H2O using single-particle inductively coupled plasma mass spectrometry (SP-

ICP-MS). SP-ICP-MS allows us to quantify the mass of individual AuNPs at single-particle resolutions to estimate their approximate sizes. The SP-ICP-MS method then allows us to determine the corresponding colloidal stability of the AuNPs as aggregates would be registered as single AuNPs of significantly larger masses (i.e. sizes) than colloidally stable AuNPs.[180,299,312,313] Figure S2.15 demonstrates that there is no significant difference ($p>0.9999$) in the means of the distributions of HEP- or PEG-AuNPs, respectively, in any of the tested conditions compared to the ultrapure H2O control group. These results suggest that the AuNPs may not significantly aggregate intracellularly. These results further suggest that the AuNP light scattering signals we acquired were not significantly affected by aggregated AuNPs.

### 2.3 Conclusion

Here, we established a 3D-super-resolution microscopy method for visualizing the distribution of metallic nanoparticles within cultured cells. The use of proExM allows for a >4X increase in the attainable spatial resolution for visualizing cultured cells with a standard CLSM. The use of label-free nanoparticle light scattering imaging in conjunction with a bulk(pan) stain following proExM allows for the localization of nanoparticles within the intracellular vesicles of cultured cells. This new method allows for more detailed analyses of nanoparticle-cellular interactions, leading to a better understanding of nanoparticle intracellular fate that will empower new research for the development of safer and more effective nanomedicine.

## Chapter 3: Quantifying Intracellular Nanoparticle Distributions with Three-Dimensional Super-Resolution Microscopy

### 3.1 Introduction

In Chapter 2, we demonstrated that proExM is compatible with label-free nanoparticle light scattering imaging for visualizing nanoparticle distribution within intracellular vesicles. However, proExM only allows expansion factors of ~4X, so with an optical resolution limit of ~200 nm laterally,[241] this process results in an expansion corrected lateral resolution limit of ~50 nm. As mentioned in Figure 1.6, most intracellular vesicles formed through the primary endocytosis pathways that are of interest for transcytosis across endothelial cells of tumor blood vessels are larger than 50 nm. While a 4X expansion should theoretically allow for most intracellular vesicles to be resolved, the actual achievable resolution with most imaging settings would be significantly lower, based on factors such as the wavelength of light being detected and the numerical aperture of the microscope objective being used.[277] Therefore, higher expansion factors are needed to resolve smaller vesicles. To achieve such higher resolutions, we adopted the pan-ExM protocol.[280] Pan-ExM uses a protease-free, iterative hydrogel expansion process that results in a linear expansion factor between ~10-20X, corresponding to a lateral resolution of ~10-20 nm. This protocol enables the resolution of many intracellular features, such as individual mitochondria. The visualizations of these intracellular features through pan-ExM have been validated by Bewersdorf et al., who compared the expansion-corrected measured distances between internal cristae of mitochondria in expanded HeLa cells to previously published reports from STED images of live HeLa cells.[280,314]

## 3.2 Results and Discussion

### 3.2.1 Super-resolution 3D imaging of nanoparticle intracellular localization

Here, we applied pan-ExM to our method of visualizing metallic nanoparticles within cultured cells. Figure 3.1 (a-b) shows non-expanded RAW 264.7 macrophages with and without intracellular HEP-AuNPs, respectively. In Figure 3.1 (c, d), we show the 3D reconstructions of CLSM Z-stacks of RAW 264.7 with and without HEP-AuNPs treatment after pan-ExM, along with two individual slices from the stacks (Movies S1, S2). We show that the nanoparticle light scattering signals were localized within intracellular vesicles throughout multiple Z positions in the HEP-AuNP group with no visible signal in the control group. This result confirms the compatibility of pan-ExM with label-free nanoparticle light scattering imaging, while demonstrating that the achievable resolution through this method is sufficient for qualitatively analyzing intracellular nanoparticle distributions.

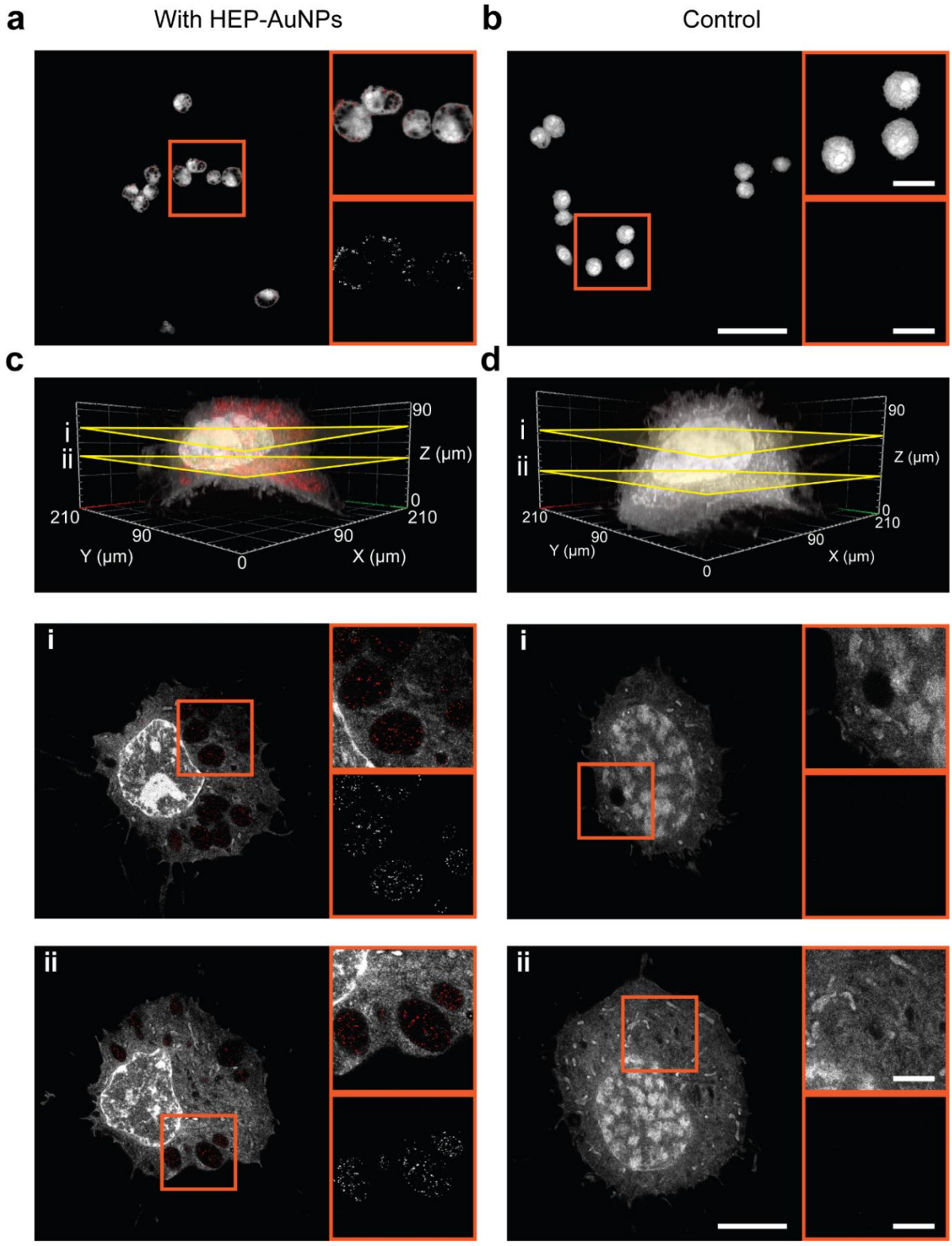


**Figure 3.1: Pan-ExM enables the 3D super-resolution imaging of cultured cells with high levels of specific AuNP localization.** Images of non-expanded RAW 264.7

macrophages stained with NHS-AF555 (grey) with- **(a)** or without **(b)** HEP-AuNPs, with the AuNP light scattering signal shown in red. Post pan-ExM images of cells **(c, d)** with 3D reconstructions of CLSM Z-stacks. Images (i) and (ii) depict individual x,y-slices. Digital magnifications of the regions of interest are shown, first with the overlay of both channels. Then the nanoparticle light scattering signal alone is shown in grayscale focused on individual vesicles revealing densely concentrated AuNPs (red) in cells. No noticeable light scattering signal in vesicles of cells that were not treated with AuNPs. The scale bars indicate 50 µm in the unmagnified images and 15 µm in the magnified images. Scale bars for images of expanded cells are the original length as taken by the microscope (i.e., not corrected for expansion factors).

We then validated the visualization of intracellular vesicles through bulk (pan) staining to verify that these were not artifacts from the expansion processes. Figure S3.1a shows non-expanded RAW 264.7 macrophages with and without HEP-AuNPs imaged with standard CLSM settings. Here, we see some dark areas within the cytoplasm that exhibit nanoparticle light scattering signals, however, there is insufficient resolution to fully localize the nanoparticle light scattering signals within the vesicles. Therefore, in Figure S3.1b, we then imaged the same samples with the Zeiss Airyscan detector, which allows for an increase in spatial resolution by up to 1.7X, as well as a 4-8X increase in the signal-to-noise ratio (SNR).[315] Here, we can much more clearly visualize the intracellular vesicles as dark area within the cytoplasm of RAW 264.7 macrophages treated with HEP-AuNPs, and better localize the nanoparticle light scattering signals within them. These observations, along with the observation that there are relatively very few dark areas visible in the cytoplasm of cells that were not treated with AuNPs, suggest that the intracellular vesicle visualizations were not artifacts from the expansion processes.

### 3.2.2 Quantifying the effect of nanoparticle surface modifications on cell uptake and intracellular localization

To further investigate how nanoparticle surface modification affects nanoparticle-cell interactions and uptake, we compared 55-nm PEG-AuNPs to AuNPs coated with bovine serum albumin proteins (BSA-AuNPs) using 4T1 cells as a model system. Albumin is a known tracer for caveolae-mediated endocytosis. It is well established that decorating nanoparticles with albumin results in an increased uptake in cancer cells compared to PEGylated nanoparticles.[127,316] We prepared BSA-AuNPs by incubating citrate-coated AuNPs in a 10 mg/mL BSA solution for 1 hour at 37°C. The successful BSA surface conjugation was confirmed by an increase in the nanoparticle hydrodynamic diameter by 26.2 +/- 2.2 nm, with an expected negative zeta potential[317] (Table S1, S2, Figure S2.3a) (*n*=3). To further verify the formation of a BSA protein corona around the AuNPs, we ran an SDS-PAGE of isolated proteins from the nanoparticle surface (Figure S3.2). The isolated surface proteins appear as a band at about the same migration distance as the free BSA control. Figure S3.3 compares the uptake of these BSA- and PEG-AuNPs in 4T1 cells with and without pan-ExM treatment. Qualitatively, more BSA-AuNPs are visible within the cells compared to PEG-AuNPs after expansion, suggesting that this method can be used for comparing the uptake of nanoparticles with different surface modifications.

To demonstrate the utility of our super-resolution imaging method for comparing the uptake and distribution of nanoparticles with different surface modifications, we chose to compare the uptake of heparosan- (HEP) and PEG-AuNPs in RAW 264.7 macrophages following a 3-hour incubation.[301] Figure S3.4(a-b) shows non-expanded cells upon

incubation with HEP- or PEG-AuNPs, respectively. Qualitatively, there was an evident difference in nanoparticle light scattering signal between the two groups. This observation was confirmed quantitatively in Figure S3.4c with image analysis showing a significantly higher nanoparticle light scattering signal (****$p<0.0001$) being measured in non-expanded RAW 264.7 macrophages treated with HEP-AuNPs compared to PEG-AuNPs. Figure 3.2 (a-b) shows the RAW 264.7 macrophages incubated with either HEP- or PEG-AuNPs, respectively, after expansion with the pan-ExM protocol.

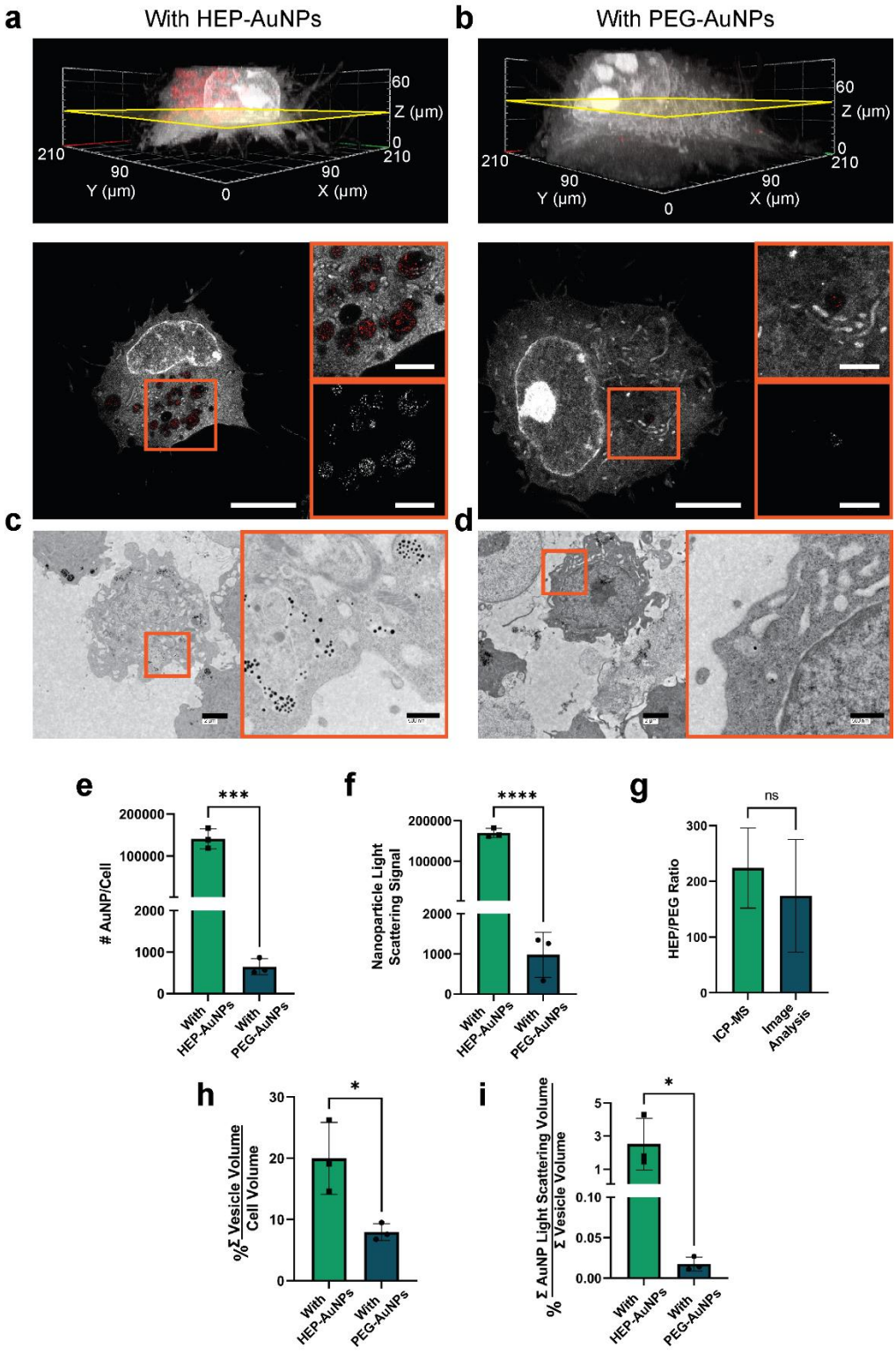


**Figure 3.2: Pan-ExM enables quantitative comparisons of nanoparticle cell uptake.** RAW 264.7 cells were incubated with HEP-AuNPs **(a)** or PEG-AuNPs **(b)** for 3 hours before being washed, fixed, and expanded via pan-ExM, with 3D reconstructions of CLSM

Z-stacks being shown along individual xy-slices, including digital magnifications focused on individual nanoparticle-containing vesicles. Digital magnifications of the regions of interest are shown, first with the overlay of both channels, and then the nanoparticle light scattering signal alone shown in grayscale. The scale bars indicate 50 µm in the unmagnified images and 15 µm in the magnified images, not corrected for expansion factors. TEM images of RAW 264.7 cells treated with HEP-AuNPs **(c)** or PEG-AuNPs **(d)** are shown, demonstrating similar AuNP (black spots) distribution patterns within a single imaging plane. The scale bars indicate 2 µm in the unmagnified images and 500 nm in the magnified images. **(e)** ICP-MS measurements of RAW 264.7 cells after incubation with HEP-AuNPs or PEG-AuNPs quantifying nanoparticle cellular uptake. Unpaired, one-tailed t-test (***$p<0.001$) (*n*=3). **(f)** Image analysis of the pan-ExM samples was done via MATLAB to quantify the nanoparticle light scattering signal to measure nanoparticle accumulation in both sample types across entire CLSM Z-stacks. Bars represent mean +/- SD, unpaired one-tailed t-test (****$p<0.0001$) (*n*=3). **(g)** The ratios HEP-AuNPs/PEG-AuNPs uptake in RAW 264.7 cells. Bars represent ratio +/- propagation of error, unpaired two-tailed t-test (ns = not significant, $p=0.66$). **(h)** The volumes of the cells and vesicles after pan-ExM across the entire CLSM Z-stacks. Unpaired one-tailed t-test (*$p<0.05$) (*n*=3). **(i)** Percentage of the total vesicle volume occupied by AuNPs. Bars represent mean +/- SD, unpaired one-tailed t-test (*$p<0.05$) (*n*=3).

We then compared our super-resolution imaging method against the traditional means of visualizing intracellular nanoparticle distribution and quantifying nanoparticle uptake. Since TEM has been the longstanding standard method for visualizing nanoparticle distribution within cells,[318,319] we compared our pan-ExM-based images to TEM images of non-expanded RAW 264.7 cells with HEP- or PEG-AuNPs in Figure 3.2(c-d). As seen from these images, there is a similar distribution pattern of intracellular nanoparticles between the two methods, and the known preference of HEP-AuNPs over PEG-AuNPs in RAW 264.7 cells is readily observable.[300,301] This finding suggests that pan-ExM combined with light scattering imaging enables the representative visualization of nanoparticle intracellular distributions. While TEM is restricted to the 2D imaging of thin (~70 nm) cell slices, we achieved robust and reliable 3D visualizations of nanoparticle distribution in entire cells.

To confirm that our method provides representative information about the number of nanoparticles in a cell, we first ran ICP-MS on non-expanded samples of RAW 264.7 macrophages treated with HEP- or PEG-AuNPs to determine the average number of nanoparticles per cell (Figure 3.2e). We then developed a MATLAB script to quantify the nanoparticle light scattering signals from pan-ExM samples to measure nanoparticle accumulation (Figure 3.2f). While the image analysis does not provide an exact count of the number of nanoparticles in the cells, given that it is currently unknown what the exact correlation between light scattering signals and nanoparticle numbers is, it does allow for relative comparisons across different nanoparticle conditions. As such, we compared the uptake ratio for HEP-AuNPs and PEG-AuNPs as measured by ICP-MS to our image analysis (Figure 3.2g). ICP-MS demonstrated that the cells took up 208+/- 72

(propagation of error) (*n*=3) times more HEP-AuNPs than they do for PEG-AuNPs, while the image analysis of the pan-ExM samples demonstrated that the ratio of HEP-AuNP uptake to PEG-AuNP uptake is 174 +/- 101 (*n*=3) with no significant difference (p=0.66) in this uptake ratio between the two methods. This analysis suggests that our method provides representative information about nanoparticle accumulation in entire cells. While ICP-MS is a destructive process that only provides information on the content of gold within a group of cells, our method reveals the spatial distribution within individual and intact single cells and can reveal cell-to-cell variability. Combined with the ability to visualize entire cells at super-resolution, we can now collect previously unobtainable spatial information about nanoparticle localization within intracellular vesicles throughout cells.

We further demonstrate the ability to determine the percentage of the cell volume occupied by intracellular vesicles. We used a MATLAB script to measure the area of the entire cell and the cumulative area of the vesicles on each Z-slice. The summations of the areas of each measurement through the Z-stack were then used to estimate their volumes (Figure 3.2h). We observed that the nanoparticle surface modifications affected not only nanoparticle uptake but also the frequency of intracellular vesicles that exist in response to nanoparticle incubation and endocytosis. The higher frequency of intracellular vesicles within RAW 264.7 macrophages treated with HEP-AuNPs compared to those treated with PEG-AuNPs may suggest that receptor-specific endocytic pathways significantly contribute toward the uptake of HEP-AuNPs. Yang *et al*. showed recently that heparosan polysaccharide-coated nanoparticles exhibit substantial endocytosis in

innate immune cells to trigger the formation of more intracellular vesicles from additional endocytosis events compared to PEG-AuNPs.[300,301]

We then estimated the percentage of the vesicle volume occupied by nanoparticles (Figure 3.2i). Since the pixel area of the detected nanoparticle light scattering signal was significantly larger than the area a nanoparticle would realistically occupy in non-expanded cells, or potentially smaller in expanded cells (following correction for expansion factors), this estimation is not an exact measure. However, this estimate does allow relative comparisons between different nanoparticle surface modifications. We show that HEP-AuNPs occupied a significantly higher percentage of the vesicle volume than PEG-AuNPs (*$p<0.05$, Figure 3.2i), which is expected given the high endocytosis rates and efficiencies of HEP-AuNPs.[300,301] We anticipate that this type of nanoparticle intracellular distribution analysis will be applied in future studies evaluating nanoparticle-cell interactions. Since the pan-ExM process is compatible with immunofluorescence labeling,[280] more specific analyses of the nanoparticle distribution across different types of intracellular vesicles or other intracellular features and compartments could be accomplished in future studies.

## 3.3 Conclusions

We demonstrated that label-free metallic nanoparticles could be visualized in 3D within individual intracellular vesicles of cultured cells in a quantifiable manner through our super-resolution imaging method. Furthermore, we showed that this method provides comparable information to the standard methods of analyzing metallic nanoparticle intracellular distribution and uptake, TEM and ICP-MS, respectively, while also allowing for analyses that were not possible through either method. Our method provides visual 3D information on (a) intracellular nanoparticle distribution in their ultrastructural context, which is not readily obtainable through TEM, along with (b) quantifiable information of relative nanoparticle accumulation within individual intracellular vesicles, which is not obtainable through ICP-MS.

We presented two expansion protocols compatible with this method, proExM and pan-ExM. While proExM does not provide sufficient resolution to fully resolve most of the smaller intracellular features, it is a significantly faster protocol. Conversely, pan-ExM provides significantly higher resolutions for separating smaller, adjacent intracellular vesicles, albeit at the cost of significantly longer processing times. Furthermore, pan-ExM does not rely on proteases, allowing for the post-expansion antibody labeling of samples, which results in better epitope accessibility by molecular de-crowding. In contrast, only certain epitopes can survive the proteinase treatment used in proExM. However, certain variants of proExM have employed protease-free homogenization, similar to pan-ExM.[280,287,294] These factors may be considered when choosing which expansion microscopy protocol to use.

We anticipate our demonstrated super-resolution imaging protocols can be applied to research involving a variety of nanomedicine formulations to broadly improve the understanding of the intracellular nanoparticle fate. The successful application of this elegant method may empower more informed research into the nano-bio interactions of nanomedicine formulations toward better clinical results and the development of more efficacious therapies for various diseases.

# Chapter 4: Three-Dimensional Super-Resolution Microscopy for Visualizing Organic Nanoparticle Localization Within Cells

## 4.1 Introduction

In Chapters 2 and 3, we described the use of metallic nanoparticles to develop a method for visualizing and quantifying the distribution of nanoparticles within cultured cells.[320] Metallic nanoparticles have been widely used as model systems for nanomedicine delivery due to their relative ease of synthesis, functionalization, and characterization.[321] However, metallic nanoparticle have thus far had limited clinical translation for cancer treatments.[322] Organic nanoparticles, on the other hand, have had significantly more clinical success, with multiple organic nanomedicine formulations being approved for clinical use by the U.S. Food and Drug Administration (FDA).[323] While these organic nanomedicine formulations do tend to promote better patient safety compared to their free drug equivalents, they are still limited by low cancer-treatment efficacy, as they also demonstrate low tumor accumulation.[14,324] Therefore, there is still a need for visualizing organic nanoparticles in their ultrastructural context.

While pan-ExM does provide sufficient resolution for the visualization of metallic nanoparticles in their ultrastructural context, its process involves the removal of lipids from cultured cell samples.[280] Given that a majority of the FDA approved organic anti-cancer nanomedicine formulations are lipid based, pan-ExM would not be ideal for organic nanoparticles, as it does not have a specific lipid anchoring step.[323] To achieve a better retention of lipids in expanded cells, we adopted the Magnify expansion microscopy protocol. Magnify is a one-gel expansion microscopy technique that allows for the

retention of proteins, nucleic acids, and lipids in cultured cell samples and results in linear expansion factors up to 11X.[325]

In this study, we established the use of Magnify for the ultrastructural visualization of liposomes. Liposomes are nanoparticles that are composed of lipid bilayers around an aqueous core and are among the most commonly used types of organic nanoparticles used in the clinic. As a result of this biphasic structure, liposomes are capable of encapsulating hydrophilic drugs within their aqueous core and hydrophobic drugs within their lipid bilayer.[326] Given that the refractive index of liposomes is highly similar to that of fixed cultured cells, light scattering imaging would not provide much contrast between the liposomes and the cells due to the minimal refractive index mismatch.[265,327,328] However, liposomes can be visualized through internalized fluorescent tags within their hydrophilic or hydrophobic regions,[329,330] presenting a variety of avenues for their compatibility with expansion microscopy.

## 4.2 Results and Discussion

### 4.2.1 Comparison of Magnify to pan-ExM

Liposomes are widely recognized as more clinically relevant for the treatment of solid tumors than metallic nanoparticles. To achieve a better understanding of the ultrastructural intracellular distribution of liposomes, we adopted the Magnify expansion microscopy protocol. Magnify provides several advantages over pan-ExM for the visualization of liposomes in cultured cells, as shown in Figure 4.1a. The main benefit of Magnify is that it retains proteins, lipids, and nucleic acids through the expansion process, whereas pan-ExM primarily retains proteins. Furthermore, Magnify is a significantly faster

and less involved process as it involves only one gelation step, compared to three for pan-ExM. However, similar to other single gelation ExM methods,[287–289,331] Magnify results in a significantly lower maximum expansion factor than pan-ExM (11X compared to 21X). Figure 4.1(b-d) show RAW 264.7 macrophages that are non-expanded, pan-ExM processed, and Magnify processed respectively. We then determined the linear expansion factors from these methods in Figure 4.1e to be ~10.4X for pan-ExM and ~5.9X for Magnify. While these expansion factors are significantly lower than the maximum reported expansion factors, likely as a result of the purity of the sodium acrylate used in the gelation solutions, most intracellular vesicles of interest for cancer nanomedicine should still be resolvable (Figure 1.6).[280,289,325]

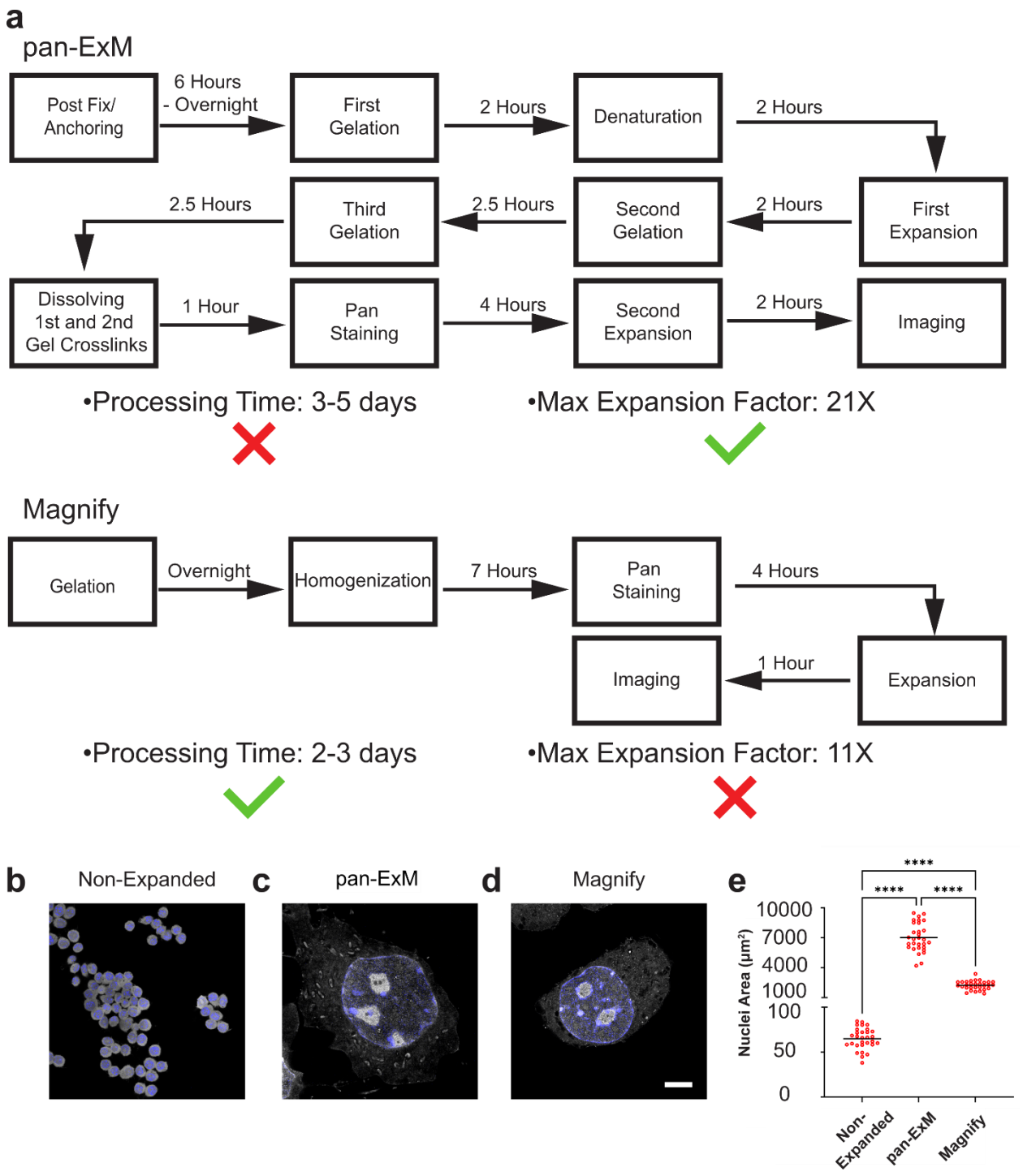


**Figure 4.1: Comparison of pan-ExM and Magnify.** a) The major steps and processing times (including relevant incubation and washing steps) for pan-ExM and Magnify are depicted in flow charts. While pan-ExM provides superior expansion factors, Magnify is a significantly faster process and allows for a wider retention of biomolecules. RAW 264.7 macrophages are shown as non-expanded (b), pan-ExM processed (c) and Magnify processed (d). Cells are stained with the DNA stain, 4′,6-diamidino-2-phenylindole (DAPI) (blue) for nuclei visualization and are bulk (pan) stained with NHS-AF488 (gray) to

visualize the entire proteome of the cell. The presence of resolved intracellular vesicles after pan-ExM and Magnify is demonstrated as the dark areas in the cytoplasm of the cells through the NHS-ester stain, having negative contrast against the surrounding protein filled regions. The scale bars indicate 20 μm in the unmagnified images and 5 μm in the magnified images, not corrected for expansion factors. (e) Quantitative analysis of the nuclei area in $\mu m^2$ of non-expanded and expanded cells, measured on ImageJ. The mean values (solid black line) were used to calculate the linear expansion factor of 10.4X and 5.9X for pan-ExM and Magnify respectively (n=30) using Equation 1. A one-way ANOVA with Tukey's multiple comparison test resulted in statistically significant differences in the means of the nuclei areas between the three groups (****$p<0.0001$).

### 4.2.2 Visualization of liposomes in expanded cells through internalized fluorescent cargo

Given that the primary goal of liposomes for cancer therapy is to deliver drugs to solid tumors, we first investigated the compatibility of liposomes with Magnify through the use of internalized fluorescent cargo. Doxorubicin (DOX) is one of the most commonly used cancer chemotherapeutic drugs in the clinic and is intrinsically fluorescent.[332] Typically, a hydrophilic version of DOX, Doxorubicin hydrochloride (DOX-HCl), is encapsulated into the aqueous phase of PEGylated liposomes, with one specific formulation, Doxil®, having gained FDA approval for the treatment of various cancers.[333] These properties make DOX-encapsulated PEGylated liposomes an attractive choice for testing the compatibility of liposomes with Magnify for visualizing intracellular distribution. Here, we used commercially available Doxoves®: DOX-encapsulated PEGylated liposomes that are similar to Doxil. We characterized the Doxoves with dynamic light scattering (DLS) (Table S3) and zeta potential (Table S4). We incubated RAW 264.7 macrophages with 100 µg/ mL Doxoves for 3 or 24 hours before washing, fixing, and staining them with DAPI and NHS-AF647. Non-expanded cells are shown in Figure S4.1(a - c). As expected, there is a visible DOX signal throughout the intracellular space of macrophages, demonstrating the uptake of the Doxoves, as well as throughout the DNA-rich portions of the nucleus, as DOX intercalates with DNA.[333] However, following Magnify expansion (Figure S4.1 (d - f)), the DOX signal is mostly lost throughout the cell, suggesting that DOX-HCl is not compatible with Magnify. It is likely that the DOX-HCl molecule is too small (579.99 Da)[334] to be retained within the gel matrix throughout the expansion process, causing it to passively flow out through the pores of the gel during wash steps. Interestingly, a certain amount of DOX signal is retained in protein-rich, DNA-

poor regions of the nuclei, appearing as “holes” in the DAPI signal. We quantified this signal in expanded cells that were treated with Doxoves and were stained only with DAPI through ImageJ and found an expected increasing signal density trend within the holes with an increased incubation time (Figure S4.1g) ($p<0.01$), suggesting that the signal that appears is not occurring through random chance or autofluorescence. Further work is needed to determine if the DOX signal within the holes in the nuclei is a true signal from DOX that was entrapped in the protein-rich surroundings while not being detectable in non-expanded cells due to a large difference in fluorophore density compared to the rest of the DOX within the cell, or if it is an artifact from the expansion process.

To address the issue of the cargo not being retained through the expansion process, we synthesized liposomes that have encapsulated larger fluorescent cargo. For this purpose, we selected 10 kDa dextran-AF488, which is fixable through the presence of free amines. Liposomes were synthesized via microfluidics using a custom syringe pump set that was constructed from an Ender3 3D printer.[335] Briefly, the two individually controlled syringe pumps are used to separately flow an organic phase (lipids and hydrophobic drugs) and an aqueous phase (hydrophilic drugs) into a T-mixer at controlled rates, with the resulting combined solution containing the newly synthesized drug-encapsulating liposomes. The size of the liposomes is dependent on the flow rate ratio (FRR) of the aqueous to the organic phase.[336,337] A schematic of the microfluidic liposome synthesis setup is shown in Figure 4.2.

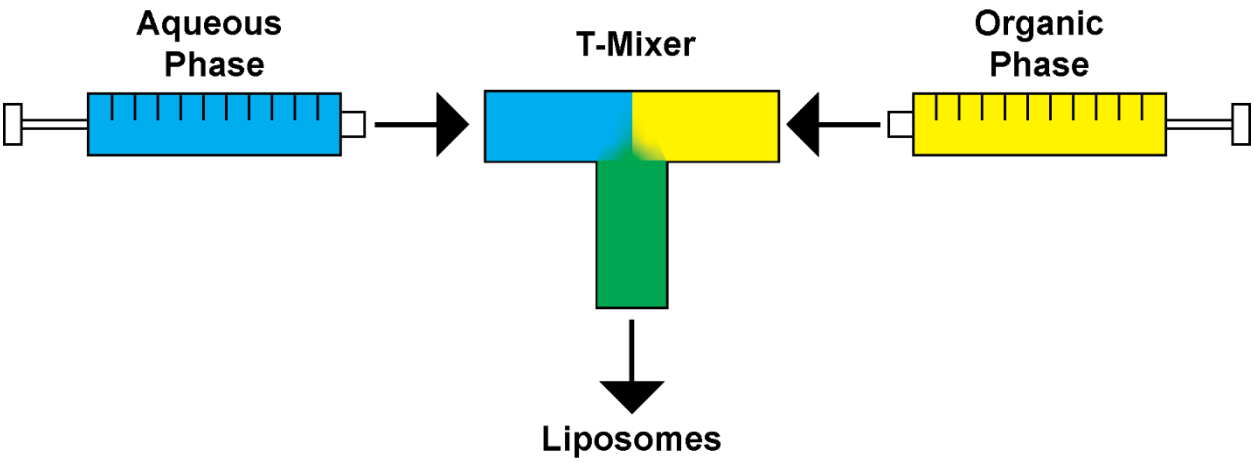


**Figure 4.2: Schematic of microfluidic liposome synthesis setup.** Two syringe pumps constructed from an Ender3 syringe pump are connected to a T-mixer. One syringe is filled with aqueous components, such as hydrophilic drugs dissolved in 1X PBS, while the other is filled with the organic components, such as lipids and hydrophobic drugs dissolved in ethanol. The syringe pumps can be controlled separately, allowing for the two phases to be mixed at different flow rates, with the resulting mixed solution containing liposomes with encapsulated drugs.

We first synthesized PEGylated liposomes consisting of 1,2-distearoyl-sn-glycero-3-phosphocholine (DSPC), cholesterol, and mPEG(2 kDa)-1,2-Distearoyl-sn-glycero-3-phosphoethanolamine (DSPE) by running those components in a 1.8: 0.6: 0.6 mass ratio dissolved in 100% ethanol and 10 kDa dextran-AF488 dissolved in 1X PBS through our microfluidics setup in a FRR of 7 (hereafter referred to as PEG-Liposomes). To remove unencapsulated dextran, the liposome solutions were filtered through several successive washes in Amicon centrifugal filters (100 kDa nominal molecular weight limit) that were pre-wet with 0.1% (w/v) bovine serum albumin (BSA) in 1X PBS (see Methods section). We characterized the resulting filtered liposomes with dynamic light scattering (DLS) (Table S3) and zeta potential (Table S4). Next, we ran an agarose gel electrophoresis to validate that a high amount of the free dextran had been removed from the liposome solution (Figure S4.2).

We then incubated RAW 264.7 macrophages with PEG-Liposomes for 24 hours and then processed them for Magnify expansion (Figure 4.3 (a,b)). Intracellular vesicles are visible in these bulk (pan) stained samples as dark areas within the cytoplasm as they are typically fluid filled compartments, thereby providing negative contrast against the protein-rich surroundings. The presence of the 10 kDa dextran-AF488 signal within intracellular vesicles in the expanded cells demonstrates that a larger cargo molecule size likely contributes to the retention of fluorescent liposomal cargo through the Magnify process.

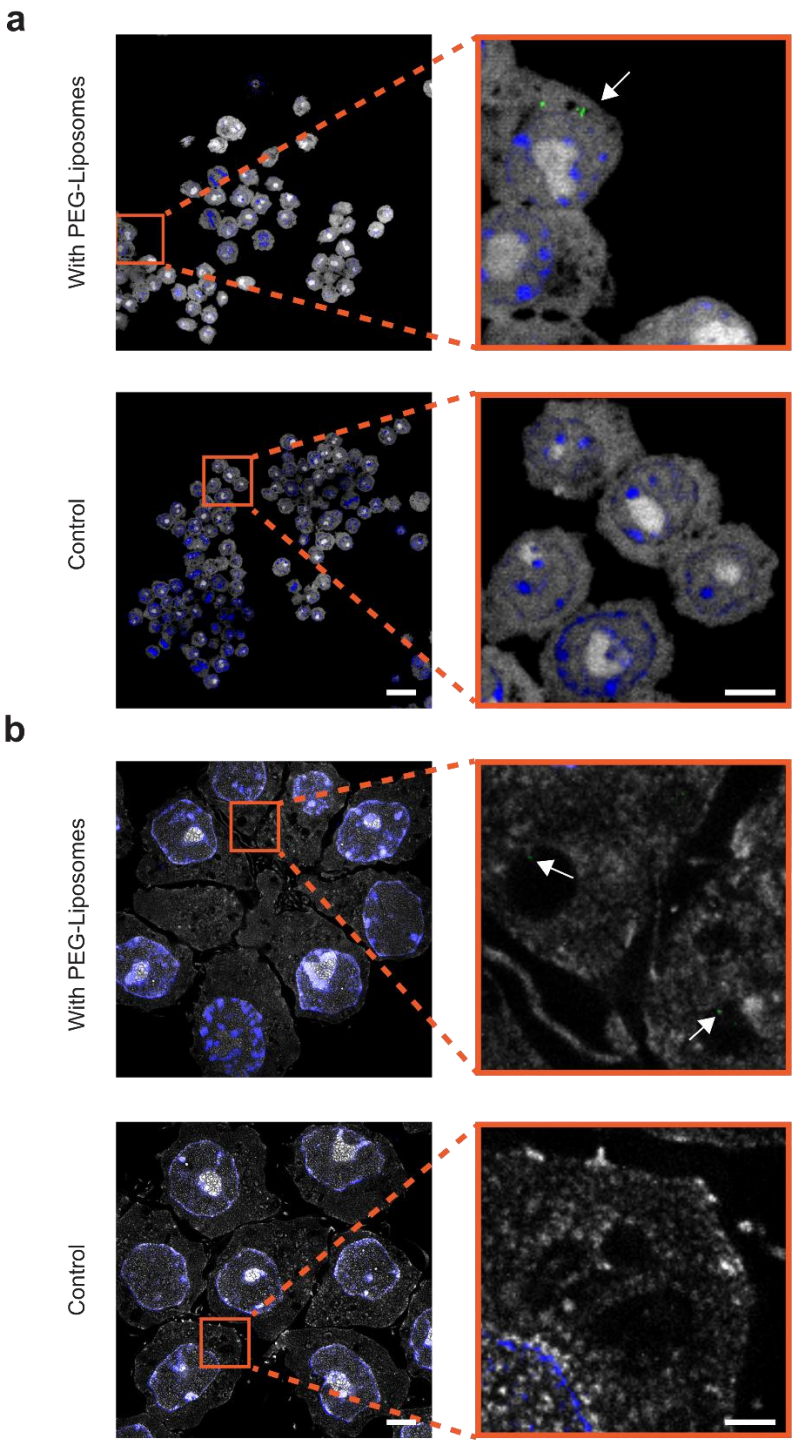


**Figure 4.3: Magnify enables the super-resolution visualization of fluorescent liposomal cargo within individual intracellular vesicles.** RAW 264.7 macrophages

were incubated with PEG-Liposomes for 24 hours before being washed, fixed, and expanded with the Magnify protocol, along with non-treated controls. Non-expanded cells are shown first **(a)**, followed by expanded cells **(b)**. Cells were stained with NHS-AF647 (gray) and DAPI (blue). First the overlay of the NHS-AF647, DAPI, and 10 kDa dextran-AF488 (green) is shown, followed by a digital magnification of a region of interest. White arrows indicate the position of 10 kDa dextran-AF488 signal within intracellular vesicles. The scale bars indicate 20 µm in the unmagnified images and 5 µm in the magnified images, not corrected for expansion factors.

Given that the 10 kDa-dextran-AF488 signal in the expanded cells was relatively weak, we next investigated ways to increase the uptake of liposomes in the cells. Previous work has demonstrated that liposomes coated with the polysaccharide heparosan (HEP) have higher uptake in RAW 264.7 macrophages than PEGylated liposomes.[301] We synthesized HEPylated liposomes by first synthesizing liposomes with a free thiol group that allows for conjugation to HEP- orthopyridyl disulfide (HEP-OPSS). We synthesized these liposomes consisting of DSPC, cholesterol, and 1,2-Dipalmitoyl-sn-Glycero-3-Phosphothioethanol (Ptd thioethanol) in a 6.0: 2.0: 0.3 mass ratio dissolved in 100% ethanol and 10 kDa dextran-AF488 dissolved in 1X PBS through our microfluidics setup in a FRR of 7 (hereafter referred to as Thiol-Liposomes). The Thiol-Liposomes were then mixed with HEP-OPSS at a 1:1 molar ratio of Ptd thioethanol to HEP-OPSS for 2 hours on a tube rotator, resulting in HEPylated liposomes (HEP-Liposomes), as validated by an increase in the hydrodynamic diameter of the liposomes by 25.6 +/- 1.5 nm (propagation of error) as measured by DLS (Table S3) and an expected negative zeta potential (Table S4). Furthermore, the low liposome uptake seen in Figure 4.3 could potentially be attributed to a low number of liposomes being incubated with the cells. Liposomes are likely to be lost after getting stuck on the Amicon centrifugal filter membranes during each filtration step, so a reduction in the number of necessary filtration steps to achieve a sufficiently purified liposome solution would be needed. To decrease the number of liposomes that are lost during the washes in the Amicon centrifugal filters, we first dialyzed the HEP-Liposomes against chilled 1X PBS overnight using a dialysis membrane with a 12-14 kDa molecular weight cutoff to remove residual ethanol in the liposome solution, which could potentially damage the centrifugal filter membrane. We observed that the

dialysis did improve the efficiency of the centrifugal filtration, with a >2.5X higher concentration increase in a single filtration step compared to undialyzed liposome solutions, thereby reducing the number of filtration steps needed to achieve a similar level of purification. We then once again ran an agarose gel electrophoresis to validate that a high amount of the free dextran had been removed from the liposome solution (Figure S4.3). Next, we incubated RAW 264.7 macrophages with HEP-Liposomes for 3 or 24 hours and then processed them for Magnify expansion. Figure 4.4(a-c) shows non-expanded RAW 264.7 macrophages that were treated with HEP-liposomes for 3 hours, 24 hours, and non-treated controls respectively. Figure 4.4 (d-f) show these same conditions after Magnify processing, first as 3D reconstructions of Z-stacks followed by individual slices from those stacks. These individual slices depict much higher levels of 10 kDa-dextran-AF488 signal within intracellular vesicles than cells that were treated with PEG-Liposomes, especially at a much shorter incubation timepoint of 3 hours compared to the 24-hour incubation of the PEG-Liposomes. Furthermore, there are visible differences in the distribution of the HEP-liposomes across the macrophages that were incubated for 3 hours compared to 24 hours. These findings suggest that this method can be used for quantifying the intracellular distribution patterns of liposome-encapsulated large molecule drugs that have demonstrated anti-cancer properties, such as chitosan[338,339] or hyaluronic acid[340,341].

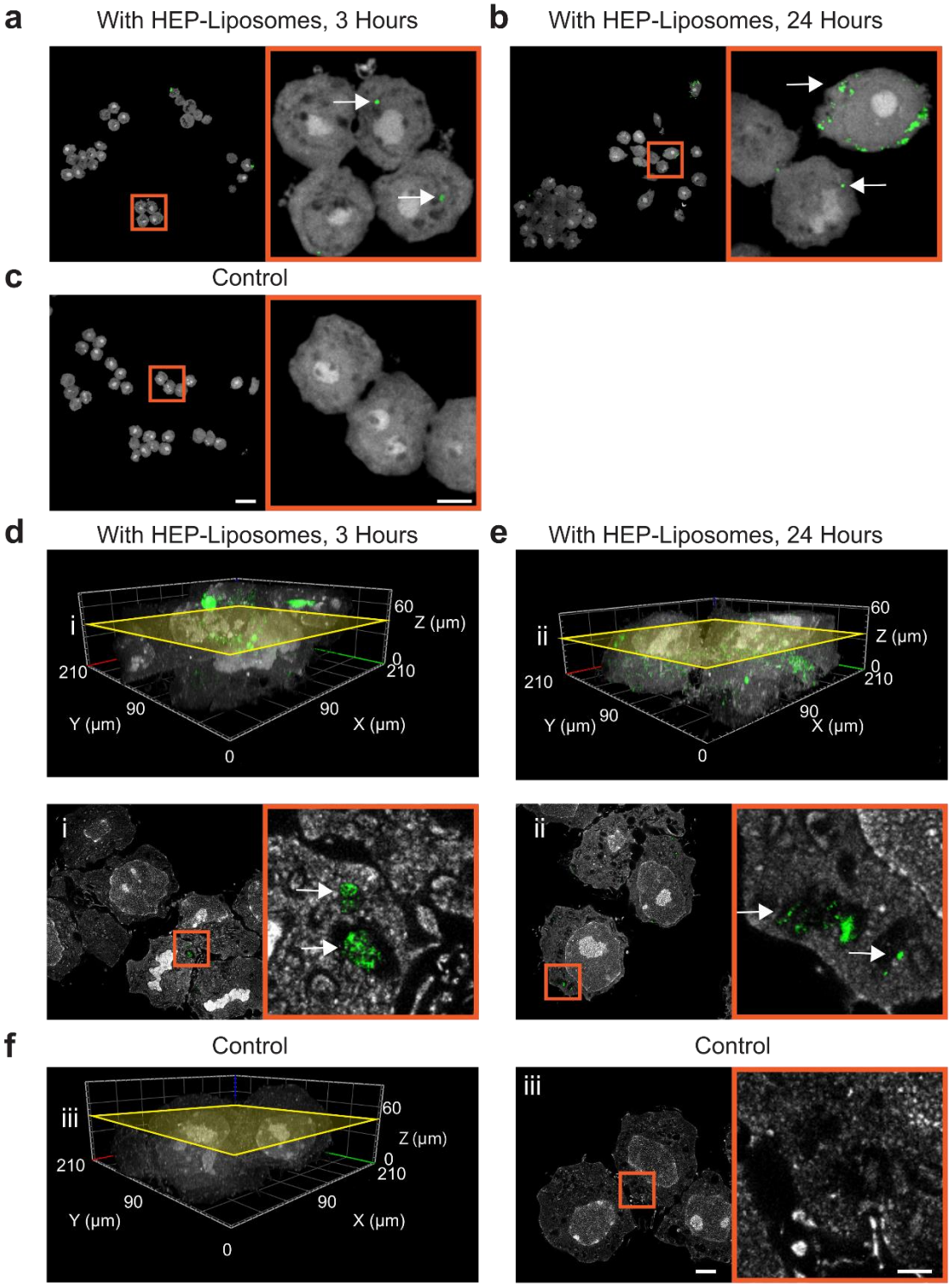


**Figure 4.4: Magnify enables the three-dimensional super-resolution visual comparison of fluorescent liposomal cargo intracellular distribution.** RAW 264.7

macrophages were incubated with HEP-Liposomes for 3 or 24 hours before being washed, fixed, and expanded with the Magnify protocol, along with non-treated controls. Non-expanded cells are shown first **(a-c)**, followed by expanded cells **(d-f)**. Cells were stained with NHS-AF647 (gray) and DAPI (blue). For non-expanded cells, first the overlay of the NHS-AF647, DAPI, and 10 kDa dextran-AF488 (green) is shown, followed by a digital magnification of a region of interest. For expanded cells, 3D reconstruction of CLSM Z-stacks are shown, with images i-iii depicting individual X, Y slices. White arrows indicate the position of 10 kDa dextran-AF488 signal. The scale bars indicate 20 µm in the unmagnified images and 5 µm in the magnified images, not corrected for expansion factors.

### 4.2.3 Pre-labelling liposomes with lipophillic dyes is incompatible with Magnify

We have thus far established that the fluorescent cargo of liposomes can be visualized within intracellular vesicles through Magnify. However, this method does not provide information on if the visualized cargo is still encapsulated or has been released from the liposomes, which is significant information for the in-depth analysis of cell-liposomal drug interactions. Therefore, a method of labelling the liposomes directly would further the applicability of our method to more types of liposomal drug delivery studies, such as those involving intracellular stability and controlled drug release.[342] Among the most common methods for visualizing liposomes directly with light microscopy is through the use of lipophillic carbocyanine dyes such as 3,3-dioctadecyloxacarbocyanine perchlorate (DiO), which intercalates within the lipid bilayer of liposomes.[329,343] Here, we synthesized DiO liposomes consisting of DSPC, cholesterol, and mPEG(2 kDa)-DSPE by running those components in a 1.8: 0.6: 0.6 mass ratio dissolved in a solution of 0.044 mg/mL DiO in ethanol and 1X PBS through our microfluidics setup in a FRR of 7 (hereafter referred to as DiO-Liposomes, Table S3). We then incubated RAW 264.7 macrophages with DiO-Liposomes for 24 hours and then processed them for Magnify expansion (Figure 4.5 (a,b)). While a DiO signal is seen in non-expanded cells, there was no visible DiO signal in the cells following expansion, suggesting that DiO is not compatible with Magnify.

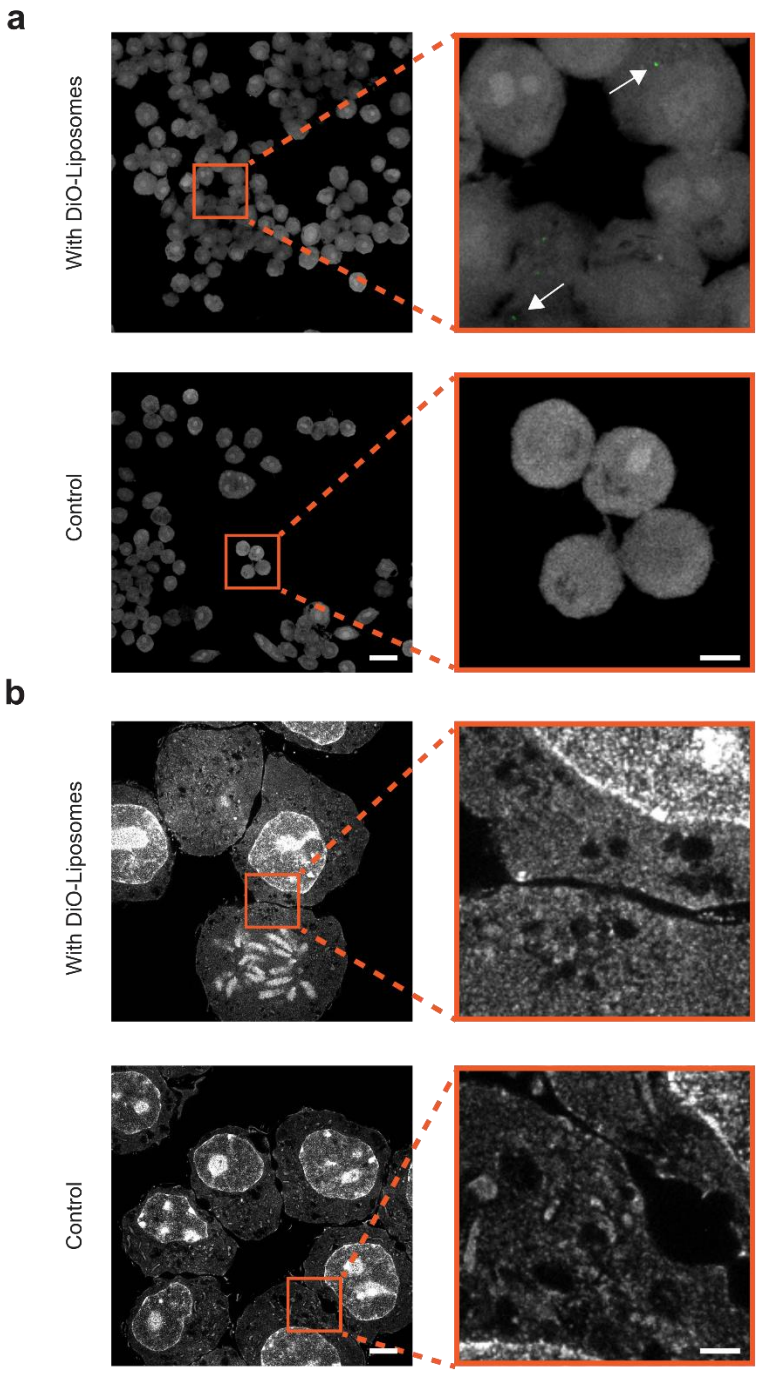


**Figure 4.5: DiO signal from liposomes is not retained through the Magnify process.** RAW 264.7 macrophages were incubated with DiO-Liposomes for 24 hours before being washed, fixed, and expanded with the Magnify protocol, along with non-treated controls. Non-expanded cells are shown first **(a)**, followed by expanded cells **(b)**. Cells were

stained with NHS-AF405 (gray). First the overlay of the NHS-AF405 and DiO (green) is shown, followed by a digital magnification of a region of interest. White arrows indicate the position of DiO signal within intracellular vesicles. No significant DiO signal was found in expanded DiO-Liposome treated cells. The scale bars indicate 20 µm in the unmagnified images and 5 µm in the magnified images, not corrected for expansion factors.

To further validate that the DiO is not compatible with Magnify, and to determine if the DiO is disassociating with the liposomes during the gel expansion steps or if the DiO signal is lost during one of the previous steps, we stained cells with DiO directly at different steps of the Magnify process. We first stained live RAW 264.7 macrophages with DiO, and then fixed them, where we were able to observe a clear DiO signal surrounding the nuclei of the cells (Figure S4.4a). We then expanded RAW 264.7 macrophages that were stained with DiO before fixation and found that the DiO signal had been essentially lost (Figure S4.4b). However, we observed that RAW 264.7 macrophages that were stained with DiO following the homogenization step of the Magnify process retained the DiO signal after the expansion was completed (Figure S4.4c). While it has been suggested that lipophillic dyes can dissociate in water,[325] our results demonstrate that we can at minimum transiently image DiO in expanded cells. We can then deduce that the DiO signal is lost during either the gelation or homogenization steps of the Magnify process. It is highly likely that the homogenization step is the cause of the DiO signal loss, as the homogenization buffer used in this step contains sodium dodecyl sulfate (SDS), which has been demonstrated by Chan et al. to greatly reduce the signal of DiO under similar conditions in the CLARITY tissue clearing protocol.[263] Given that the DiO signal cannot be retained on liposomes through the Magnify process when administered to cells while they are alive, and that DiO alone cannot feasibly be used to stain intracellular liposomes without staining other features of the cell following the homogenization step, we can conclude that DiO is not suitable for labelling liposomes for Magnify experiments. Further work is therefore necessary for determining a method of staining liposomes directly in a manner that is compatible with the Magnify protocol. Potential solutions include using a

fluorophore attached to a crosslinkable peptide that can attach to liposomes for labelling before fixation, such as the REMNANT tag described by Chen et al.,[263] or by using click chemistry tags to label the intracellular liposomes after the homogenization step.[344]

### 4.3 Conclusion

Here, we demonstrated that the Magnify expansion microscopy protocol can allow for the visualization of the intracellular distribution of fluorescent, large molecule drugs encapsulated within liposomes with 3D super-resolution. This method allows for more informed research into the delivery of liposomal anti-cancer therapeutics towards improved clinical outcomes. While small molecule drugs, which are typically used in cancer nanomedicines, were not initially retained through the expansion process, it is possible that increasing the crosslinker density of the expansion gel may allow for an improved retention and enable post-expansion visualization, albeit at the cost of a lowered maximum expansion factor. We further discussed potential methods that could enable the direct visualization of liposomes after expansion alongside their cargo. We anticipate that this method will empower research into bettering the understanding of organic nanoparticle-cellular interactions for better clinical translation of nanomedicine formulations

## Chapter 5: Conclusions and Future Directions

A deeper understanding of how nanoparticles transport across tumor blood vessels is necessary for the design of more efficacious anti-cancer nanomedicines. Given that current methods of analyzing nanoparticle-cellular interactions, such as transmission electron microscopy (TEM) and inductively coupled plasma mass spectrometry (ICP-MS) have limitations in terms of how much information can be attained about the intracellular distribution of nanoparticles at the single cell level, new methods of analysis were needed. Here, we established methods for visualizing and quantifying metallic and organic nanoparticle intracellular distribution with ultrastructural context through 3D super-resolution microscopy. We adopted three expansion microscopy methods- proExM, pan-ExM, and Magnify to demonstrate compatibility with nanoparticle studies, and discussed which applications they would best be suited for. ProExM is a relatively quick process, though it does not allow for sufficient lateral resolution for visualizing nanoparticle distribution within individual intracellular vesicles. Pan-ExM does allow for sufficient lateral resolution for these visualizations, albeit with significantly longer processing times. Both of these methods are compatible with light scattering imaging for visualizing metallic nanoparticle distribution, and we demonstrated that with pan-ExM, we can quantify relative nanoparticle accumulation within intracellular vesicles to acquire information that was not previously accessible through TEM or ICP-MS. We then applied the Magnify protocol for visualizing intracellular liposome distribution, as this process allows for better lipid retention than proExM and pan-ExM, and demonstrated that we can visualize fluorescent large-molecule drug cargo of liposomes with 3D super-resolution.

We anticipate that these methods can be applied to a variety of studies involving understanding nanoparticle intracellular fate. As mentioned in Chapter 1, only about 0.7% (median) of the injected dose of systemically administered nanoparticles reach solid tumors, with even lower percentages of nanoparticles being internalized within cancer cells.[14] This low delivery efficiency greatly limits the efficacy of nanomedicine for treating solid tumors. Recent evidence has demonstrated that nanoparticles primarily reach solid tumors through active transport processes across endothelial cells that comprise tumor blood vessels.[30] Among these active transport processes is transcytosis, which involves the endocytosis of nanoparticles in the tumor vascular lumen into intracellular vesicles which are trafficked through the endothelial cells before being exocytosed into the tumor microenvironment.[293] However, the mechanisms of nanoparticle transcytosis are currently not well understood. By studying the mechanisms that enable nanoparticles to reach tumors, new nanomedicine formulations can be designed to have significantly higher accumulation in the tumor microenvironment than the current median amount by targeting transcytotic pathways, allowing for better therapeutic efficacy. An understanding of how specific endocytosis pathways, such as clathrin mediated endocytosis and caveolae mediated endocytosis, contribute to the transcytosis of nanoparticles across tumor endothelial cells is necessary for designing nanomedicine formulations that promote transcytosis. Given that the intracellular vesicles formed by these endocytic pathways are typically smaller than the resolution limit of light microscopy, and that electron microscopy is typically limited to 2D visualizations, there was a need for a new method for studying these nanoparticle-cellular interactions. Our 3D super-resolution methods for visualizing and quantifying nanoparticle intracellular distribution allows for an

in-depth analysis of nanoparticle accumulation within individual intracellular vesicles, which can allow for a full characterization of the contributions of specific endocytic pathways to nanoparticle uptake for the understanding of transcytosis mechanisms. One particular weakness of this approach is that it is not compatible with live cell or live animal imaging, so many samples at different timepoints and tissue locations would be needed to fully understand transcytosis pathways, as they are active transport processes. Furthermore, these methods do not allow for absolute quantifications of nanoparticle numbers within cells. However, relative comparisons of nanoparticle uptake within individual intracellular vesicles are very valuable information for studying nanoparticle transcytosis mechanisms.

The initial next step of this research is the establishment of a label for directly visualizing liposomes in a manner that is compatible with Magnify. Further future work involves the use of antibodies against proteins that are involved with specific endocytic uptake pathways, such as caveolin-1 and clathrin heavy chain, in conjunction with metallic nanoparticles and pan-ExM, along with transwell assays,[345] to determine which endocytic pathways result in the highest amount of transcytosis. Studies can then be done on new surface modifications for metallic nanoparticles to target preferrable pathways for increasing transcytosis. The most optimal surface modifications can then be translated to organic nanoparticle studies, which can be validated with Magnify. Expansion microscopy methods have also been developed for thick tissue sections (50-100 μm) from animal models, so these same studies can then be applied *ex vivo* with mouse tissue sections to visualize and quantify nanoparticle transport across tumor blood vessels.[325,346] The successful application of these methods will empower new research into the transcytosis

of nanoparticles across tumor blood vessels, towards the goal of developing more clinically efficacious anti-cancer nanomedicine.

## References


(1) Sung, H.; Ferlay, J.; Siegel, R. L.; Laversanne, M.; Soerjomataram, I.; Jemal, A.; Bray, F. Global Cancer Statistics 2020: GLOBOCAN Estimates of Incidence and Mortality Worldwide for 36 Cancers in 185 Countries. *CA. Cancer J. Clin.* **2021**, *71* (3), 209–249. https://doi.org/10.3322/caac.21660.

(2) Chen, H. H. W.; Kuo, M. T. Improving Radiotherapy in Cancer Treatment: Promises and Challenges. *Oncotarget* **2017**, *8* (37), 62742–62758. https://doi.org/10.18632/oncotarget.18409.

(3) Shou, K.; Tang, Y.; Chen, H.; Chen, S.; Zhang, L.; Zhang, A.; Fan, Q.; Yu, A.; Cheng, Z. Diketopyrrolopyrrole-Based Semiconducting Polymer Nanoparticles for in Vivo Second near-Infrared Window Imaging and Image-Guided Tumor Surgery. *Chem. Sci.* **2018**, *9* (12), 3105–3110. https://doi.org/10.1039/c8sc00206a.

(4) Chen, F.; Madajewski, B.; Ma, K.; Karassawa Zanoni, D.; Stambuk, H.; Turker, M. Z.; Monette, S.; Zhang, L.; Yoo, B.; Chen, P.; Meester, R. J. C.; Jonge, S. de; Montero, P.; Phillips, E.; Quinn, T. P.; Gönen, M.; Sequeira, S.; de Stanchina, E.; Zanzonico, P.; Wiesner, U.; Patel, S. G.; Bradbury, M. S. Molecular Phenotyping and Image-Guided Surgical Treatment of Melanoma Using Spectrally Distinct Ultrasmall Core-Shell Silica Nanoparticles. *Sci. Adv.* **2019**, *5* (12), eaax5208. https://doi.org/10.1126/sciadv.aax5208.

(5) Alqathami, M.; Blencowe, A.; Yeo, U. J.; Doran, S. J.; Qiao, G.; Geso, M. Novel Multicompartment 3-Dimensional Radiochromic Radiation Dosimeters for Nanoparticle-Enhanced Radiation Therapy Dosimetry. *Int. J. Radiat. Oncol.* **2012**, *84* (4), e549–e555. https://doi.org/10.1016/j.ijrobp.2012.05.029.

(6) Kwatra, D.; Venugopal, A.; Anant, S. Nanoparticles in Radiation Therapy: A Summary of Various Approaches to Enhance Radiosensitization in Cancer. *Transl. Cancer Res.* **2013**, *2* (4), 330–342. https://doi.org/10.3978/j.issn.2218-676X.2013.08.06.

(7) Choi, M.-R.; Stanton-Maxey, K. J.; Stanley, J. K.; Levin, C. S.; Bardhan, R.; Akin, D.; Badve, S.; Sturgis, J.; Robinson, J. P.; Bashir, R.; Halas, N. J.; Clare, S. E. A Cellular Trojan Horse for Delivery of Therapeutic Nanoparticles into Tumors. *Nano Lett.* **2007**, *7* (12), 3759–3765. https://doi.org/10.1021/nl072209h.

(8) Anselmo, A. C.; Mitragotri, S. Nanoparticles in the Clinic: An Update. *Bioeng. Transl. Med.* **2019**, *4* (3), 1–16. https://doi.org/10.1002/btm2.10143.

(9) Velpurisiva, P.; Gad, A.; Piel, B.; Jadia, R.; Rai, P. Nanoparticle Design Strategies for Effective Cancer Immunotherapy. *J. Biomed.* **2017**, *2*, 64–77. https://doi.org/10.7150/jbm.18877.

(10) Al-Ghananeem, A. M.; Malkawi, A. H.; Muammer, Y. M.; Balko, J. M.; Black, E. P.; Mourad, W.; Romond, E. Intratumoral Delivery of Paclitaxel in Solid Tumor from Biodegradable Hyaluronan Nanoparticle Formulations. *AAPS PharmSciTech* **2009**, *10* (2), 410–417. https://doi.org/10.1208/s12249-009-9222-5.

(11) Huai, Y.; Hossen, M. N.; Wilhelm, S.; Bhattacharya, R.; Mukherjee, P.

Nanoparticle Interactions with the Tumor Microenvironment. *Bioconjug. Chem.* **2019**, *30* (9), 2247–2263. https://doi.org/10.1021/acs.bioconjchem.9b00448.

(12) Kingston, B. R.; Syed, A. M.; Ngai, J.; Sindhwani, S.; Chan, W. C. W. Assessing Micrometastases as a Target for Nanoparticles Using 3D Microscopy and Machine Learning. *Proc. Natl. Acad. Sci. U. S. A.* **2019**, *116* (30), 14937–14946. https://doi.org/10.1073/pnas.1907646116.

(13) Zhou, Z.; Liu, X.; Zhu, D.; Wang, Y.; Zhang, Z.; Zhou, X.; Qiu, N.; Chen, X.; Shen, Y. Nonviral Cancer Gene Therapy: Delivery Cascade and Vector Nanoproperty Integration. *Adv. Drug Deliv. Rev.* **2017**, *115*, 115–154. https://doi.org/10.1016/j.addr.2017.07.021.

(14) Wilhelm, S.; Tavares, A. J.; Dai, Q.; Ohta, S.; Audet, J.; Dvorak, H. F.; Chan, W. C. W. Analysis of Nanoparticle Delivery to Tumours. *Nat. Rev. Mater.* **2016**, *1* (May 2018). https://doi.org/10.1038/natrevmats.2016.14.

(15) Walkey, C. D.; Chan, W. C. W. Understanding and Controlling the Interaction of Nanomaterials with Proteins in a Physiological Environment. *Chem. Soc. Rev.* **2012**, *41* (7), 2780–2799. https://doi.org/10.1039/c1cs15233e.

(16) Walkey, C. D.; Olsen, J. B.; Song, F.; Liu, R.; Guo, H.; Olsen, D. W. H.; Cohen, Y.; Emili, A.; Chan, W. C. W. Protein Corona Fingerprinting Predicts the Cellular Interaction of Gold and Silver Nanoparticles. *ACS Nano* **2014**, *8* (3), 2439–2455. https://doi.org/10.1021/nn406018q.

(17) Walkey, C. D.; Olsen, J. B.; Guo, H.; Emili, A.; Chan, W. C. W. Nanoparticle Size and Surface Chemistry Determine Serum Protein Adsorption and Macrophage Uptake. *J. Am. Chem. Soc.* **2012**, *134* (4), 2139–2147. https://doi.org/10.1021/ja2084338.

(18) Yang, W.; Wang, L.; Mettenbrink, E. M.; DeAngelis, P. L.; Wilhelm, S. Nanoparticle Toxicology. *Annu. Rev. Pharmacol. Toxicol.* **2021**, *61* (1), annurev-pharmtox-032320-110338. https://doi.org/10.1146/annurev-pharmtox-032320-110338.

(19) Nguyen, V. H.; Lee, B.-J. Protein Corona: A New Approach for Nanomedicine Design. *Int. J. Nanomedicine* **2017**, *Volume 12*, 3137–3151. https://doi.org/10.2147/IJN.S129300.

(20) Lazarovits, J.; Chen, Y. Y.; Sykes, E. A.; Chan, W. C. W. Nanoparticle–Blood Interactions: The Implications on Solid Tumour Targeting. *Chem. Commun.* **2015**, *51* (14), 2756–2767. https://doi.org/10.1039/C4CC07644C.

(21) Blanco, E.; Shen, H.; Ferrari, M. Principles of Nanoparticle Design for Overcoming Biological Barriers to Drug Delivery. *Nat. Biotechnol.* **2015**, *33* (9), 941–951. https://doi.org/10.1038/nbt.3330.

(22) Suk, J. S.; Xu, Q.; Kim, N.; Hanes, J.; Ensign, L. M. PEGylation as a Strategy for Improving Nanoparticle-Based Drug and Gene Delivery. *Adv. Drug Deliv. Rev.* **2016**, *99*, 28–51. https://doi.org/10.1016/j.addr.2015.09.012.

(23) Hu, C. M. J.; Zhang, L.; Aryal, S.; Cheung, C.; Fang, R. H.; Zhang, L. Erythrocyte Membrane-Camouflaged Polymeric Nanoparticles as a Biomimetic Delivery Platform. *Proc. Natl. Acad. Sci. U. S. A.* **2011**, *108* (27), 10980–10985. https://doi.org/10.1073/pnas.1106634108.

(24) Ouyang, B.; Poon, W.; Zhang, Y.-N.; Lin, Z. P.; Kingston, B. R.; Tavares, A. J.; Zhang, Y.; Chen, J.; Valic, M. S.; Syed, A. M.; MacMillan, P.; Couture-Senécal, J.; Zheng, G.; Chan, W. C. W. The Dose Threshold for Nanoparticle Tumour Delivery. *Nat. Mater.* **2020**. https://doi.org/10.1038/s41563-020-0755-z.

(25) Narum, S. M.; Le, T.; Le, D. P.; Lee, J. C.; Donahue, N. D.; Yang, W.; Wilhelm, S. Passive Targeting in Nanomedicine: Fundamental Concepts, Body Interactions, and Clinical Potential. In *Nanoparticles for Biomedical Applications*; Elsevier, 2020; pp 37–53. https://doi.org/10.1016/B978-0-12-816662-8.00004-7.

(26) Maeda, H.; Wu, J.; Sawa, T.; Matsumura, Y.; Hori, K. Tumor Vascular Permeability and the EPR Effect in Macromolecular Therapeutics: A Review. *J. Control. Release* **2000**, *65* (1–2), 271–284. https://doi.org/10.1016/S0168-3659(99)00248-5.

(27) Torosean, S.; Flynn, B.; Axelsson, J.; Gunn, J.; Samkoe, K. S.; Hasan, T.; Doyley, M. M.; Pogue, B. W. Nanoparticle Uptake in Tumors Is Mediated by the Interplay of Vascular and Collagen Density with Interstitial Pressure. *Nanomedicine Nanotechnology, Biol. Med.* **2013**, *9* (2), 151–158. https://doi.org/10.1016/j.nano.2012.07.002.

(28) Engin, A. B.; Nikitovic, D.; Neagu, M.; Henrich-Noack, P.; Docea, A. O.; Shtilman, M. I.; Golokhvast, K.; Tsatsakis, A. M. Mechanistic Understanding of Nanoparticles' Interactions with Extracellular Matrix: The Cell and Immune System. *Part. Fibre Toxicol.* **2017**, *14* (1), 1–16. https://doi.org/10.1186/s12989-017-0199-z.

(29) Huang, S. K.; Martin, F. J.; Jay, G.; Vogel, J.; Papahadjopoulos, D.; Friend, D. S. Extravasation and Transcytosis of Liposomes in Kaposi's Sarcoma-like Dermal Lesions of Transgenic Mice Bearing the HIV Tat Gene. *Am. J. Pathol.* **1993**, *143* (1), 10–14.

(30) Sindhwani, S.; Syed, A. M.; Ngai, J.; Kingston, B. R.; Maiorino, L.; Rothschild, J.; MacMillan, P.; Zhang, Y.; Rajesh, N. U.; Hoang, T.; Wu, J. L. Y.; Wilhelm, S.; Zilman, A.; Gadde, S.; Sulaiman, A.; Ouyang, B.; Lin, Z.; Wang, L.; Egeblad, M.; Chan, W. C. W. The Entry of Nanoparticles into Solid Tumours. *Nat. Mater.* **2020**, *19* (5), 566–575. https://doi.org/10.1038/s41563-019-0566-2.

(31) Dvorak, H. F. Tumor Stroma, Tumor Blood Vessels, and Antiangiogenesis Therapy. *Cancer J. (United States)* **2015**, *21* (4), 237–243. https://doi.org/10.1097/PPO.0000000000000124.

(32) De Palma, M.; Biziato, D.; Petrova, T. V. Microenvironmental Regulation of Tumour Angiogenesis. *Nat. Rev. Cancer* **2017**, *17* (8), 457–474. https://doi.org/10.1038/nrc.2017.51.

(33) Wei, R.; Liu, S.; Zhang, S.; Min, L.; Zhu, S. Cellular and Extracellular Components in Tumor Microenvironment and Their Application in Early Diagnosis of Cancers. *Anal. Cell. Pathol.* **2020**, *2020* (Figure 1). https://doi.org/10.1155/2020/6283796.

(34) Zhang, Y.; Elechalawar, C. K.; Hossen, M. N.; Francek, E. R.; Dey, A.; Wilhelm, S.; Bhattacharya, R.; Mukherjee, P. Gold Nanoparticles Inhibit Activation of Cancer-Associated Fibroblasts by Disrupting Communication from Tumor and Microenvironmental Cells. *Bioact. Mater.* **2021**, *6* (2), 326–332. https://doi.org/10.1016/j.bioactmat.2020.08.009.

(35) Dagogo-Jack, I.; Shaw, A. T. Tumour Heterogeneity and Resistance to Cancer Therapies. *Nat. Rev. Clin. Oncol.* **2018**, *15* (2), 81–94. https://doi.org/10.1038/nrclinonc.2017.166.

(36) Dai, Q.; Wilhelm, S.; Ding, D.; Syed, A. M.; Sindhwani, S.; Zhang, Y.; Chen, Y. Y.; Macmillan, P.; Chan, W. C. W. Quantifying the Ligand-Coated Nanoparticle Delivery to Cancer Cells in Solid Tumors. *ACS Nano* **2018**, *12* (8), 8423–8435. https://doi.org/10.1021/acsnano.8b03900.

(37) Sykes, E. A.; Dai, Q.; Sarsons, C. D.; Chen, J.; Rocheleau, J. V.; Hwang, D. M.; Zheng, G.; Cramb, D. T.; Rinker, K. D.; Chan, W. C. W. Tailoring Nanoparticle Designs to Target Cancer Based on Tumor Pathophysiology. *Proc. Natl. Acad. Sci.* **2016**, *113* (9), E1142–E1151. https://doi.org/10.1073/pnas.1521265113.

(38) Boumahdi, S.; de Sauvage, F. J. The Great Escape: Tumour Cell Plasticity in Resistance to Targeted Therapy. *Nat. Rev. Drug Discov.* **2020**, *19* (1), 39–56. https://doi.org/10.1038/s41573-019-0044-1.

(39) Vessoni, A. T.; Filippi-Chiela, E. C.; Lenz, G.; Batista, L. F. Z. Tumor Propagating Cells: Drivers of Tumor Plasticity, Heterogeneity, and Recurrence. *Oncogene* **2020**, *39* (10), 2055–2068. https://doi.org/10.1038/s41388-019-1128-4.

(40) Moore, M. A. S. Putting the Neo into Neoangiogenesis. *J. Clin. Invest.* **2002**, *109* (3), 313–315. https://doi.org/10.1172/JCI0214940.

(41) Zhao, X.; Liu, H. Q.; Li, J.; Liu, X. L. Endothelial Progenitor Cells Promote Tumor Growth and Progression by Enhancing New Vessel Formation (Review). *Oncol. Lett.* **2016**, *12* (2), 793–799. https://doi.org/10.3892/ol.2016.4733.

(42) Metheny-Barlow, L. J.; Li, L. Y. The Enigmatic Role of Angiopoietin-1 in Tumor Angiogenesis. *Cell Res.* **2003**, *13* (5), 309–317. https://doi.org/10.1038/sj.cr.7290176.

(43) Nagy, J. A.; Chang, S. H.; Dvorak, A. M.; Dvorak, H. F. Why Are Tumour Blood Vessels Abnormal and Why Is It Important to Know? *Br. J. Cancer* **2009**, *100* (6), 865–869. https://doi.org/10.1038/sj.bjc.6604929.

(44) Bergers, G.; Song, S. The Role of Pericytes in Blood-Vessel Formation and Maintenance. *Neuro. Oncol.* **2005**, *7* (4), 452–464. https://doi.org/10.1215/s1152851705000232.

(45) Kang, E.; Shin, J. W. Pericyte-Targeting Drug Delivery and Tissue Engineering.

*Int. J. Nanomedicine* **2016**, *11*, 2397–2406. https://doi.org/10.2147/IJN.S105274.

(46) Nguyen, L. N. M.; Lin, Z. P.; Sindhwani, S.; MacMillan, P.; Mladjenovic, S. M.; Stordy, B.; Ngo, W.; Chan, W. C. W. The Exit of Nanoparticles from Solid Tumours. *Nat. Mater.* **2023**, *22* (10), 1261–1272. https://doi.org/10.1038/s41563-023-01630-0.

(47) Bertrand, N.; Wu, J.; Xu, X.; Kamaly, N.; Farokhzad, O. C. Cancer Nanotechnology: The Impact of Passive and Active Targeting in the Era of Modern Cancer Biology. *Adv. Drug Deliv. Rev.* **2014**, *66*, 2–25. https://doi.org/10.1016/j.addr.2013.11.009.

(48) Jain, R. K.; Stylianopoulos, T. Delivering Nanomedicine to Solid Tumors. *Nat. Rev. Clin. Oncol.* **2010**, *7* (11), 653–664. https://doi.org/10.1038/nrclinonc.2010.139.

(49) Golombek, S. K.; May, J. N.; Theek, B.; Appold, L.; Drude, N.; Kiessling, F.; Lammers, T. Tumor Targeting via EPR: Strategies to Enhance Patient Responses. *Adv. Drug Deliv. Rev.* **2018**, *130*, 17–38. https://doi.org/10.1016/j.addr.2018.07.007.

(50) Shi, J.; Kantoff, P. W.; Wooster, R.; Farokhzad, O. C. Cancer Nanomedicine: Progress, Challenges and Opportunities. *Nat. Rev. Cancer* **2017**, *17* (1), 20–37. https://doi.org/10.1038/nrc.2016.108.

(51) Kong, N.; Tao, W.; Ling, X.; Wang, J.; Xiao, Y.; Shi, S.; Ji, X.; Shajii, A.; Gan, S. T.; Kim, N. Y.; Duda, D. G.; Xie, T.; Farokhzad, O. C.; Shi, J. Synthetic MRNA Nanoparticle-Mediated Restoration of P53 Tumor Suppressor Sensitizes P53-Deficient Cancers to MTOR Inhibition. *Sci. Transl. Med.* **2019**, *11* (523), eaaw1565. https://doi.org/10.1126/scitranslmed.aaw1565.

(52) Islam, M. A.; Xu, Y.; Tao, W.; Ubellacker, J. M.; Lim, M.; Aum, D.; Lee, G. Y.; Zhou, K.; Zope, H.; Yu, M.; Cao, W.; Oswald, J. T.; Dinarvand, M.; Mahmoudi, M.; Langer, R.; Kantoff, P. W.; Farokhzad, O. C.; Zetter, B. R.; Shi, J. Restoration of Tumour-Growth Suppression in Vivo via Systemic Nanoparticle-Mediated Delivery of PTEN MRNA. *Nat. Biomed. Eng.* **2018**, *2* (11), 850–864. https://doi.org/10.1038/s41551-018-0284-0.

(53) Zhang, C.; Zhang, X.; Zhao, W.; Zeng, C.; Li, W.; Li, B.; Luo, X.; Li, J.; Jiang, J.; Deng, B.; McComb, D. W.; Dong, Y. Chemotherapy Drugs Derived Nanoparticles Encapsulating MRNA Encoding Tumor Suppressor Proteins to Treat Triple-Negative Breast Cancer. *Nano Res.* **2019**, *12* (4), 855–861. https://doi.org/10.1007/s12274-019-2308-9.

(54) Wilhelm, S. Perspectives for Upconverting Nanoparticles. *ACS Nano*. November 28, 2017, pp 10644–10653. https://doi.org/10.1021/acsnano.7b07120.

(55) Wang, Z.; Tiruppathi, C.; Cho, J.; Minshall, R. D.; Malik, A. B. Delivery of Nanoparticle-Complexed Drugs across the Vascular Endothelial Barrier via Caveolae. *IUBMB Life* **2011**, *63* (8), 659–667. https://doi.org/10.1002/iub.485.

(56) Kingston, B. R.; Lin, Z. P.; Ouyang, B.; MacMillan, P.; Ngai, J.; Syed, A. M.; Sindhwani, S.; Chan, W. C. W. Specific Endothelial Cells Govern Nanoparticle Entry into Solid Tumors. *ACS Nano* **2021**, *1*, acsnano.1c04510. https://doi.org/10.1021/acsnano.1c04510.

(57) Dvorak, A. M.; Kohn, S.; Morgan, E. S.; Fox, P.; Nagy, J. A.; Dvorak, H. F. The Vesiculo-Vacuolar Organelle (VVO): A Distinct Endothelial Cell Structure That Provides a Transcellular Pathway for Macromolecular Extravasation. *J. Leukoc. Biol.* **1996**, *59* (1), 100–115. https://doi.org/10.1002/jlb.59.1.100.

(58) Vasile, E.; Qu-Hong; Dvorak, H. F.; Dvorak, A. M. Caveolae and Vesiculo-Vacuolar Organelles in Bovine Capillary Endothelial Cells Cultured with VPF/VEGF on Floating Matrigel-Collagen Gels. *J. Histochem. Cytochem.* **1999**, *47* (2), 159–167. https://doi.org/10.1177/002215549904700205.

(59) Cogger, V. C.; McNerney, G. P.; Nyunt, T.; DeLeve, L. D.; McCourt, P.; Smedsrød, B.; Le Couteur, D. G.; Huser, T. R. Three-Dimensional Structured Illumination Microscopy of Liver Sinusoidal Endothelial Cell Fenestrations. *J. Struct. Biol.* **2010**, *171* (3), 382–388. https://doi.org/10.1016/j.jsb.2010.06.001.

(60) Ballermann, B. J. Glomerular Endothelial Cell Differentiation. *Kidney Int.* **2005**, *67* (5), 1668–1671. https://doi.org/10.1111/j.1523-1755.2005.00260.x.

(61) Feng, D.; Nagy, J. A.; Dvorak, A. M.; Dvorak, H. F. Different Pathways of Macromolecule Extravasation from Hyperpermeable Tumor Vessels. *Microvasc. Res.* **2000**, *59* (1), 24–37. https://doi.org/10.1006/mvre.1999.2207.

(62) Pradhan, S.; Smith, A. M.; Garson, C. J.; Hassani, I.; Seeto, W. J.; Pant, K.; Arnold, R. D.; Prabhakarpandian, B.; Lipke, E. A. A Microvascularized Tumor-Mimetic Platform for Assessing Anti-Cancer Drug Efficacy. *Sci. Rep.* **2018**, *8* (1), 1–15. https://doi.org/10.1038/s41598-018-21075-9.

(63) Chen, Y. Y.; Kingston, B. R.; Chan, W. C. W. Transcribing In Vivo Blood Vessel Networks into In Vitro Perfusable Microfluidic Devices. *Adv. Mater. Technol.* **2020**, 2000103. https://doi.org/10.1002/admt.202000103.

(64) Claude, A.; Porter, K. R.; Pickels, E. G. Electron Microscope Study of Chicken Tumor Cells. *Cancer Res.* **1947**, *7* (7), 421–430.

(65) Bangham, A. D.; Horne, R. W. Negative Staining of Phospholipids and Their Structural Modification by Surface-Active Agents as Observed in the Electron Microscope. *J. Mol. Biol.* **1964**, *8* (5), 660-IN10. https://doi.org/10.1016/S0022-2836(64)80115-7.

(66) Leserman, L. D.; Weinstein, J. N.; Blumenthal, R.; Sharrow, S. O.; Terry, W. D. Binding of Antigen-Bearing Fluorescent Liposomes to the Murine Myeloma Tumor MOPC 315. *J. Immunol.* **1979**, *122* (2), 585–591.

(67) Huang, A.; Kennel, S. J.; Huang, L. Immunoliposome Labeling: A Sensitive and Specific Method for Cell Surface Labeling. *J. Immunol. Methods* **1981**, *46* (2), 141–151. https://doi.org/10.1016/0022-1759(81)90131-9.

(68) Weinstein, J. N.; Magin, R. L.; Yatvin, M. B.; Zaharko, D. S. Liposomes and Local Hyperthermia: Selective Delivery. *Science (80-. ).* **1979**, *204* (4389), 188–191.

(69) Kong, G.; Dewhirst, M. W. Hyperthermia and Liposomes. *Int. J. Hyperth.* **1999**, *15* (5), 345–370. https://doi.org/10.1080/026567399285558.

(70) Leserman, L. D.; Weinstein, J. N.; Blumenthal, R.; Terry, W. D. Receptor-Mediated Endocytosis of Antibody-Opsonized Liposomes by Tumor Cells. *Proc. Natl. Acad. Sci. U. S. A.* **1980**, *77* (7 II), 4089–4093. https://doi.org/10.1073/pnas.77.7.4089.

(71) Matsumura, Y.; Maeda, H. A New Concept for Macromolecular Therapeutics in Cancer Chemotherapy: Mechanism of Tumoritropic Accumulation of Proteins and the Antitumor Agent Smancs. *Cancer Res.* **1986**, *46* (8), 6387–6392.

(72) Sprandel, U.; Lanz, D.-J.; von Hörsten, W. Magnetically Responsive Erythrocyte Ghosts. In *Methods in Enzymology*; 1987; Vol. 149, pp 301–312. https://doi.org/10.1016/0076-6879(87)49068-X.

(73) Brenner, J. S.; Pan, D. C.; Myerson, J. W.; Marcos-Contreras, O. A.; Villa, C. H.; Patel, P.; Hekierski, H.; Chatterjee, S.; Tao, J. Q.; Parhiz, H.; Bhamidipati, K.; Uhler, T. G.; Hood, E. D.; Kiseleva, R. Y.; Shuvaev, V. S.; Shuvaeva, T.; Khoshnejad, M.; Johnston, I.; Gregory, J. V.; Lahann, J.; Wang, T.; Cantu, E.; Armstead, W. M.; Mitragotri, S.; Muzykantov, V. Red Blood Cell-Hitchhiking Boosts Delivery of Nanocarriers to Chosen Organs by Orders of Magnitude. *Nat. Commun.* **2018**, *9* (1). https://doi.org/10.1038/s41467-018-05079-7.

(74) Yuan, F.; Chen, Y.; Dellian, M.; Safabakhsh, N.; Ferrara, N.; Jain, R. K. Time-Dependent Vascular Regression and Permeability Changes in Established Human Tumor Xenografts Induced by an Anti-Vascular Endothelial Growth Factor/Vascular Permeability Factor Antibody. *Proc. Natl. Acad. Sci. U. S. A.* **1996**, *93* (25), 14765–14770. https://doi.org/10.1073/pnas.93.25.14765.

(75) Jain, R. K. Normalizing Tumor Vasculature with Anti-Angiogenic Therapy: A New Paradigm for Combination Therapy. *Nat. Med.* **2001**, *7* (9), 987–989. https://doi.org/10.1038/nm0901-987.

(76) Huang, N.; Liu, Y.; Fang, Y.; Zheng, S.; Wu, J.; Wang, M.; Zhong, W.; Shi, M.; Xing, M.; Liao, W. Gold Nanoparticles Induce Tumor Vessel Normalization and Impair Metastasis by Inhibiting Endothelial Smad2/3 Signaling. *ACS Nano* **2020**, *14* (7), 7940–7958. https://doi.org/10.1021/acsnano.9b08460.

(77) Zhang, Y.; Xiong, X.; Huai, Y.; Dey, A.; Hossen, M. N.; Roy, R. V.; Elechalawar, C. K.; Rao, G.; Bhattacharya, R.; Mukherjee, P. Gold Nanoparticles Disrupt Tumor Microenvironment - Endothelial Cell Cross Talk to Inhibit Angiogenic Phenotypes in Vitro. *Bioconjug. Chem.* **2019**, *30* (6), 1724–1733. https://doi.org/10.1021/acs.bioconjchem.9b00262.

(78) Esenaliev, R. O. Interaction of Radiation with Microparticles for Enhancement of Drug Delivery in Tumors. *Laser-Tissue Interact. X Photochem. Photothermal, Photomech.* **1999**, *3601* (June 1999), 166. https://doi.org/10.1117/12.350000.

(79) Pitt, W. G.; Husseini, G. A.; Roeder, B. L.; Dickinson, D. J.; Warden, D. R.; Hartley, J. M.; Jones, P. W. Preliminary Results of Combining Low Frequency Low Intensity Ultrasound and Liposomal Drug Delivery to Treat Tumors in Rats. *J. Nanosci. Nanotechnol.* **2011**, *11* (3), 1866–1870. https://doi.org/10.1166/jnn.2011.3117.

(80) Pellow, C.; O'Reilly, M. A.; Hynynen, K.; Zheng, G.; Goertz, D. E. Simultaneous Intravital Optical and Acoustic Monitoring of Ultrasound-Triggered Nanobubble Generation and Extravasation. *Nano Lett.* **2020**, *20* (6), 4512–4519. https://doi.org/10.1021/acs.nanolett.0c01310.

(81) Cole, C.; Qiao, J.; Kottke, T.; Diaz, R. M.; Ahmed, A.; Sanchez-Perez, L.; Brunn, G.; Thompson, J.; Chester, J.; Vile, R. G. Tumor-Targeted, Systemic Delivery of Therapeutic Viral Vectors Using Hitchhiking on Antigen-Specific T Cells. *Nat. Med.* **2005**, *11* (10), 1073–1081. https://doi.org/10.1038/nm1297.

(82) Hong, S.; Zheng, D.; Zhang, C.; Huang, Q.; Cheng, S.; Zhang, X. Vascular Disrupting Agent Induced Aggregation of Gold Nanoparticles for Photothermally Enhanced Tumor Vascular Disruption. *Sci. Adv.* **2020**, *6* (23), eabb0020. https://doi.org/10.1126/sciadv.abb0020.

(83) Sun, T.; Dasgupta, A.; Zhao, Z.; Nurunnabi, M.; Mitragotri, S. Physical Triggering Strategies for Drug Delivery. *Adv. Drug Deliv. Rev.* **2020**. https://doi.org/10.1016/j.addr.2020.06.010.

(84) Sugahara, K. N.; Braun, G. B.; De Mendoza, T. H.; Kotamraju, V. R.; French, R. P.; Lowy, A. M.; Teesalu, T.; Ruoslahti, E. Tumor-Penetrating IRGD Peptide Inhibits Metastasis. *Mol. Cancer Ther.* **2015**, *14* (1), 120–128. https://doi.org/10.1158/1535-7163.MCT-14-0366.

(85) Liu, X.; Lin, P.; Perrett, I.; Lin, J.; Liao, Y.-P.; Chang, C. H.; Jiang, J.; Wu, N.; Donahue, T.; Wainberg, Z.; Nel, A. E.; Meng, H. Tumor-Penetrating Peptide Enhances Transcytosis of Silicasome-Based Chemotherapy for Pancreatic Cancer. *J. Clin. Invest.* **2017**, *127* (5), 2007–2018. https://doi.org/10.1172/JCI92284.

(86) Shah, S. A.; Khan, M. U. A.; Arshad, M.; Awan, S. U.; Hashmi, M. U.; Ahmad, N. Colloids and Surfaces B : Biointerfaces Doxorubicin-Loaded Photosensitive Magnetic Liposomes for Multi-Modal Cancer Therapy. *Colloids Surfaces B Biointerfaces* **2016**, *148*, 157–164. https://doi.org/10.1016/j.colsurfb.2016.08.055.

(87) Du, S.; Xiong, H.; Xu, C.; Lu, Y.; Yao, J. Attempts to Strengthen and Simplify the Tumor Vascular Normalization Strategy Using Tumor Vessel Normalization Promoting Nanomedicines. *Biomater. Sci.* **2019**, *7* (3), 1147–1160. https://doi.org/10.1039/c8bm01350k.

(88) Zhang, Q.; Dehaini, D.; Zhang, Y.; Zhou, J.; Chen, X.; Zhang, L.; Fang, R. H.; Gao, W.; Zhang, L. Neutrophil Membrane-Coated Nanoparticles Inhibit Synovial Inflammation and Alleviate Joint Damage in Inflammatory Arthritis. *Nat. Nanotechnol.* **2018**, *13* (12), 1182–1190. https://doi.org/10.1038/s41565-018-

0254-4.

(89) Setyawati, M. I.; Tay, C. Y.; Chia, S. L.; Goh, S. L.; Fang, W.; Neo, M. J.; Chong, H. C.; Tan, S. M.; Loo, S. C. J.; Ng, K. W.; Xie, J. P.; Ong, C. N.; Tan, N. S.; Leong, D. T. Titanium Dioxide Nanomaterials Cause Endothelial Cell Leakiness by Disrupting the Homophilic Interaction of VE-Cadherin. *Nat. Commun.* **2013**, *4*, 1–12. https://doi.org/10.1038/ncomms2655.

(90) Setyawati, M. I.; Tay, C. Y.; Bay, B. H.; Leong, D. T. Gold Nanoparticles Induced Endothelial Leakiness Depends on Particle Size and Endothelial Cell Origin. *ACS Nano* **2017**, *11* (5), 5020–5030. https://doi.org/10.1021/acsnano.7b01744.

(91) Setyawati, M. I.; Wang, Q.; Ni, N.; Tee, J. K.; Ariga, K.; Ke, P. C.; Ho, H. K.; Wang, Y.; Leong, D. T. Engineering Tumoral Vascular Leakiness with Gold Nanoparticles. *Nat. Commun.* **2023**, *14* (1). https://doi.org/10.1038/s41467-023-40015-4.

(92) Matsumoto, Y.; Nichols, J. W.; Toh, K.; Nomoto, T.; Cabral, H.; Miura, Y.; Christie, R. J.; Yamada, N.; Ogura, T.; Kano, M. R.; Matsumura, Y.; Nishiyama, N.; Yamasoba, T.; Bae, Y. H.; Kataoka, K. Vascular Bursts Enhance Permeability of Tumour Blood Vessels and Improve Nanoparticle Delivery. *Nat. Nanotechnol.* **2016**, *11* (6), 533–538. https://doi.org/10.1038/nnano.2015.342.

(93) Li, X.; Cai, Q.; Wilson, B. A.; Fan, H.; Dave, H.; Giannotta, M.; Bachoo, R.; Qin, Z. Mechanobiological Modulation of Blood–Brain Barrier Permeability by Laser Stimulation of Endothelial-Targeted Nanoparticles. *Nanoscale* **2023**. https://doi.org/10.1039/D2NR05062E.

(94) Villaseñor, R.; Lampe, J.; Schwaninger, M.; Collin, L. Intracellular Transport and Regulation of Transcytosis across the Blood–Brain Barrier. *Cell. Mol. Life Sci.* **2019**, *76* (6), 1081–1092. https://doi.org/10.1007/s00018-018-2982-x.

(95) Liu, X.; Jiang, J.; Meng, H. Transcytosis - An Effective Targeting Strategy That Is Complementary to “EPR Effect” for Pancreatic Cancer Nano Drug Delivery. *Theranostics* **2019**, *9* (26), 8018–8025. https://doi.org/10.7150/thno.38587.

(96) Nel, A.; Ruoslahti, E.; Meng, H. New Insights into “Permeability” as in the Enhanced Permeability and Retention Effect of Cancer Nanotherapeutics. *ACS Nano* **2017**, *11* (10), 9567–9569. https://doi.org/10.1021/acsnano.7b07214.

(97) Qiu, L.; Shan, X.; Long, M.; Ahmed, K. S.; Zhao, L.; Mao, J.; Zhang, H.; Sun, C.; You, C.; Lv, G.; Chen, J. Elucidation of Cellular Uptake and Intracellular Trafficking of Heparosan Polysaccharide-Based Micelles in Various Cancer Cells. *Int. J. Biol. Macromol.* **2019**, *130*, 755–764. https://doi.org/10.1016/j.ijbiomac.2019.02.133.

(98) Gao, X.; Wang, T.; Wu, B.; Chen, J.; Chen, J.; Yue, Y.; Dai, N.; Chen, H.; Jiang, X. Quantum Dots for Tracking Cellular Transport of Lectin-Functionalized Nanoparticles. *Biochem. Biophys. Res. Commun.* **2008**, *377* (1), 35–40. https://doi.org/10.1016/j.bbrc.2008.09.077.

(99) McMahon, H. T.; Boucrot, E. Molecular Mechanism and Physiological Functions of Clathrin-Mediated Endocytosis. *Nat. Rev. Mol. Cell Biol.* **2011**, *12* (8), 517–533. https://doi.org/10.1038/nrm3151.

(100) Chang, M. P.; Mallet, W. G.; Mostov, K. E.; Brodsky, F. M. Adaptor Self-Aggregation, Adaptor-Receptor Recognition and Binding of Alpha-Adaptin Subunits to the Plasma Membrane Contribute to Recruitment of Adaptor (AP2) Components of Clathrin-Coated Pits. *EMBO J.* **1993**, *12* (5), 2169–2180. https://doi.org/10.1002/j.1460-2075.1993.tb05865.x.

(101) Kelly, B. T.; Graham, S. C.; Liska, N.; Dannhauser, P. N.; Höning, S.; Ungewickell, E. J.; Owen, D. J. AP2 Controls Clathrin Polymerization with a Membrane-Activated Switch. *Science (80-. ).* **2014**, *345* (6195), 459–463. https://doi.org/10.1126/science.1254836.

(102) Miller, S. E.; Mathiasen, S.; Bright, N. A.; Pierre, F.; Kelly, B. T.; Kladt, N.; Schauss, A.; Merrifield, C. J.; Stamou, D.; Höning, S.; Owen, D. J. CALM Regulates Clathrin-Coated Vesicle Size and Maturation by Directly Sensing and Driving Membrane Curvature. *Dev. Cell* **2015**, *33* (2), 163–175. https://doi.org/10.1016/j.devcel.2015.03.002.

(103) Cocucci, E.; Gaudin, R.; Kirchhausen, T. Dynamin Recruitment and Membrane Scission at the Neck of a Clathrin-Coated Pit. *Mol. Biol. Cell* **2014**, *25* (22), 3595–3609. https://doi.org/10.1091/mbc.E14-07-1240.

(104) Tsuji, T.; Yoshitomi, H.; Usukura, J. Endocytic Mechanism of Transferrin-Conjugated Nanoparticles and the Effects of Their Size and Ligand Number on the Efficiency of Drug Delivery. *J. Electron Microsc. (Tokyo).* **2013**, *62* (3), 341–352. https://doi.org/10.1093/jmicro/dfs080.

(105) Krantz, K. C.; Puchalla, J.; Thapa, R.; Kobayashi, C.; Bisher, M.; Viehweg, J.; Carr, C. M.; Rye, H. S. Clathrin Coat Disassembly by the Yeast Hsc70/Ssa1p and Auxilin/Swa2p Proteins Observed by Single-Particle Burst Analysis Spectroscopy. *J. Biol. Chem.* **2013**, *288* (37), 26721–26730. https://doi.org/10.1074/jbc.M113.491753.

(106) Lakadamyali, M.; Rust, M. J.; Zhuang, X. Ligands for Clathrin-Mediated Endocytosis Are Differentially Sorted into Distinct Populations of Early Endosomes. *Cell* **2006**, *124* (5), 997–1009. https://doi.org/10.1016/j.cell.2005.12.038.

(107) Donahue, N. D.; Acar, H.; Wilhelm, S. Concepts of Nanoparticle Cellular Uptake, Intracellular Trafficking, and Kinetics in Nanomedicine. *Adv. Drug Deliv. Rev.* **2019**, *143*, 68–96. https://doi.org/10.1016/j.addr.2019.04.008.

(108) Nazir Hossen, M.; Wang, L.; Chinthalapally, H. R.; Robertson, J. D.; Fung, K. M.; Wilhelm, S.; Bieniasz, M.; Bhattacharya, R.; Mukherjee, P. Switching the Intracellular Pathway and Enhancing the Therapeutic Efficacy of Small Interfering RNA by Auroliposome. *Sci. Adv.* **2020**, *6* (30), eaba5379. https://doi.org/10.1126/sciadv.aba5379.

(109) Preston, J. E.; Joan Abbott, N.; Begley, D. J. Transcytosis of Macromolecules at the Blood–Brain Barrier. In *Physiological Reviews*; Elsevier Inc., 2014; Vol. 83, pp 147–163. https://doi.org/10.1016/bs.apha.2014.06.001.

(110) Tuma, P. L.; Hubbard, A. L. Transcytosis: Crossing Cellular Barriers. *Physiological Reviews*. July 2003, pp 871–932. https://doi.org/10.1152/physrev.00001.2003.

(111) Xiao, G.; Gan, L. S. Receptor-Mediated Endocytosis and Brain Delivery of Therapeutic Biologics. *Int. J. Cell Biol.* **2013**, *2013*. https://doi.org/10.1155/2013/703545.

(112) You, L.; Wang, J.; Liu, T.; Zhang, Y.; Han, X.; Wang, T.; Guo, S.; Dong, T.; Xu, J.; Anderson, G. J.; Liu, Q.; Chang, Y. Z.; Lou, X.; Nie, G. Targeted Brain Delivery of Rabies Virus Glycoprotein 29-Modified Deferoxamine-Loaded Nanoparticles Reverses Functional Deficits in Parkinsonian Mice. *ACS Nano* **2018**, *12* (5), 4123–4139. https://doi.org/10.1021/acsnano.7b08172.

(113) Gosk, S.; Moos, T.; Gottstein, C.; Bendas, G. VCAM-1 Directed Immunoliposomes Selectively Target Tumor Vasculature in Vivo. *Biochim. Biophys. Acta - Biomembr.* **2008**, *1778* (4), 854–863. https://doi.org/10.1016/j.bbamem.2007.12.021.

(114) Sharma, D. K.; Brown, J. C.; Choudhury, A.; Peterson, T. E.; Holicky, E.; Marks, D. L.; Simari, R.; Parton, R. G.; Pagano, R. E. Selective Stimulation of Caveolar Endocytosis by Glycosphingolipids and Cholesterol. *Mol. Biol. Cell* **2004**, *15* (7), 3114–3122. https://doi.org/10.1091/mbc.e04-03-0189.

(115) Couet, J.; Belanger, M. M.; Roussel, E.; Drolet, M.-C. Cell Biology of Caveolae and Caveolin. *Adv. Drug Deliv. Rev.* **2001**, *49* (3), 223–235. https://doi.org/10.1016/S0169-409X(01)00139-9.

(116) Sinha, B.; Köster, D.; Ruez, R.; Gonnord, P.; Bastiani, M.; Abankwa, D.; Stan, R. V.; Butler-Browne, G.; Vedie, B.; Johannes, L.; Morone, N.; Parton, R. G.; Raposo, G.; Sens, P.; Lamaze, C.; Nassoy, P. Cells Respond to Mechanical Stress by Rapid Disassembly of Caveolae. *Cell* **2011**, *144* (3), 402–413. https://doi.org/10.1016/j.cell.2010.12.031.

(117) Fridolfsson, H. N.; Roth, D. M.; Insel, P. A.; Patel, H. H. Regulation of Intracellular Signaling and Function by Caveolin. *FASEB J.* **2014**, *28* (9), 3823–3831. https://doi.org/10.1096/fj.14-252320.

(118) Chow, B. W.; Nuñez, V.; Kaplan, L.; Granger, A. J.; Bistrong, K.; Zucker, H. L.; Kumar, P.; Sabatini, B. L.; Gu, C. Caveolae in CNS Arterioles Mediate Neurovascular Coupling. *Nature* **2020**, *579* (7797), 106–110. https://doi.org/10.1038/s41586-020-2026-1.

(119) Gerbod-Giannone, M. C.; Dallet, L.; Naudin, G.; Sahin, A.; Decossas, M.; Poussard, S.; Lambert, O. Involvement of Caveolin-1 and CD36 in Native LDL Endocytosis by Endothelial Cells. *Biochim. Biophys. Acta - Gen. Subj.* **2019**, *1863* (5), 830–838. https://doi.org/10.1016/j.bbagen.2019.01.005.

(120) Sowa, G. Novel Insights into the Role of Caveolin-2 in Cell- and Tissue-Specific Signaling and Function. *Biochem. Res. Int.* **2011**, *2011*. https://doi.org/10.1155/2011/809259.

(121) Williams, T. M.; Lisanti, M. P. The Caveolin Proteins. *Genome Biol.* **2004**, *5* (3), 1–8. https://doi.org/10.1186/gb-2004-5-3-214.

(122) Kovtun, O.; Tillu, V. A.; Ariotti, N.; Parton, R. G.; Collins, B. M. Cavin Family Proteins and the Assembly of Caveolae. *J. Cell Sci.* **2015**, *128* (7), 1269–1278. https://doi.org/10.1242/jcs.167866.

(123) Henley, J. R.; Krueger, E. W. A.; Oswald, B. J.; McNiven, M. A. Dynamin-Mediated Internalization of Caveolae. *J. Cell Biol.* **1998**, *141* (1), 85–99. https://doi.org/10.1083/jcb.141.1.85.

(124) Schnitzer, J. E. Caveolae: From Basic Trafficking Mechanisms to Targeting Transcytosis for Tissue-Specific Drug and Gene Delivery in Vivo. *Adv. Drug Deliv. Rev.* **2001**, *49* (3), 265–280. https://doi.org/10.1016/S0169-409X(01)00141-7.

(125) Choi, S. Il; Maeng, Y. S.; Kim, T. I.; Lee, Y.; Kim, Y. S.; Kim, E. K. Lysosomal Trafficking of TGFBIp via Caveolae-Mediated Endocytosis. *PLoS One* **2015**, *10* (4), 1–23. https://doi.org/10.1371/journal.pone.0119561.

(126) Le, P. U.; Nabi, I. R. Distinct Caveolae-Mediated Endocytic Pathways Target the Golgi Apparatus and the Endoplasmic Reticulum. *J. Cell Sci.* **2003**, *116* (6), 1059–1071. https://doi.org/10.1242/jcs.00327.

(127) Wang, Z.; Tiruppathi, C.; Minshall, R. D.; Malik, A. B. Size and Dynamics of Caveolae Studied Using Nanoparticles in Living Endothelial Cells. *ACS Nano* **2009**, *3* (12), 4110–4116. https://doi.org/10.1021/nn9012274.

(128) Borlan, R.; Tatar, A.-S.; Soritau, O.; Maniu, D.; Marc, G.; Florea, A.; Focsan, M.; Astilean, S. Design of Fluorophore-Loaded Human Serum Albumin Nanoparticles for Specific Targeting of NIH:OVCAR3 Ovarian Cancer Cells. *Nanotechnology* **2020**, *31* (31), 315102. https://doi.org/10.1088/1361-6528/ab8b90.

(129) Suen, W. L. L.; Chau, Y. Size-Dependent Internalisation of Folate-Decorated Nanoparticles via the Pathways of Clathrin and Caveolae-Mediated Endocytosis in ARPE-19 Cells. *J. Pharm. Pharmacol.* **2014**, *66* (4), 564–573. https://doi.org/10.1111/jphp.12134.

(130) Oh, P.; Borgström, P.; Witkiewicz, H.; Li, Y.; Borgström, B. J.; Chrastina, A.; Iwata, K.; Zinn, K. R.; Baldwin, R.; Testa, J. E.; Schnitzer, J. E. Live Dynamic Imaging of Caveolae Pumping Targeted Antibody Rapidly and Specifically across Endothelium in the Lung. *Nat. Biotechnol.* **2007**, *25* (3), 327–337. https://doi.org/10.1038/nbt1292.

(131) Oh, P.; Testa, J. E.; Borgstrom, P.; Witkiewicz, H.; Li, Y.; Schnitzer, J. E. In Vivo Proteomic Imaging Analysis of Caveolae Reveals Pumping System to Penetrate Solid Tumors. *Nat. Med.* **2014**, *20* (9), 1062–1068. https://doi.org/10.1038/nm.3623.

(132) Kerr, M. C.; Teasdale, R. D. Defining Macropinocytosis. *Traffic* **2009**, *10* (4), 364–371. https://doi.org/10.1111/j.1600-0854.2009.00878.x.

(133) Palm, W. Metabolic Functions of Macropinocytosis. *Philos. Trans. R. Soc. B Biol. Sci.* **2019**, *374* (1765), 0–3. https://doi.org/10.1098/rstb.2018.0285.

(134) Araki, N.; Johnson, M. T.; Swanson, J. A. A Role for Phosphoinositide 3-Kinase in the Completion of Macropinocytosis and Phagocytosis by Macrophages. *J. Cell Biol.* **1996**, *135* (5), 1249–1260. https://doi.org/10.1083/jcb.135.5.1249.

(135) Hewlett, L. J.; Prescott, A. R.; Watts, C. The Coated Pit and Macropinocytic Pathways Serve Distinct Endosome Populations. *J. Cell Biol.* **1994**, *124* (5), 689–703. https://doi.org/10.1083/jcb.124.5.689.

(136) Lim, J. P.; Gleeson, P. A. Macropinocytosis: An Endocytic Pathway for Internalising Large Gulps. *Immunol. Cell Biol.* **2011**, *89* (8), 836–843. https://doi.org/10.1038/icb.2011.20.

(137) Kasahara, K.; Nakayama, Y.; Sato, I.; Ikeda, K.; Hoshino, M.; Endo, T.; Yamaguchi, N. Role of Src-Family Kinases in Formation and Trafficking of Macropinosomes. *J. Cell. Physiol.* **2007**, *211* (1), 220–232. https://doi.org/10.1002/jcp.20931.

(138) Commisso, C.; Flinn, R. J.; Bar-Sagi, D. Determining the Macropinocytic Index of Cells through a Quantitative Image-Based Assay. *Nat. Protoc.* **2014**, *9* (1), 182–192. https://doi.org/10.1038/nprot.2014.004.

(139) Lee, E.; Knecht, D. A. Visualization of Actin Dynamics during Macropinocytosis and Exocytosis. *Traffic* **2002**, *3* (3), 186–192. https://doi.org/10.1034/j.1600-0854.2002.030304.x.

(140) Recouvreux, M. V.; Commisso, C. Macropinocytosis: A Metabolic Adaptation to Nutrient Stress in Cancer. *Front. Endocrinol. (Lausanne).* **2017**, *8* (SEP), 1–7. https://doi.org/10.3389/fendo.2017.00261.

(141) Williams, T. D.; Kay, R. R. The Physiological Regulation of Macropinocytosis during Dictyostelium Growth and Development. *J. Cell Sci.* **2018**, *131* (6). https://doi.org/10.1242/jcs.213736.

(142) Commisso, C.; Davidson, S. M.; Soydaner-Azeloglu, R. G.; Parker, S. J.; Kamphorst, J. J.; Hackett, S.; Grabocka, E.; Nofal, M.; Drebin, J. A.; Thompson, C. B.; Rabinowitz, J. D.; Metallo, C. M.; Vander Heiden, M. G.; Bar-Sagi, D. Macropinocytosis of Protein Is an Amino Acid Supply Route in Ras-Transformed Cells. *Nature* **2013**, *497* (7451), 633–637. https://doi.org/10.1038/nature12138.

(143) Charpentier, J. C.; Chen, D.; Lapinski, P. E.; Turner, J.; Grigorova, I.; Swanson, J. A.; King, P. D. Macropinocytosis Drives T Cell Growth by Sustaining the Activation of MTORC1. *Nat. Commun.* **2020**, *11* (1), 1–9. https://doi.org/10.1038/s41467-019-13997-3.

(144) Flannagan, R. S.; Jaumouillé, V.; Grinstein, S. The Cell Biology of Phagocytosis. *Annu. Rev. Pathol. Mech. Dis.* **2012**, *7* (1), 61–98.

https://doi.org/10.1146/annurev-pathol-011811-132445.

(145) Ji, S.; Dong, W.; Qi, Y.; Gao, H.; Zhao, D.; Xu, M.; Li, T.; Yu, H.; Sun, Y.; Ma, R.; Shi, J.; Gao, C. Phagocytosis by Endothelial Cells Inhibits Procoagulant Activity of Platelets of Essential Thrombocythemia in Vitro. *J. Thromb. Haemost.* **2020**, *18* (1), 222–233. https://doi.org/10.1111/jth.14617.

(146) Xie, R.; Gao, C.; Li, W.; Zhu, J.; Novakovic, V.; Wang, J.; Ma, R.; Zhou, J.; Gilbert, G. E.; Shi, J. Phagocytosis by Macrophages and Endothelial Cells Inhibits Procoagulant and Fibrinolytic Activity of Acute Promyelocytic Leukemia Cells. *Blood* **2012**, *119* (10), 2325–2334. https://doi.org/10.1182/blood-2011-06-362186.

(147) Mayor, S.; Parton, R. G.; Donaldson, J. G. Clathrin-Independent Pathways of Endocytosis. *Cold Spring Harb. Perspect. Biol.* **2014**, *6* (6), a016758–a016758. https://doi.org/10.1101/cshperspect.a016758.

(148) Lundmark, R.; Doherty, G. J.; Howes, M. T.; Cortese, K.; Vallis, Y.; Parton, R. G.; McMahon, H. T. The GTPase-Activating Protein GRAF1 Regulates the CLIC/GEEC Endocytic Pathway. *Curr. Biol.* **2008**, *18* (22), 1802–1808. https://doi.org/10.1016/j.cub.2008.10.044.

(149) Sathe, M.; Muthukrishnan, G.; Rae, J.; Disanza, A.; Thattai, M.; Scita, G.; Parton, R. G.; Mayor, S. Small GTPases and BAR Domain Proteins Regulate Branched Actin Polymerisation for Clathrin and Dynamin-Independent Endocytosis. *Nat. Commun.* **2018**, *9* (1), 1835. https://doi.org/10.1038/s41467-018-03955-w.

(150) Wei, X.; She, G.; Wu, T.; Xue, C.; Cao, Y. PEDV Enters Cells through Clathrin-, Caveolae-, and Lipid Raft-Mediated Endocytosis and Traffics via the Endo-/Lysosome Pathway. *Vet. Res.* **2020**, *51* (1), 1–18. https://doi.org/10.1186/s13567-020-0739-7.

(151) Sevcsik, E.; Brameshuber, M.; Fölser, M.; Weghuber, J.; Honigmann, A.; Schütz, G. J. GPI-Anchored Proteins Do Not Reside in Ordered Domains in the Live Cell Plasma Membrane. *Nat. Commun.* **2015**, *6*, 1–10. https://doi.org/10.1038/ncomms7969.

(152) Sugahara, K. N.; Teesalu, T.; Karmali, P. P.; Kotamraju, V. R.; Agemy, L.; Girard, O. M.; Hanahan, D.; Mattrey, R. F.; Ruoslahti, E. Tissue-Penetrating Delivery of Compounds and Nanoparticles into Tumors. *Cancer Cell* **2009**, *16* (6), 510–520. https://doi.org/10.1016/j.ccr.2009.10.013.

(153) Pang, H. B.; Braun, G. B.; Ruoslahti, E. Neuropilin-1 and Heparan Sulfate Proteoglycans Cooperate in Cellular Uptake of Nanoparticles Functionalized by Cationic Cell-Penetrating Peptides. *Sci. Adv.* **2015**, *1* (10), 1–8. https://doi.org/10.1126/sciadv.1500821.

(154) Lee, J. C.; Donahue, N. D.; Mao, A. S.; Karim, A.; Komarneni, M.; Thomas, E. E.; Francek, E. R.; Yang, W.; Wilhelm, S. Exploring Maleimide-Based Nanoparticle Surface Engineering to Control Cellular Interactions. *ACS Appl. Nano Mater.* **2020**. https://doi.org/10.1021/acsanm.9b02541.

(155) Wilhelm, S.; Hirsch, T.; Patterson, W. M.; Scheucher, E.; Mayr, T.; Wolfbeis, O. S. Multicolor Upconversion Nanoparticles for Protein Conjugation. *Theranostics* **2013**, *3* (4), 239–248. https://doi.org/10.7150/thno.5113.

(156) Lazarovits, J.; Chen, Y. Y.; Song, F.; Ngo, W.; Tavares, A. J.; Zhang, Y. N.; Audet, J.; Tang, B.; Lin, Q.; Cruz Tleugabulova, M.; Wilhelm, S.; Krieger, J. R.; Mallevaey, T.; Chan, W. C. W. Synthesis of Patient-Specific Nanomaterials. *Nano Lett.* **2019**, *19* (1), 116–123. https://doi.org/10.1021/acs.nanolett.8b03434.

(157) Merlot, A. M.; Kalinowski, D. S.; Richardson, D. R. Unraveling the Mysteries of Serum Albumin-More than Just a Serum Protein. *Front. Physiol.* **2014**, *5 AUG* (August), 1–7. https://doi.org/10.3389/fphys.2014.00299.

(158) Tiruppathi, C.; Finnegan, A.; Malik, A. B. Isolation and Characterization of a Cell Surface Albumin-Binding Protein from Vascular Endothelial Cells. *Proc. Natl. Acad. Sci. U. S. A.* **1996**, *93* (1), 250–254. https://doi.org/10.1073/pnas.93.1.250.

(159) Xie, J.; Wang, J.; Niu, G.; Huang, J.; Chen, K.; Li, X.; Chen, X. Human Serum Albumin Coated Iron Oxide Nanoparticles for Efficient Cell Labeling. *Chem. Commun.* **2010**, *46* (3), 433–435. https://doi.org/10.1039/b917195a.

(160) Zhang, J.; Nie, S.; Zu, Y.; Abbasi, M.; Cao, J.; Li, C.; Wu, D.; Labib, S.; Brackee, G.; Shen, C.-L.; Wang, S. Anti-Atherogenic Effects of CD36-Targeted Epigallocatechin Gallate-Loaded Nanoparticles. *J. Control. Release* **2019**, *303*, 263–273. https://doi.org/10.1016/j.jconrel.2019.04.018.

(161) Kelley, J. L.; Ozment, T. R.; Li, C.; Schweitzer, J. B.; Williams, D. L. Scavenger Receptor-A (CD204): A Two-Edged Sword in Health and Disease. *Crit. Rev. Immunol.* **2014**, *34* (3), 241–261. https://doi.org/10.1615/CritRevImmunol.2014010267.

(162) Dunzendorfer, S.; Lee, H.-K.; Soldau, K.; Tobias, P. S. TLR4 Is the Signaling but Not the Lipopolysaccharide Uptake Receptor. *J. Immunol.* **2004**, *173* (2), 1166–1170. https://doi.org/10.4049/jimmunol.173.2.1166.

(163) Lipinski, M. J.; Amirbekian, V.; Frias, J. C.; Aguinaldo, J. G. S.; Mani, V.; Briley-Saebo, K. C.; Fuster, V.; Fallon, J. T.; Fisher, E. A.; Fayad, Z. A. MRI to Detect Atherosclerosis with Gadolinium-Containing Immunomicelles Targeting the Macrophage Scavenger Receptor. *Magn. Reson. Med.* **2006**, *56* (3), 601–610. https://doi.org/10.1002/mrm.20995.

(164) Zhang, X.; Sessa, W. C.; Fernández-Hernando, C. Endothelial Transcytosis of Lipoproteins in Atherosclerosis. *Front. Cardiovasc. Med.* **2018**, *5* (September), 1–6. https://doi.org/10.3389/fcvm.2018.00130.

(165) Strickland, D. K.; Gonias, S. L.; Argraves, W. S. Diverse Roles for the LDL Receptor Family. *Trends Endocrinol. Metab.* **2002**, *13* (2), 66–74. https://doi.org/10.1016/S1043-2760(01)00526-4.

(166) Wang, Z.; Duan, X.; Lv, Y.; Zhao, Y. Low Density Lipoprotein Receptor (LDLR)-Targeted Lipid Nanoparticles for the Delivery of Sorafenib and Dihydroartemisinin

in Liver Cancers. *Life Sci.* **2019**, *239*, 117013. https://doi.org/10.1016/j.lfs.2019.117013.

(167) Pyzik, M.; Sand, K. M. K.; Hubbard, J. J.; Andersen, J. T.; Sandlie, I.; Blumberg, R. S. The Neonatal Fc Receptor (FcRn): A Misnomer? *Front. Immunol.* **2019**, *10* (JULY). https://doi.org/10.3389/fimmu.2019.01540.

(168) Pridgen, E. M.; Alexis, F.; Kuo, T. T.; Levy-Nissenbaum, E.; Karnik, R.; Blumberg, R. S.; Langer, R.; Farokhzad, O. C. Transepithelial Transport of Fc-Targeted Nanoparticles by the Neonatal Fc Receptor for Oral Delivery. *Sci. Transl. Med.* **2013**, *5* (213), 213ra167-213ra167. https://doi.org/10.1126/scitranslmed.3007049.

(169) Goebl, N. A.; Babbey, C. M.; Datta-Mannan, A.; Witcher, D. R.; Wroblewski, V. J.; Dunn, K. W. Neonatal Fc Receptor Mediates Internalization of Fc in Transfected Human Endothelial Cells. *Mol. Biol. Cell* **2008**, *19* (12), 5490–5505. https://doi.org/10.1091/mbc.e07-02-0101.

(170) Mayle, K. M.; Le, A. M.; Kamei, D. T. The Intracellular Trafficking Pathway of Transferrin. *Biochim. Biophys. Acta - Gen. Subj.* **2012**, *1820* (3), 264–281. https://doi.org/10.1016/j.bbagen.2011.09.009.

(171) Li, H.; Qian, Z. M. Transferrin/Transferrin Receptor-Mediated Drug Delivery. *Med. Res. Rev.* **2002**, *22* (3), 225–250. https://doi.org/10.1002/med.10008.

(172) Chang, J.; Jallouli, Y.; Kroubi, M.; Yuan, X.; Feng, W.; Kang, C.; Pu, P.; Betbeder, D. Characterization of Endocytosis of Transferrin-Coated PLGA Nanoparticles by the Blood–Brain Barrier. *Int. J. Pharm.* **2009**, *379* (2), 285–292. https://doi.org/10.1016/j.ijpharm.2009.04.035.

(173) Choi, C. H. J.; Alabi, C. A.; Webster, P.; Davis, M. E. Mechanism of Active Targeting in Solid Tumors with Transferrin-Containing Gold Nanoparticles. *Proc. Natl. Acad. Sci. U. S. A.* **2010**, *107* (3), 1235–1240. https://doi.org/10.1073/pnas.0914140107.

(174) Bryant, D. M.; Kerr, M. C.; Hammond, L. A.; Joseph, S. R.; Mostov, K. E.; Teasdale, R. D.; Stow, J. L. EGF Induces Macropinocytosis and SNX1-Modulated Recycling of E-Cadherin. *J. Cell Sci.* **2007**, *120* (10), 1818–1828. https://doi.org/10.1242/jcs.000653.

(175) Herbst, R. S. Review of Epidermal Growth Factor Receptor Biology. *Int. J. Radiat. Oncol. Biol. Phys.* **2004**, *59* (2 SUPPL.), S21–S26. https://doi.org/10.1016/j.ijrobp.2003.11.041.

(176) Sugahara, K. N.; Teesalu, T.; Karmali, P. P.; Kotamraju, V. R.; Agemy, L.; Greenwald, D. R.; Ruoslahti, E. Coadministration of a Tumor-Penetrating Peptide Enhances the Efficacy of Cancer Drugs. *Science (80-. ).* **2010**, *328* (5981), 1031–1035. https://doi.org/10.1126/science.1183057.

(177) Singh, R. D.; Puri, V.; Valiyaveettil, J. T.; Marks, D. L.; Bittman, R.; Pagano, R. E. Selective Caveolin-1–Dependent Endocytosis of Glycosphingolipids. *Mol. Biol. Cell* **2003**, *14* (8), 3254–3265. https://doi.org/10.1091/mbc.e02-12-0809.

(178) Lin, H. P.; Singla, B.; Ghoshal, P.; Faulkner, J. L.; Cherian-Shaw, M.; O'Connor, P. M.; She, J. X.; Belin de Chantemele, E. J.; Csányi, G. Identification of Novel Macropinocytosis Inhibitors Using a Rational Screen of Food and Drug Administration-Approved Drugs. *Br. J. Pharmacol.* **2018**, *175* (18), 3640–3655. https://doi.org/10.1111/bph.14429.

(179) Li, Y.; Monteiro-Riviere, N. A. Mechanisms of Cell Uptake, Inflammatory Potential and Protein Corona Effects with Gold Nanoparticles. *Nanomedicine* **2016**, *11* (24), 3185–3203. https://doi.org/10.2217/nnm-2016-0303.

(180) Donahue, N. D.; Francek, E. R.; Kiyotake, E.; Thomas, E. E.; Yang, W.; Wang, L.; Detamore, M. S.; Wilhelm, S. Assessing Nanoparticle Colloidal Stability with Single-Particle Inductively Coupled Plasma Mass Spectrometry (SP-ICP-MS). *Anal. Bioanal. Chem.* **2020**, *412* (22), 5205–5216. https://doi.org/10.1007/s00216-020-02783-6.

(181) Wilhelm, S.; Bensen, R. C.; Kothapalli, N. R.; Burgett, A. W. G.; Merrifield, R.; Stephan, C. Quantification of Gold Nanoparticle Uptake into Cancer Cells Using Single Cell ICP-MS, PerkinElmer Appl. Note. PerkinElmer Appl. 2018.

(182) Schnitzer, J. E.; Oh, P.; Pinney, E.; Allard, J. Filipin-Sensitive Caveolae-Mediated Transport in Endothelium: Reduced Transcytosis, Scavenger Endocytosis, and Capillary Permeability of Select Macromolecules. *J. Cell Biol.* **1994**, *127* (5), 1217–1232. https://doi.org/10.1083/jcb.127.5.1217.

(183) Chang, C.-C.; Wu, M.; Yuan, F. Role of Specific Endocytic Pathways in Electrotransfection of Cells. *Mol. Ther. - Methods Clin. Dev.* **2014**, *1*, 14058. https://doi.org/10.1038/mtm.2014.58.

(184) Ho, Y. T.; Kamm, R. D.; Kah, J. C. Y. Influence of Protein Corona and Caveolae-Mediated Endocytosis on Nanoparticle Uptake and Transcytosis. *Nanoscale* **2018**, *10* (26), 12386–12397. https://doi.org/10.1039/c8nr02393j.

(185) Ao, M.; Wu, L.; Zhou, X.; Chen, Y. Methyl-β-Cyclodextrin Impairs the Monocyte-Adhering Ability of Endothelial Cells by down-Regulating Adhesion Molecules and Caveolae and Reorganizing the Actin Cytoskeleton. *Biol. Pharm. Bull.* **2016**, *39* (6), 1029–1034. https://doi.org/10.1248/bpb.b16-00047.

(186) Rodal, S. K.; Skretting, G.; Garred, Ø.; Vilhardt, F.; van Deurs, B.; Sandvig, K. Extraction of Cholesterol with Methyl-β-Cyclodextrin Perturbs Formation of Clathrin-Coated Endocytic Vesicles. *Mol. Biol. Cell* **1999**, *10* (4), 961–974. https://doi.org/10.1091/mbc.10.4.961.

(187) Schnitzer, J. E.; Allard, J.; Oh, P. NEM Inhibits Transcytosis, Endocytosis, and Capillary Permeability: Implication of Caveolae Fusion in Endothelia. *Am. J. Physiol. Circ. Physiol.* **1995**, *268* (1), H48–H55. https://doi.org/10.1152/ajpheart.1995.268.1.H48.

(188) Predescu, S. A.; Predescu, D. N.; Palade, G. E. Endothelial Transcytotic Machinery Involves Supramolecular Protein-Lipid Complexes. *Mol. Biol. Cell* **2001**, *12* (4), 1019–1033. https://doi.org/10.1091/mbc.12.4.1019.

(189) Huang, Y. Z.; Gao, J. Q.; Chen, J. L.; Liang, W. Q. Cationic Liposomes Modified with Non-Ionic Surfactants as Effective Non-Viral Carrier for Gene Transfer. *Colloids Surfaces B Biointerfaces* **2006**, *49* (2), 158–164. https://doi.org/10.1016/j.colsurfb.2006.03.014.

(190) Sandvig, K.; Llorente, A.; Rodal, S. K.; Eker, P.; Garred, Ø.; Stahlhut, M.; Van Deurs, B. Apical Macropinocytosis in Polarized MDCK Cells: Regulation by N-Ethylmaleimide-Sensitive Proteins. *Eur. J. Cell Biol.* **2000**, *79* (7), 447–457. https://doi.org/10.1078/0171-9335-00071.

(191) Malyukova, I.; Murray, K. F.; Zhu, C.; Boedeker, E.; Kane, A.; Patterson, K.; Peterson, J. R.; Donowitz, M.; Kovbasnjuk, O. Macropinocytosis in Shiga Toxin 1 Uptake by Human Intestinal Epithelial Cells and Transcellular Transcytosis. *Am. J. Physiol. Liver Physiol.* **2009**, *296* (1), G78–G92. https://doi.org/10.1152/ajpgi.90347.2008.

(192) Rothberg, K. G.; Heuser, J. E.; Donzell, W. C.; Ying, Y. S.; Glenney, J. R.; Anderson, R. G. W. Caveolin, a Protein Component of Caveolae Membrane Coats. *Cell* **1992**, *68* (4), 673–682. https://doi.org/10.1016/0092-8674(92)90143-Z.

(193) Kim, J. H.; Singh, A.; Del Poeta, M.; Brown, D. A.; London, E. The Effect of Sterol Structure upon Clathrin-Mediated and Clathrin-Independent Endocytosis. *J. Cell Sci.* **2017**, *130* (16), 2682–2695. https://doi.org/10.1242/jcs.201731.

(194) Zhu, X.-D.; Zhuang, Y.; Ben, J.-J.; Qian, L.-L.; Huang, H.-P.; Bai, H.; Sha, J.-H.; He, Z.-G.; Chen, Q. Caveolae-Dependent Endocytosis Is Required for Class A Macrophage Scavenger Receptor-Mediated Apoptosis in Macrophages. *J. Biol. Chem.* **2011**, *286* (10), 8231–8239. https://doi.org/10.1074/jbc.M110.145888.

(195) Puri, V.; Watanabe, R.; Singh, R. D.; Dominguez, M.; Brown, J. C.; Wheatley, C. L.; Marks, D. L.; Pagano, R. E. Clathrin-Dependent and -Independent Internalization of Plasma Membrane Sphingolipids Initiates Two Golgi Targeting Pathways. *J. Cell Biol.* **2001**, *154* (3), 535–547. https://doi.org/10.1083/jcb.200102084.

(196) Kim, H. R.; Gil, S.; Andrieux, K.; Nicolas, V.; Appel, M.; Chacun, H.; Desmaële, D.; Taran, F.; Georgin, D.; Couvreur, P. Low-Density Lipoprotein Receptor-Mediated Endocytosis of PEGylated Nanoparticles in Rat Brain Endothelial Cells. *Cell. Mol. Life Sci.* **2007**, *64* (3), 356–364. https://doi.org/10.1007/s00018-007-6390-x.

(197) Vercauteren, D.; Vandenbroucke, R. E.; Jones, A. T.; Rejman, J.; Demeester, J.; De Smedt, S. C.; Sanders, N. N.; Braeckmans, K. The Use of Inhibitors to Study Endocytic Pathways of Gene Carriers: Optimization and Pitfalls. *Mol. Ther.* **2010**, *18* (3), 561–569. https://doi.org/10.1038/mt.2009.281.

(198) Sandvig, K.; Kavaliauskiene, S.; Skotland, T. Clathrin-Independent Endocytosis: An Increasing Degree of Complexity. *Histochem. Cell Biol.* **2018**, *150* (2), 107–118. https://doi.org/10.1007/s00418-018-1678-5.

(199) Shu, L. Glycosphingolipid Mediated Caveolin-1 Oligomerization. *J. Glycomics Lipidomics* **2012**, *01* (S1), 3197–3210. https://doi.org/10.4172/2153-0637.S2-003.

(200) Cheng, Z.-J.; Singh, R. D.; Sharma, D. K.; Holicky, E. L.; Hanada, K.; Marks, D. L.; Pagano, R. E. Distinct Mechanisms of Clathrin-Independent Endocytosis Have Unique Sphingolipid Requirements. *Mol. Biol. Cell* **2006**, *17* (7), 3197–3210. https://doi.org/10.1091/mbc.e05-12-1101.

(201) Bhattacharyya, S.; Singh, R. D.; Pagano, R.; Robertson, J. D.; Bhattacharya, R.; Mukherjee, P. Switching the Targeting Pathways of a Therapeutic Antibody by Nanodesign. *Angew. Chemie - Int. Ed.* **2012**, *51* (7), 1563–1567. https://doi.org/10.1002/anie.201105432.

(202) Smart, E. J.; Ying, Y. S.; Anderson, R. G. W. Hormonal Regulation of Caveolae Internalization. *J. Cell Biol.* **1995**, *131* (4), 929–938. https://doi.org/10.1083/jcb.131.4.929.

(203) Smart, E. J.; Estes, K.; Anderson, R. G. W. Inhibitors That Block Both the Internalization of Caveolae and the Return of Plasmalemmal Vesicles. *Cold Spring Harb. Symp. Quant. Biol.* **1995**, *60* (Anderson 1993), 243–248. https://doi.org/10.1101/SQB.1995.060.01.028.

(204) Kamen, B. A.; Johnson, C. A.; Wang, M. T.; Anderson, R. G. W. Regulation of the Cytoplasmic Accumulation of 5-Methyltetrahydrofolate in MA104 Cells Is Independent of Folate Receptor Regulation. *J. Clin. Invest.* **1989**, *84* (5), 1379–1386. https://doi.org/10.1172/JCI114310.

(205) Yumoto, R.; Nishikawa, H.; Okamoto, M.; Katayama, H.; Nagai, J.; Takano, M. Clathrin-Mediated Endocytosis of FITC-Albumin in Alveolar Type II Epithelial Cell Line RLE-6TN. *Am. J. Physiol. Cell. Mol. Physiol.* **2006**, *290* (5), L946–L955. https://doi.org/10.1152/ajplung.00173.2005.

(206) Francia, V.; Reker-Smit, C.; Boel, G.; Salvati, A. Limits and Challenges in Using Transport Inhibitors to Characterize How Nano-Sized Drug Carriers Enter Cells. *Nanomedicine* **2019**, *14* (12), 1533–1549. https://doi.org/10.2217/nnm-2018-0446.

(207) Huang, M.; Ma, Z.; Khor, E.; Lim, L. Y. Uptake of FITC-Chitosan Nanoparticles by A549 Cells. *Pharm. Res.* **2002**, *19* (10), 1488–1494. https://doi.org/10.1023/A:1020404615898.

(208) Macia, E.; Ehrlich, M.; Massol, R.; Boucrot, E.; Brunner, C.; Kirchhausen, T. Dynasore, a Cell-Permeable Inhibitor of Dynamin. *Dev. Cell* **2006**, *10* (6), 839–850. https://doi.org/10.1016/j.devcel.2006.04.002.

(209) Smith, P. J.; Giroud, M.; Wiggins, H. L.; Gower, F.; Thorley, J. A.; Stolpe, B.; Mazzolini, J.; Dyson, R. J.; Rappoport, J. Z. Cellular Entry of Nanoparticles via Serum Sensitive Clathrin-Mediated Endocytosis, and Plasma Membrane Permeabilization. *Int. J. Nanomedicine* **2012**, *7*, 2045–2055. https://doi.org/10.2147/IJN.S29334.

(210) Chen, C. L.; Hou, W. H.; Liu, I. H.; Hsiao, G.; Huang, S. S.; Huang, J. S. Inhibitors

of Clathrin-Dependent Endocytosis Enhance TGFβ Signaling and Responses. *J. Cell Sci.* **2009**, *122* (11), 1863–1871. https://doi.org/10.1242/jcs.038729.

(211) Sarkar, K.; Kruhlak, M. J.; Erlandsen, S. L.; Shaw, S. Selective Inhibition by Rottlerin of Macropinocytosis in Monocyte-Derived Dendritic Cells. *Immunology* **2005**, *116* (4), 513–524. https://doi.org/10.1111/j.1365-2567.2005.02253.x.

(212) Cooper, J. A. Effects of Cytochalasin and Phalloidin on Actin. *J. Cell Biol.* **1987**, *105* (4), 1473–1478. https://doi.org/10.1083/jcb.105.4.1473.

(213) Qaddoumi, M. G.; Ueda, H.; Yang, J.; Davda, J.; Labhasetwar, V.; Lee, V. H. L. The Characteristics and Mechanisms of Uptake of PLGA Nanoparticles in Rabbit Conjunctival Epithelial Cell Layers. *Pharm. Res.* **2004**, *21* (4), 641–648. https://doi.org/10.1023/B:PHAM.0000022411.47059.76.

(214) Koivusalo, M.; Welch, C.; Hayashi, H.; Scott, C. C.; Kim, M.; Alexander, T.; Touret, N.; Hahn, K. M.; Grinstein, S. Amiloride Inhibits Macropinocytosis by Lowering Submembranous PH and Preventing Rac1 and Cdc42 Signaling. *J. Cell Biol.* **2010**, *188* (4), 547–563. https://doi.org/10.1083/jcb.200908086.

(215) Dausend, J.; Musyanovych, A.; Dass, M.; Walther, P.; Schrezenmeier, H.; Landfester, K.; Mailänder, V. Uptake Mechanism of Oppositely Charged Fluorescent Nanoparticles in Hela Cells. *Macromol. Biosci.* **2008**, *8* (12), 1135–1143. https://doi.org/10.1002/mabi.200800123.

(216) Fernando, L. P.; Kandel, P. K.; Yu, J.; McNeill, J.; Ackroyd, P. C.; Christensen, K. A. Mechanism of Cellular Uptake of Highly Fluorescent Conjugated Polymer Nanoparticles. *Biomacromolecules* **2010**, *11* (10), 2675–2682. https://doi.org/10.1021/bm1007103.

(217) Kjeken, R.; Mousavi, S. A.; Brech, A.; Griffiths, G.; Berg, T. Wortmannin-Sensitive Trafficking Steps in the Endocytic Pathway in Rat Liver Endothelial Cells. *Biochem. J.* **2001**, *357* (2), 497. https://doi.org/10.1042/0264-6021:3570497.

(218) van der Hoeven, D.; Cho, K.; Zhou, Y.; Ma, X.; Chen, W.; Naji, A.; Montufar-Solis, D.; Zuo, Y.; Kovar, S. E.; Levental, K. R.; Frost, J. A.; van der Hoeven, R.; Hancock, J. F. Sphingomyelin Metabolism Is a Regulator of K-Ras Function. *Mol. Cell. Biol.* **2017**, *38* (3), 1–17. https://doi.org/10.1128/mcb.00373-17.

(219) Valberg, P. A.; Brain, J. D.; Kane, D. Effects of Colchicine or Cytochalasin B on Pulmonary Macrophage Endocytosis in Vivo. *J. Appl. Physiol. Respir. Environ. Exerc. Physiol.* **1981**, *50* (3), 621–629. https://doi.org/10.1152/jappl.1981.50.3.621.

(220) Zhang, J.; Yu, J.; Jiang, J.; Chen, X.; Sun, Y.; Yang, Z.; Yang, T.; Cai, C.; Zhao, X.; Ding, P. Uptake Pathways of Guandinylated Disulfide Containing Polymers as Nonviral Gene Carrier Delivering DNA to Cells. *J. Cell. Biochem.* **2017**, *118* (4), 903–913. https://doi.org/10.1002/jcb.25769.

(221) Singla, B.; Ghoshal, P.; Lin, H.; Wei, Q.; Dong, Z.; Csányi, G. PKCδ-Mediated Nox2 Activation Promotes Fluid-Phase Pinocytosis of Antigens by Immature

Dendritic Cells. *Front. Immunol.* **2018**, *9* (MAR). https://doi.org/10.3389/fimmu.2018.00537.

(222) Alvarez, C.; Sztul, E. S. Brefeldin A (BFA) Disrupts the Organization of the Micuotubule and the Actin Cytoskeletons. *Eur. J. Cell Biol.* **1999**, *78* (1), 1–14. https://doi.org/10.1016/S0171-9335(99)80002-8.

(223) Cam, A.; Sivaguru, M.; Gonzalez de Mejia, E. Endocytic Mechanism of Internalization of Dietary Peptide Lunasin into Macrophages in Inflammatory Condition Associated with Cardiovascular Disease. *PLoS One* **2013**, *8* (9). https://doi.org/10.1371/journal.pone.0072115.

(224) Hunziker, W.; Andrew Whitney, J.; Mellman, I. Selective Inhibition of Transcytosis by Brefeldin A in MDCK Cells. *Cell* **1991**, *67* (3), 617–627. https://doi.org/10.1016/0092-8674(91)90535-7.

(225) Tokuda, H.; Masuda, S.; Takakura, Y.; Sezaki, H.; Hashida, M. Specific Uptake of Succinylated Proteins Via a Scavenger Receptor-Mediated Mechanism in Cultured Brain Microvessel Endothelial Cells. *Biochem. Biophys. Res. Commun.* **1993**, *196* (1), 18–24. https://doi.org/10.1006/bbrc.1993.2210.

(226) Campbell, F.; Bos, F. L.; Sieber, S.; Arias-Alpizar, G.; Koch, B. E.; Huwyler, J.; Kros, A.; Bussmann, J. Directing Nanoparticle Biodistribution through Evasion and Exploitation of Stab2-Dependent Nanoparticle Uptake. *ACS Nano* **2018**, *12* (3), 2138–2150. https://doi.org/10.1021/acsnano.7b06995.

(227) Jang, S. J.; Ohtani, K.; Fukuoh, A.; Yoshizaki, T.; Fukuda, M.; Motomura, W.; Mori, K.; Fukuzawa, J.; Kitamoto, N.; Yoshida, I.; Suzuki, Y.; Wakamiya, N. Scavenger Receptor Collectin Placenta 1 (CL-P1) Predominantly Mediates Zymosan Phagocytosis by Human Vascular Endothelial Cells. *J. Biol. Chem.* **2009**, *284* (6), 3956–3965. https://doi.org/10.1074/jbc.M807477200.

(228) Jansen, R. W.; Molema, G.; Ching, T. L.; Oosting, R.; Harms, G.; Moolenaar, F.; Hardonk, M. J.; Meijer, D. K. F. Hepatic Endocytosis of Various Types of Mannose-Terminated Albumins: What Is Important, Sugar Recognition, Net Charge, or the Combination of These Features. *J. Biol. Chem.* **1991**, *266* (5), 3343–3348.

(229) Meyer, S. G. E.; Wendt, A. E.; Scherer, M.; Liebisch, G.; Kerkweg, U.; Schmitz, G.; De Groot, H. Myriocin, an Inhibitor of Serine Palmitoyl Transferase, Impairs the Uptake of Transferrin and Low-Density Lipoprotein in Mammalian Cells. *Arch. Biochem. Biophys.* **2012**, *526* (1), 60–68. https://doi.org/10.1016/j.abb.2012.07.006.

(230) Ma, Y.; Jin, J.; Dong, C.; Cheng, E. C.; Lin, H.; Huang, Y.; Qiu, C. High-Efficiency SiRNA-Based Gene Knockdown in Human Embryonic Stem Cells. *Rna* **2010**, *16* (12), 2564–2569. https://doi.org/10.1261/rna.2350710.

(231) Scherer, L. J.; Rossi, J. J. Approaches for the Sequence-Specific Knockdown of MRNA. *Nat. Biotechnol.* **2003**, *21* (12), 1457–1465. https://doi.org/10.1038/nbt915.

(232) Gonzalez, E.; Nagiel, A.; Lin, A. J.; Golan, D. E.; Michel, T. Small Interfering RNA-Mediated down-Regulation of Caveolin-1 Differentially Modulates Signaling Pathways in Endothelial Cells. *J. Biol. Chem.* **2004**, *279* (39), 40659–40669. https://doi.org/10.1074/jbc.M407051200.

(233) Miyawaki-Shimizu, K.; Predescu, D.; Shimizu, J.; Broman, M.; Predescu, S.; Malik, A. B. SiRNA-Induced Caveolin-1 Knockdown in Mice Increases Lung Vascular Permeability via the Junctional Pathway. *Am. J. Physiol. - Lung Cell. Mol. Physiol.* **2006**, *290* (2), 405–413. https://doi.org/10.1152/ajplung.00292.2005.

(234) Hinrichsen, L.; Harborth, J.; Andrees, L.; Weber, K.; Ungewickell, E. J. Effect of Clathrin Heavy Chain- and α-Adaptin-Specific Small Inhibitory RNAs on Endocytic Accessory Proteins and Receptor Trafficking in HeLa Cells. *J. Biol. Chem.* **2003**, *278* (46), 45160–45170. https://doi.org/10.1074/jbc.M307290200.

(235) Maekawa, M.; Terasaka, S.; Mochizuki, Y.; Kawai, K.; Ikeda, Y.; Araki, N.; Skolnik, E. Y.; Taguchi, T.; Arai, H. Sequential Breakdown of 3-Phosphorylated Phosphoinositides Is Essential for the Completion of Macropinocytosis. *Proc. Natl. Acad. Sci. U. S. A.* **2014**, *111* (11). https://doi.org/10.1073/pnas.1311029111.

(236) Razani, B.; Engelman, J. A.; Wang, X. B.; Schubert, W.; Zhang, X. L.; Marks, C. B.; Macalusol, F.; Russell, R. G.; Li, M.; Pestell, R. G.; Di Vizio, D.; Hou, H.; Kneitz, B.; Lagaud, G.; Christ, G. J.; Edelmann, W.; Lisanti, M. P. Caveolin-1 Null Mice Are Viable but Show Evidence of Hyperproliferative and Vascular Abnormalities. *J. Biol. Chem.* **2001**, *276* (41), 38121–38138. https://doi.org/10.1074/jbc.M105408200.

(237) Gao, C.; Li, R.; Huan, J.; Li, W. Caveolin-1 SiRNA Increases the Pulmonary Microvascular and Alveolar Epithelial Permeability in Rats. *J. Trauma - Inj. Infect. Crit. Care* **2011**, *70* (1), 210–219. https://doi.org/10.1097/TA.0b013e3181e7432d.

(238) Tatiparti, K.; Sau, S.; Kashaw, S. K.; Iyer, A. K. SiRNA Delivery Strategies: A Comprehensive Review of Recent Developments. *Nanomaterials* **2017**, *7* (4), 1–17. https://doi.org/10.3390/nano7040077.

(239) Dalby, B. Advanced Transfection with Lipofectamine 2000 Reagent: Primary Neurons, SiRNA, and High-Throughput Applications. *Methods* **2004**, *33* (2), 95–103. https://doi.org/10.1016/j.ymeth.2003.11.023.

(240) Li, D.; Qiu, Z.; Shao, Y.; Chen, Y.; Guan, Y.; Liu, M.; Li, Y.; Gao, N.; Wang, L.; Lu, X.; Zhao, Y.; Liu, M. Heritable Gene Targeting in the Mouse and Rat Using a CRISPR-Cas System. *Nat. Biotechnol.* **2013**, *31* (8), 681–683. https://doi.org/10.1038/nbt.2661.

(241) Betzig, E.; Trautman, J. K. Near-Field Optics: Microscopy, Spectroscopy, and Surface Modification beyond the Diffraction Limit. *Science (80-. ).* **1992**, *257* (5067), 189–195. https://doi.org/10.1126/science.257.5067.189.

(242) Smith, D. J. Ultimate Resolution in the Electron Microscope? *Mater. Today* **2008**, *11* (SUPPL.), 30–38. https://doi.org/10.1016/S1369-7021(09)70005-7.

(243) Titze, B.; Genoud, C. Volume Scanning Electron Microscopy for Imaging Biological Ultrastructure. *Biol. Cell* **2016**, *108* (11), 307–323. https://doi.org/10.1111/boc.201600024.

(244) Lereu, A. L.; Passian, A.; Dumas, P. Near Field Optical Microscopy: A Brief Review. *Int. J. Nanotechnol.* **2012**, *9* (3–7), 488–501. https://doi.org/10.1504/IJNT.2012.045353.

(245) Tam, J.; Merino, D. Stochastic Optical Reconstruction Microscopy (STORM) in Comparison with Stimulated Emission Depletion (STED) and Other Imaging Methods. *J. Neurochem.* **2015**, *135* (4), 643–658. https://doi.org/10.1111/jnc.13257.

(246) Chen, F.; Tillberg, P. W.; Boyden, E. S. Expansion Microscopy. *Science (80-. ).* **2015**, *347* (6221), 543–548. https://doi.org/10.1126/science.1260088.

(247) Zhao, Y.; Bucur, O.; Irshad, H.; Chen, F.; Weins, A.; Stancu, A. L.; Oh, E. Y.; Distasio, M.; Torous, V.; Glass, B.; Stillman, I. E.; Schnitt, S. J.; Beck, A. H.; Boyden, E. S. Nanoscale Imaging of Clinical Specimens Using Pathology-Optimized Expansion Microscopy. *Nat. Biotechnol.* **2017**, *35* (8), 757–764. https://doi.org/10.1038/nbt.3892.

(248) Dewey, C. F.; Bussolari, S. R.; Gimbrone, M. A.; Davies, P. F. The Dynamic Response of Vascular Endothelial Cells to Fluid Shear Stress. *J. Biomech. Eng.* **1981**, *103* (3), 177–185. https://doi.org/10.1115/1.3138276.

(249) Resnick, N.; Yahav, H.; Shay-Salit, A.; Shushy, M.; Schubert, S.; Zilberman, L. C. M.; Wofovitz, E. Fluid Shear Stress and the Vascular Endothelium: For Better and for Worse. *Prog. Biophys. Mol. Biol.* **2003**, *81* (3), 177–199. https://doi.org/10.1016/S0079-6107(02)00052-4.

(250) Samuel, S. P.; Jain, N.; O'Dowd, F.; Paul, T.; Kashanin, D.; Gerard, V. A.; Gun'ko, Y. K.; Prina-Mello, A.; Volkov, Y. Multifactorial Determinants That Govern Nanoparticle Uptake by Human Endothelial Cells under Flow. *Int. J. Nanomedicine* **2012**, *7*, 2943–2956. https://doi.org/10.2147/IJN.S30624.

(251) Brandenberg, N.; Lutolf, M. P. In Situ Patterning of Microfluidic Networks in 3D Cell-Laden Hydrogels. *Adv. Mater.* **2016**, *28* (34), 7450–7456. https://doi.org/10.1002/adma.201601099.

(252) Heintz, K. A.; Bregenzer, M. E.; Mantle, J. L.; Lee, K. H.; West, J. L.; Slater, J. H. Fabrication of 3D Biomimetic Microfluidic Networks in Hydrogels. *Adv. Healthc. Mater.* **2016**, *5* (17), 2153–2160. https://doi.org/10.1002/adhm.201600351.

(253) Fleischer, S.; Tavakol, D. N.; Vunjak-Novakovic, G. From Arteries to Capillaries: Approaches to Engineering Human Vasculature. *Adv. Funct. Mater.* **2020**, 1910811. https://doi.org/10.1002/adfm.201910811.

(254) Pradhan, S.; Banda, O. A.; Farino, C. J.; Sperduto, J. L.; Keller, K. A.; Taitano, R.; Slater, J. H. Biofabrication Strategies and Engineered In Vitro Systems for Vascular Mechanobiology. *Adv. Healthc. Mater.* **2020**, *9* (8), 1901255.

https://doi.org/10.1002/adhm.201901255.

(255) Yang, A. C.; Stevens, M. Y.; Chen, M. B.; Lee, D. P.; Stähli, D.; Gate, D.; Contrepois, K.; Chen, W.; Iram, T.; Zhang, L.; Vest, R. T.; Chaney, A.; Lehallier, B.; Olsson, N.; du Bois, H.; Hsieh, R.; Cropper, H. C.; Berdnik, D.; Li, L.; Wang, E. Y.; Traber, G. M.; Bertozzi, C. R.; Luo, J.; Snyder, M. P.; Elias, J. E.; Quake, S. R.; James, M. L.; Wyss-Coray, T. Physiological Blood–Brain Transport Is Impaired with Age by a Shift in Transcytosis. *Nature* **2020**, 1–6. https://doi.org/10.1038/s41586-020-2453-z.

(256) Moss, J. I.; Barjat, H.; Emmas, S. A.; Strittmatter, N.; Maynard, J.; Goodwin, R. J. A.; Storm, G.; Lammers, T.; Puri, S.; Ashford, M. B.; Barry, S. T. High-Resolution 3D Visualization of Nanomedicine Distribution in Tumors. *Theranostics* **2020**, *10* (2), 880–897. https://doi.org/10.7150/thno.37178.

(257) Tam, A. L.; Melancon, M. P.; Abdelsalam, M.; Figueira, T. A.; Dixon, K.; McWatters, A.; Zhou, M.; Huang, Q.; Mawlawi, O.; Dunner, K.; Li, C.; Gupta, S. Imaging Intratumoral Nanoparticle Uptake after Combining Nanoembolization with Various Ablative Therapies in Hepatic VX2 Rabbit Tumors. *J. Biomed. Nanotechnol.* **2016**, *12* (2), 296–307. https://doi.org/10.1166/jbn.2016.2174.

(258) Sharma, A.; Cornejo, C.; Mihalic, J.; Geyh, A.; Bordelon, D. E.; Korangath, P.; Westphal, F.; Gruettner, C.; Ivkov, R. Physical Characterization and in Vivo Organ Distribution of Coated Iron Oxide Nanoparticles. *Sci. Rep.* **2018**, *8* (1), 1–12. https://doi.org/10.1038/s41598-018-23317-2.

(259) Fukumura, D.; Duda, D. G.; Munn, L. L.; Jain, R. K. Tumor Microvasculature and Microenvironment: Novel Insights Through Intravital Imaging in Pre-Clinical Models. *Microcirculation* **2010**, *17* (3), 206–225. https://doi.org/10.1111/j.1549-8719.2010.00029.x.

(260) Cheng, S. H.; Li, F. C.; Souris, J. S.; Yang, C. S.; Tseng, F. G.; Lee, H. S.; Chen, C. T.; Dong, C. Y.; Lo, L. W. Visualizing Dynamics of Sub-Hepatic Distribution of Nanoparticles Using Intravital Multiphoton Fluorescence Microscopy. *ACS Nano* **2012**, *6* (5), 4122–4131. https://doi.org/10.1021/nn300558p.

(261) Richardson, D. S.; Lichtman, J. W. Clarifying Tissue Clearing. *Cell* **2015**, *162* (2), 246–257. https://doi.org/10.1016/j.cell.2015.06.067.

(262) Sindhwani, S.; Syed, A. M.; Wilhelm, S.; Glancy, D. R.; Chen, Y. Y.; Dobosz, M.; Chan, W. C. W. Three-Dimensional Optical Mapping of Nanoparticle Distribution in Intact Tissues. *ACS Nano* **2016**, *10* (5), 5468–5478. https://doi.org/10.1021/acsnano.6b01879.

(263) Syed, A. M.; MacMillan, P.; Ngai, J.; Wilhelm, S.; Sindhwani, S.; Kingston, B. R.; Wu, J. L. Y.; Llano-Suárez, P.; Lin, Z. P.; Ouyang, B.; Kahiel, Z.; Gadde, S.; Chan, W. C. W. Liposome Imaging in Optically Cleared Tissues. *Nano Lett.* **2020**, *20* (2), 1362–1369. https://doi.org/10.1021/acs.nanolett.9b04853.

(264) Sindhwani, S.; Syed, A. M.; Wilhelm, S.; Chan, W. C. W. Exploring Passive Clearing for 3D Optical Imaging of Nanoparticles in Intact Tissues. *Bioconjug.*

*Chem.* **2017**, *28* (1), 253–259. https://doi.org/10.1021/acs.bioconjchem.6b00500.

(265) Syed, A. M.; Sindhwani, S.; Wilhelm, S.; Kingston, B. R.; Lee, D. S. W.; Gommerman, J. L.; Chan, W. C. W. Three-Dimensional Imaging of Transparent Tissues via Metal Nanoparticle Labeling. *J. Am. Chem. Soc.* **2017**, *139* (29), 9961–9971. https://doi.org/10.1021/jacs.7b04022.

(266) Cai, R.; Pan, C.; Ghasemigharagoz, A.; Todorov, M. I.; Förstera, B.; Zhao, S.; Bhatia, H. S.; Parra-Damas, A.; Mrowka, L.; Theodorou, D.; Rempfler, M.; Xavier, A. L. R.; Kress, B. T.; Benakis, C.; Steinke, H.; Liebscher, S.; Bechmann, I.; Liesz, A.; Menze, B.; Kerschensteiner, M.; Nedergaard, M.; Ertürk, A. Panoptic Imaging of Transparent Mice Reveals Whole-Body Neuronal Projections and Skull–Meninges Connections. *Nat. Neurosci.* **2019**, *22* (2), 317–327. https://doi.org/10.1038/s41593-018-0301-3.

(267) Power, R. M.; Huisken, J. A Guide to Light-Sheet Fluorescence Microscopy for Multiscale Imaging. *Nat. Methods* **2017**, *14* (4), 360–373. https://doi.org/10.1038/nmeth.4224.

(268) Li, R.; Ng, T. S. C.; Garlin, M. A.; Weissleder, R.; Miller, M. A. Understanding the In Vivo Fate of Advanced Materials by Imaging. **2020**, *1910369*, 1–42. https://doi.org/10.1002/adfm.201910369.

(269) Todorov, M. I.; Paetzold, J. C.; Schoppe, O.; Tetteh, G.; Shit, S.; Efremov, V.; Todorov-Völgyi, K.; Düring, M.; Dichgans, M.; Piraud, M.; Menze, B.; Ertürk, A. Machine Learning Analysis of Whole Mouse Brain Vasculature. *Nat. Methods* **2020**, *17* (April). https://doi.org/10.1038/s41592-020-0792-1.

(270) Stephan, M. T.; Moon, J. J.; Um, S. H.; Bersthteyn, A.; Irvine, D. J. Therapeutic Cell Engineering with Surface-Conjugated Synthetic Nanoparticles. *Nat. Med.* **2010**, *16* (9), 1035–1041. https://doi.org/10.1038/nm.2198.

(271) Hua, S.; de Matos, M. B. C.; Metselaar, J. M.; Storm, G. Current Trends and Challenges in the Clinical Translation of Nanoparticulate Nanomedicines: Pathways for Translational Development and Commercialization. *Front. Pharmacol.* **2018**, *9* (JUL), 1–14. https://doi.org/10.3389/fphar.2018.00790.

(272) Kumari, S.; Mg, S.; Mayor, S. Endocytosis Unplugged: Multiple Ways to Enter the Cell. *Cell Res.* **2010**, *20* (3), 256–275. https://doi.org/10.1038/cr.2010.19.

(273) Rennick, J. J.; Johnston, A. P. R.; Parton, R. G. Key Principles and Methods for Studying the Endocytosis of Biological and Nanoparticle Therapeutics. *Nat. Nanotechnol.* **2021**, *16* (3), 266–276. https://doi.org/10.1038/s41565-021-00858-8.

(274) Malatesta, M. Transmission Electron Microscopy as a Powerful Tool to Investigate the Interaction of Nanoparticles with Subcellular Structures. *Int. J. Mol. Sci.* **2021**, *22* (23). https://doi.org/10.3390/ijms222312789.

(275) Egerton, R. F.; Watanabe, M. Spatial Resolution in Transmission Electron Microscopy. *Micron* **2022**, *160* (May), 103304.

https://doi.org/10.1016/j.micron.2022.103304.

(276) Harris, K. M.; Perry, E.; Bourne, J.; Feinberg, M.; Ostroff, L.; Hurlburt, J. Uniform Serial Sectioning for Transmission Electron Microscopy. *J. Neurosci.* **2006**, *26* (47), 12101–12103. https://doi.org/10.1523/JNEUROSCI.3994-06.2006.

(277) Jonkman, J.; Brown, C. M.; Wright, G. D.; Anderson, K. I.; North, A. J. Tutorial: Guidance for Quantitative Confocal Microscopy. *Nat. Protoc.* **2020**, *15* (5), 1585–1611. https://doi.org/10.1038/s41596-020-0313-9.

(278) Jackson, W.; Yamada, M.; Moninger, T.; Grose, C. Visualization and Quantitation of Abundant Macroautophagy in Virus-Infected Cells by Confocal Three-Dimensional Fluorescence Imaging. *J. Virol. Methods* **2013**, *193* (1), 244–250. https://doi.org/10.1016/j.jviromet.2013.06.018.

(279) Galbraith, C. G.; Galbraith, J. A. Super-Resolution Microscopy at a Glance. *J. Cell Sci.* **2011**, *124* (10), 1607–1611. https://doi.org/10.1242/jcs.080085.

(280) M'Saad, O.; Bewersdorf, J. Light Microscopy of Proteins in Their Ultrastructural Context. *Nat. Commun.* **2020**, *11* (1), 3850. https://doi.org/10.1038/s41467-020-17523-8.

(281) Sousa De Almeida, M.; Susnik, E.; Drasler, B.; Taladriz-Blanco, P.; Petri-Fink, A.; Rothen-Rutishauser, B. Understanding Nanoparticle Endocytosis to Improve Targeting Strategies in Nanomedicine. *Chem. Soc. Rev.* **2021**, *50* (9), 5397–5434. https://doi.org/10.1039/d0cs01127d.

(282) Xiao, Y.; Xu, W.; Komohara, Y.; Fujiwara, Y.; Hirose, H.; Futaki, S.; Niidome, T. Effect of Surface Modifications on Cellular Uptake of Gold Nanorods in Human Primary Cells and Established Cell Lines. *ACS Omega* **2020**, *5* (50), 32744–32752. https://doi.org/10.1021/acsomega.0c05162.

(283) Rodriguez-Lorenzo, L.; Fytianos, K.; Blank, F.; von Garnier, C.; Rothen-Rutishauser, B.; Petri-Fink, A. Fluorescence-Encoded Gold Nanoparticles: Library Design and Modulation of Cellular Uptake into Dendritic Cells. *Small* **2014**, *10* (7), 1341–1350. https://doi.org/10.1002/smll.201302889.

(284) Cauzzo, J.; Nystad, M.; Holsæter, A. M.; Basnet, P.; Škalko-Basnet, N. Following the Fate of Dye-Containing Liposomes in Vitro. *Int. J. Mol. Sci.* **2020**, *21* (14), 1–17. https://doi.org/10.3390/ijms21144847.

(285) Mettenbrink, E. M.; Yang, W.; Wilhelm, S. Bioimaging with Upconversion Nanoparticles. *Adv. Photonics Res.* **2022**, *3* (12), 2200098. https://doi.org/10.1002/adpr.202200098.

(286) Wang, F.; Chen, B.; Yan, B.; Yin, Y.; Hu, L.; Liang, Y.; Song, M.; Jiang, G. Scattered Light Imaging Enables Real-Time Monitoring of Label-Free Nanoparticles and Fluorescent Biomolecules in Live Cells. *J. Am. Chem. Soc.* **2019**, *141* (36), 14043–14047. https://doi.org/10.1021/jacs.9b05894.

(287) Tillberg, P. W.; Chen, F.; Piatkevich, K. D.; Zhao, Y.; Yu, C. C.; English, B. P.; Gao, L.; Martorell, A.; Suk, H. J.; Yoshida, F.; Degennaro, E. M.; Roossien, D. H.;

Gong, G.; Seneviratne, U.; Tannenbaum, S. R.; Desimone, R.; Cai, D.; Boyden, E. S. Protein-Retention Expansion Microscopy of Cells and Tissues Labeled Using Standard Fluorescent Proteins and Antibodies. *Nat. Biotechnol.* **2016**, *34* (9), 987–992. https://doi.org/10.1038/nbt.3625.

(288) Truckenbrodt, S.; Maidorn, M.; Crzan, D.; Wildhagen, H.; Kabatas, S.; Rizzoli, S. O. X10 Expansion Microscopy Enables 25-nm Resolution on Conventional Microscopes. *EMBO Rep.* **2018**, *19* (9), 1–12. https://doi.org/10.15252/embr.201845836.

(289) Damstra, H. G.; Mohar, B.; Eddison, M.; Akhmanova, A.; Kapitein, L. C.; Tillberg, P. W. Visualizing Cellular and Tissue Ultrastructure Using Ten-Fold Robust Expansion Microscopy (TREx). *Elife* **2022**, *11*, 1–52. https://doi.org/10.7554/eLife.73775.

(290) Chang, J. B.; Chen, F.; Yoon, Y. G.; Jung, E. E.; Babcock, H.; Kang, J. S.; Asano, S.; Suk, H. J.; Pak, N.; Tillberg, P. W.; Wassie, A. T.; Cai, D.; Boyden, E. S. Iterative Expansion Microscopy. *Nat. Methods* **2017**, *14* (6), 593–599. https://doi.org/10.1038/nmeth.4261.

(291) Nakamoto, M. L.; Forró, C.; Zhang, W.; Tsai, C.; Cui, B. Expansion Microscopy for Imaging the Cell–Material Interface. *ACS Nano* **2022**. https://doi.org/10.1021/acsnano.1c11015.

(292) Sim, J.; Park, C. E.; Cho, I.; Min, K.; Lee, J.-S.; Chong, Y.; Kim, J.; Kang, J. S.; Piatkevich, K. D.; Jung, E. E.; Kwon, S.-K.; Yoon, Y.-G.; Boyden, E. S.; Chang, J.-B. Nanoscale Resolution Imaging of the Whole Mouse Embryos and Larval Zebrafish Using Expansion Microscopy. *bioRxiv*. 2022. https://doi.org/10.1101/2021.05.18.443629.

(293) Sheth, V.; Wang, L.; Bhattacharya, R.; Mukherjee, P.; Wilhelm, S. Strategies for Delivering Nanoparticles across Tumor Blood Vessels. *Adv. Funct. Mater.* **2020**, *2007363*, 1–20. https://doi.org/10.1002/adfm.202007363.

(294) Asano, S. M.; Gao, R.; Wassie, A. T.; Tillberg, P. W.; Chen, F.; Boyden, E. S. Expansion Microscopy: Protocols for Imaging Proteins and RNA in Cells and Tissues. *Curr. Protoc. Cell Biol.* **2018**, *80* (1), 1–41. https://doi.org/10.1002/cpcb.56.

(295) Alberts, B.; Johnson, A.; Lewis, J.; Raff, M.; Roberts, K.; Walter, P. *Molecular Biology of the Cell (4th Ed)*; 2002; Vol. 37. https://doi.org/10.1080/00219266.2002.9655847.

(296) Foroozandeh, P.; Aziz, A. A. Insight into Cellular Uptake and Intracellular Trafficking of Nanoparticles. *Nanoscale Res. Lett.* **2018**, *13*. https://doi.org/10.1186/s11671-018-2728-6.

(297) Chithrani, B. D.; Ghazani, A. A.; Chan, W. C. W. Determining the Size and Shape Dependence of Gold Nanoparticle Uptake into Mammalian Cells. *Nano Lett.* **2006**, *6* (4), 662–668. https://doi.org/10.1021/nl052396o.

(298) Perrault, S. D.; Chan, W. C. W. Synthesis and Surface Modification of Highly Monodispersed, Spherical Gold Nanoparticles of 50-200 Nm. *J. Am. Chem. Soc.* **2009**, *131* (47), 17042–17043. https://doi.org/10.1021/ja907069u.

(299) Frickenstein, A. N.; Mukherjee, S.; Harcourt, T.; He, Y.; Sheth, V.; Wang, L.; Malik, Z.; Wilhelm, S. Quantification of Monodisperse and Biocompatible Gold Nanoparticles by Single-Particle ICP-MS. *Anal. Bioanal. Chem.* **2023**, No. 0123456789. https://doi.org/10.1007/s00216-023-04540-x.

(300) Yang, W.; Frickenstein, A. N.; Sheth, V.; Holden, A.; Mettenbrink, E. M.; Wang, L.; Woodward, A. A.; Joo, B. S.; Butterfield, S. K.; Donahue, N. D.; Green, D. E.; Thomas, A. G.; Harcourt, T.; Young, H.; Tang, M.; Malik, Z. A.; Harrison, R. G.; Mukherjee, P.; DeAngelis, P. L.; Wilhelm, S. Controlling Nanoparticle Uptake in Innate Immune Cells with Heparosan Polysaccharides. *Nano Lett.* **2022**. https://doi.org/10.1021/acs.nanolett.2c02226.

(301) Yang, W.; Wang, L.; Fang, M.; Sheth, V.; Zhang, Y.; Holden, A. M.; Donahue, N. D.; Green, D. E.; Frickenstein, A. N.; Mettenbrink, E. M.; Schwemley, T. A.; Francek, E. R.; Haddad, M.; Hossen, M. N.; Mukherjee, S.; Wu, S.; DeAngelis, P. L.; Wilhelm, S. Nanoparticle Surface Engineering with Heparosan Polysaccharide Reduces Serum Protein Adsorption and Enhances Cellular Uptake. *Nano Lett.* **2022**, *22* (5), 2103–2111. https://doi.org/10.1021/acs.nanolett.2c00349.

(302) Green, T. A. Gold Etching for Microfabrication. *Gold Bull.* **2014**, *47* (3), 205–216. https://doi.org/10.1007/s13404-014-0143-z.

(303) Demchenko, A. P. Photobleaching of Organic Fluorophores: Quantitative Characterization, Mechanisms, Protection. *Methods Appl. Fluoresc.* **2020**, *8* (2). https://doi.org/10.1088/2050-6120/ab7365.

(304) Ho, L. W. C.; Chan, C. K. W.; Han, R.; Lau, Y. F. Y.; Li, H.; Ho, Y.; Zhuang, X.; Choi, C. H. J. Mammalian Cells Exocytose Alkylated Gold Nanoparticles via Extracellular Vesicles. *ACS Nano* **2022**, acsnano.1c07418. https://doi.org/10.1021/acsnano.1c07418.

(305) Sheykhzadeh, S.; Luo, M.; Peng, B.; White, J.; Abdalla, Y.; Tang, T.; Mäkilä, E.; Voelcker, N. H.; Tong, W. Y. Transferrin-Targeted Porous Silicon Nanoparticles Reduce Glioblastoma Cell Migration across Tight Extracellular Space. *Sci. Rep.* **2020**, *10* (1), 1–16. https://doi.org/10.1038/s41598-020-59146-5.

(306) Poon, W.; Zhang, Y. N.; Ouyang, B.; Kingston, B. R.; Wu, J. L. Y.; Wilhelm, S.; Chan, W. C. W. Elimination Pathways of Nanoparticles. *ACS Nano* **2019**, *13* (5), 5785–5798. https://doi.org/10.1021/acsnano.9b01383.

(307) Checa, M.; Millan-Solsona, R.; Mares, A. G.; Pujals, S.; Gomila, G. Fast Label-Free Nanoscale Composition Mapping of Eukaryotic Cells Via Scanning Dielectric Force Volume Microscopy and Machine Learning. *Small Methods* **2021**, *5* (7). https://doi.org/10.1002/smtd.202100279.

(308) Cox, D.; Lee, D. J.; Dale, B. M.; Calafat, J.; Greenberg, S. A Rab11-Containing Rapidly Recycling Compartment in Macrophages That Promotes Phagocytosis.

*Proc. Natl. Acad. Sci. U. S. A.* **2000**, *97* (2), 680–685. https://doi.org/10.1073/pnas.97.2.680.

(309) Sherry, D. M.; Stiles, M. A. Improved Fluorescent Signal in Expansion Microscopy Using Fluorescent Fab Fragment Secondary Antibodies. *MethodsX* **2022**, *9* (June), 101796. https://doi.org/10.1016/j.mex.2022.101796.

(310) Kong, D.; Loncarek, J. Analyzing Centrioles and Cilia by Expansion Microscopy. *Methods in Molecular Biology*. 2021, pp 249–263. https://doi.org/10.1007/978-1-0716-1538-6_18.

(311) Innes, E.; Yiu, H. H. P.; McLean, P.; Brown, W.; Boyles, M. Simulated Biological Fluids–a Systematic Review of Their Biological Relevance and Use in Relation to Inhalation Toxicology of Particles and Fibres. *Crit. Rev. Toxicol.* **2021**, *51* (3), 217–248. https://doi.org/10.1080/10408444.2021.1903386.

(312) Donahue, N. D.; Sheth, V.; Frickenstein, A. N.; Holden, A.; Kanapilly, S.; Stephan, C.; Wilhelm, S. Absolute Quantification of Nanoparticle Interactions with Individual Human B Cells by Single Cell Mass Spectrometry. *Nano Lett.* **2022**, *22* (10), 4192–4199. https://doi.org/10.1021/acs.nanolett.2c01037.

(313) Donahue, N. D.; Kanapilly, S.; Stephan, C.; Marlin, M. C.; Francek, E. R.; Haddad, M.; Guthridge, J.; Wilhelm, S. Quantifying Chemical Composition and Reaction Kinetics of Individual Colloidally Dispersed Nanoparticles. *Nano Lett.* **2022**, *22* (1), 294–301. https://doi.org/10.1021/acs.nanolett.1c03752.

(314) Stephan, T.; Roesch, A.; Riedel, D.; Jakobs, S. Live-Cell STED Nanoscopy of Mitochondrial Cristae. *Sci. Rep.* **2019**, *9* (1), 1–6. https://doi.org/10.1038/s41598-019-48838-2.

(315) Huff, J. The Airyscan Detector from ZEISS: Confocal Imaging with Improved Signal-to-Noise Ratio and Super-Resolution. *Nat. Methods* **2015**, *12* (12), ii. https://doi.org/10.1038/NMETH.F.388.

(316) Bolaños, K.; Kogan, M. J.; Araya, E. Capping Gold Nanoparticles with Albumin to Improve Their Biomedical Properties. *Int. J. Nanomedicine* **2019**, *14*, 6387–6406. https://doi.org/10.2147/IJN.S210992.

(317) Bukackova, M.; Rusnok, P.; Marsalek, R. Mathematical Methods in the Calculation of the Zeta Potential of BSA. *J. Solution Chem.* **2018**, *47* (12), 1942–1952. https://doi.org/10.1007/s10953-018-0830-0.

(318) Connor, E. E.; Mwamuka, J.; Gole, A.; Murphy, C. J.; Wyatt, M. D. Gold Nanoparticles Are Taken up by Human Cells but Do Not Cause Acute Cytotoxicity. *Small* **2005**, *1* (3), 325–327. https://doi.org/10.1002/smll.200400093.

(319) Reifarth, M.; Hoeppener, S.; Schubert, U. S. Uptake and Intracellular Fate of Engineered Nanoparticles in Mammalian Cells: Capabilities and Limitations of Transmission Electron Microscopy-Polymer-Based Nanoparticles. *Adv. Mater.* **2018**, *30* (9), 1703704. https://doi.org/10.1002/adma.201703704.

(320) Sheth, V.; Chen, X.; Mettenbrink, E. M.; Yang, W.; Jones, M. A.; M'Saad, O.;

Thomas, A. G.; Newport, R. S.; Francek, E.; Wang, L.; Frickenstein, A. N.; Donahue, N. D.; Holden, A.; Mjema, N. F.; Green, D. E.; DeAngelis, P. L.; Bewersdorf, J.; Wilhelm, S. Quantifying Intracellular Nanoparticle Distributions with Three-Dimensional Super-Resolution Microscopy. *ACS Nano* **2023**, *17* (9), 8376–8392. https://doi.org/10.1021/acsnano.2c12808.

(321) Klębowski, B.; Depciuch, J.; Parlińska-Wojtan, M.; Baran, J. Applications of Noble Metal-Based Nanoparticles in Medicine. *Int. J. Mol. Sci.* **2018**, *19* (12), 4031. https://doi.org/10.3390/ijms19124031.

(322) Zhang, R.; Kiessling, F.; Lammers, T.; Pallares, R. M. Clinical Translation of Gold Nanoparticles. *Drug Deliv. Transl. Res.* **2023**, *13* (2), 378–385. https://doi.org/10.1007/s13346-022-01232-4.

(323) Giri, P. M.; Banerjee, A.; Layek, B. A Recent Review on Cancer Nanomedicine. *Cancers (Basel).* **2023**, *15* (8). https://doi.org/10.3390/cancers15082256.

(324) Sun, D.; Zhou, S.; Gao, W. What Went Wrong with Anticancer Nanomedicine Design and How to Make It Right. *ACS Nano* **2020**, *14* (10), 12281–12290. https://doi.org/10.1021/acsnano.9b09713.

(325) Klimas, A.; Gallagher, B. R.; Wijesekara, P.; Fekir, S.; DiBernardo, E. F.; Cheng, Z.; Stolz, D. B.; Cambi, F.; Watkins, S. C.; Brody, S. L.; Horani, A.; Barth, A. L.; Moore, C. I.; Ren, X.; Zhao, Y. Magnify Is a Universal Molecular Anchoring Strategy for Expansion Microscopy. *Nat. Biotechnol.* **2023**. https://doi.org/10.1038/s41587-022-01546-1.

(326) Fulton, M. D.; Najahi-Missaoui, W. Liposomes in Cancer Therapy: How Did We Start and Where Are We Now. *Int. J. Mol. Sci.* **2023**, *24* (7). https://doi.org/10.3390/ijms24076615.

(327) Kashkanova, A. D.; Blessing, M.; Gemeinhardt, A.; Soulat, D.; Sandoghdar, V. Precision Size and Refractive Index Analysis of Weakly Scattering Nanoparticles in Polydispersions. *Nat. Methods* **2022**, *19* (5), 586–593. https://doi.org/10.1038/s41592-022-01460-z.

(328) Baczewska, M.; Eder, K.; Ketelhut, S.; Kemper, B.; Kujawińska, M. Refractive Index Changes of Cells and Cellular Compartments Upon Paraformaldehyde Fixation Acquired by Tomographic Phase Microscopy. *Cytom. Part A* **2021**, *99* (4), 388–398. https://doi.org/10.1002/cyto.a.24229.

(329) Donahue, N. D.; Vance, E. A.; Sheth, V.; Francek, E. R.; Wilhelm, S. Synthesis, Characterization, and Acute Cytotoxicity Evaluation of Chloroquine Encapsulating Liposomes. *Micro* **2023**, *3* (1), 51–59. https://doi.org/10.3390/micro3010005.

(330) Khan, D. R.; Rezler, E. M.; Lauer-Fields, J.; Fields, G. B. Effects of Drug Hydrophobicity on Liposomal Stability. *Chem. Biol. Drug Des.* **2008**, *71* (1), 3–7. https://doi.org/10.1111/j.1747-0285.2007.00610.x.

(331) Li, H.; Warden, A. R.; He, J.; Shen, G.; Ding, X. Expansion Microscopy with Ninefold Swelling (NIFS) Hydrogel Permits Cellular Ultrastructure Imaging on

Conventional Microscope. *Sci. Adv.* **2022**, *8* (18), 1–11. https://doi.org/10.1126/sciadv.abm4006.

(332) Shah, S.; Chandra, A.; Kaur, A.; Sabnis, N.; Lacko, A.; Gryczynski, Z.; Fudala, R.; Gryczynski, I. Fluorescence Properties of Doxorubicin in PBS Buffer and PVA Films. *J. Photochem. Photobiol. B Biol.* **2017**, *170* (4), 65–69. https://doi.org/10.1016/j.jphotobiol.2017.03.024.

(333) Sritharan, S.; Sivalingam, N. A Comprehensive Review on Time-Tested Anticancer Drug Doxorubicin. *Life Sci.* **2021**, *278*, 119527. https://doi.org/10.1016/j.lfs.2021.119527.

(334) Yang, Y.; Bajaj, N.; Xu, P.; Ohn, K.; Tsifansky, M. D.; Yeo, Y. Development of Highly Porous Large PLGA Microparticles for Pulmonary Drug Delivery. *Biomaterials* **2009**, *30* (10), 1947–1953. https://doi.org/10.1016/j.biomaterials.2008.12.044.

(335) Baas, S.; Saggiomo, V. Ender3 3D Printer Kit Transformed into Open, Programmable Syringe Pump Set. *HardwareX* **2021**, *10*, e00219. https://doi.org/10.1016/j.ohx.2021.e00219.

(336) Evers, M. J. W.; Kulkarni, J. A.; van der Meel, R.; Cullis, P. R.; Vader, P.; Schiffelers, R. M. State-of-the-Art Design and Rapid-Mixing Production Techniques of Lipid Nanoparticles for Nucleic Acid Delivery. *Small Methods* **2018**, *2* (9), 1–20. https://doi.org/10.1002/SMTD.201700375.

(337) Woo, S. W.; Jo, Y. K.; Yoo, Y. E.; Kim, S. K. High-Throughput Synthesis of Liposome Using an Injection-Molded Plastic Micro-Fluidic Device. *Micromachines* **2021**, *12* (2). https://doi.org/10.3390/mi12020170.

(338) Adhikari, H. S.; Yadav, P. N. Anticancer Activity of Chitosan, Chitosan Derivatives, and Their Mechanism of Action. *Int. J. Biomater.* **2018**, *2018*, 1–29. https://doi.org/10.1155/2018/2952085.

(339) Huang, Y. Z.; Gao, J. Q.; Liang, W. Q.; Nakagawa, S. Preparation and Characterization of Liposomes Encapsulating Chitosan Nanoparticles. *Biol. Pharm. Bull.* **2005**, *28* (2), 387–390. https://doi.org/10.1248/bpb.28.387.

(340) Michalczyk, M.; Humeniuk, E.; Adamczuk, G.; Korga-Plewko, A. Hyaluronic Acid as a Modern Approach in Anticancer Therapy-Review. *Int. J. Mol. Sci.* **2023**, *24* (1). https://doi.org/10.3390/ijms24010103.

(341) Vázquez-González, M. L.; Calpena, A. C.; Domènech, Ò.; Montero, M. T.; Borrell, J. H. Enhanced Topical Delivery of Hyaluronic Acid Encapsulated in Liposomes: A Surface-Dependent Phenomenon. *Colloids Surfaces B Biointerfaces* **2015**, *134*, 31–39. https://doi.org/10.1016/j.colsurfb.2015.06.029.

(342) Liu, P.; Chen, G.; Zhang, J. A Review of Liposomes as a Drug Delivery System: Current Status of Approved Products, Regulatory Environments, and Future Perspectives. *Molecules* **2022**, *27* (4), 1372. https://doi.org/10.3390/molecules27041372.

(343) Yefimova, S. L.; Kurilchenko, I. Y.; Tkacheva, T. N.; Rozhkov, V. A.; Sorokin, A. V.; Lukianova, N. Y.; Bezdenezhnykh, N. A.; Malyukin, Y. V.; Chekhun, V. F. Comparative Study of Dye-Loaded Liposome Accumulation in Sensitive and Resistant Human Breast Cancer Cells. *Exp. Oncol.* **2012**, *34* (2), 101–106.

(344) Oude Blenke, E.; Klaasse, G.; Merten, H.; Plückthun, A.; Mastrobattista, E.; Martin, N. I. Liposome Functionalization with Copper-Free “Click Chemistry.” *J. Control. Release* **2015**, *202*, 14–20. https://doi.org/10.1016/j.jconrel.2015.01.027.

(345) Qaddoumi, M. G.; Gukasyan, H. J.; Davda, J.; Labhasetwar, V.; Kim, K. J.; Lee, V. H. L. Clathrin and Caveolin-1 Expression in Primary Pigmented Rabbit Conjunctival Epithelial Cells: Role in PLGA Nanoparticle Endocytosis. *Mol. Vis.* **2003**, *9* (May 2014), 559–568.

(346) Truckenbrodt, S. Expansion Microscopy: Super-Resolution Imaging with Hydrogels. *Anal. Chem.* **2023**, *95* (1), 3–32. https://doi.org/10.1021/acs.analchem.2c04921.

(347) Denisin, A. K.; Pruitt, B. L. Tuning the Range of Polyacrylamide Gel Stiffness for Mechanobiology Applications. *ACS Appl. Mater. Interfaces* **2016**, *8* (34), 21893–21902. https://doi.org/10.1021/acsami.5b09344.

(348) Papadopulos, F.; Spinelli, M.; Valente, S.; Foroni, L.; Orrico, C.; Alviano, F.; Pasquinelli, G. Common Tasks in Microscopic and Ultrastructural Image Analysis Using ImageJ. *Ultrastruct. Pathol.* **2007**, *31* (6), 401–407. https://doi.org/10.1080/01913120701719189.

(349) Kannan, K. S.; Manoj, K.; Arumugam, S. Labeling Methods for Identifying Outliers. *Int. J. Stat. Syst.* **2015**, No. October.

(350) Otsu, N. A Threshold Selection Method from Gray-Level Histograms. *IEEE Trans. Syst. Man. Cybern.* **1979**, *9* (1), 62–66. https://doi.org/10.1109/TSMC.1979.4310076.

## Appendix A: Abbreviations

- AuNP: Gold Nanoparticle
- AgNP: Silver Nanoparticle
- DLS: Dynamic Light Scattering
- PDI: Polydispersity Index
- UV-Vis: Ultraviolet-Visible Spectrophotometry
- PEG: Poly (ethylene glycol)
- HEP: Heparosan
- BSA: Bovine Serum Albumin
- CLSM: Confocal Laser Scanning Microscope
- ExM: Expansion Microscopy
- proExM: Protein Retention Expansion Microscopy
- TEM: Transmission Electron Microscopy
- ICP-MS: Inductively Coupled Plasma Mass Spectrometry
- SP-ICP-MS: Single-Particle Inductively Coupled Plasma Mass Spectrometry
- SDS-PAGE: Sodium Dodecyl Sulfate-Polyacrylamide Gel Electrophoresis
- DSPC: 1,2-Distearoyl-sn-glycero-3-phosphocholine
- DSPE: 1,2-Distearoyl-sn-glycero-3-phosphoethanolamine
- Ptd thioethanol:1,2-Dipalmitoyl-sn-glycero-3-phosphothioethanol
- DiO: 3,3-Dioctadecyloxacarbocyanine perchlorate

## Appendix B: Materials and Methods

### Materials

Hydrochloric acid (HCl) (Sigma-Aldrich, 320331); Nitric acid ($HNO_3$) (Sigma-Aldrich, 438073); Gold(III) chloride trihydrate (Sigma-Aldrich, 520918); Sodium citrate tribasic dihydrate (Sigma-Aldrich, S4641); Hydroquinone (Sigma-Aldrich, H9003); TWEEN® 20 (Sigma-Aldrich, P9416); mPEG-OPSS, MW 10,000 (Laysan Bio Inc., MPEG-OPSS-10K-1g); $NH_2$-PEG-Thiol, MW 5,000 (Laysan Bio Inc., NH2-PEG-SH-5000-1g); Streptavidin - 60nm Silver Conjugate (SC-60-04-05, Cytodiagnostics); Streptavidin - 40nm Silver Conjugate (SC-40-04, Cytodiagnostics); Sodium tetrathionate dihydrate (Fisher Scientific, AC461920250); Cy5 NHS Ester (Click Chemistry Tools, 1076); NAP™-25 20 ST (Sigma-Aldrich, GE17-0852-01); 10X PBS Solution (Bio Basic, PD8117); 4T1, Mammary Tumor Mouse Cells (ATCC, CRL-2539); RAW 264.7 Mouse Macrophages (ATCC, TIB-71); DC 2.4 Mouse Dendritic Cells (Sigma Aldrich, SCC142M); DMEM, high glucose, pyruvate (Thermo Fisher, 11995065); RPMI-1640 Medium (ATCC, 30-2001); Fetal Bovine Serum (Thermo Fisher, 16000044); Penicillin Streptomycin (Thermo Fisher, 15-140-122); Trypsin-EDTA (Thermo Fisher, 25200072); Paraformaldehyde Solution (PFA), 4% in PBS (Thermo Fisher, J19943K2); Triton™ X-100 (Sigma-Aldrich, T8787); Bovine Serum Albumin (BSA) (Sigma-Aldrich, A7906); Transferrin From Human Serum, Tetramethylrhodamine Conjugate (TRITC transferrin) (Thermo Fisher, T2872); Wheat germ agglutinin (WGA), CF488A conjugate (Biotium, 29022-1); NucBlue™ Fixed Cell ReadyProbes™ Reagent (DAPI) (Thermo Fisher, R37606); NucBlue™ Live ReadyProbes™ Reagent (Hoechst 33342) (Thermo Fisher, R37605); Acryloyl-X, SE, 6-((acryloyl)amino)hexanoic Acid, Succinimidyl Ester (Thermo Fisher, A20770); Sodium Acrylate (Sigma-Aldrich, 408220); N,N′-Methylenebisacrylamide (Bis) (Sigma-Aldrich,

M7279); Acrylamide Solution, 40% (Sigma-Aldrich, A4058); N,N′-(1,2-Dihydroxyethylene)bisacrylamide (DHEBA) (Sigma-Aldrich, 294381); Sodium Bicarbonate (Sigma-Aldrich, S6014); Sodium Hydroxide (Sigma-Aldrich, 221465); Sulfuric Acid (VWR, JT9681); Hydrogen Peroxide (Sigma-Aldrich, 216763); Gelatin from Bovine Skin Type B (Sigma-Aldrich, G9391); Paraformaldehyde 16% Solution, EM Grade (Electron Microscopy Sciences, 15710-S); Glutaraldehyde (Electron Microscopy Sciences, 16020); Sodium Borohydride (Sigma-Aldrich, 213462); Glycine (Sigma-Aldrich, 50046); Sodium Dodecyl Sulfate (SDS) (Fisher Scientific, AC230421000); Dimethyl Sulfoxide (DMSO) (Sigma-Aldrich, D2650); AF555Dye NHS Ester (Click Chemistry Tools, 1341); Sodium Chloride (Sigma-Aldrich, S7653); Ammonium Persulfate (APS) (Sigma-Aldrich, A36378); N,N,N′,N′-Tetramethylethylenediamine (TEMED) (Sigma-Aldrich, T7024); Proteinase K (New England Biolabs, P8107S); Ethylenediaminetetraacetic acid (EDTA) (Sigma-Aldrich, EDS); Guanidine hydrochloride (Sigma-Aldrich, G3272); Tris (Thermo Fisher, AM9855); NuPAGE LDS Sample Buffer (4X) (Thermo Fisher, NP0007); 4-12% Bis-Tris Protein Gels, 1.0 mm, 12-well (Thermo Fisher, NP0322BOX); NuPAGE MOPS SDS Running Buffer (20X) (Thermo Fisher, NP0001); SYPRO Tangerine Protein Gel Stain (Thermo Fisher, S12010); PageRuler Plus Prestained 10 250kDa Protein Ladder (Thermo Fisher, PI26619); Dithiothreitol (DTT) (Fisher Scientific, FERR0861); Acetic acid (Sigma Aldrich, 695092); Sodium phosphate dibasic (Sigma Aldrich, 795410); Gold Etchant (Sigma-Aldrich, 651842); Gold Standard 1000 µg/mL (High Purity Standards, 100021-2); Iridium Standard 1000 µg/mL (High Purity Standards, 100025-2); 0.22 µm Syringe Filter (Sigma, SLGP033NB); LoBind Microcentrifuge Tubes (Sigma-Aldrich, Z666491); 18 mm Round Coverslips #1 (VWR, 16004-300); #1.5H Glass Bottom

Dishes (Fisher Scientific, 50-305-807); 12-Well Cell Culture Plate (VWR, 10062-894); 6-Well Cell Culture Plate (VWR, 10062-892); Cell Scrapers (Fisher, 08-100-241); TEM Grid, Carbon Type-B, 300 Mesh, Copper (Ted Pella, 01813-F); Uranyl Acetate (Ted Pella, 19481); Lead Citrate, UranyLess EM Stain (Electron Microscopy Sciences, 22409); Sodium Tartrate Dibasic Dihydrate (Sigma-Aldrich, 71994); Sodium DL-Lactate (Sigma-Aldrich, 71720); Sodium Pyruvate (Sigma-Aldrich, P5280); Calcium Chloride Dihydrate (Sigma-Aldrich, C3306); Magnesium Chloride (Sigma-Aldrich, M8266); Sodium Sulfate (Sigma-Aldrich, 239313); Citric Acid (Fisher Scientific, MK-0627-500); Potassium Persulfate (Sigma-Aldrich, 379824); Methacrolein, 95% (Sigma-Aldrich, 133035); N,N-Dimethylacrylamide (DMAA) (Sigma-Aldrich, 274135); Urea (Sigma-Aldrich, U5378); Doxoves PEGylated Liposomal Doxorubicin HCl (Fisher Scientific, NC1488582); Amicon Ultra-4 Centrifugal Filters-100,000 NMWL (Sigma-Aldrich, UFC810096); 1,2-distearoyl-sn-glycero-3-phosphocholine DSPC (Avanti Polar Lipids, 850365P-1g); Cholesterol (Avanti Polar Lipids, 700000-BULK); DiOC18(3) (3,3'-Dioctadecyloxacarbocyanine Perchlorate) (DiO) (Fisher Scientific, D275); mPEG-DSPE, MW 2,000 (Laysan Bio, MPEG-DSPE-2000-1g); 1,2-Dipalmitoyl-sn-Glycero-3-Phosphothioethanol (Ptd thioethanol) (Avanti Polar Lipids, 870160P-100mg); Dextran, Alexa Fluor 488, 10,000 MW, anionic, fixable (Thermo Fisher, D22910); Spectra/Por™ 2 12-14 kD MWCO Standard RC Dry Dialysis Kits (Fisher Scientific, 08-801-243); Agarose (Fisher, BP160-500); Tris-Borate-EDTA Buffer (TBE) (Fisher Scientific, BP1333-1); Ficoll 400 (Polysucrose 400) (Fisher Scientific, 50-488-658)

## Methods

### Gold Nanoparticle (AuNP) Synthesis and PEGylation

Fifty-five nm citrate-coated gold nanoparticles (AuNPs) were synthesized using previously reported methods.[154,298] A 250-mL reaction flask and magnetic stir bar were cleaned using an aqua regia solution made from 37 % HCl and 70% $HNO_3$ and in a 3:1 ratio (v/v) for 15 minutes and then thoroughly washed with deionized water. Next, 98.9 g of ultrapure $H_2O$ (18.2 MΩ,) was added to the flask along with 1 mL of 30 mg/mL sodium citrate tribasic dihydrate and was brought to a boil on a hotplate set to 300°C and stirring at 200 rpm. One hundred µL of 250 mM of gold (III) chloride solution ($HAuCl_4$) was added to the flask and stirring was increased to 400 rpm for 7 minutes to produce 14-nm AuNPs seeds. Flasks were then cooled and the hydrodynamic diameter and polydispersity index (PDI) of the AuNPs were measured using the Malvern Zetasizer Nano ZS dynamic light scattering (DLS). Gold nanoparticles with a polydispersity index (PDI) >0.1 were discarded. The concentrations of the AuNPs were calculated using absorbance readings from an Agilent Cary 5000 UV-Vis-NIR (UV-Vis) spectrophotometer.

Subsequently, 55-nm AuNPs were synthesized via seed-mediated growth using the 14-nm AuNPs.[154,180] In short, 95.63 mL of ultrapure $H_2O$, 0.986 mL of 25-mM HAuCl4, 0.986 mL of 15-mM sodium citrate tribasic, 1.41 mL of 2.5-nM of 14-nm AuNPs, and 0.986 mL of 25-mM hydroquinone were added to a clean flask at room temperature (RT) and stirred at 400 rpm overnight. The DLS and UV-Vis spectrophotometry measurements were taken, and then 1 mL of 10% (v/v) Tween 20 was added to the flask and stirred. The AuNPs were then concentrated by centrifugation at 2,000 xg (RCF, relative centrifugal force) for 2 hours at 4°C. The supernatants were removed, and the nanoparticles were

resuspended in a solution of 0.01% (v/v) Tween 20 and 0.01% (w/v) sodium citrate tribasic dihydrate (Tween-citrate) and were then centrifuged at 2,000 xg for 30 minutes at 4°C and resuspended in Tween-citrate three times. The citrate-coated AuNPs were coated with 10-kDa MW methoxy-polyethylene glycol-OPSS (mPEG-OPSS) to surface area saturation for 30 minutes at RT. Surface saturation was defined as the point of increasing PEG molecules/$nm^2$ of AuNP surface area at which the increase of the hydrodynamic diameter of the AuNPs plateaus, as measured by DLS.[154] Excess PEG was removed by centrifugation at 2,200 xg for 30 minutes at 4°C and resuspended in 0.05% (v/v) Tween 20 in PBS three times.

To synthesize Cy5-PEG, first a solution of 100 mg/mL 5-kDa amine-PEG-thiol ($NH_2$-PEG-SH) in 0.1 M of sodium bicarbonate was oxidized in 0.5 molar equivalents of sodium tetrathionate for 1 hour, as described by Dai et al.[36] The solution was dialyzed with a Pierce Minidialysis unit with a molecular weight cutoff of 3.5 kDa for 1 hour with gentle stirring on a stir plate at RT. The pH of the solution was then adjusted to 8.0 using sodium bicarbonate, and 0.5 mg of Cy5-NHS ester was added to solution and vortexed for 3 hours. DTT (100 molar equivalents) was added to the solution and incubated for 1 hour. The solution was passed through a NAP-25 column equilibrated with 0.1 M sodium bicarbonate (pH 8.0), and excess dye was removed using a 3.5-kDa molecular weight (mW) dialysis membrane overnight at 4°C against deionized $H_2O$. Cy5-AuNPs were formed by coating Cy5-PEG onto the 55-nm citrate-coated AuNPs at a density of 0.5 Cy5-PEG/ $nm^2$ of NP surface area for 30 minutes, with centrifugations to remove excess PEG as previously described. The Cy5-AuNPs were then coated to surface area saturation

with 10-kDa mPEG-OPSS similarly to the citrate-coated AuNPs. Fluorescence emission spectra were measured using a Horiba PTI Quantamaster Spectrofluorometer.

Heparosan-coated 55-nm gold nanoparticles (HEP-AuNPs) were synthesized through a pH reduction method as described by Yang *et al*.[300,301] Briefly, 13-kDa HEP-OPSS was mixed with dilute HCl solution with a pH of 3.0. The solution was then mixed with citrate-coated AuNPs and was incubated at room temperature (RT) for 5 minutes. Saline was then added to the solution to a final concentration of 0.3 M and was incubated at RT for 20 minutes. More NaCl was then added to the solution to a final concentration to 0.7 M. Excess HEP and NaCl were removed by centrifugation at 2,300 xg for 30 minutes at 4°C and resuspension in 0.05% (v/v) Tween 20 in PBS thrice.

Bovine serum albumin-coated 55-nm gold nanoparticles (BSA-AuNPs) were made through a direct incubation of the Tween 20 and citrate-coated AuNPs in a 10-mg/mL solution of BSA in 1X PBS for 1 hour at 37°C. Excess BSA was removed by centrifugation at 2,300 xg for 30 minutes with pellet resuspension in 1X PBS thrice.

**Liposome Synthesis**

A commercially available Ender3 3D printer was converted into three individual syringe pumps based on instructions described by Saggiomo *et al*.[335] Organic components (lipids and 0.044 mg/mL DiO as necessary) dissolved in 100% ethanol were filled in a 1 mL syringe while 32 mg of 10 kDa dextran-AF488 in 1X PBS at 7 times the volume of the organic components was filled in a 10 mL syringe. These syringes were connected to a T-mixer by PEEK tubing and were pushed by the syringe pumps at a flow rate ratio of 7 (aqueous: organic). Liposomes that were made with Ptd thioethanol were

HEPylated by mixing with HEP-OPSS at a 1:1 molar ratio of Ptd thioethanol to HEP-OPSS for 2 hours on a tube rotator. If necessary, dialysis was accomplished by filling the liposome solutions in 12-14 kDa dialysis membranes, and placed in a chilled beaker filled with 1X PBS while stirring overnight. Amicon centrifugal filters (100 kDa nominal molecular weight limit) that were pre-wet with 0.1% (w/v) BSA in 1X PBS by centrifuging at 1500 xg for 15 minutes at 4 C. To remove unencapsulated dextran, liposomes were washed in BSA coated Amicon centrifugal filters at 3000 xg for 30 minutes and resuspended in 1X PBS repeatedly until the total volume reduction factor was >1000X.

**Cell Culture**

The 4T1 cells and RAW 264.7 macrophages were grown in culture media consisting of DMEM supplemented with 10% FBS and 1% penicillin/streptomycin. The DC 2.4 cells were grown in RPMI 1640 supplemented with 10% FBS and 1% penicillin/streptomycin. During passages, 0.25% trypsin-EDTA was used to detach 4T1 and DC 2.4 cells from culture flasks, while cell scrapers were used for the RAW 264.7 cells. Prior to plating cells, 18-mm glass coverslips were cleaned using piranha solution (3:1 (v/v) 95% sulfuric acid: 30% hydrogen peroxide) for 15 minutes before being washed with ultrapure $H_2O$ three times, placed in 12-well plates, and sterilized by UV light in a biosafety hood for 10 minutes. The coverslips were then incubated in 2-mg/mL gelatin for 2 hours and washed with 1X PBS three times. Cells in complete culture media were plated on to the coverslips in 12-well culture plates at a density of 30,000 cells/well and were allowed to adhere overnight. All AuNP incubations with cells were at a concentration of 200 pM AuNP in culture media for 24 hours in 4T1 cells and 3 hours in DC 2.4 cells and RAW 264.7

macrophages, based on previously published work with these conditions.[300,301] All AgNP incubations with RAW 264.7 macrophages were at 1:10 dilutions from the purchased stock concentrations in cell culture media for 24 hours, which would approximately be 28.4 pM for the 40-nm Strep-AgNPs and 8.4 pM for the 60-nm Strep-AgNPs. Doxoves incubations in RAW 264.7 macrophages were done at a drug concentration of 100 µg/mL in complete DMEM for 3 or 12 hours. All other liposomes were first concentrated 4X with Amicon centrifugal filters and diluted 1:10 in complete DMEM before being incubated with RAW 264.7 cells for 3 or 24 hours. Following the incubations, the cells were washed with 1X PBS thrice before fixation and further processing.

**Cell Expansion**

Four X expansion was performed based on the proExM protocol described by Boyden *et al*.[294] Briefly, cell samples grown on 18-mm glass coverslips were fixed with 4% PFA and permeabilized with 0.1% Triton X-100 before being incubated in 3% BSA for 10 minutes and stained with DAPI and WGA CF488A or NHS-AF555. Samples were treated with 100 µL of 0.1 mg/mL Acryloyl-X, SE on strips of parafilm in a humidified chamber for 6 hours. Polyacrylamide monomer solutions were made as 86 mg/mL sodium acrylate, 25 mg/mL acrylamide, 1.5 mg/mL N, Bis, and 117 mg/mL sodium chloride. Active gelation solutions were formed with 470 µL of monomer solution, 10 µL of ultrapure $H_2O$, 10 µL of 10% APS, and 10 µL of TEMED. Immediately following the addition of the APS and TEMED, the active gelation solution was vortexed, and 200 µL of the solution was injected between the samples and a cover slip and was allowed to form a gel for 1 hour. The structural proteins in the cells were digested in 1 mL of a digestion buffer (50 mg/mL Triton X-100,

1 mM EDTA, 50 mM Tris-Cl, 46.7 mg/mL sodium chloride, 8 U/mL proteinase K, pH adjusted to 8.0 with HCl) overnight in a humidified chamber at 55°C. The gels were placed in petri dishes and filled with ultrapure $H_2O$ for expansion. The ultrapure $H_2O$ was aspirated out and replaced after 20 minutes 3-4 times to allow for full gel expansion.

Pan-ExM was performed based on a protocol described by Bewersdorf *et al*.[280] Cells were fixed with a solution of 3% PFA and 0.1% glutaraldehyde in 1X PBS for 15 minutes and then washed 3X with PBS. The samples were quenched with 1 mg/mL sodium borohydride in PBS for 10 minutes and then 100 mM of glycine in 1X PBS for 20 minutes before being washed 3 times with PBS. Samples were then incubated in a solution of 0.7% PFA and 0.1% acrylamide in 1X PBS for 6 hours at 37°C and then washed thrice with 1X PBS. Gel monomer solutions were prepared as 19% (w/v) sodium acrylate, 10% (w/v) acrylamide, and 0.1% (w/v) DHEBA in PBS. Activated gel solutions were prepared with 198 µL of monomer solution with 1 µL of 50% APS and 1 µL of 50% TEMED. 90 µL of active gel solution was injected between the samples and a cover slip, and were allowed to form a gel for 15 minutes at RT and then 1.5 hours at 37°C. Samples were then incubated in a digestion buffer made of 200 mM SDS, 200 mM NaCl, and 50 mM Tris in ultrapure $H_2O$ (pH adjusted to 6.7 with HCl) for 15 minutes at RT and then for 1 hour at 37°C. A small portion of the gels were then expanded in a similar manner as the 4X gels. A portion of the expanded gels were then re-embedded in a neutral hydrogel, with a monomer solution consisting of 10% (w/v) acrylamide and 0.05% (w/v) DHEBA in 1X PBS. Activated gel solutions were made with 2,970 µL of monomer solution, 15 µL of 10% (w/v) APS, and 15 µL of 10% (v/v) TEMED, which the samples are incubated in at RT on an orbital shaker 3 times for 20 minutes each. The samples were then gently

pressed with Kimwipe paper wipes to remove excess solution before being placed between a coverslip and glass slide and placed in a humified chamber. Oxygen was purged from the chamber and replaced with nitrogen, and the sample was incubated for 2 hours at 37°C. The samples were then incubated in a second gel solution, with a monomer solution consisting of 19% (w/v) sodium acrylate, 10% (w/v) acrylamide, and 0.1% (w/v) Bis in 1X PBS. Once again, activated gel solutions were made with 2,970 µL of monomer solution, 15 µL of 10% (w/v) APS, and 15 µL of 10% (v/v) TEMED, which the samples are incubated in on ice on an orbital shaker thrice for 15 minutes each. The steps following the neutral gel embedding until the second gel incubation are repeated for this gel. Following the 2-hour incubation in the nitrogen chamber, samples were incubated in a 200-mM NaOH solution for 1 hour and then washed with 1X PBS thrice for 30 minutes each. Samples were then stained with a 20 µg/mL solution of AF555Dye NHS ester in a 100-mM sodium bicarbonate solution for 1.5 hours on an orbital shaker and were then washed with 1X PBS at least three times for 20 minutes each until the gels were visibly clear. The samples were then expanded in a similar manner to the 4X gels.

Magnify was performed based on a protocol described by Zhao *et al*.[325] Cells were fixed with a solution of 3% PFA and 0.1% glutaraldehyde in 1X PBS for 15 minutes and then washed 3X with PBS. The samples were quenched with 1 mg/mL sodium borohydride in PBS for 10 minutes and then 100 mM of glycine in 1X PBS for 20 minutes before being washed 3 times with PBS. Gel monomer solutions were prepared as 34% (w/v) sodium acrylate, 10% (w/v) acrylamide, 4.16% (v/v) DMAA, 1% (w/v) sodium chloride, 0.01% (w/v) Bis in PBS. Activated gel solutions were prepared with 1 mL of monomer solution with 1 µL of methacrolein, 10 µL of 10% (w/v) TEMED and 50 µL of

5% (w/v) potassium persulfate. 90 µL of active gel solution was injected between the samples and a cover slip and were allowed to form a gel overnight at 37°C in a humidified chamber. Samples were then incubated in 1 mL each of homogenization buffer made of 10% (w/v) SDS, 8 M urea, and 25 mM EDTA in 2X PBS (pH adjusted to 7.5) for 6 hours at 80°C, then washed with 1X PBS thrice for 10 minutes each at RT, and then washed with 1% (v/v) Tween 20 in 1X PBS thrice for 10 minutes each at 60°C. Samples were then stained with a 20 µg/mL solution of NHS ester dye (AF405, AF488, or AF647) in a 100-mM sodium bicarbonate solution for 1.5 hours on an orbital shaker and were then washed with 1X PBS at least three times for 20 minutes each until the gels were visibly clear. The gels were placed in petri dishes and filled with ultrapure $H_2O$ for expansion. The ultrapure $H_2O$ was aspirated out and replaced after 10 minutes 3-4 times to allow for full gel expansion.

**Confocal Microscopy**

To prevent pan-ExM gels from sliding while imaging, they were first placed on a 35-mm #1.5H glass bottom dish. Henkel Duro brand super glue was applied around the bottom edge of the gel and the plate and was allowed to harden for 10-15 minutes. The tops of the gels were lightly washed with ultrapure $H_2O$ to remove any superglue that had crusted over, and a round 18-mm coverglass was placed on top of each gel. Following this, a stiff acrylamide gel, consisting of 18.4% acrylamide and 1.6% $Bis^{347}$, (activated with 1960 µL of monomer solution, 20 µL of 10% APS, and 20 µL of TEMED) was poured over the glass and gels until they are fully submerged. Ultrapure $H_2O$ was then poured over the gels to prevent drying until imaging. To prevent Magnify gels from sliding while imaging,

they were placed on 35-mm #1.5H glass bottom dishes that were coated with 0.1% (w/v) poly-L-lysine in ultrapure $H_2O$.

Fluorescence images were taken on a Zeiss LSM 880 confocal laser scanning microscope (CLSM) on the Zeiss Zen Black software using a 40X water immersion objective (NA=1.20) and a 405-nm diode laser, 488-nm argon laser, 561-nm diode-pumped solid-state laser, a 594-nm helium-neon laser, and a 633-nm helium-neon laser with a main beam splitter (MBS) 488/561/633 filter and photomultiplier tube (PMT) detectors. Transmitted light images were acquired through a 405-nm diode laser through a main beam splitter 488/561/633 filter to the PMT detector (T-PMT). The AuNP signal was acquired using light scattering principles described by Jiang et al.[286] with the 561-nm laser and a MBS T80/R20 filter, using a 1.5-20% laser power for unexpanded and 4X samples, and a 45% laser power for pan-ExM samples. The detector range for light scattering on samples that were not stained with AF55-NHS was 561 +/- 10 nm. For samples that were stained with AF555-NHS, the detector range was 561 +/- 5 nm to reduce crosstalk from the AF555. Airyscan images were acquired using the Airyscan detector on the Zeiss LSM 880 CLSM with a 63X Oil immersion objective (NA=1.40). The standard CLSM images used to compare against the Airyscan images in Figure S3.1 were also taken with 63X Oil immersion objective (NA=1.40).

**Image Analysis**

Cell nuclei cross-sectional areas, whole cell nanoparticle light scattering signal intensities and fluorescence signal intensities were measured on ImageJ.

To confirm the successful adoption of the proExM protocol, we randomly selected CLSM images of 90 non-expanded and expanded cells taken at the z-positions where their nuclei have their largest cross-sectional area. Next, we applied common thresholding methods in ImageJ[348] to measure the cross-sectional areas of the corresponding cell nuclei. The thresholded images were despeckled by erosion operations, which were then corrected by dilation operations. Adjacent nuclei were separated with watershed segmentation. The pixel areas of the thresholded nuclei were measured, which were then converted to units of $\mu m^2$ via the image scale factor. We then calculated the resulting linear expansion factor of ~4.1X using Equation 1,

$$Expansion\ Factor = \sqrt{\frac{\overline{Nuclei\ Area}_{Expanded}}{\overline{Nuclei\ Area}_{Non\text{-}Expanded}}}$$

**Equation 1**

where $\overline{Nuclei\ Area}_{Non\text{-}Expanded}$ and $\overline{Nuclei\ Area}_{Expanded}$ refer to the mean areas of the measured nuclei in non-expanded and expanded cells, respectively. Similar methods were applied to calculate the expansion factors from the pan-ExM and Magnify protocols.

To quantify the increase in image resolution, we applied a grid of equally spaced lines across the images of non-expanded and expanded nuclei and measured the pixel intensities corresponding to a blue-fluorescent DNA stain, DAPI, along these lines (Figure S2a). We counted the peak numbers in the pixel intensity graphs across the line profiles for each analyzed nucleus and divided that count by the total length of the line profiles to determine the number of intensity peaks/μm as an unbiased measurement of resolution. The lengths of the line profiles across expanded nuclei were scaled down by the

previously determined expansion factor of 4.1X for comparison against the non-expanded nuclei.

To randomly select cells for analysis, all the cells on each imaging frame were measured and collectively assigned a number tag from a random number generator. These number tags were then arranged in numerical order, allowing for any number of random cells to be selected from the top of the list. For nanoparticle light scattering and fluorescence signal intensities, the brightness of each channel was first set through the histogram in the Zen Lite software, before individual regions of interest were drawn around the membranes of the cells in ImageJ, and the integrated density was measured for the signals of interest. Outliers were removed based on Tukey's method.[349]

Nanoparticle light scattering signal counting, as well as cell and vesicle volumes for pan-ExM samples, were analyzed with MATLAB. The NHS-AF555 signal was set to appear gray and the light scattering channel was set to appear red, and then Z-stacks were converted from 12-bit images into 8-bit RGB images, having pixel values ranging from 0 to 255, through Zen Lite. Only the R channel was analyzed given that the NHS-AF555 was equivalent to grayscale and the light scattering signal had pixel values of 0 for the G and B channels. For nanoparticle counting, we found and utilized several useful patterns. First, the pixel values of the background areas in controls were equal or smaller than 10. This means that thresholds up to 10 may cause background noise to be counted towards nanoparticle signal counts. To safely filter out the background noise, three times the noise level was used as a reliable threshold (i.e. 30). Second, we observed that each nanoparticle occupied a grid of size 3×3 with the brightest pixel located in the center. Given a nanoparticle, denote the brightest pixel value as P, then the values of the

surrounding eight pixels fell within [1, P]. By considering these two important patterns, our algorithm calculated the number of nanoparticles and the area occupied. The volumes of the cells, as well as the cumulative nanoparticle and vesicle volumes, were approximated by the summation of the areas of each respective category throughout the entire Z-stacks. To delineate cell boundary, Otsu's method[350] was first used to choose an optimal threshold and create a binary image where cell regions are separated from background. This method works by minimizing the intraclass variance of the thresholded cell and background pixels. Then, morphological operations (e.g., dilation, erosion, image opening, etc.) were applied to fill small holes, remove small, isolated regions to obtain a refined cell mask, denoted as M1. In this mask, white pixels represent cell, whereas black pixels are background and vesicles. Most vesicles (black holes) were located inside the mask, and the rest located on the boundary of the mask. We further applied a series of morphological operations to fill out the black holes. This resulted in a much more compact cell mask denoted as M2, and cell area was calculated using this mask. Subtracting M1 from M2 resulted in a map where all vesicle regions were highlighted. Morphological operations were further applied to refine the results and generate a final mask M3 depicting vesicle regions. With the compact cell and vesicle masks, we computed cell and vesicle areas. When calculating the number of red dots areas that fall in vesicle regions, it should be noted that we purposely lowered the red dot threshold to 20. This can more accurately reflect the area of nanoparticles because the area of less bright surrounding pixels is considered instead of only considering the brightest pixels.

**Transmission Electron Microscopy (TEM)**

TEM images of gold nanoparticles were acquired using a JEOL2010F 200-kV field emission analytical transmission electron microscope with a DE-12 camera on copper TEM grids. Negative staining was done with 0.2% uranyl acetate. TEM images of cell samples were acquired using a Hitachi H-7600 Transmission Electron Microscope. Cells were fixed in a solution of 2% (v/v) glutaraldehyde and 4% paraformaldehyde (v/v) in 0.2-M cacodylate buffer at room temperature for 1 hour and were then stored at 4°C until sectioning. Samples were negative stained with a 3% lead citrate solution.

**Agarose gel electrophoresis**

Agarose gel electrophoresis was run based on a protocol described by Yang *et al*.[301] Briefly, agarose was melted in 0.5X TBE buffer to a 0.5% (w/v) concentration, and then casted in a gel tray with a comb. The gel was placed in a gel running tank which was then filled with 0.5X TBE buffer. Samples were mixed with 150 mg/mL Ficoll 400 at a ratio of 2 µL Ficoll per 10 µL of sample. 10 µL of each sample was then loaded into the wells of the gel. The agarose gels were then run at 70 V for AuNPs or 80 V for liposomes for 30-40 minutes. The gel was then rinsed with deionized water, and then imaged on an Azure C600 gel imager.

**Sodium dodecyl sulfate-polyacrylamide gel electrophoresis (SDS-PAGE)**

SDS-PAGE was run based on a protocol described by Yang *et al*.[301] Briefly, samples with 20 $cm^2$ of surface area of citrate-coated and PEGylated AuNPs were incubated in 700 µL of 100% fetal bovine serum (FBS) at 37°C for 16 hours in LoBind tubes (Eppendorf). Control samples were incubated in 1X PBS for PEGylated AuNPs and ultrapure $H_2O$ for

citrate-coated AuNPs for better colloidal stability. The samples were then washed to remove free serum by centrifugation at 2,300 xg for 30 minutes at 4°C and resuspension in 0.05% (v/v) Tween 20 in PBS (0.05% Tween 20 in ultrapure $H_2O$ for citrate-coated control) thrice. After the final centrifugation, the AuNP pellets were resuspended in 8 µL of 4X NuPAGE LDS sample buffer and 4 µL of 500-mM DTT and incubated at 70°C for 1 hour to separate adsorbed proteins from the surface of the AuNPs. The samples were then centrifuged at 18,000 xg for 15 minutes to separate the removed proteins from the residual AuNPs. Supernatants were removed, and their volumes were equalized before the addition of 4 µL of 4X NuPAGE LDS sample buffer and 2 µL of 500-mM DTT and an incubation at 95°C for 5 minutes to completely denature the proteins. Following the denaturation, 20 µL of protein samples and 2 µL of 10-250 kDa protein ladder were loaded onto a 4-12% Bis-Tris protein gel in MOPS SDS running buffer, and were run at 200 V for 50 minutes. The gel was then removed from its encasing and rinsed with deionized water several times. The gel was fixed with 10% (v/v) acetic acid and 40% (v/v) ethanol overnight on an orbital shaker. After rinsing with deionized water, the gel was stained with 50 mL of 1X SYPRO Tangerine in 50-mM sodium phosphate dibasic and 150-mM sodium chloride for 1 hour on an orbital shaker. The gel was then rinsed with deionized water, and then imaged on an Azure C600 gel imager. A similar procedure was done with BSA-AuNPs and free BSA.

**Inductively Coupled Plasma Mass Spectrometry (ICP-MS)**

Gold and iridium 1,000-µg/mL standard solutions were used to create a standard calibration curve for ICP-MS measurements. A 0.5-ppb iridium-acid water solution was

made in 20-mM $HNO_3$ and 60-mM HCl in ultrapure $H_2O$, which is used for serial dilutions of the gold standard to make samples with gold contents of 200 µg/mL, 100 µg/mL, 50 µg/mL, 10 µg/mL, 5 µg/mL, and 1 µg/mL, with a 0 µg/mL sample being pure 0.5-ppb iridium-acid water. 4T1 cells were cultured directly on 12-well culture plates at a density of 100,000 cells/well and were incubated with 200-pM of PEG-AuNPs in complete culture media for 24 hours, or just complete culture media for controls, and were then washed with PBS thrice. RAW 264.7 cells were cultured in similar conditions and incubated with 200-pM of HEP-AuNPs or PEG-AuNPs. Cell standard curves were prepared for both cell lines with samples ranging from $1x10^4$ to $3x10^6$ cells as a basis of intracellular magnesium contents. Solutions from the proExM process were centrifuged at 4,000 xg for 30 minutes to pellet AuNPs, and the supernatants were removed. Samples were then digested with an aqua regia solution composed of 70% $HNO_3$ and 37% HCl in a 4:1 ratio (V/V) for 30 minutes at room temperature. Following digestion, samples were transferred to 1.5-mL tubes and incubated at 60°C for 1 hour. Samples were then cooled and pulsed on a centrifuge before being diluted in a 1:10 or 1:20 ratio in 0.5-ppb iridium solution in ultrapure $H_2O$, without HCl or $HNO_3$. Samples from the proExM process were filtered through 0.22-µm syringe filters. Au197 and Mg24 content measurements were taken with a PerkinElmer NexIon 2000 ICP-MS using the Prepfast IC Sample Introduction system. The gold and cell standard curves were used to calculate the number of AuNPs/cell.

When running residual solutions from proExM through ICP-MS, a significant difference in the detected gold content of cells that were treated with AuNPs compared to untreated controls at the first step, the Acryloyl-X, SE treatment (****$p<0.0001$) was detected (Figure S14b). It is not likely that the gold content that was detected in this step is from intracellular

AuNPs that were removed from the cell in this step, given that this treatment is not a destructive process. It is more likely that the detected gold content was from uninternalized AuNPs that were stuck to the glass coverslip, which had been mechanically dislodged during the Acryloyl-X treatment. The next group that was digested for ICP-MS was the bottom coverslip that the cells had been grown on following the removal of the hydrogel. A significant difference in the detected gold content between the two groups was also detected here (**$p<0.01$). However, it is once again not likely that this difference originated from lost intracellular AuNPs, but rather from cells that were not transferred to the gel, given that the gel would not cover the entire top surface area of the coverslip. Furthermore, small pieces of the gel tend to tear off the top coverslip as it is being separated from the bottom coverslip, resulting in more AuNP-containing cells being measured through ICP-MS at this step. There was not a significant difference in the detected gold content between the two groups ($p>0.99$) in the digestion buffer, the top coverslip after the gels were peeled off, or the combination of the three washes that the gels were expanded in. Given that the digestion buffer and expansion washes are directly involved in the chemical and physical disruption of the mechanical structure of the cells, it would be expected that any intracellular AuNPs that would be lost would be found within those solutions.

To test the colloidal stability of HEP- and PEG-AuNPs in intracellular conditions, the AuNPs were incubated in ultrapure $H_2O$, culture media (DMEM), complete culture media (DMEM +10% FBS + 1% penicillin streptomycin (P/S)), or artificial lysosomal fluid for 3 hours at 37°C. The artificial lysosomal fluid was prepared based on specifications described by Innes et al.[311] Following the incubation, the AuNPs were centrifuged at 2,300

xg for 30 minutes and resuspended in Tween-citrate twice. The AuNPs were then diluted to a concentration of $3x10^{-16}$ M and measured on the PerkinElmer NexION 2000 ICP-MS in single-particle mode.[180,299]

## Appendix C: Supporting Figures and Tables

Table S1. Metallic Nanoparticle Characterization using Dynamic Light Scattering

| Nanoparticle Size (nm) | Material | Surface Modification | Hydrodynamic Diameter (nm)[a] | PDI[b] |
|---|---|---|---|---|
| 14 | Gold | Citrate | 18.0 +/- 0.1 | 0.01 |
| 55 | Gold | Citrate | 63.6 +/- 0.7 | 0.08 |
| 55 | Gold | Citrate, Tween 20 | 76.0 +/- 0.9 | 0.07 |
| 55 | Gold | mPEG(10-kDa)-OPSS | 99.5 +/- 0.1 | 0.06 |
| 55 | Gold | mPEG(5-kDa)-SH | 91.3 +/- 0.4 | 0.05 |
| 55 | Gold | Cy5-PEG(5-kDa)-SH, mPEG(10-kDa)-OPSS | 107.9 +/- 2.9 | 0.05 |
| 55 | Gold | HEP | 133.8 +/- 2.5 | 0.03 |
| 40 | Silver | Streptavidin | 65.3 +/- 1.0 | 0.25 |
| 60 | Silver | Streptavidin | 136.5 +/- 8.5 | 0.22 |
| 55 | Gold | Bovine Serum Albumin | 98.2 +/- 2.0 | 0.10 |

[a] Mean +/- standard deviation, *n*=3

[b] Polydispersity Index

Table S2. Metallic Nanoparticle Characterization via Zeta Potential

| **Nanoparticle Size (nm)** | **Material** | **Surface Modification** | **Zeta Potential (mV)[a]** |
|---|---|---|---|
| 55 | Gold | Citrate, Tween 20 | -21.8 +/- 0.4 |
| 55 | Gold | mPEG(10-kDa)-OPSS | -3.8 +/- 0.1 |
| 55 | Gold | 13 kDa-Heparosan-OPSS | -25.7 +/- 0.6 |
| 55 | Gold | Bovine Serum Albumin | -26.9 +/- 0.4 |
| 40 | Silver | Streptavidin | -18.7 +/- 3.2 |
| 60 | Silver | Streptavidin | -24.3 +/- 1.0 |

[a] Mean +/- standard deviation, *n*=3

Table S3. Liposome Characterization using Dynamic Light Scattering

| **Liposome Type** | **Hydrodynamic Diameter (nm)[a]** | **PDI[b]** |
|---|---|---|
| Doxoves | 86.4 +/- 1.0 | 0.04 |
| 10 kDa Dextran-AF488-PEG-Liposomes (PEG-Liposomes) | 113.4 +/- 3.3 | 0.18 |
| 10 kDa Dextran-AF488-Ptd Thioethanol-Liposomes (Thiol-Liposomes) | 76.9 +/- 0.3 | 0.15 |
| 10 kDa Dextran-AF488-HEP-Liposomes (HEP-Liposomes) | 102.5 +/- 1.5 | 0.15 |
| DiO-Liposomes | 114.2 +/- 4.1 | 0.14 |

[a] Mean +/- standard deviation, *n*=3

[b] Polydispersity Index

Table S4. Liposome Characterization via Zeta Potential

| **Liposome Type** | **Zeta Potential (mV)[a]** |
|---|---|
| Doxoves | -20.8 +/- 1.2 |
| 10 kDa Dextran-AF488-PEG-Liposomes (PEG-Liposomes) | -8.8 +/- 0.8 |
| 10 kDa Dextran-AF488-HEP-Liposomes (HEP-Liposomes) | -33.2 +/- 1.4 |

[a] Mean +/- standard deviation, *n*=3

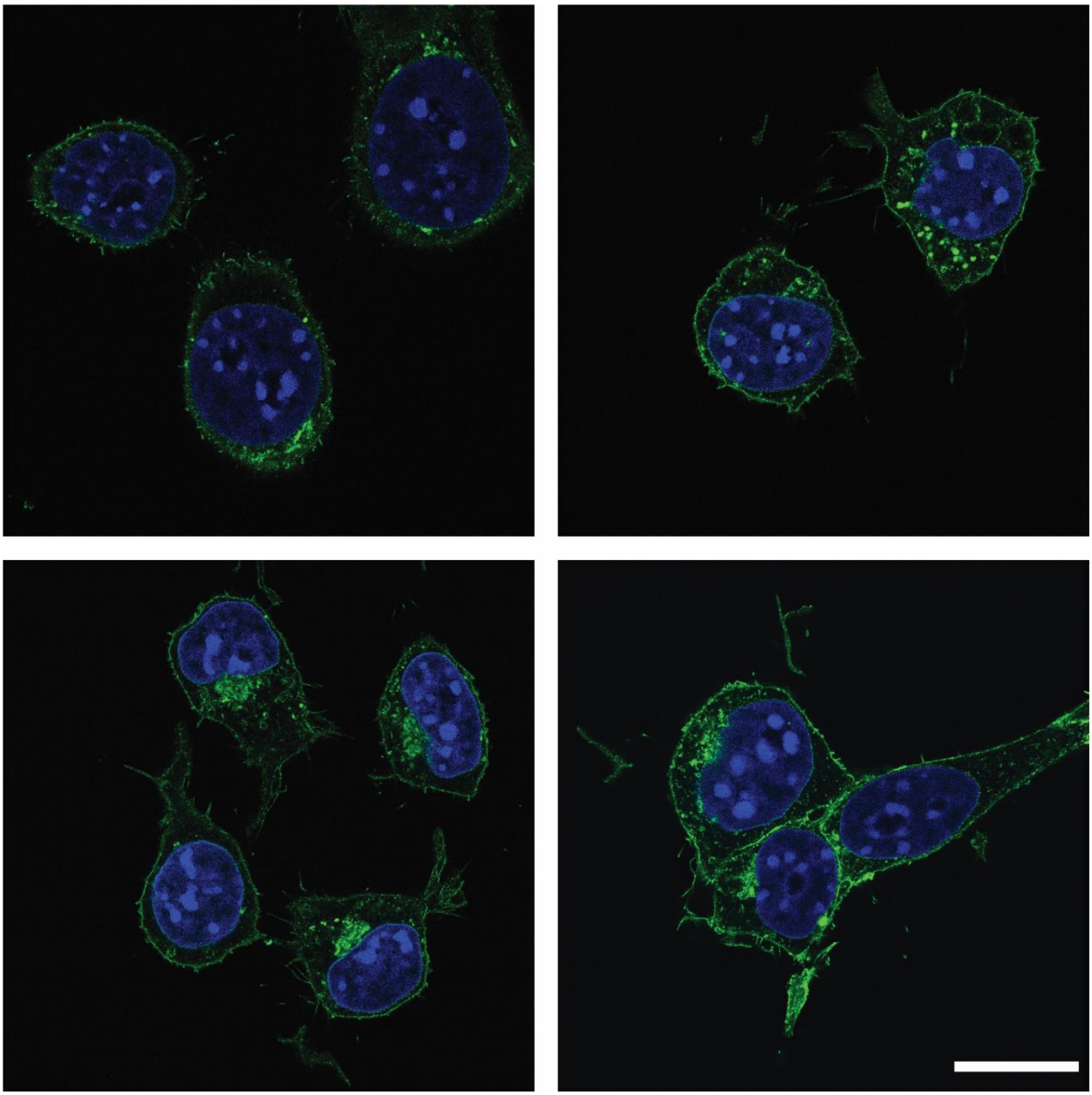

Figure S2.1. Additional images of expanded 4T1 mammary tumor mouse cells. 4T1 cells after expansion were stained with DAPI (blue) for nuclei visualization and WGA-CF488A (green) for cell membrane visualization. Scale bar indicates 50 µm. Scale bars for images of expanded cells are the original length as taken by the microscope (i.e. not corrected for expansion factors).

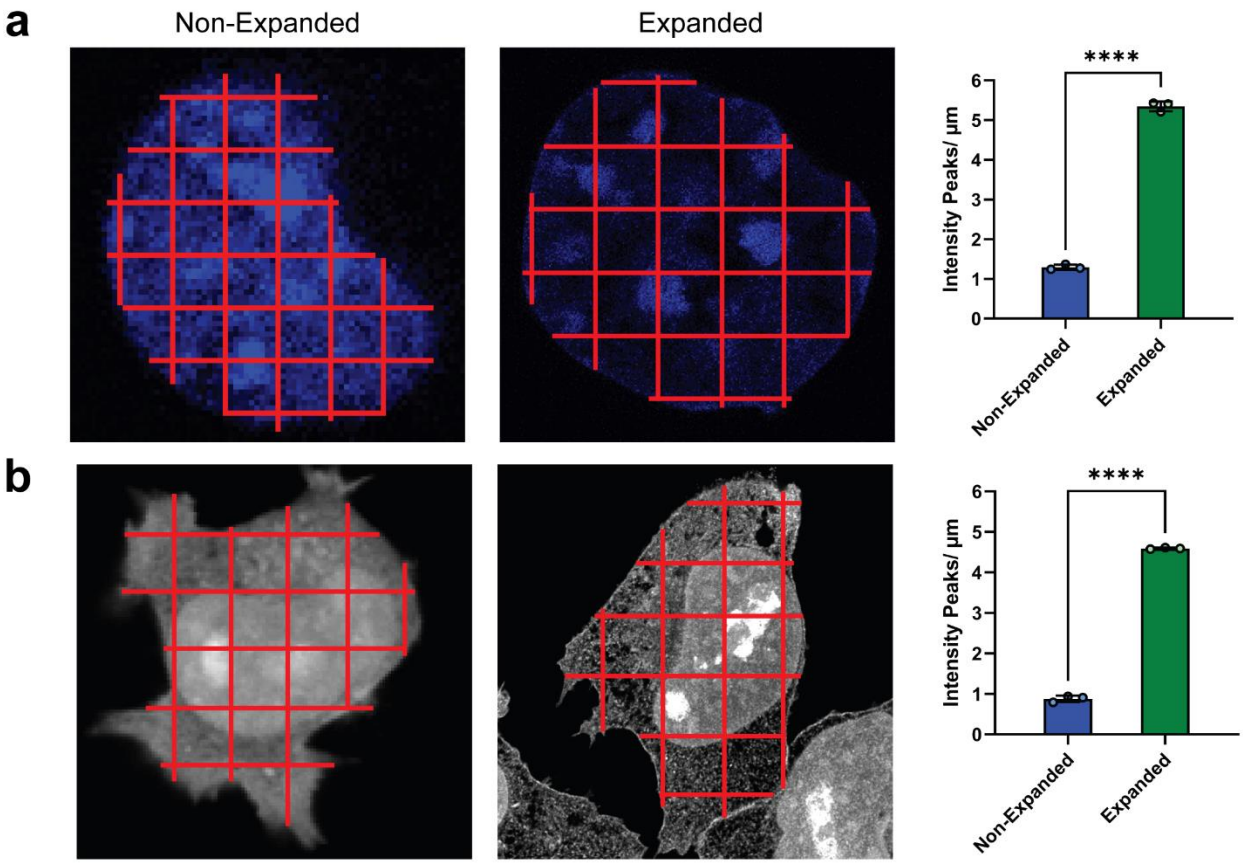


Figure S2.2. Line profiles to analyze the spatial resolution of non-expanded and expanded cells. Line profiles (orange) were drawn in equally spaced grids across cells in ImageJ to measure the signal intensity of the channel being analyzed for the following conditions: **(a)** nuclei stained with DAPI, **(b)** cell proteome stained with NHS-AF55. The number of peaks in the signal intensity was counted for all the line profiles and then divided by the length of the line profile, with the lengths of the line profiles for the expanded cells being scaled down by the expansion factor of 4.1. Bars indicate mean +/- standard deviation (SD). Unpaired one-tailed t-tests demonstrated significant statistical differences in the means of the non-expanded and expanded groups for both stains (****$p<0.0001$) ($n=3$).

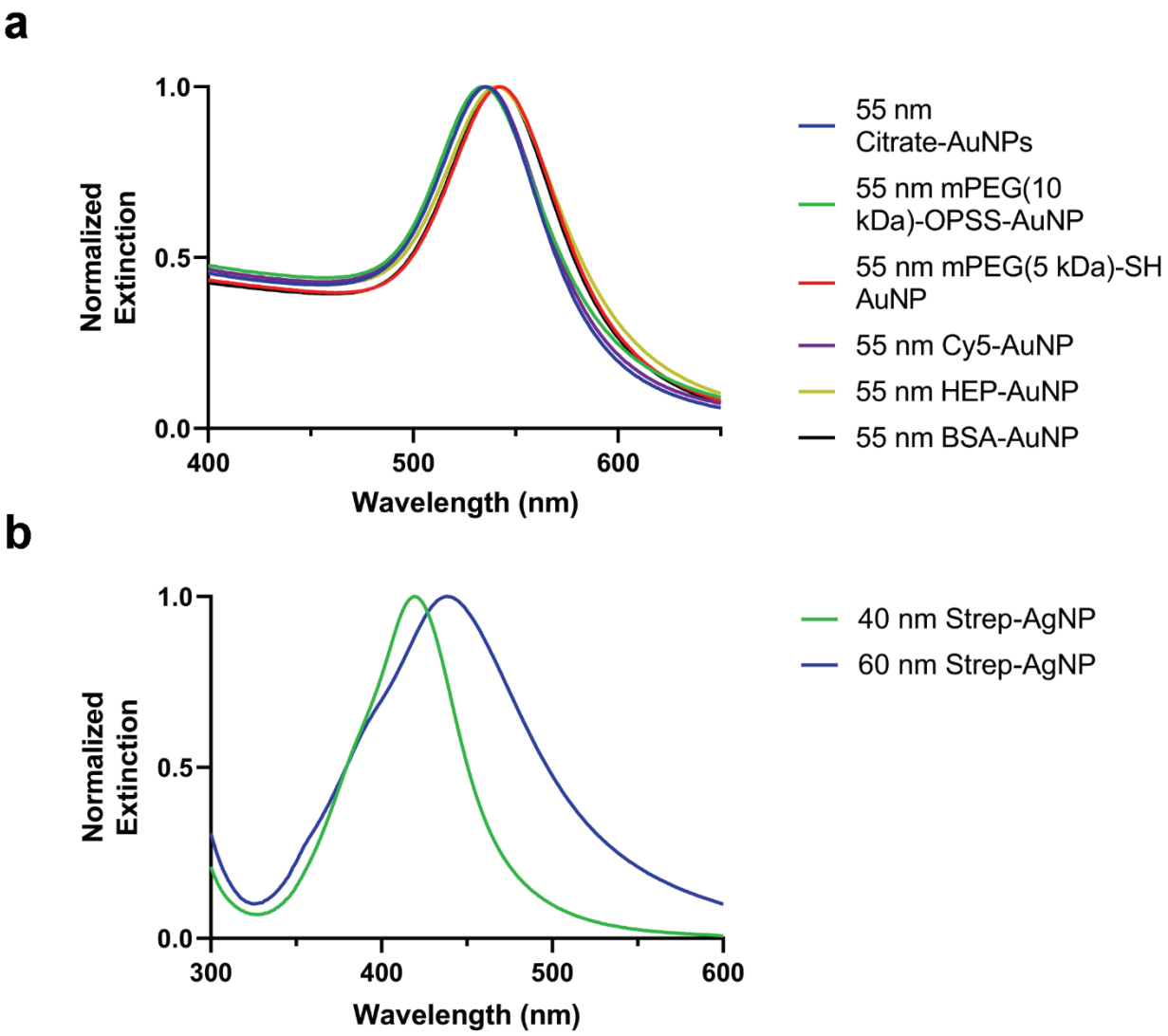


Figure S2.3. UV-Vis spectrophotometry extinction spectra of nanoparticles. Extinction spectra of **(a)** various surface-modified 55-nm AuNPs and **(b)** 40-nm and 60-nm Strep-AgNPs.

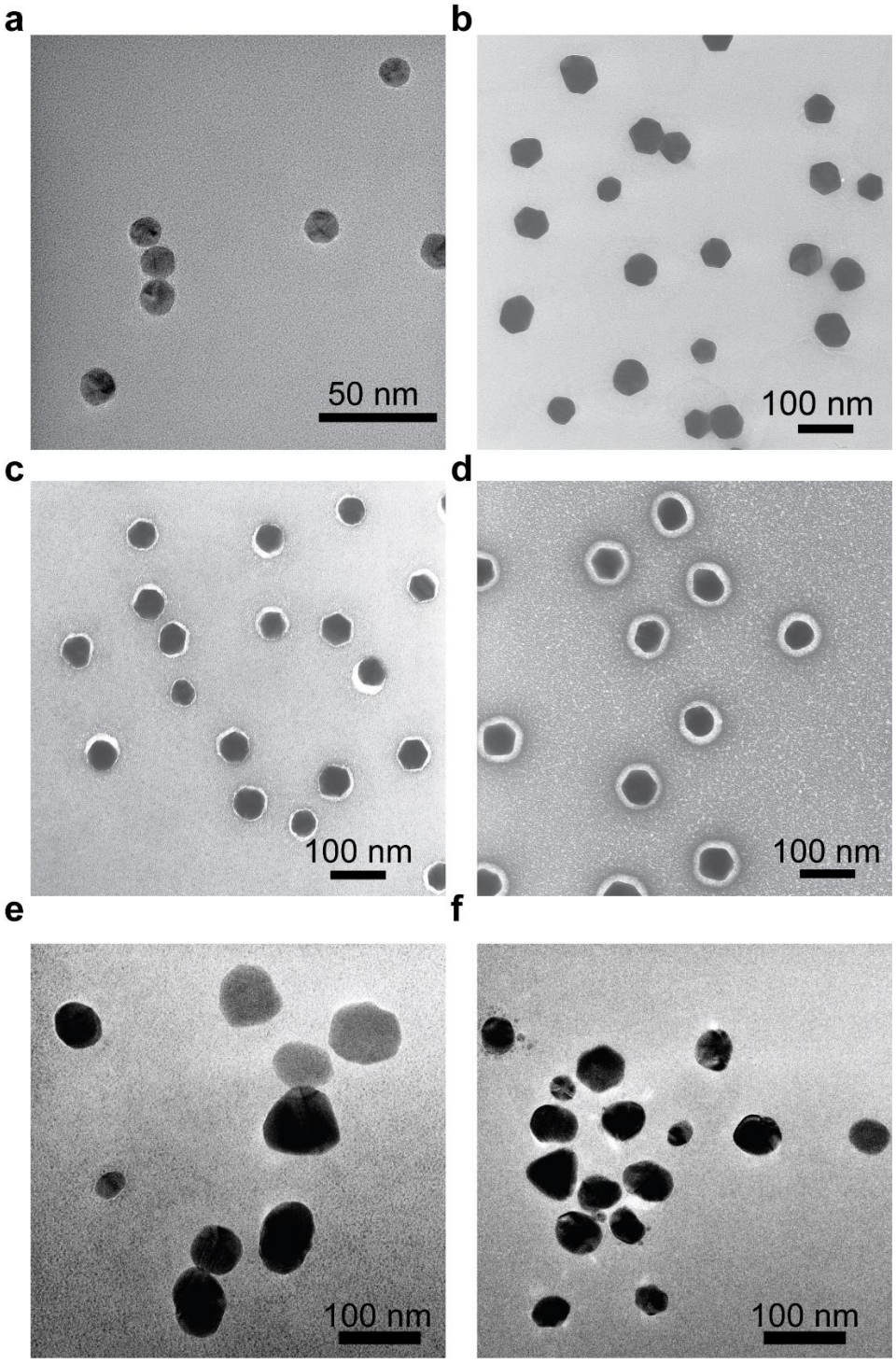


Figure S2.4. Transmission electron micrograph of 14-nm and 55-nm citrate coated AuNPs. **(a)** 14-nm citrate-coated AuNPs, negative stained with uranyl acetate. **(b)** 55-nm citrate-coated AuNPs, without negative staining. **(c)** PEG-AuNPs, negative stained with uranyl acetate. **(d)** HEP-AuNPs, negative stained with uranyl acetate. **(e)** 60-nm Strep-AgNPs, without negative staining. **(f)** 40-nm Strep-AgNPs, without negative staining.

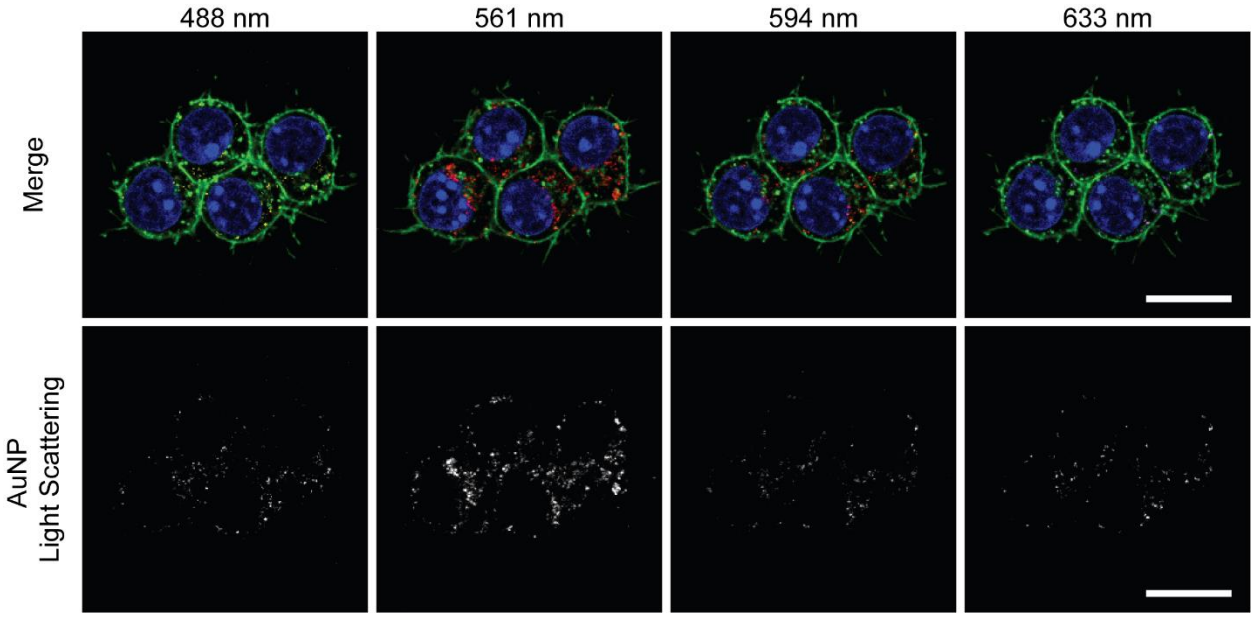


Figure S2.5: AuNP light scattering imaging is compatible with a range of laser wavelengths. RAW 264.7 macrophages were incubated with 55-nm AuNPs coated with 5 kDa mPEG-SH for 3 hours before being washed, fixed, and stained with DAPI (blue) and WGA CF488A (green). AuNPs were visualized with light scattering imaging using a 488-nm argon laser (yellow), a 561-nm diode-pumped solid-state laser (red), a 594-nm helium-neon laser (orange), and a 633-nm helium-neon laser (purple). Grayscale images of the light scattering channels alone are also shown. The scale bars indicate 15 μm.

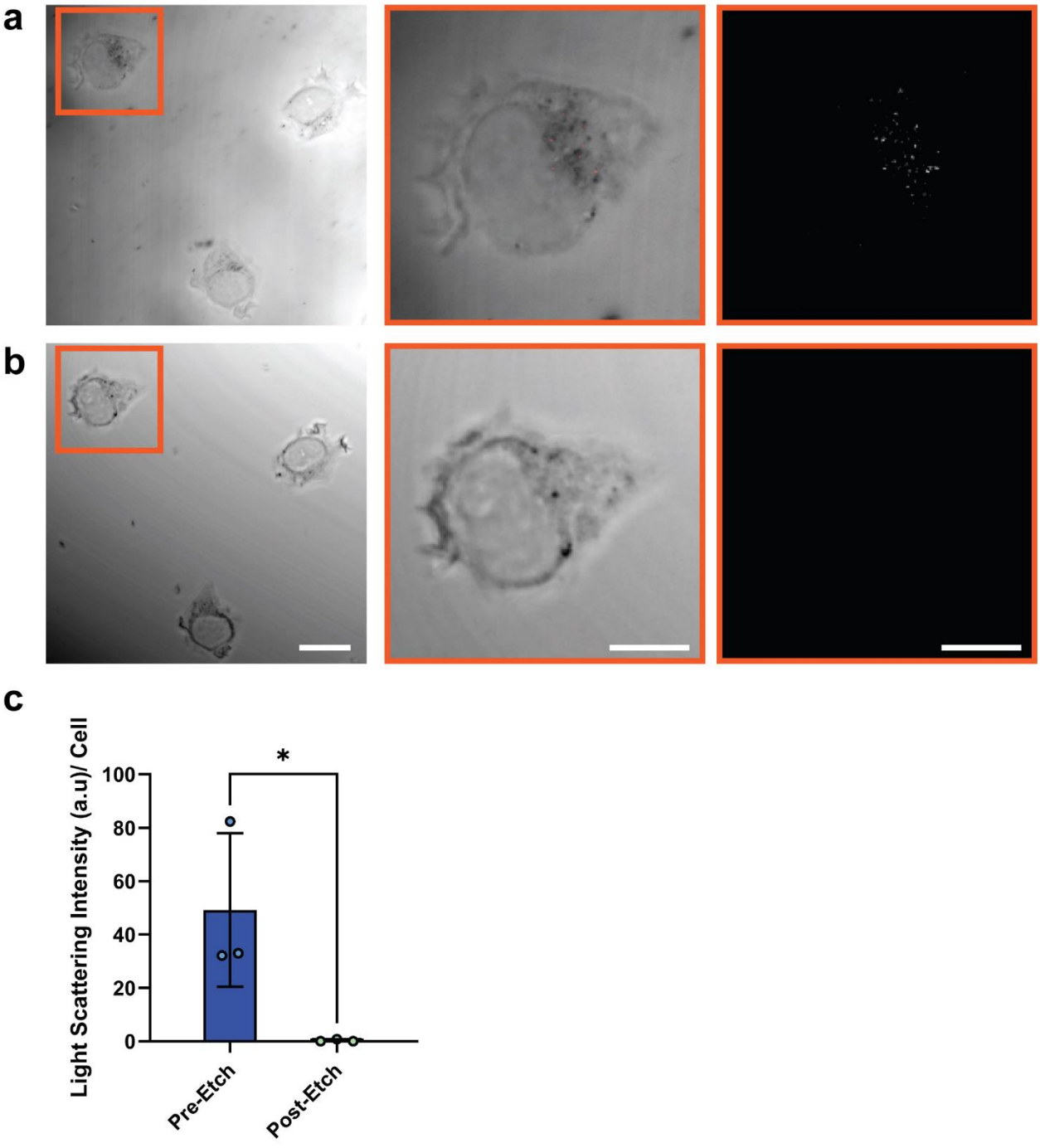


Figure S2.6: Validating the AuNP light scattering signal by gold etching. The 4T1 cells were incubated with 55-nm PEG AuNPs for 24 hours before being washed and fixed. **(a)** Transmitted light image of 4T1 cells with light scattering (red) followed by a digital magnification of a single cell, with the nanoparticle light scattering signal shown alone in grayscale. **(b)** The cells were treated with a gold etching solution consisting of $KI/I_2$, and following three washes with 1X PBS, the same cells from (a) were reimaged, with the light scattering signal no longer being clearly visible. The scale bars indicate 20 µm for the

unmagnified images, and 10 μm for the magnified image **(c)** Quantitative analysis of the light scattering signal from the PEG-AuNPs, measured by the integrated density of the light scattering signal in regions of interest drawn around the membrane of the cells on ImageJ. Bars indicate mean +/- SD. An unpaired one-tailed t-test demonstrated a significant statistical difference in the means of the two groups (*$p<0.05$) ($n$=3).

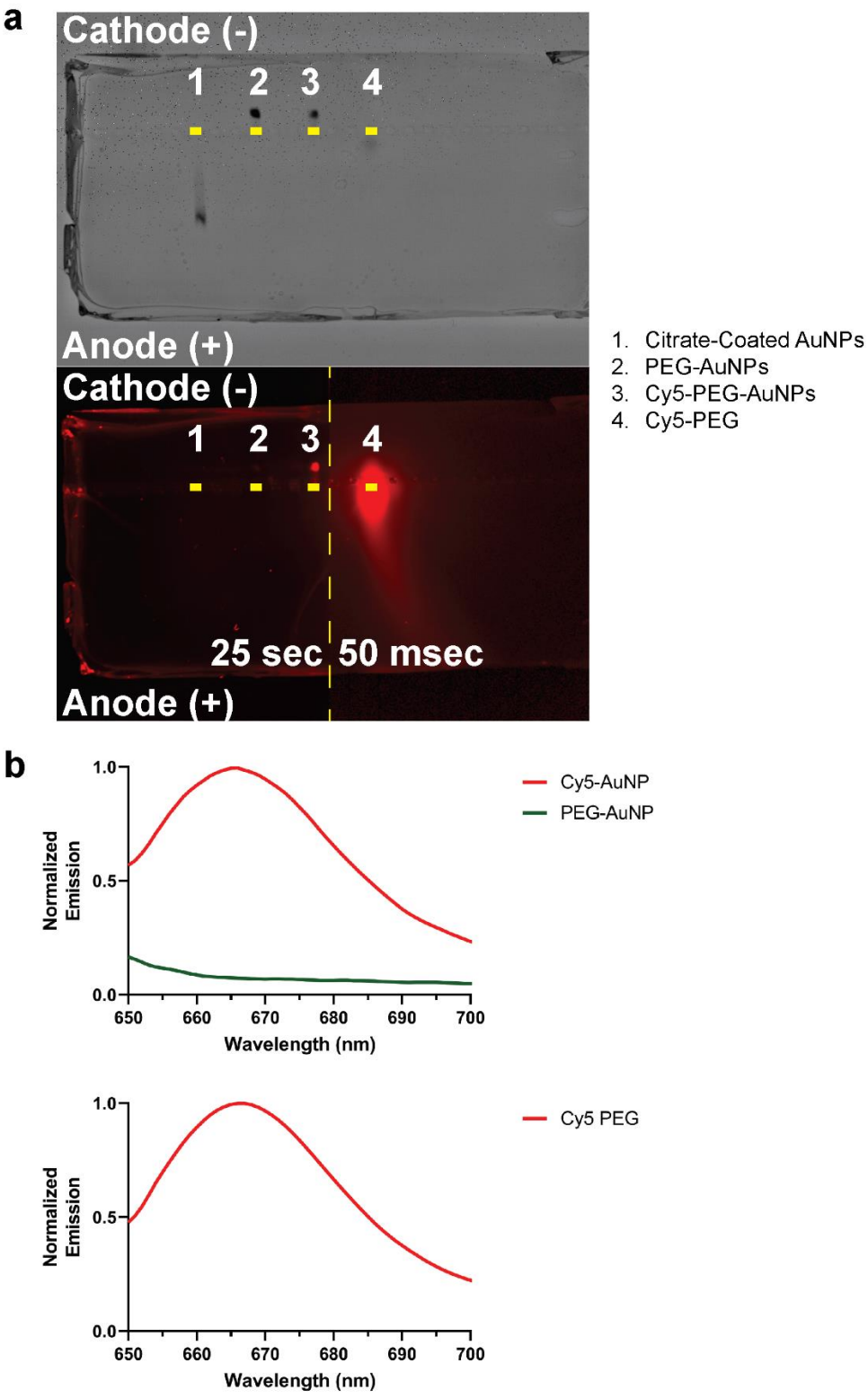


Figure S2.7: Validating the conjugation of Cy5-PEG to 55-nm AuNPs. (a) Top: a visible light image of agarose gel. Bottom: Cy5 image of the same gel, split to image at different exposure times to account for differences in signal intensity between samples. The

citrate-coated AuNPs (1) migrated towards the cathode, while the PEG-AuNPs (2) and Cy5-PEG-AuNPs (3) migrated about the same distance towards the anode, demonstrating a successful conjugation of the PEG to the AuNPs. The Cy5 image demonstrates a fluorescent signal coming from the position where the Cy5-PEG-AuNPs are, as well as the free Cy5-PEG (4), but not where the PEG-AuNPs or citrate-coated AuNPs are, confirming a successful conjugation and functionality of Cy5-PEG-AuNPs. **(b)** The fluorescence emission spectra of Cy5-AuNPs and PEG-AuNPs (top) compared to the fluorescence emission spectra of free Cy5-PEG (bottom).

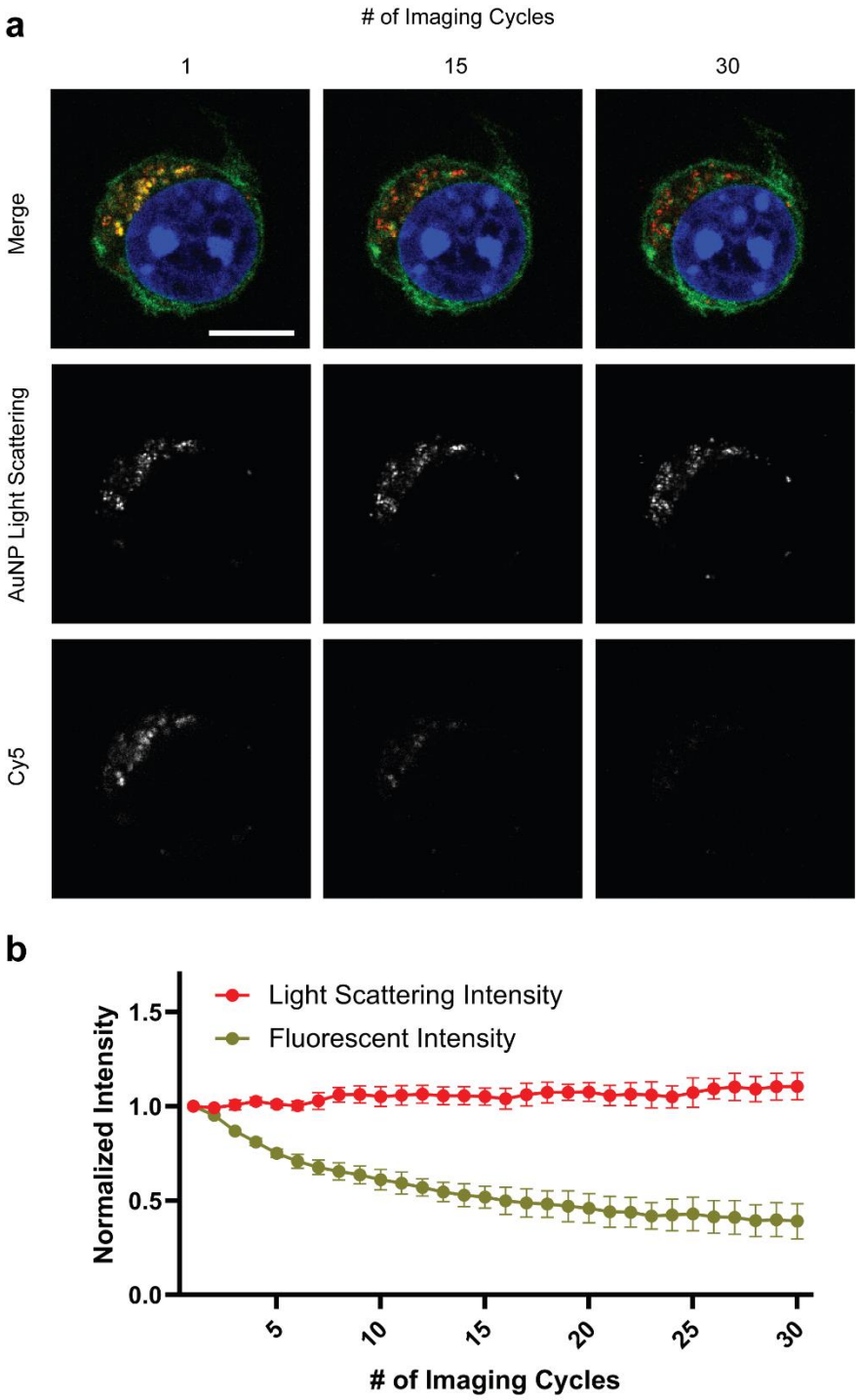


Figure S2.8: Nanoparticle light scattering imaging of AuNPs is impervious to photobleaching. 4T1 cells were incubated with 55-nm Cy5-PEG-coated AuNPs for 24 hours before being washed, fixed, and stained with DAPI (blue) and WGA-CF488A (green). **(a)** A time series of a single, non-expanded 4T1 cell being imaged 30 times, at a rate of 1 image/min. The AuNPs were imaged both with confocal light scattering (red) as well as with excitation of the Cy5 tag (yellow). The individual light scattering and Cy5

channels are shown in grayscale below the complete overlays with the DAPI and WGA-CF488A channels. **(b)** The signal intensities of the light scattering and Cy5 channels of cells were quantified by drawing regions of interest around the membranes of the cells and measuring the integrated densities of the two channels on ImageJ over the course of the timeseries and were then normalized relative to the original intensities from the first time point (*n*=3 cells). The scale bars indicate 10 μm.

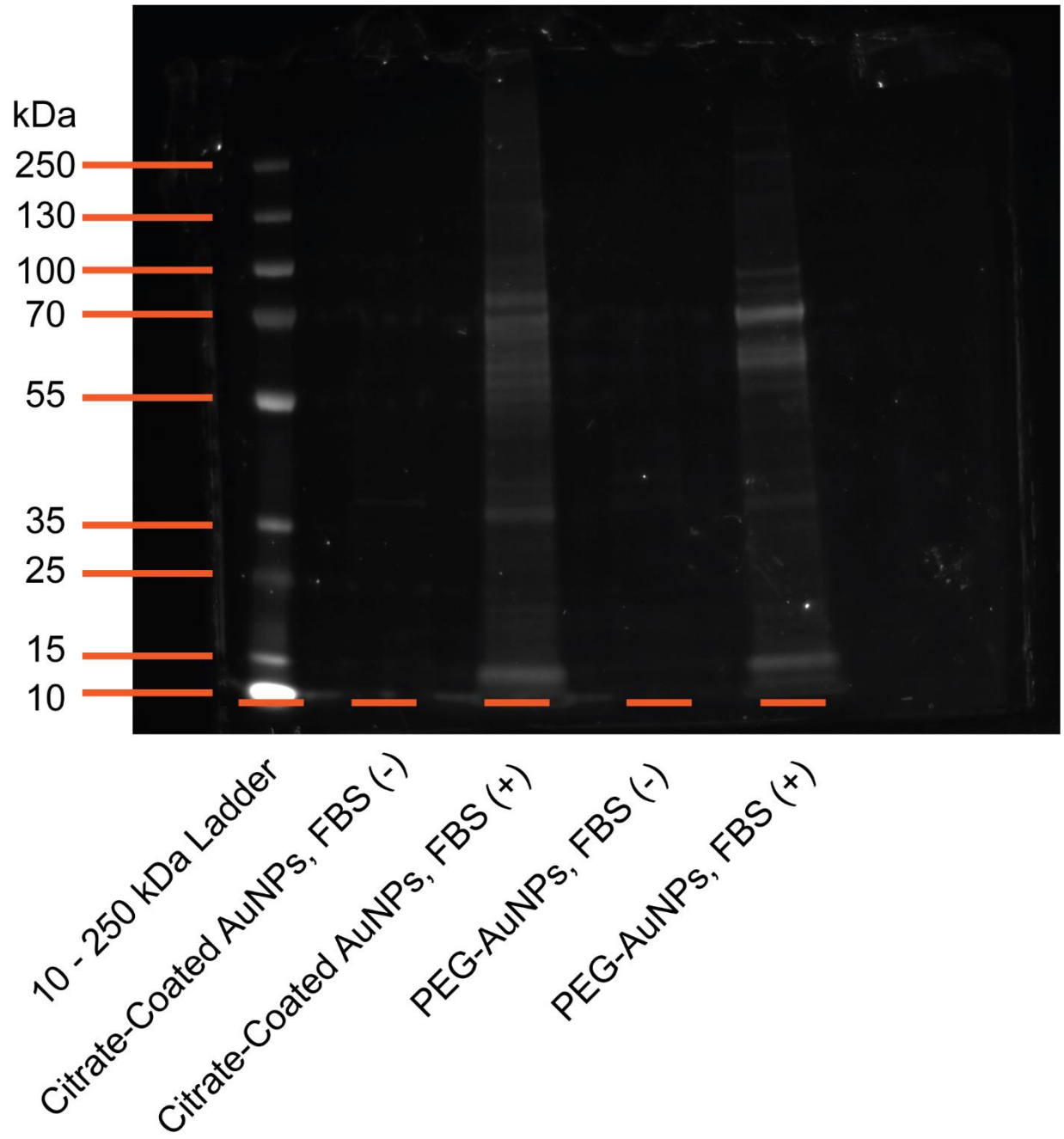


Figure S2.9: Protein coronas form around PEG-AuNPs after incubation with fetal bovine serum. Citrate coated- and PEG-AuNPs were incubated with fetal bovine serum (FBS), nanopure $H_2O$ (Citrate AuNP, FBS(-)), or 1X PBS ((PEG AuNP, FBS(-)) for 16 hours. A sodium dodecyl sulfate-polyacrylamide gel electrophoresis (SDS-PAGE) demonstrates that PEGylation does not eliminate the proteins that spontaneously adsorb on AuNPs, as seen by the visible protein bands on the samples that were incubated with FBS, with no visible protein bands being visible on the samples that were not incubated with FBS.

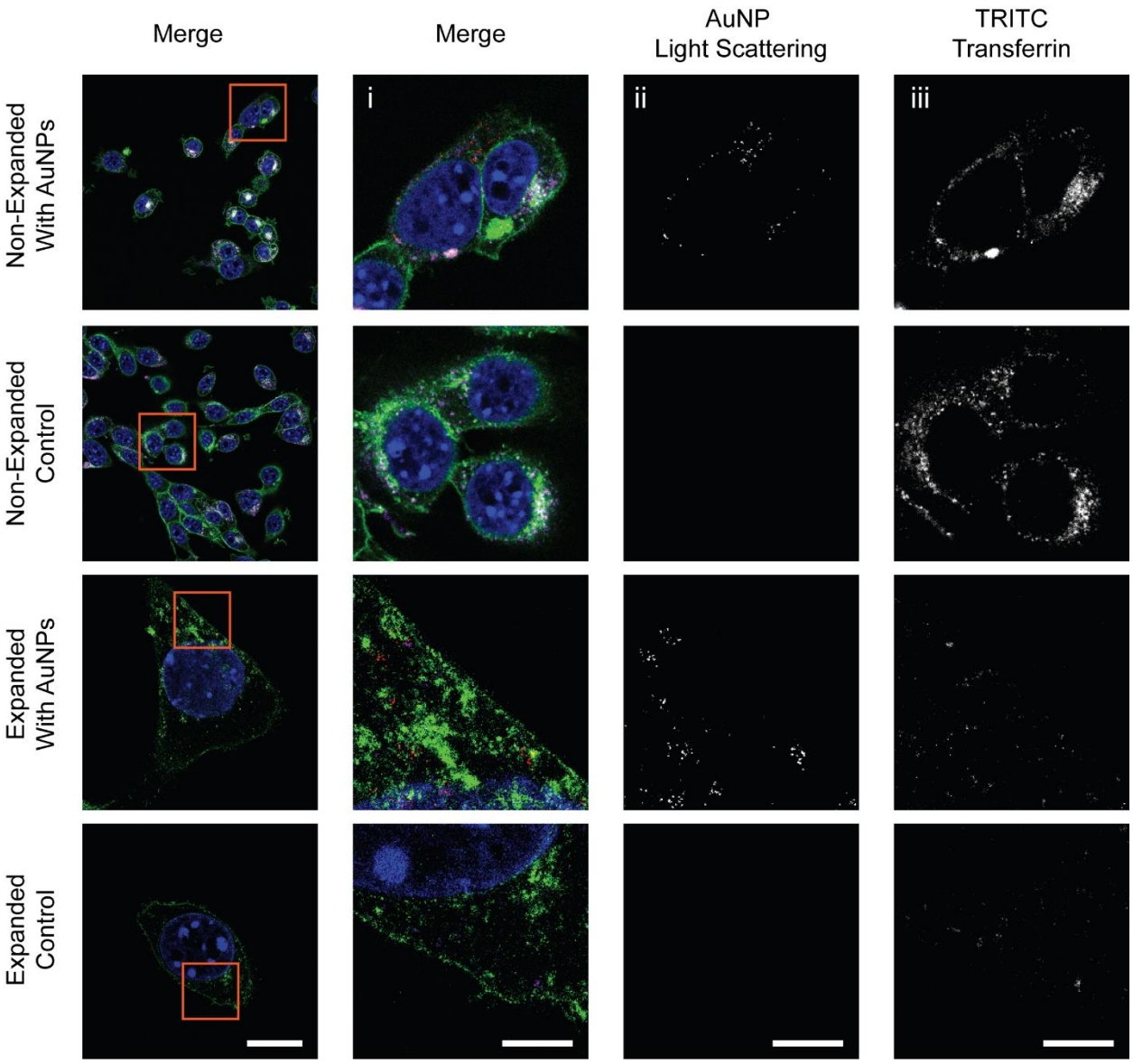


Figure S2.10: Expansion microscopy allows for the super-resolution visualization of endocytic tracers. 4T1 cells were incubated with 25 µg/mL TRITC-transferrin with or without PEG-AuNPs for 24 hours before being washed and subjected to the expansion microscopy protocol. The overlay of all four channels – DAPI (blue), WGA-CF488a (green), light scattering (red), and TRITC (purple) is shown first, followed by magnifications of the regions of interest, indicated by the orange boxes. (i) depicts the direct magnifications of the regions of interest, with (ii) showing only the magnification of the light scattering channel of those regions in grayscale and (iii) showing only the magnification of the TRITC channel of those regions in grayscale. The scale bars indicate 50 µm in the unmagnified images and 15 µm in the magnified images. Scale bars for images of expanded cells are the original length as taken by the microscope (i.e. not corrected for expansion factors).

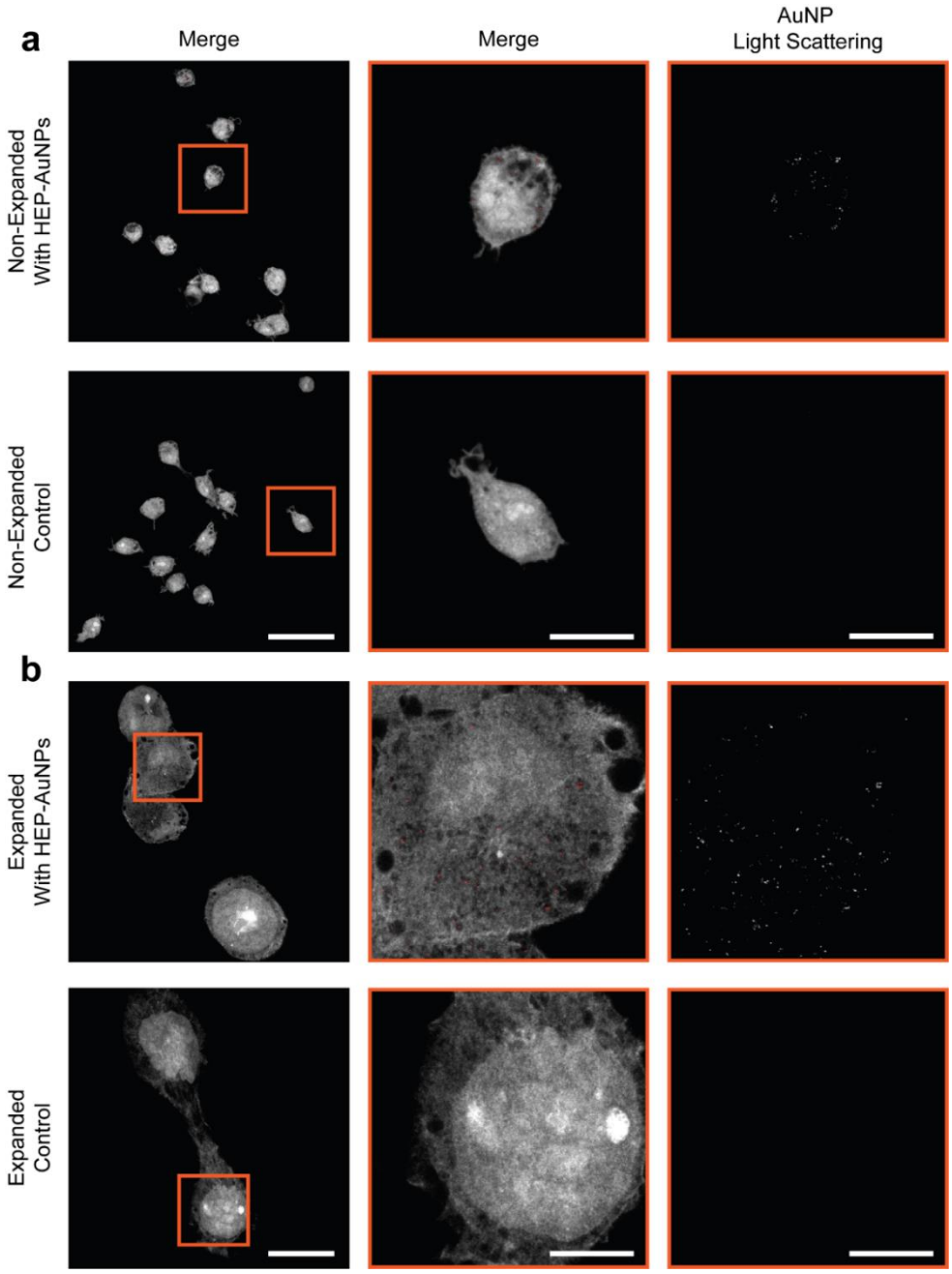


Figure S2.11: Expansion microscopy of DC 2.4 cells is compatible with nanoparticle light scattering imaging of HEP-AuNPs. DC 2.4 cells were incubated with or without HEP-AuNPs for 3 hours before being washed, fixed, and stained with NHS-AF555 (grey) and imaged with light scattering (red). **(a)** Non-expanded cells with or without HEP-AuNPs. **(b)** expanded cell with or without HEP-AuNPs. The direct magnifications of the regions of interest are shown, followed by the nanoparticle light scattering channel only in grayscale. The scale bars indicate 50 µm for the unmagnified images, and 15 µm for the magnified images. Scale bars for images of expanded cells are the original length as taken by the microscope (i.e. not corrected for expansion factors).

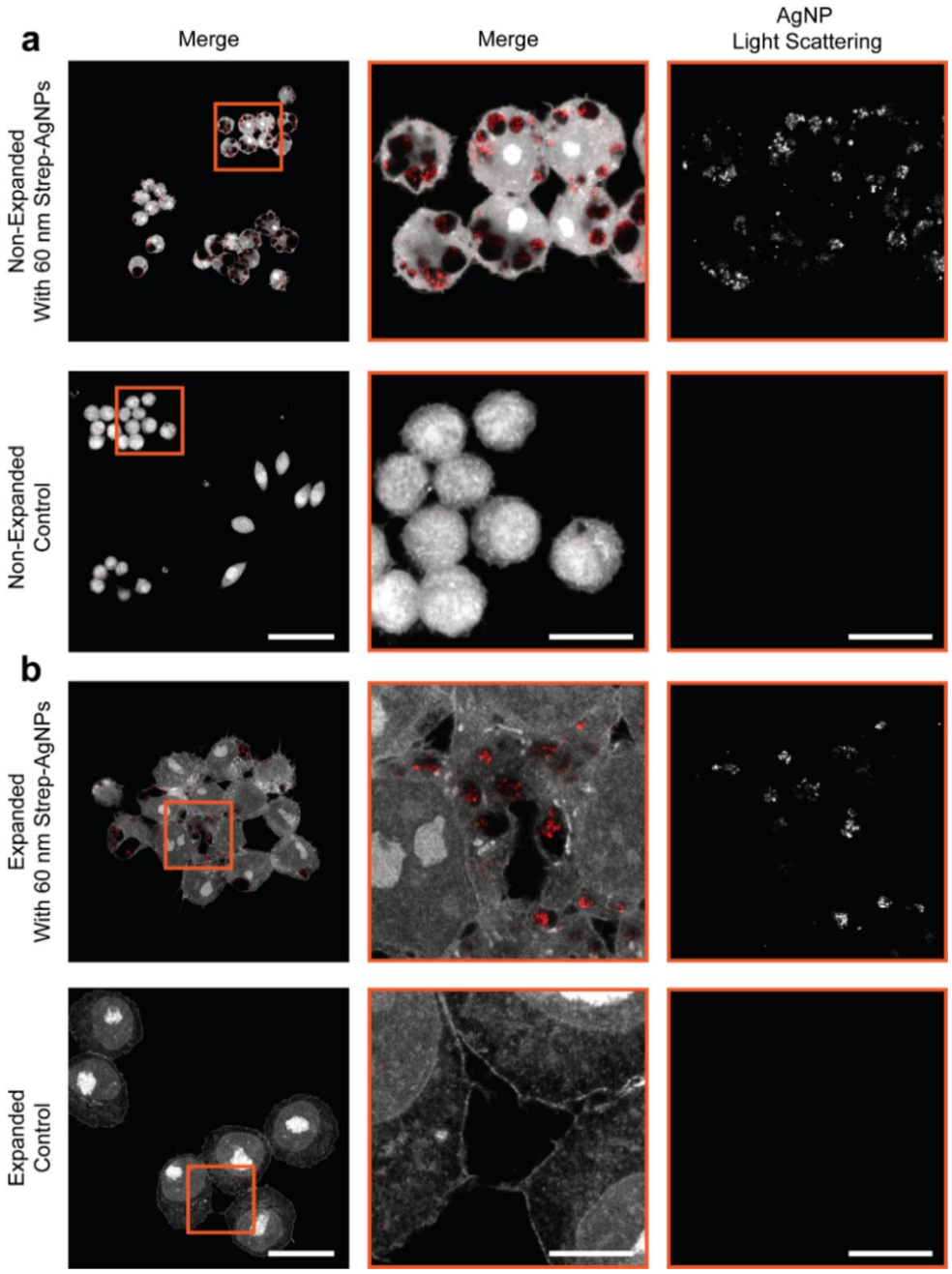


Figure S2.12: Expansion microscopy of RAW 264.7 macrophages is compatible with nanoparticle light scattering imaging of 60-nm Strep-AgNPs**.** RAW 264.7 macrophages were incubated with or without 60-nm Strep-AgNPs for 24 hours before being washed, fixed, and stained with NHS-AF555 (grey) and imaged with light scattering (red). **(a)** Non-expanded cells with or without HEP-AuNPs. **(b)** expanded cell with or without HEP-AuNPs. The direct magnifications of the regions of interest are shown, followed by the nanoparticle light scattering channel only in grayscale. The scale bars indicate 50 µm for the unmagnified images, and 15 µm for the magnified images. Scale bars for images of expanded cells are the original length as taken by the microscope (i.e. not corrected for expansion factors).

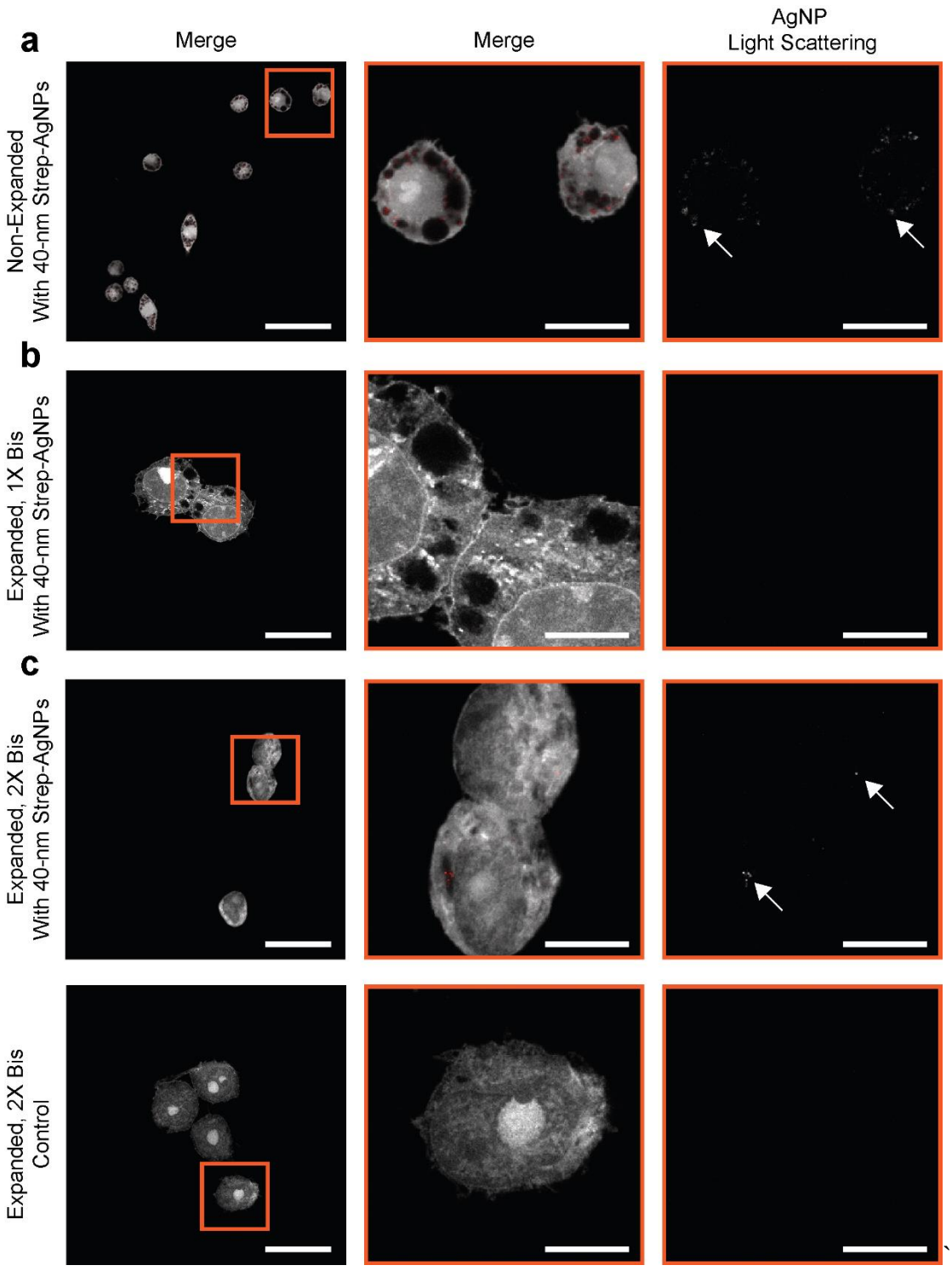


Figure S2.13: Increasing the crosslinker density of the expansion gel allows for smaller nanoparticles to be visualized post-expansion. RAW 264.7 macrophages were incubated with or without 40-nm Strep-AgNPs for 24 hours before being washed, fixed, and stained with NHS-AF555 (grey) and imaged with light scattering (red). The white arrows indicate the position of the 40-nm Strep-AgNPs. **(a)** Non-expanded cells with 40-nm AgNPs. **(b)**

In expanded cells with 40-nm AgNPs, however, there is no visible light scattering signal within the cells. Increasing the crosslinker density of the acrylamide gel creates a stiffer gel matrix, which likely prevents smaller nanoparticles from flowing out through the pores of the gel. Here, we used a gel with double the crosslinker concentration in the gel monomer solution. **(c)** Expanded cells with or without AgNPs in 2X crosslinker gels. The direct magnifications of the regions of interest are shown, followed by the nanoparticle light scattering channel only in grayscale. The scale bars indicate 50 μm for the unmagnified images, and 15 μm for the magnified images. Scale bars for images of expanded cells are the original length as taken by the microscope (i.e. not corrected for expansion factors).

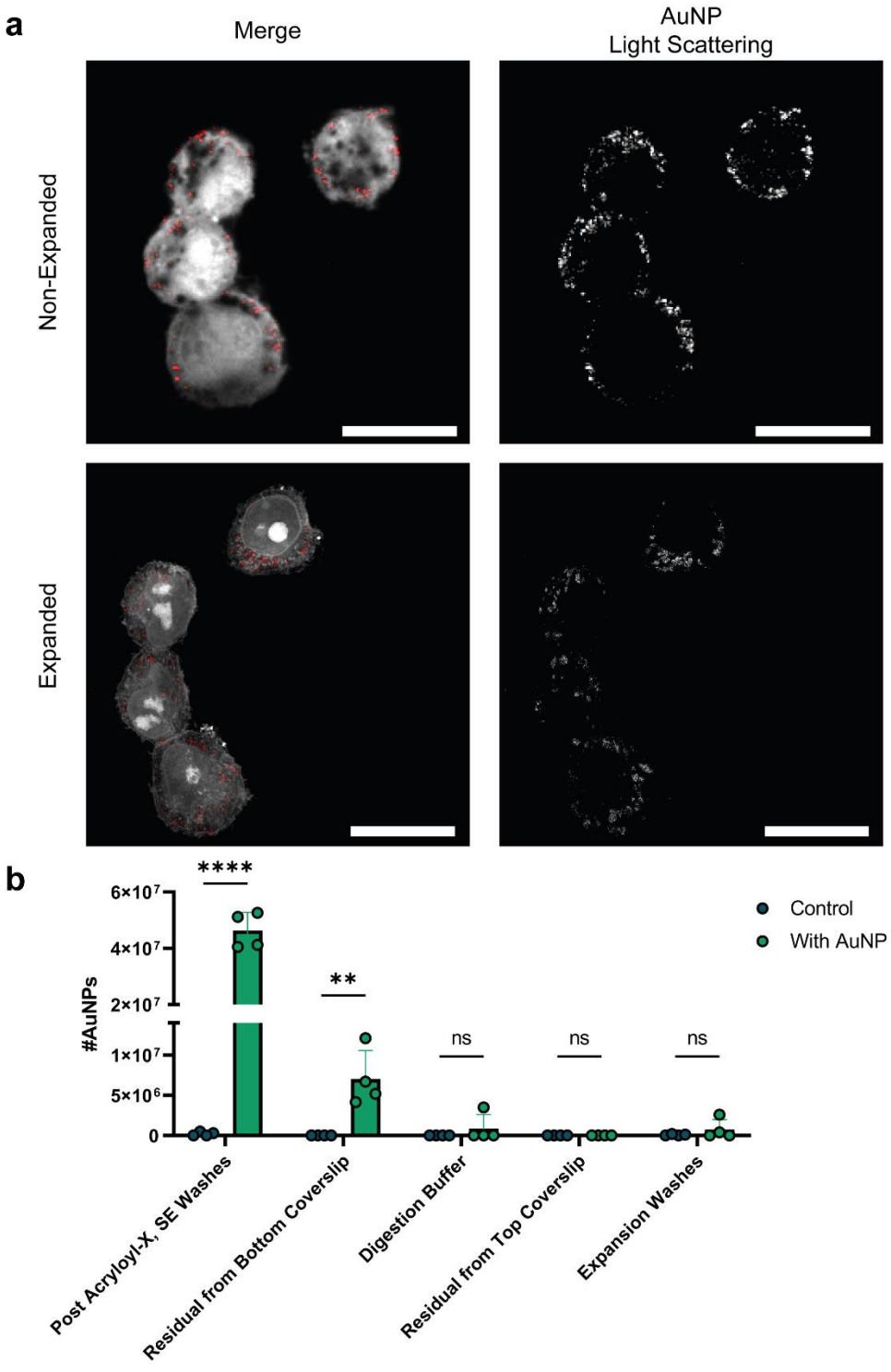


Figure S2.14: Determining potential intracellular AuNP loss from expansion. **(a)** RAW 264.7 macrophages were incubated with HEP-AuNPs for 3 hours before being washed, fixed, and stained with NHS-AF555 (grey) with nanoparticle light scattering imaging (red), first with the overlay of both channels, and then the nanoparticle light scattering signal alone shown in grayscale. The same groups of cells were imaged before and after the

proExM process. The expanded cells shown are a maximum intensity projection of 4 slices around the center of a Z-stack to account for the 3D volumetric spreading of the nanoparticles within the cells. The scale bars indicate 15 µm in the non-expanded cell images, and 50 µm in the expanded cell images. Scale bars for images of expanded cells are the original length as taken by the microscope (i.e., not corrected for expansion factors). **(b)** Inductively coupled plasma mass spectrometry (ICP-MS) analysis of the intracellular AuNP loss through the expansion process. Bars represent mean +/- SD. A two-way ANOVA with Šidák's multiple comparison test showed a statistical significance in the detected gold content between cells that were treated with AuNPs and untreated controls in the washes after the Acryloyl X, SE treatment (****$p<0.0001$) as well as the residual cells that remained on the bottom coverslip during gelation (**$p<0.01$), but no statistical significance in the remaining steps (ns = not significant, $p>0.99$). The gold content detected in the first two steps is not likely to be from intracellular AuNPs. The Acryloyl-X treatment is not a destructive process, so the detected gold content was likely from uninternalized AuNPs that were mechanically dislodged during the treatment. Similarly, the gold content from the second step was likely from cells that did not transfer to gel or from cells in pieces of the gel that remained stuck to the coverslip. Since the remaining steps of the proExM process (digestion and expansions) involve chemically and physically disrupting the mechanical structure of the cell, it would be expected that any potentially lost intracellular AuNPs would be found within those solutions ($n$=4).

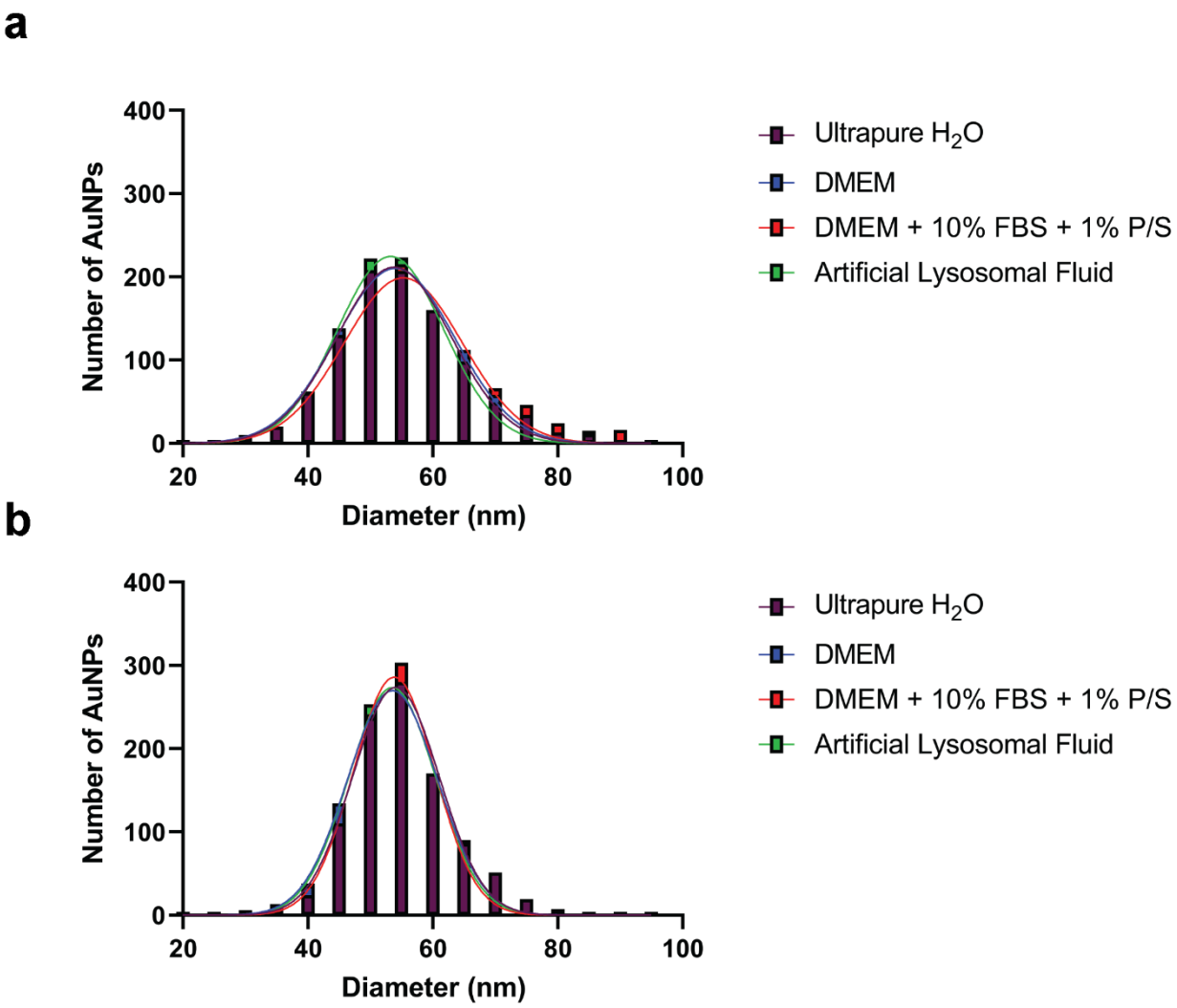


Figure S2.15: Testing AuNP colloidal stability using single`-particle inductively coupled plasma mass spectrometry. **(a)** HEP-AuNPs and **(b)** PEG-AuNPs were incubated in ultrapure $H_2O$, DMEM, DMEM + 10% fetal bovine serum (FBS) + 1% penicillin/streptomycin (P/S), or artificial lysosomal fluid for 3 hours at 37°C. Following washing through centrifugation, the AuNPs were characterized with single-particle inductively coupled plasma mass spectrometry (SP-ICP-MS). The Kruskal-Wallis test with Dunn's multiple comparison test did not show significant differences in the means of the distributions of either type of AuNPs after incubation in DMEM, DMEM + 10% FBS + 1% P/S, or artificial lysosomal fluid compared to the ultrapure $H_2O$ control ($p>0.9999$) ($n$=1,000).

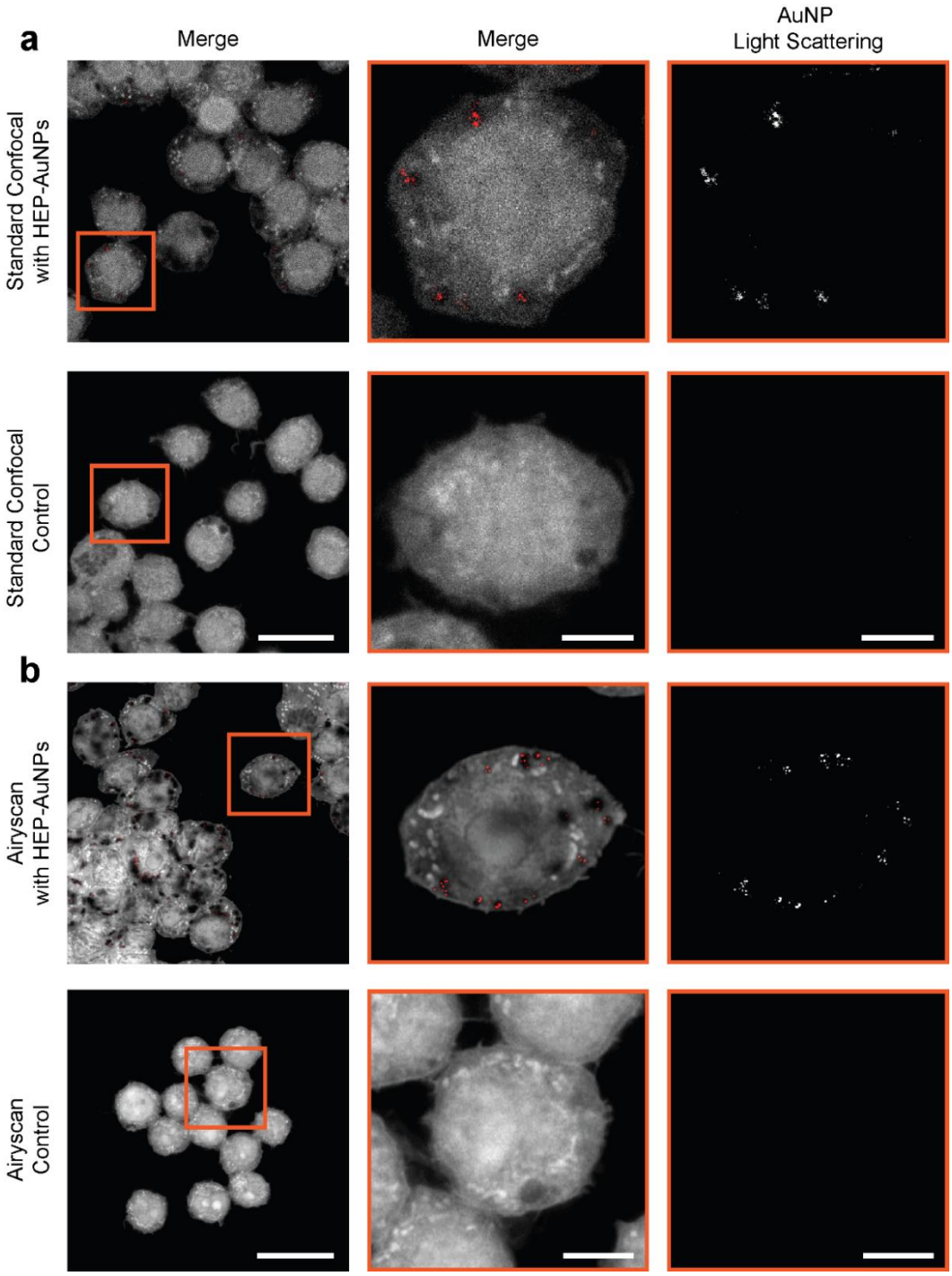


Figure S3.1: Validation of pan-ExM results with Airyscan. RAW 264.7 macrophages were incubated with HEP-AuNPs for 3 hours before being washed, fixed, and stained with NHS-AF555 (grey) with nanoparticle light scattering imaging (red), first with the overlay of both channels, and then the nanoparticle light scattering signal alone shown in grayscale. The cells were first imaged under standard confocal conditions **(a)** and then with the Airyscan detector **(b)** for super-resolution imaging. The scale bars indicate 20 µm for the unmagnified images, and 5 µm for the magnified images.

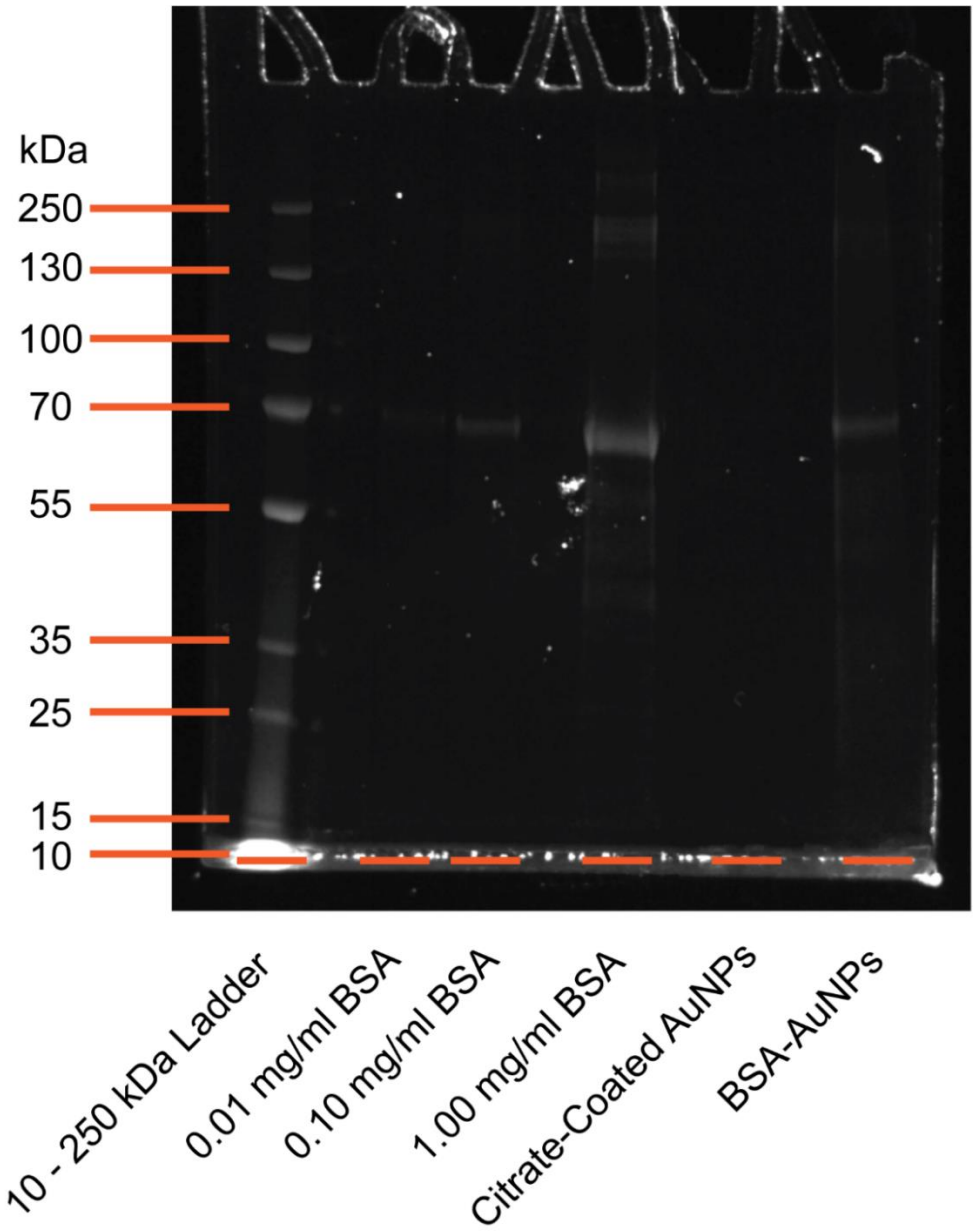


Figure S3.2: Verifying the formation of a BSA protein corona on 55 nm AuNPs via SDS-PAGE. BSA-AuNP and citrate-coated AuNPs, along with a range of concentrations of free BSA (processed in the same way as the nanoparticles) were run through SDS-PAGE. BSA has a molecular weight of approximately 66.5 kDa, which is corroborated by the protein bands of the free BSA appearing strongly between the 55-kDa and 70-kDa bands of the protein ladder. A strong band appears on the BSA AuNP lane at approximately the same position, with no band appearing on the citrate-coated AuNP lane, which validates that a BSA protein corona had formed on the BSA-AuNPs.

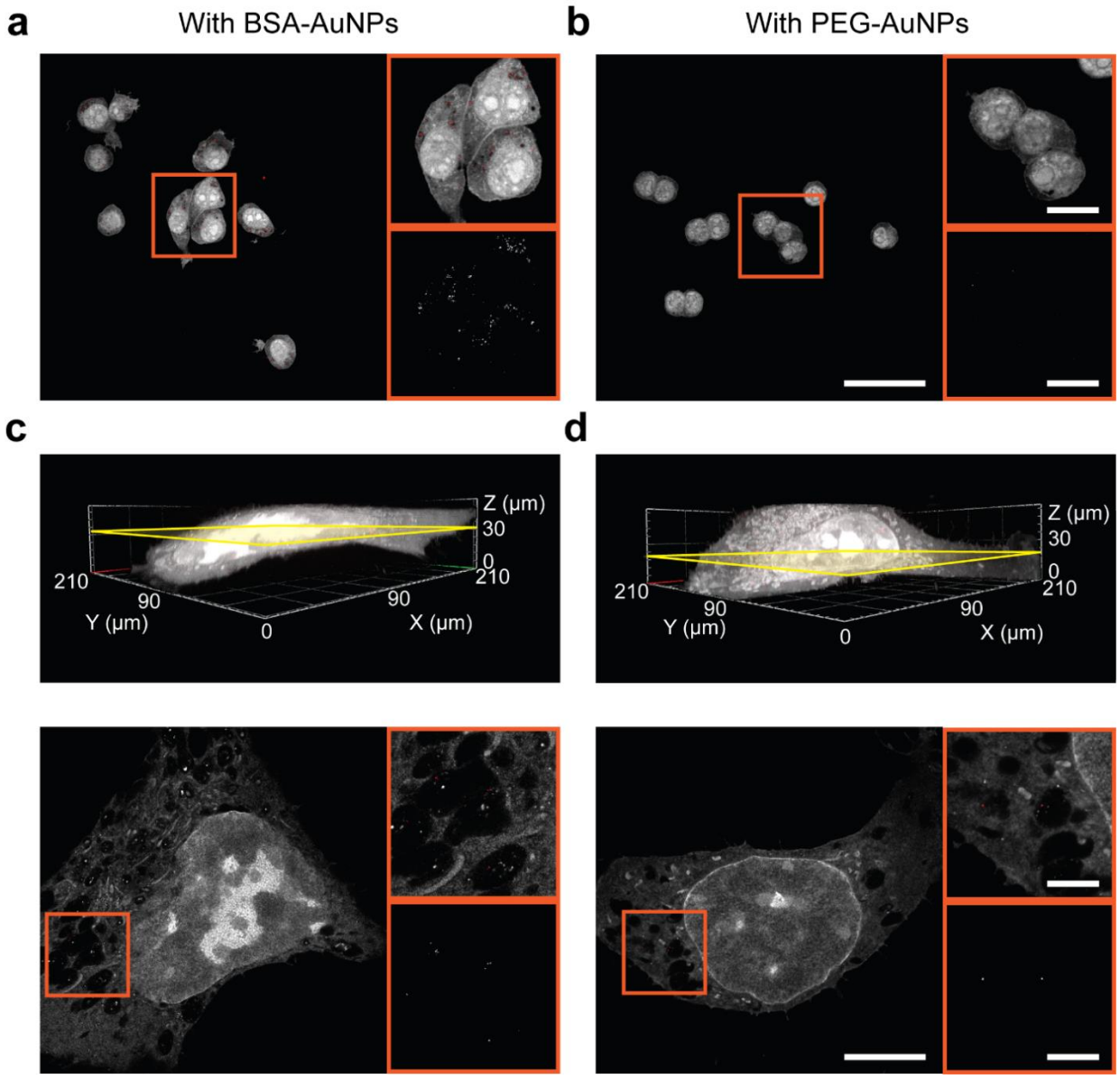


Figure S3.3: Pan-ExM with nanoparticle light scattering imaging allows for the comparison of the uptake of AuNPs with different surface modifications. Non-expanded 4T1 cells stained with NHS-AF555 (grey) incubated with BSA-AuNPs **(a)** or PEG-AuNPs **(b)**, with the AuNP light scattering signal (red). Digital magnifications of the regions of interest are shown, first with the overlay of both channels, and then the nanoparticle light scattering signal alone is shown in grayscale. Pan-ExM was then performed on cells incubated with BSA-AuNPs **(c)** or PEG-AuNPs **(d)**, with 3D reconstructions of CLSM Z-stacks being shown. The yellow regions of interest depict individual slices from the z-stacks, with similar digital magnifications. Similar to the non-expanded cells, more BSA-AuNPs are visible in the expanded cells compared to PEG-AuNPs. The scale bars indicate 50 µm in the unmagnified image, and 15 µm in the magnified image. Scale bars for images of

expanded cells are the original length as taken by the microscope (i.e. not corrected for expansion factors).

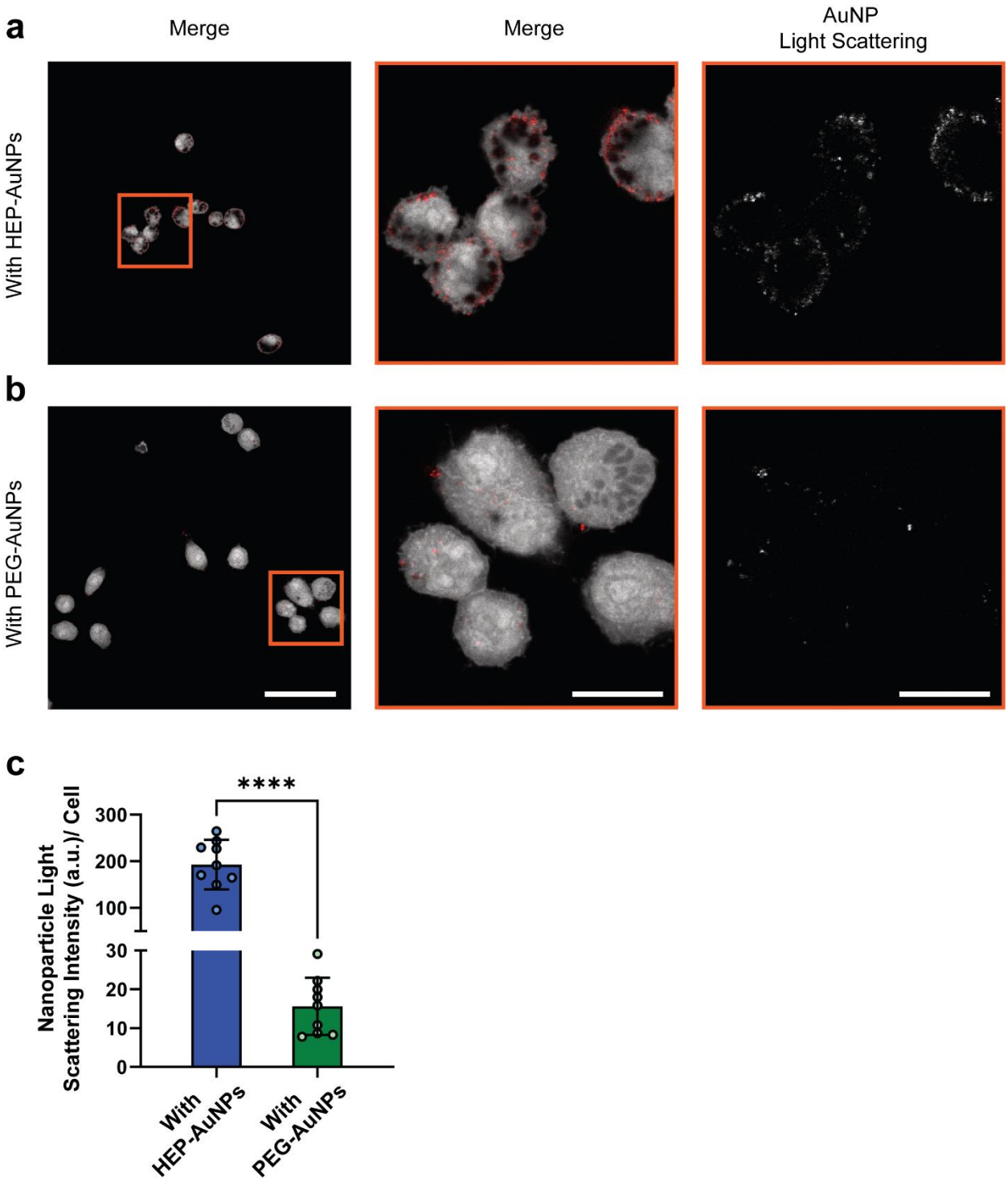


Figure S3.4: Non-expanded RAW 264.7 macrophages treated with HEP- or PEG-AuNPs. RAW 264.7 macrophages were incubated with or without **(a)** HEP-AuNPs or **(b)** PEG-AuNPs for 3 hours before being washed, fixed, and stained with NHS-AF555 (grey) with nanoparticle light scattering imaging (red). Digital magnifications of the regions of interest are shown, first with the overlay of both channels, and then the nanoparticle light scattering signal alone shown in grayscale. The scale bars indicate 50 μm for the

unmagnified images, and 15 μm for the magnified images. **(c)** Quantitative analysis of the light scattering signal from the HEP- and PEG-AuNPs, measured by the integrated density of the light scattering signal in regions of interest drawn around the membrane of the cells on ImageJ. An unpaired one-tailed t-test demonstrated a significant statistical difference in the means of the two groups (****$p<0.0001$) ($n=9$).

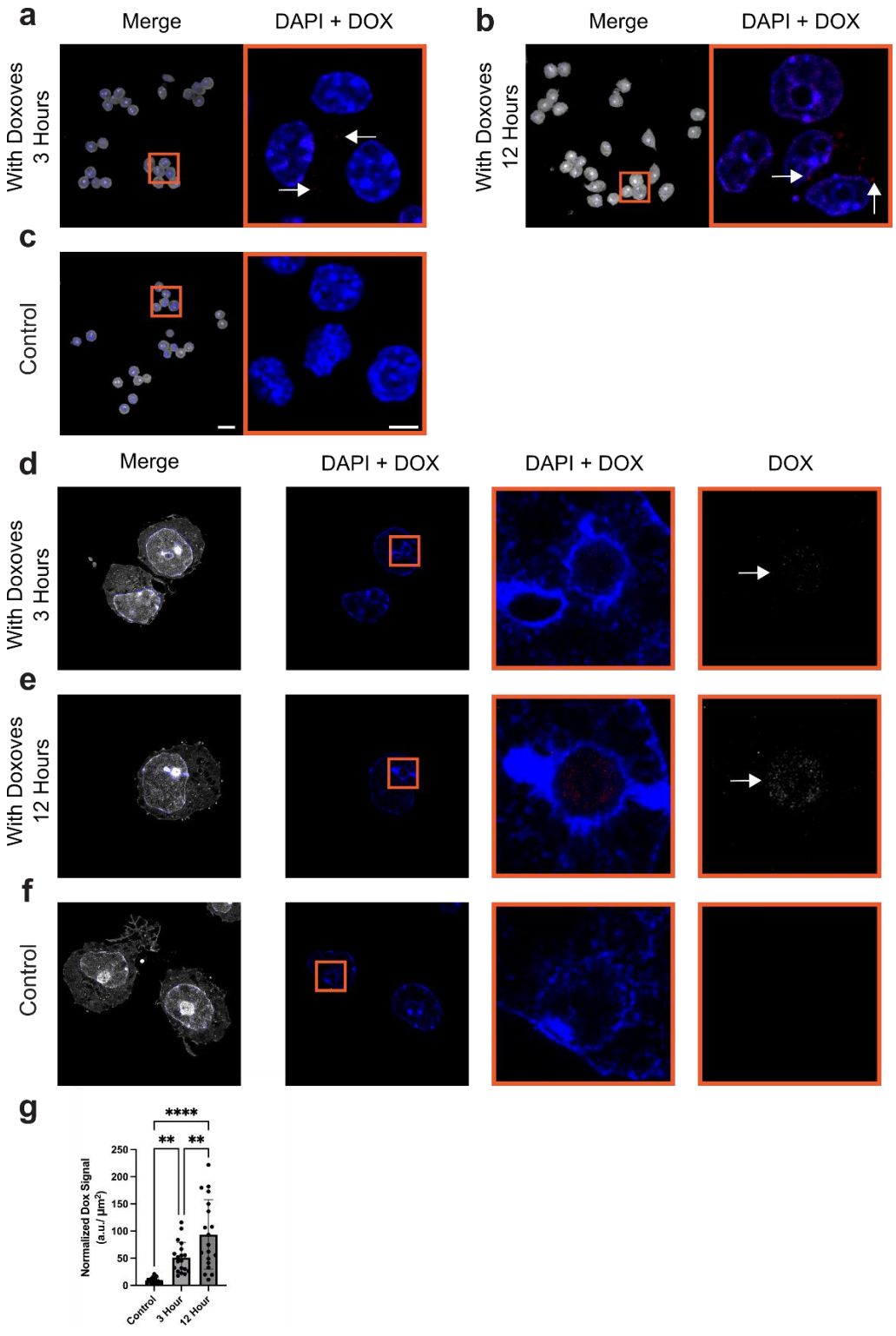


Figure S4.1: RAW 264.7 macrophages treated with Doxoves. RAW 264.7 macrophages were incubated with 100 µg/mL Doxoves for 3 or 12 hours, along with non-treated controls, before being washed, fixed, and expanded with the Magnify protocol. Non-

expanded cells shown first **(a - c)**, followed by expanded cells **(d - f)**. Cells were stained with NHS-AF647 (gray) and DAPI (blue). First the overlay of the NHS-AF647, DAPI, and DOX (red) is shown. For non-expanded samples, a digital magnification of a region of interest showing the overlay of only the DAPI and DOX signals is included. For expanded samples, the full overlay of only the DAPI and DOX is shown, followed by a digital magnification of a region of interest of those two channels, and then the DOX signal is shown alone in grayscale. White arrows indicate the position of DOX signal. **(g)** Quantitative analysis of the integrated density of DOX signal within regions of interests drawn around the holes of the nuclei in expanded cells that were not stained with NHS-AF647 on ImageJ, normalized by the area of the region of interest in $\mu m^2$. A one-way ANOVA with Tukey's multiple comparison test resulted in statistically significant differences in the means of the DOX signal between the three groups (**$p<0.01$, ****$p<0.0001$). The scale bars indicate 20 µm in the unmagnified images and 5 µm in the magnified images.

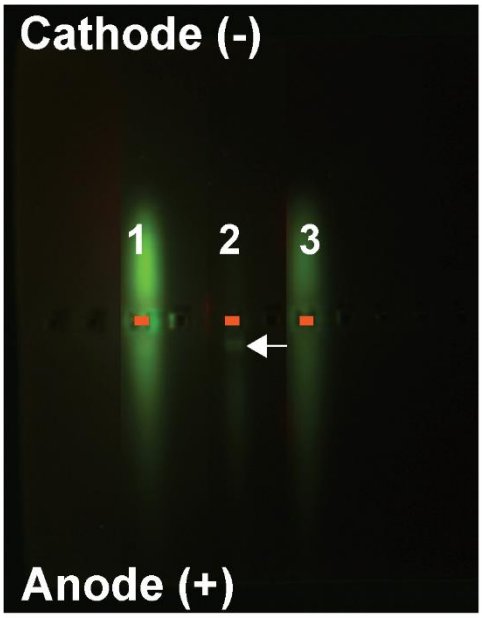


1. 10 kDa Dextran-AF488-PEG-Liposomes before Filtering
2. 10 kDa Dextran-AF488-PEG-Liposomes after Filtering
3. Free 10 kDa Dextran-AF488, 25 µg/mL

Figure S4.2: Agarose gel electrophoresis of 10 kDa Dextran-PEG-Liposomes. 10 kDa dextran-AF488-PEG-liposomes, before and after filtering with Amicon centrifugal filters, along with free 10 kDa dextran-AF488 were run through a 0.5% agarose gel for 60 minutes at 80 V. The orange lines indicate the positions of the wells of the gel. The white arrow indicates the position of the fluorescent band of the PEG-Liposomes, present in lanes with the PEG-Liposomes, which have migrated towards the anode, while being absent in the free dextran lane, as expected. The lane with the PEG-Liposomes following filtration shows much less of the signal that is visible in the free dextran lane, suggesting that the filtration was successful in removing a high amount of free dextran from the liposome solution.

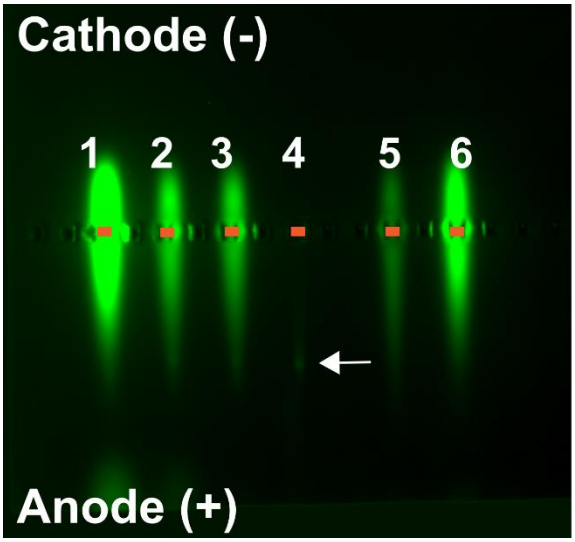


1. 10 kDa Dextran-AF488-Thiol Lipid-Liposomes
2. 10 kDa Dextran-AF488-HEP-Liposomes before Dialysis
3. 10 kDa Dextran-AF488-HEP-Liposomes after Dialysis
4. 10 kDa Dextran-AF488-HEP-Liposomes after Dialysis and Filtering
5. Free 10 kDa Dextran-AF488, 5 µg/mL
6. Free 10 kDa Dextran-AF488, 25 µg/mL

Figure S4.3: Agarose gel electrophoresis of 10 kDa Dextran-HEP-Liposomes. 10 kDa dextran-AF488-Thiol-liposomes and 10 kDa dextran-AF488-HEP-liposomes before and after dialysis against 1X PBS through a dialysis membrane and filtering with Amicon centrifugal filters, along with free 10 kDa dextran-AF488 were run through a 0.5% agarose gel for 40 minutes at 80 V. The orange lines indicate the positions of the wells of the gel. The white arrow indicates the position of the fluorescent band of the HEP-Liposomes, present in lanes with the HEP-Liposomes, which have migrated towards the anode, while being absent in the free dextran lane, as expected. The lane with the HEP-Liposomes following filtration shows much less of the signal that is visible in the free dextran lane, suggesting that the filtration was successful in removing a high amount of free dextran from the liposome solution.

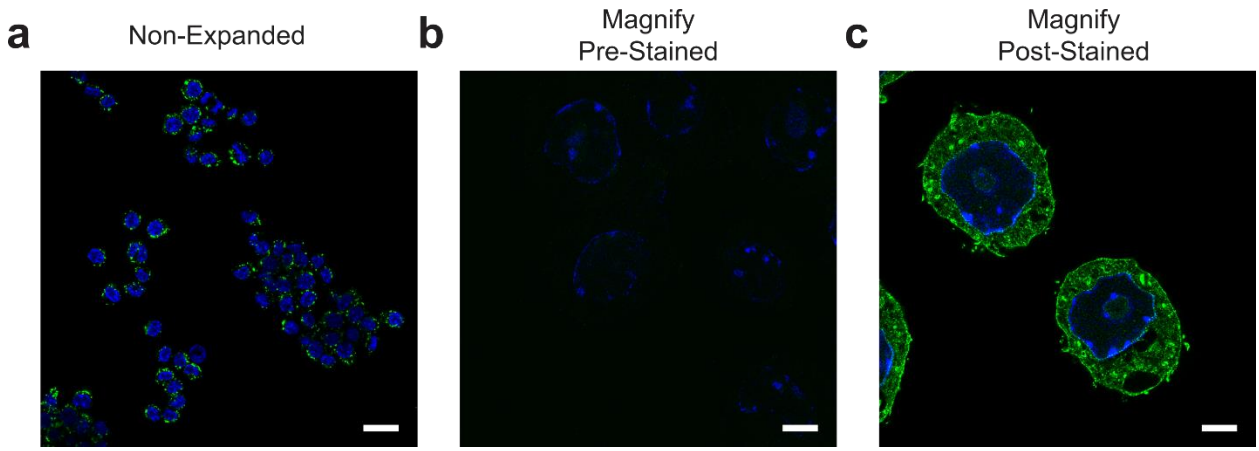


Figure S4.4: DiO signal in Magnify samples is lost before expansion. **(a)** Live RAW 264.7 macrophages were stained with 5 µM DiO (green) and the DNA stain Hoechst (blue) before being fixed, with a visible DiO signal. **(b)** RAW 264.7 macrophages that were stained with 5 µM DiO and Hoechst while still alive, following Magnify processing, with no visible DiO signal. **(c)** RAW 264.7 macrophages that were stained with 5 µM DiO and DAPI (blue) following the homogenization step of the Magnify process, prior to expansion, with a visible DiO signal. The scale bars indicate 20 µm, not corrected for expansion factors.

Supporting Movies are available at https://pubs.acs.org/doi/10.1021/acsnano.2c12808

Supporting Movie 1

An animation of a Z-stack (48 slices) of a RAW 264.7 macrophage treated with HEP-AuNPs, following the pan-ExM process, shown in Figure 5C. First the individual Z-slices are shown, followed by a 3D reconstruction of the entire stack. The cell is bulk (pan) stained with NHS-AF555 (gray), with label-free AuNPs visualized through light scattering imaging (red). The data set was captured using a 40X/1.2 NA water immersion objective on a conventional inverted confocal laser scanning microscope (Zeiss LSM 880).

Supporting Movie 2

An animation of a Z-stack (51 slices) of a RAW 264.7 macrophage without AuNP treatment, following the pan-ExM process, shown in Figure 5D. First the individual Z-slices are shown, followed by a 3D reconstruction of the entire stack. The cell is bulk (pan) stained with NHS-AF555 (gray), with label-free AuNPs visualized through light scattering imaging (red). The data set was captured using a 40X/1.2 NA water immersion objective on a conventional inverted confocal laser scanning microscope (Zeiss LSM 880).

## Appendix D: Chapter Authors and Acknowledgements

### Chapter 1:

Authors: **Vinit Sheth**, Lin Wang, Resham Bhattacharya, Priyabrata Mukherjee, Stefan Wilhelm

Author Contributions:

- Vinit Sheth – Composed most sections and figures/ tables
- Lin Wang – Composed Section 1.2, and Figures 1.2 and 1.3
- Resham Bhattacharya, Priyabrata Mukherjee – Provided discussion about content
- Stefan Wilhelm – Oversaw manuscript completion

Acknowledgements: Authors thank W. Yang for feedback and discussions, and S. Quine for assistance with illustrations. SW acknowledges funding support from the University of Oklahoma IBEST-OUHSC Seed Grant for Interdisciplinary Research, the Oklahoma Tobacco Settlement Endowment Trust awarded to the University of Oklahoma - Stephenson Cancer Center, and the Oklahoma Center for Advancement of Science and Technology (OCAST) Health Research program.

### Chapters 2 and 3:

Authors: **Vinit Sheth**, Xuxin Chen, Evan M. Mettenbrink, Wen Yang, Meredith A. Jones, Ons M'Saad, Abigail G. Thomas, Rylee S. Newport, Emmy R. Francek, Lin Wang, Alex N. Frickenstein, Nathan D. Donahue, Alyssa M. Holden, Nathan Mjema, Dixy E. Green, Paul L. DeAngelis, Joerg Bewersdorf, Stefan Wilhelm

Author Contributions:

- Vinit Sheth – Project lead, primary experiment coordinator and performer, primary writer
- Xuxin Chen, Meredith Jones – Wrote code for automatic analysis of light scattering signal in pan-ExM samples
- Evan M. Mettenbrink – Assisted with nanoparticle synthesis and functionalization, and agarose gel experiments
- Wen Yang, Lin Wang – Assisted with SDS-PAGE, discussion of data analysis and interpretation
- Ons M'Saad, Joerg Bewersdorf – Advised on pan-ExM experiments
- Abigail G. Thomas, Rylee Newport – Assisted with experiments, confocal imaging, data analysis, and figure design
- Alex N. Frickenstein, Nathan D. Donahue, Alyssa Holden – Assisted with ICP-MS experiments
- Emmy Francek, Alyssa Holden - Assisted with nanoparticle synthesis and functionalization and figure design
- Nathan Mjema – Assisted with nanoparticle synthesis and functionalization and image analysis
- Dixy E. Green, Paul L. DeAngelis – Provided and advised on heparosan
- Stefan Wilhelm – Project advisor and corresponding author

Acknowledgements: The authors thank N. Koc, A. Karim, E. Joyce, S. Butterfield, M. Haddad, Y. He, and S. Lyu for their assistance with experiments. We also thank Drs. B.

Zheng, T. Gu, S. Foster, and J. Grime as well as B. Fowler, J. Wilge, and J. Crane for their assistance, and the Chen Lab for kindly providing the DC 2.4 cells. We also thank P. Kidd and Dr. Y. Tian for providing training on pan-Expansion Microscopy. Additionally, the authors acknowledge the University of Oklahoma (OU) Samuel Roberts Noble Microscopy Laboratory (SRNML), the OU Mass Spectrometry, Proteomics & Metabolomics (MSPM) Core, the Oklahoma Medical Research Foundation (OMRF) Imaging Core Facility, and the Oklahoma COBRE in Cancer Imaging Research (Oklahoma Center of Medical Imaging for Translational Cancer Research). This work was supported in part by awards from NIH COBRE (P20GM135009), NSF CAREER (2048130), and OCAST HR20-106. J.B. acknowledges support by the Wellcome Trust (203285/B/16/Z) and NIH (P30 DK045735).

**Chapters 4:**

Authors: **Vinit Sheth***, Abigail G. Thomas*, Hamilton Young, Amberlynn Demko, Lin Wang, Dixy E. Green, Paul L. DeAngelis, Stefan Wilhelm

* Denotes equal contribution

- Vinit Sheth* – Project lead, primary experiment coordinator and performer, primary writer
- Abigail G. Thomas* - Original investigator in visualizing liposomes with Magnify, assisted in method development and liposome synthesis
- Hamilton Young, Amberlynn Demko – established liposome synthesis protocol, and assisted with liposome synthesis

- Lin Wang - Assisted with agarose gel electrophoresis experiments
- Dixy E. Green, Paul L. DeAngelis – Provided and advised on heparosan
- Stefan Wilhelm – Project advisor and corresponding author

Acknowledgements: The authors thank S. Butterfield, M. Jamei, and Y. He, for their assistance with experiments. We also thank B. Fowler, J. Wilge, and J. Crane for their assistance. Additionally, the authors acknowledge the Oklahoma Medical Research Foundation (OMRF) Imaging Core Facility, and the Oklahoma COBRE in Cancer Imaging Research (Oklahoma Center of Medical Imaging for Translational Cancer Research). This work was supported in part by awards from NIH COBRE (P20GM135009), NSF CAREER (2048130), and NIH R35 MIRA (R35GM150758)

## Appendix E: Permissions

### Right to Reuse for Chapter 1

Used with permission of John Wiley & Sons - Books, from Strategies for Delivering Nanoparticles across Tumor Blood Vessels, Sheth, Vinit; Wang, Lin; Bhattacharya, Resham; Mukherjee, Priyabrata; Wilhelm, Stefan, 31, 2020; permission conveyed through Copyright Clearance Center, Inc.

### Right to Reuse for Chapters 2 and 3

Reprinted (adapted) with permission from Sheth, V.; Chen, X.; Mettenbrink, E. M.; Yang, W.; Jones, M. A.; M'Saad, O.; Thomas, A. G.; Newport, R. S.; Francek, E.; Wang, L.; Frickenstein, A. N.; Donahue, N. D.; Holden, A.; Mjema, N. F.; Green, D. E.; DeAngelis, P. L.; Bewersdorf, J.; Wilhelm, S. Quantifying Intracellular Nanoparticle Distributions with Three-Dimensional Super-Resolution Microscopy. ACS Nano 2023, 17 (9), 8376–8392. https://doi.org/10.1021/acsnano.2c12808., Copyright 2023 American Chemical Society